CONVECTIVE PRECIPITATION OVER COMPLEX TERRAIN, CURRENT AND FUTURE CLIMATE

A Thesis Submitted to the College of
Graduate and Postdoctoral Studies
In Partial Fulfillment of the Requirements
For the Degree of Doctor of Philosophy
In the School of Environment and Sustainability
University of Saskatchewan
Saskatoon

By

MARIA LUCIA SCAFF FUENZALIDA

PERMISSION TO USE

In presenting this thesis in partial fulfilment of the requirements for a Postgraduate degree from the University of Saskatchewan, I agree that the Libraries of this University may make it freely available for inspection. I further agree that permission for copying of this thesis in any manner, in whole or in part, for scholarly purposes may be granted by the professor or professors who supervised my thesis work or, in their absence, by the Head of the Department or the Dean of the College in which my thesis work was done. It is understood that any copying or publication or use of this thesis or parts thereof for financial gain shall not be allowed without my written permission. It is also understood that due recognition shall be given to me and to the University of Saskatchewan in any scholarly use which may be made of any material in my thesis.

Requests for permission to copy or to make other use of material in this thesis in whole or part should be addressed to:

Executive Director

School of Environment and Sustainability at the University of Saskatchewan

Room 323, Kirk Hall 117 Science Place, Saskatoon, SK S7N 5C8, Canada.

Phone: (306) 966-1985 Fax: (306) 966-2298 Email: sens.info@usask.ca

OR

Dean

College of Graduate and Postdoctoral Studies University of Saskatchewan

116 Thorvaldson Building, 110 Science Place Saskatoon, Saskatchewan S7N 5C9 Canada.

ABSTRACT

Given the significance of climate models for assessing climate change impacts, and recent increases in their resolution, there is a need to understand strengths and weaknesses of climate models in reproducing key atmospheric processes, and to assess their performance using accurate ground-based observations. This thesis first investigates the inconsistencies in ground-based observations for cold environments, second, the role of ground-based observations for empirical model validation over complex terrain, and third, uses both observations and model output, to describe a mesoscale process associated with precipitation and their changes in a simulated future climate. Regional climate modelling in a convection-permitting configuration improves simulation of mesoscale systems in which convection initiates and develops, adding value to estimates of convective precipitation compared to models that rely on deep convective parameterization schemes. On the leeside of the Canadian Rocky Mountains, in extratropical regions, convective precipitation is influenced by a strong longitudinal gradient of low-level moisture across the foothills. Known as the dryline, this gradient is the result of the convergence of moist air from the interior of the continent and the dry air from the subsidence on the lee side of the Rocky Mountains. The dryline plays a key role in initiating convective precipitation. To find robust answers to questions about a future transient climate, a better understanding is needed of the dryline's relationship to the location and timing of convective initiation. This research has three objectives: 1) to critically quantify the systematic bias of precipitation measurements on two sides of the northern Canada-U.S. border since the two countries use different standard instrumentation to observe liquid and solid precipitation; 2) to study if a convection-permitting model can reproduce the warm season's diurnal cycle of precipitation at a continental scale, and 3) to describe a mesoscale mechanism related to the initiation of convective precipitation in the Rocky Mountains vulnerable to climate change at the end of the century.

Results show that a correction due to wind-undercatch in monthly solid precipitation is up to 31% during January in the Yukon, whereas across the border in Alaskan stations, it is up to 136%. This correction leads to a smaller and inverted horizontal precipitation gradient in the northern part of the border. In July, the correction for monthly liquid precipitation is around 20% in Alaska and 4% in the Yukon. This inconsistency has to be considered in any regional study using precipitation in cold and windy environments. The research to validate the precipitation diurnal cycle characteristics using a convection-permitting model, uses ground-based observations and a gridded product. Results show that the convection-permitting model can represent the main continental patterns and also represent the precipitation peak transitions from the afternoon to night on the leeside of the Rocky Mountains. However, in the central and eastern region of the study domain, the convection-permitting model performance deteriorates during the diurnal cycle for observed morning peaks (in the central-east U.S.) and overestimates the magnitude of the observed diurnal cycle in the southeast region in the U.S. When a warmer climate scenario is simulated at the end of the century, persistent increase is shown both, in the amplitude of the precipitation diurnal cycle and in the precipitation intensity throughout the domain. The warmer climate

simulation also presents an increase in precipitation frequency in the northern region in early summer. These increases may impact the agricultural sector and alter flood risk. Finally, it is found that the convection-permitting model can simulate the dryline, showing an average magnitude of 0.48 g kg^{-1} km^{-1} and its maximum intensity being in July. The dryline is present in 37% of the biggest precipitation events (storms with at least one day above the 85% quantile in 13 years period). Although the percentage of the dryline frequency associated with convective initiation in the future scenario is not substantially changed, the dryline is both more intense (0.55 g kg^{-1} km^{-1}) and narrower. Furthermore, in the simulation of the future climate, an intensification in the north and a dissipation in the southern part of the region was found in a standardized number of occurrences of convective initiation east of the dryline. This finding is associated with a change in the thermodynamical forcing of the most intense precipitation on the selected events in the southern part of the region. By describing the dryline, this research provides a reference point to assess the convective initiation forecasts and offers information on precipitation changes in a warmer scenario at the end of the century.

ACKNOWLEDGMENTS

I would like to thank my supervisor, Dr. Yanping Li, for being an empathic and generous guide, always available to discuss ideas and give me space to pursue my research in a collaborative environment. Thanks to the advisory committee for valuable revisions in this thesis. Thanks to Dr. D. Yang for his dedication in my first manuscript during my Ph.D. Thank you to the research group in the Hydrometeorological Application at the National Center for Atmospheric Research, who provides critical tools and resources to perform my research. Thanks to Dr. A. Prein for his endless support in my study and encouragement to keep exploring in the topics I am interested the most.

Thank you to the supporting agencies that made this Ph.D. possible. To *Becas Chile* program at the *Comisión Nacional de Investigación científica y tecnológica* from the Chilean government. To the Global Institute for Water Security and to the Global Water Futures.

I am especially grateful to Sebastián Krogh, my husband, who has been an amazing partner in all these years, with whom I had shared great conversations about hydrometeorological issues and who has helped me to find a critical perspective for my research. Thanks to my parents, Camilo and Lucía, who has been extremely supportive throughout my life and taught me most of what I am today. Thank you to my siblings: Pía, Loreto and Camilo, who have been always by my side and believing in what I love to do, study the atmosphere.

TABLE OF CONTENT

LIST OF TABLES

LIST OF FIGURES

LIST OF ABBREVIATIONS

AK-YK	Alaska - Yukon
ARW-WRF	Advanced Research Weather-Research and Forecasting model
CAPE	Convective Available Potential Energy
CCAR	Climate Change and Atmospheric Research Initiative
CCRN	Changing Cold Regions Network
CI	Convective Initiation
CIN	Convective Inhibition
CMIP5	Coupled Model Intercomparison Project Phase 5
CONICYT	National Commission for Scientific and Technological Research (in Chile)
CONUS	the continuous U.S.
COOP	Cooperative Observer Network
CPM	Convection-Permitting Modeling
CPU	Central Processing Unit
DFIR	Double fence intercomparison reference
DMC	Double mass curves
DSI-3240	Cooperative Hourly Precipitation across US, 1951 to present
EA3	Fixed radiosonde station from the Weather Modification Inc.
EC	Environment Canada
EL	Equilibrium Level
ERA Interim	ECMWF Re-Analysis- interim
GCM	Global Climate Model
GPU	Graphics Processing Unit
LCL	Lifting Condensation Level,
LFC	Level of Free Convection
LST	Local Solar Time
MB1	Mobile Balloons 1
MB2	Mobile Balloons 2

MCS	Mesoscale Convective Systems
NCAR	National Center for Atmospheric Research
NCEI	National Centers for Environmental Information
NOAA	National Oceanic and Atmospheric Administration
Noah-MP	Noah Multi-Physics (Land-surface model)
NSERC	Natural Sciences and Engineering Research Council of Canada
NSF	National Science Foundation
NWS	National Weather Service
OBS	OBServational dataset
RCM	Regional Climate Model
RCP8.5	Representative Concentration Pathway with a radiative forcing of 8.5 W m^{-2} at the end of the century.
RRTMG	Rapid Radiative Transfer Model (long and short-wave radiation scheme)
sIV	stage IV dataset
SPICE	Solid Precipitation Intercomparison Experiment
SWCN	Surface Weather and Climate Network
TD3240	Cooperative Hourly Precipitation across the U.S., 1900 to 2011
UNSTABLE	Understanding Severe Thunderstorms and Alberta Boundary Layers Experiment
US	United States
USCRN	The U.S. Climate Reference Network
UTC	Universal Time Coordinate
WMO	World Meteorological Organization
WRF-CTR	Weather Research and Forecasting model for a ConTRol simulation
WRF-PGW	Weather Research and Forecasting model for a Pseudo Global Warming simulation
WSR-88	Weather Surveillance Radar-1988 Doppler radars
WVX	Fixed radiosonde station from Environment Canada.
YSU	Yonsei University (planetary boundary layer scheme)

CHAPTER 1

INTRODUCTION

1.1 Motivation and relevance

Heavy precipitation events are abnormal episodes, which are difficult to observe. Observed data associated with these events are usually scarce, discontinuous, or unreliable. Observational methods have recently improved, but because these events occur infrequently and little is known about their underlying physical processes, it is difficult to perform a reliable forecast or straightforward analysis. Both low-resolution and high-resolution convection-permitting atmospheric models have been used to simulate the physical processes associated with precipitation. Although low-resolution models are more feasible to run for long periods of time over large spatial domains, high-resolution models have several advantages: first, they can be used after validation to reconstruct the atmospheric conditions with better accuracy on the mesoscale processes compared to models performed at lower resolution, which do not resolve the spatial scale of the critical processes associated with convective precipitation; and second, they can help to represent the spatial variability of meteorology in regions that have high variability, such as complex mountainous terrain.

Despite the advantages of validated high-resolution atmospheric models, scientists still need to know more about the uncertainties in observations. This knowledge improves the understanding of the modelling performance and provides a source of information to use as a tool for decision making on water-related issues. The next sections present a literature review about general characteristics of precipitation; how precipitation is measured, how mountains influence the surrounding atmosphere and thus precipitation, and the differences in the two main types of precipitation: convective and stratiform. In the second half of the literature review, more details are presented on convective precipitation, its diurnal cycle and the challenge in identifying convective initiation. Finally, a review of the main observed and projected changes of precipitation over North America in a warmer climate is provided.

1.2 Theoretical background

1.2.1 Observed precipitation

The first and best approach to an improved understanding of the physical processes that modulate rainfall, snow, and any other type of precipitation is observations of the weather. Many different methods to observe precipitation are available, such as rainfall gauges using tipping buckets or weight sensors, snowfall gauges using weight sensors (e.g., snow pillows), acoustic sensors or manual measurement (using a ruler) to obtain the snow depth. For each type of measurement, different types and brands of instruments can be chosen to perform the observations.

Although the diversity of instrumentation provides a range of measurement alternatives, these instruments are unable to standardize observations accurately on a large spatial and temporal scale. One issue with instrumentation is the lack of consistency of long-term measurements. This problem is more apparent over cold and windy regions with high amounts of snow, a frequent scenario in high latitudes and in mountainous environments. One advance that partially addresses the inconsistency is a windshield, which reduces this systematic bias by decreasing the wind speed around the instrument. For snow measurements, the windshield can reduce the error by half (Goodison et al., 1998). Efficiency varies from 20% in an unshielded NWS 8-inch gauge to up to 70% in a Canadian Nipher with an integrated shield at 6 m s^{-1} (Yang et al., 1998). Despite the windshield's effectiveness, 72% of the automatic instruments used to measure solid precipitation from the countries with the World Meteorological Organization (approximately 54 countries) do not incorporate a windshield (Nitu and Wong, 2010). The systematic precipitation undercatch due to wind affecting the gauge (wind-undercatch) has a complex dependency on the precipitation type, the instrument used and the type of windshield (Smith, 2008; Kochendorfer et al., 2018; Rasmussen et al., 2012; Martin, 1999; Rasmussen et al., 2014; Thériault et al., 2012; Chubb et al., 2015). When precipitation records are critical to the analysis, the consequences of the uncertainty of the wind-undercatch precipitation bias can overshadow scientific answers. Some examples are seen in mountains in which the precipitation records are used to validate an atmospheric model and then analyze snowfall changes in future projections (Steger et al., 2013). A recent, interesting study done over an alpine environment demonstrated how the wind-undercatch precipitation bias affects the spatial orographic precipitation gradient in the mountains, even showing an average negative precipitation gradient (Collados-Lara et al., 2018). In this study, a comparison of liquid and solid precipitation with and without the wind-undercatch correction will be analyzed on the Alaska-Yukon border.

When comparing point measurements of precipitation to spatially distributed gridded precipitation products, or atmospheric model simulations, several limitations must be considered. Many precipitation products are estimated using different interpolation methods, such as distance-angular weighting schemes (Isotta et al., 2014) or Kriging techniques, which can consider the orographic effect on the interpolation (e.g., Goovaerts, 2000; Collados-Lara et al., 2018) over complex terrain. These methods normally underestimate high precipitation intensity in the gridded

products (Haylock et al., 2008; Isotta et al., 2014). On the other hand, the output of regional atmospheric models provides precipitation on the mass points (grid box center) that represent the average over the grid area, so when they are compared to point measurements, one could expect a smoothing signal in the simulated data. Both comparisons are subject to uncertainties, and a broader set of different types of data to compare in any model validation will offer a better quantification of the uncertainties. In this thesis, a verification of warm season precipitation from a regional climate model will be performed against observational data and a gridded product from ground-based weather stations and radar measurements in the U.S.

1.2.2 Mountain meteorology

Mountains are complex terrain that influence the weather and climate. The atmosphere develops unique features over mountainous areas, such as a strong precipitation gradient (e.g., Roe, 2005), mountain waves (Smith, 1979), diurnal circulations (Zardi and Whiteman, 2013), and barrier jets or other dynamical-related circulation (Jackson et al., 2013). Mountains affect cloud formation and precipitation by different mechanisms. One of these occurs when a stable airmass, uplifted due to the slope, causes the air to cool and the water vapour to condense, leading to the formation of cloud and precipitation droplets. Although the mechanisms that produce clouds and precipitation over the mountains comprise complicated linear and non-linear interactions, some efforts have been made to generalize the patterns of how orographic precipitation is generated. Roe (2005) and Colle et al. (2013) have classified the main features associated with orographic precipitation: (1) the microphysics on a small scale, (2) the interaction between the ambient flow and the topography, and (3) the large-scale dynamics. Houze (2012) also highlights thermodynamic forcing as a critical factor in the formation of precipitating cloud. Different patterns have been identified, from a linear upslope flow, to more complex influences of mountains on the flow around them and precipitation. Some examples of these interaction are: accretion growth of precipitation from a seeder-feeder mechanism between high and low clouds; orographic waves effect to initiate precipitation; blocking air at low-levels to increase the upslope motion; and the boundary layer evolution to produce precipitation through the capping lid dissipation when an inversion layer is present (Houze, 2012).

Precipitation around mountains is usually accompanied by a baroclinic disturbance that helps to create a favourable unstable environment to trigger precipitation and extend storms (Colle et al., 2013). The interaction between the mountain-forced effect on precipitation and the baroclinic disruptions has been extensively studied because of its obvious impact on human beings. Some examples are as follows: (1) in the Andes Mountains, the effect of cutoff lows on the subtropical Andes (Garreaud and Fuenzalida, 2007), midlatitude disturbances (Barrett et al., 2009; Seluchi et al., 2006), and non-linear effects of the Andes barrier jet over the spatial precipitation distribution (Scaff et al., 2017), and (2) in the Sierra Nevada and Rocky Mountains, the role of the atmospheric rivers in efficiently bringing moisture from the ocean to the west coast of the U.S. (Neiman et al., 2008), the spatial precipitation distribution affected by topography (Lundquist et al., 2010), and the relationship between orography and the initial development of extreme events in Canada (Szeto

et al., 2011). In this last study, Szeto et al. (2011) found that coupling of a surface low pressure system and an upper level cutoff low generated the diffluent flows over the foothills which are associated with a strong updraft. This configuration created a long-lived and slow-moving storm in the region.

In mesoscale[1] dynamics, mountain circulation systems, associated with the diurnal mountain wind system, mountain waves, and barrier jets are the main mechanisms that modulate the intensification of precipitation (Jackson et al., 2013; Zardi and Whiteman, 2013). Along with forced uplift, these features help to develop convergence lines, water vapor transportation, and the generation of vorticity, all of which, in turn, enhance the atmospheric conditions that intensify convective precipitation (Sherwood et al., 2010). As well as the orographic effect, different types of precipitation – stratiform and convective – can also be present over complex topography. Convective precipitation is normally responsible for intensifying storms and for making the greatest contribution to flash flooding events in steep terrain (Akaeda et al., 1995; Hapuarachchi et al., 2011; Spencer and Stensrud, 1998; Yates et al., 2001).

1.2.3 Convective precipitation

Convective precipitation is relevant to extreme events over foothills, particularly in spring and summer, when conditions such as an unstable atmosphere, a convergence zone along the foothills, and sufficient moisture and energy are present (Wallace and Hobbs, 2006). The concepts of convective precipitation and stratiform precipitation still have no clear division. Indeed as Steiner (2004, p.958) commented, referring to the convective and stratiform precipitation separation, *"It is obvious that nature is not binary, and there is thus ongoing debate about the need to classify and how best to accomplish it."*. However, it is known that convective and stratiform precipitation are different in at least two respects: their vertical profiles of latent heat and the horizontal mass convergence as shown by Houze (1997). Latent heat flux and horizontal mass convergence are more pronounced close to the ground for convective precipitation (Houze., 1997), and latent heat near the surface is the source of high convectively available potential energy (CAPE) in classical convection (but probably not for night-elevated convection). In convective precipitation, a more pronounced convergence produces more vertical uplift than in the stratiform precipitation, and thus major buoyant parcels in convective clouds. Convective precipitation has vigorous air parcel lifts, with vertical wind speed peaks of around 10 m s^{-1}, while a slower uplift (vertical wind speed below 2 m s^{-1}) and a broader area of influence characterize stratiform precipitation.

At a smaller scale, the microphysical processes of cloud and precipitable droplets are clearly different for these two types of precipitation. Convective precipitation droplets usually grow by collection (coalescence and rimming), whereas stratiform particles are mostly formed by vapor deposition. The separation between convective and stratiform precipitation has been assessed

[1] The horizontal scale of mesoscale phenomena is defined at around 2-2000 km, and the temporal scale is defined by the buoyancy oscillation and a pendulum day (1 hour to 1 day approx.) (Lin, 2007, chapter 1).

using a variety of datasets such as satellites and dual-polarized Doppler radars, all of them giving a different result of this separation (Lang et al., 2003). Theoretically, Houze (2014) maintains that for stratiform precipitation, the mean vertical velocity of the surrounding air needs to be substantially larger than the typical terminal fall velocity of ice hydrometeors.

During an intense precipitation event, which may contain convective precipitation, several environmental factors can impact the intensity and volume of precipitation. For example, the land-atmosphere interaction plays a critical role in the energy and mass fluxes, and thus in the available local moisture and energy (Betts et al., 1996). Other examples are (1) the snow melt effect on soil moisture and the available energy to evaporate and destabilize the atmosphere (Seneviratne et al., 2010), (2) the effect of soil moisture on local rainfall through the moisture recycling process (Eltahir et al., 1996; Szeto, 2002), and (3) the evolution of an atmospheric trough associated with a low-pressure system passing through and its role in the destabilization of the lower atmosphere.

Over the foothills and in spring and summer, the increase of solar radiation and available moisture within the convergence zone condition the convective environment over several mountain ranges around the world, such as the leeside of the Rocky Mountains (Smith and Yau, 1993; Hobbs et al., 1996; Weckwerth and Parsons 2006), the leeside of the subtropical Andes (Zipser et al., 2006; Rasmussen et al., 2011) and the Pakistani and Indian Hindu-Kush-Himalayas (Medina et al., 2010; Houze et al., 2007). This warm and moist environment increases CAPE, destabilizes the atmosphere, and, together with the convergence lines, promotes Convective Initiation (CI). This environmental setup may lead to the development of complex convective systems over the foothills, which can range from a few hours to days and are usually embedded in a diurnal and semidiurnal forcing related to the mountain plain circulation and the propagation of the systems (Carbone et al., 2002).

1.2.4 Diurnal cycle of convection

The diurnal and semidiurnal forcing that affect the generation of convective precipitation and the propagation of the systems are determined by incoming solar radiation and its effect on generating thermal convection, cold-pool gravity currents (Rotunno et al., 1988), and inertia-gravity waves (Li and Smith, 2010). The diurnal cycle of convective precipitation has been identified in the Amazonia using observations, with a maximum convective activity seen around 18:00 h (local standard time; LST), as opposed to the 12:00 h (LST) estimated using an atmospheric model (Betts, 2002). Betts argues that the model, which cannot simulate the growth of the dry convective boundary layer in the morning, caused this difference. Mesoscale convective systems (MCS) in China have shown that convective precipitation has a large diurnal variation across the country (Yu et al., 2007). This variation in China can be explained by the propagation of the systems and the topography differences, similar to those in the U.S., where many studies have been conducted on the diurnal variation and the propagation of MCS. For example, the timing of maximum convective precipitation between the east side of the Great Plains (in the afternoon) and the foothills of the Rockies and the central Great Plains (at night) has been discussed (e.g. Jiang et al., 2006; Carbone and Tuttle, 2008), highlighting that the differences are caused by the eastward

propagation of the convective systems from the Rocky Mountains and to the Appalachians Mountains (e.g. Carbone et al., 2002; Li and Smith ,2010). The diurnal cycle is a key characteristic of convective precipitation, therefore its representation on model simulations is critical to correctly simulate convective precipitation. This thesis validates the diurnal cycle of warm season precipitation of a regional climate model in a convection-permitting configuration at 4-km resolution for a decadal and continental scale.

1.2.5 Convective Indices

Convective indices are a simple and useful approach to evaluate the influence of atmospheric stability on the development of convection. Common indices are the convective available potential energy (CAPE) and the convective inhibition index (CIN; c.f., Wallace et al., 2006, p.346), both of which are calculated from vertical profiles of temperature and humidity. CIN quantify the energy needed to raise a parcel to the Level of Free Convection (LFC) (Figure 1 - 1). The convective indices are especially helpful in the analysis of the capping lid development through radiosondes records. The capping lid is a warm and very stable layer (i.e., an inverted temperature layer in which the temperature increases with altitude), which maintains the moist air below it (in the boundary layer) and a very unstable atmosphere aloft (Browning et al., 2007). The quantification of CIN and CAPE helps to explain the removal of the capping lid through (1) moistening, and/or (2) warming at lower levels, or (3) the lifting of the air mass, for example, by around 150 meters in a mountainous environment, which produces enough increase of CAPE and decrease of CIN to sustain convection (Browning et al., 2007).

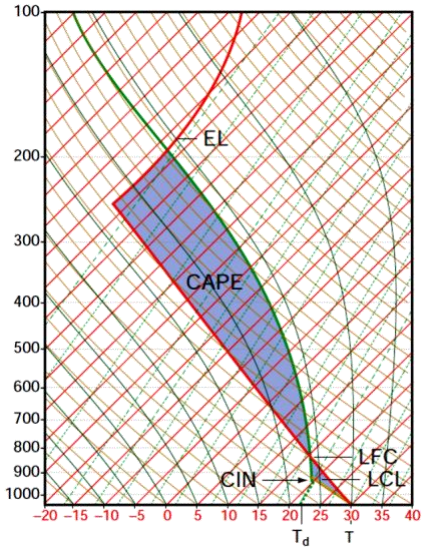

Figure 1 - 1 Skew-T Log-P diagram with the two convective indices: CAPE and CIN (shaded areas). LCL is the Lifting Condensation Level, LFC is the Level of Free Convection and EL is the Equilibrium Level. The solid red line is the environment temperature profile, and the solid green line is the theoretical temperature air parcel profile which is lifted from the surface adiabatically up to the LCL and then through the pseudo-adiabatic. Wallace and Hobbs (2006).

1.2.6 Convective initiation

Having enough CAPE is necessary but not sufficient to trigger convection. To develop moist convection, a combination of different mechanisms is needed, such as a strong low-level moisture gradient, orographic waves or thermodynamic processes (Sherwood et al., 2010). Although a complete understanding of these factors and their interaction is lacking (Sherwood et al., 2010), one known factor with a critical role in the generation of convection is convergence zones, (e.g., Weckwerth and Parsons, 2006; Wilson and Roberts, 2006; Sherwood et al., 2010). These zones provide a pre-storm sign of convection development. Some examples of atmospheric convergence that influence CI are: a strong humidity gradient, known as the dryline; a storm outflow, known as a gust front; and temperature gradients, known as fronts. All of these convergence features influence wind circulation and thermodynamic fields such as humidity, temperature, pressure, and density. Studies have related gust fronts to long-lived storms in the Great Plains in the U.S. (Wilson and Roberts, 2006). The gust fronts have a smaller scale of detection and usually precede a second storm in a moist convective environment; i.e., the gust fronts help to maintain existing storms. (Wilson et al., 2010; Lothon et al., 2011). Another example of a convergence zone is a line of strong moisture gradient, which is a key pre-storm feature over the leeside of the Rocky mountains in southern Wyoming (Bergmaier and Geerts, 2015; Campbell et al., 2013), the central Great Plains (Ziegler et al., 1997) and the Canadian Rockies (Strong, 1989; Taylor et al., 2011). The dryline generates an imbalance in the atmosphere that is solenoidally forced. The solenoidal circulation is in a baroclinic fluid, in which the pressure and density levels are not parallel. The solenoidal circulation produces lifting air parcels at the moist side that helps balance the strong moisture gradient and favors convective clouds. Ziegler and Rasmussen (1998) argue that the critical key is to produce sufficient lifting of the moist parcels above the Level of Free Convection (LFC), which must occur before the parcels leave the mesoscale updraft zone, to be able to trigger CI. If the LFC is not reached, the parcels will tend to fall back (downdraft) to the outflow rolls (Fig. 17 in Ziegler and Rasmussen, 1998). Although advances has improved in understanding CI, the accurate prediction of CI is still a challenge (Alexander et al., 2018; Burlingame et al., 2017; Clark et al., 2015). In this thesis, the CI associated to the dryline, is studied using a convection-permitting model.

1.2.7 A warmer climate in North America

Many characteristics in the atmosphere are rapidly changing due to an accelerated warmer climate (Hartmann et al., 2013), thus affecting precipitation through different feedback. This section presents a summary of observed and projected changes of temperature and precipitation in North America.

In North America, changes have been observed in both temperature and precipitation patterns. A clear positive trend in temperature has been documented (Stocker et al., 2013). However, in recent decades, significant uncertainty related to the proper siting of observations (such as having artificial heating sources too close to stations) in several stations has been a concern and may

compromise the ability to accurately quantify temperature trends. Fall et al. (2011) argue that the temperature records over the U.S. have to be corrected (approx. 58% of the USHCN network had errors ≥ 2ºC, CRN=4 and 5, NOAA and NESDIS, 2002). For example, in Reno, Nevada, a significant adjustment was made to obtain a more certain trend in minimum temperatures, which were adjusted by up to 4°C for several years (Menne et al., 2009). The current trend from the fully adjusted observed mean temperature is 0.07°C/decade over the contiguous U.S. (CONUS) (Menne et al., 2009). The current (from 1910 to 2001) precipitation trends in the CONUS also show an increase in the total values and in the number of days with heavy to extreme precipitation (Groisman et al., 2005).

In Canada, trends also show increased warming and substantial spatial variability to changes in precipitation. The greatest temperature change is reflected in fewer cold nights, cold days and frost days (Vincent and Mekis, 2006). This warming is mainly explained by a substantial increase in minimum temperature (Vincent et al., 2012; Zhang et al., 2000). Western Canada shows the greatest warming, especially in spring and summer seasons (Vincent et al., 2012; Zhang et al., 2000). In the Rocky Mountains, although the interannual variability of temperature is strongly dominated by the Pacific Decadal Oscillation (PDO) (Jacques et al., 2013), an obvious warming trend in spring cannot be explained by the PDO index variations alone (Stewart et al., 2005). The extreme daily precipitation shows no consistent change in Canada (Vincent and Mekis, 2006); but a considerable spatial variation in precipitation trends across Canada is described in regional studies (e.g., Vincent and Mekis, 2006; Mekis and Vincent, 2011), and clear trends in precipitation amounts over sub-regions have been documented. For example, an increase in multiple day precipitation events in the Canadian Prairies (Shook and Pomeroy, 2012); a negative trend of annual snowfall has been observed in southern Canada, as opposed to northern Canada, which shows positive trends in annual snowfall (Akinremi et al., 1999; Vincent et al., 2006; Mekis et al., 2011); and an increase in rainfall over snowfall ratio has also been observed (Zhang et al., 2000), primarily driven by warmer temperatures (DeBeer et al., 2016). These changes impact the streamflow regime, in which spring runoff occurs earlier, snowmelt-driven peak streamflow are declining and summer and autumn streamflow is substantially reduced (Rood et al., 2008; Bawden et al., 2014; Whitfield and Pomeroy, 2016). To plan anticipatory actions on adaptation these observed changes need to be explored.

Future changes can be estimated using global or regional climate models under a future emission scenario as input. To increase the confidence of the results and to reduce the uncertainty arising from these model simulations, their reliability (likelihood or confidence) needs to be estimated. Despite the presence of biases generated by the model dynamics and physics, the projections for this century show a consistent increase in precipitation in most of the major basins in North America, except in the Mississippi River Basin (Sushama et al., 2006), A projected increase of up to 12% by the end of the century is documented for Western Canada (Dore and Simcisko, 2013). Both historical records and future projections show an increase in rainfall ratio (Krasting et al., 2013), due to warmer temperatures. The projected increase on the number of storms, wetter winter and springs will be more frequent in northwest Canada (Guinard et al., 2015). This change in

precipitation distribution might alter the characteristics of storms in ways that needs to be investigated (Wentz et al., 2007). Recent studies have found that projected annual maximum precipitation shows a shift from summer to spring or to autumn, as well as more intense and frequent precipitation events in many regions across Canada and the U.S. (Mailhot et al., 2010; Prein et al., 2016), with the smallest change over the west coast (Mailhot et al., 2012). The influence of the climate projections using a regional atmospheric model (e.g., the weather and research forecasting model, WRF) on significant events still needs to be further examined to explain the dominant processes associated with heavy storms (Mailhot et al., 2012; Vincent and Mekis, 2006). Several studies have explored the uncertainty associated with these observed and projected changes (Deser et al., 2012; Mearns et al., 2013). Even though a common spatial pattern of projected average precipitation change in winter shows an increase in the north and a decrease in the south, the variability of different model outputs shows the high uncertainty, both regionally and locally (Deser et al., 2012). To understand better the projected changes in precipitation, more details on the mains characteristics and processes associated with precipitation will be described and discussed in this thesis.

1.3 Research design

1.3.1 Purpose of research

The purpose of this research is to provide a better understanding of the main atmospheric mechanisms that contribute to CI over complex topography for the historical period and a representative future climate projection, using 19 global climate models as initial and boundary conditions on a regional climate model. The importance of systematic biases in observational datasets is first explained, followed by a discussion of the regional climate model in a convection-permitting configuration. These results are validated against observed datasets and used to reconstruct the atmospheric environment for the historical climate and to project the convective environment under the global warming scenario on a high emission projection.

1.3.2 Objectives

To achieve the goals of this research, three objectives are presented. These objectives focus on various time scales and data sources to approach different challenges in atmospheric science.

Objective 1

To quantify the inconsistency in precipitation measurements across the northern national border between the U.S. and Canada

Hypothesis

Differences in the national standards to measure precipitation cause a discontinuity in the spatially distributed precipitation measurements. This discontinuity is associated with the dependence of the main systematic wind-undercatch bias on the instrumentation type.

Objective 2

To investigate if a convection-permitting model in North America can reproduce the diurnal cycle of convective precipitation and to study how a warmer climate would change the characteristics of the precipitation diurnal cycle

Hypothesis

Most of summer precipitation in North America is dominated by a diurnal and semidiurnal cycle forcing. A regional climate model in a convection-permitting configuration should be able to realistically represent the characteristics of precipitation and be a reliable tool to determine how these characteristics will change in the future climate.

Objective 3

To characterize the contribution of a mesoscale feature in initiating convective precipitation on the leeside of the Canadian Rockies and to assess the projected changes associated with this feature in a future warmer climate

Hypothesis

The initiation of convection is partly modulated by mesoscale features and the diurnal cycle, which can be characterized by a regional climate model in a convective permitting configuration for historical and future climates.

1.4 Contribution

This work will contribute to the understanding both of precipitation in extratropical latitudes and of the influence of complex terrain on precipitation. First, when regional spatially-distributed precipitation is needed for atmospheric or hydrological studies, quantifying the inconsistencies of precipitation measurements across national borders will help to correct precipitation records. Second, to properly asses the performance of the model, the simulated diurnal cycle of precipitation in a long-term regional climate model needs to be verified. The evaluation of future projections of the diurnal cycle of precipitation events will provide insight into the possible changes in the occurrence and amplification of the cycle compared with the current situation. This knowledge could contribute to long-term water security-related issues and make use of the model results for further analysis. Finally, understanding mesoscale dynamics associated with convective precipitation in mountainous terrain would help us to improve the parametrization of these key processes in atmospheric models and thus to make better predictions. Predictions that are more accurate would provide more precise information to policy makers who need to make better decisions to plan and prevent catastrophes caused by heavy rainfall and flooding.

1.4.1 Outline

Chapter 2 of this thesis presents a study that quantifies inconsistencies in precipitation measurements across the national border between Alaska (U.S.) and the Yukon Territory (Canada). This research analyzes an unsolved problem regarding the systematic wind-bias. The snowfall records in national border areas of cold and windy regions are inconsistent because countries use different standard gauges, which are subject to varying wind-undercatch biases. We have accounted for the differences of the bias correction on both sides of the Alaska and Yukon border. The results of this research were published in the open access, peer-reviewed *The* Cryosphere EGU journal, in December 2015 as part of the special issue; "The World Meteorological Organization Solid Precipitation Inter-Comparison Experiment (WMO-SPICE) and its applications". The manuscript, entitled "Inconsistency in Precipitation Measurements across the Alaska-Yukon border", was authored by Lucia Scaff, Daqing Yang, Yanping Li, and Eva Mekis.

Chapter 3 presents the verification of the simulated diurnal cycle of summer precipitation from a regional climate model in a convection-permitting configuration for 13 years and on a continental scale. This study provides a detailed description of the model's performance in reproducing diurnal changes in summer precipitation across diverse environments in North America. With this information, the potential changes in the diurnal cycle of precipitation due to a warmer climate are assessed. This investigation is accepted in the scientific peer-reviewed journal Climate Dynamics as a part of a special issue: "Advances in Convection-Permitting Climate modeling". The manuscript, entitled "Simulating the Convective Precipitation Diurnal Cycle in North America's Current and Future Climate" is authored by Lucia Scaff, Andreas F. Prein, Yanping Li, Changhai Liu, Roy Rasmussen, and Kyoko Ikeda.

Chapter 4 presents an analysis of a mesoscale feature that modulates the initiation of convection on the leeside of the Canadian Rockies. The study characterizes the importance of the strong humidity gradient – the dryline – for the events that contributes the most precipitation in the province of Alberta and explains how a warmer climate scenario would modify the main characteristics.

Chapter 5 summarizes and concludes the thesis. It discusses the current challenges and limitations involved with measuring solid precipitation and with using regional climate models in a convection-permitting configuration. A final subsection reviews the main topics and suggests areas for future research.

CHAPTER 2

INCONSISTENCY IN PRECIPITATION MEASUREMENTS ACROSS ALASKA AND YUKON BORDER

This manuscript has been modified for inclusion in this thesis. It was originally published as:

Scaff Lucia, Yang Daqing, Li Yanping, Mekis Eva (2015) Inconsistency in precipitation measurements across Alaska and Yukon border. *The Cryosphere* 9:3709–3739. doi: 10.5194/tcd-9-3709-2015

Author contributions: L. Scaff and D. Yang designed the study and wrote the paper. Y. Li and E. Mekis contributed to the interpretation of the results and reviewed the manuscript.

Keywords

Snowfall, national precipitation gauge, measurement errors, bias correction, precipitation gradient and distribution.

Abstract

This study quantifies the inconsistency in gauge precipitation observations across the border of Alaska and Yukon. It analyses the precipitation measurements by the national standard gauges (NWS 8-in gauge and Nipher gauge), and the bias-corrected data to account for wind effect on the gauge catch, wetting loss and trace events. The bias corrections show a significant amount of errors in the gauge records due to the windy and cold environment in the northern areas of Alaska and Yukon. Monthly corrections increase solid precipitation by 136% in January, 20% for July at the Barter Island in Alaska, and about 31% for January and 4% for July at the Yukon stations. Regression analyses of the monthly precipitation data show a stronger correlation for the warm months (mainly rainfall) than for cold months (mainly snowfall) between the station pairs, and small changes in the previously found precipitation correlation due to the bias corrections. Double mass curves also indicate change in the cumulative precipitation over the study periods. This change leads to a smaller and inverted precipitation gradient across the border, representing a significant modification in the precipitation pattern over the northern region. Overall, this study discovers significant inconsistency in the precipitation measurements across the U.S. and Canada border. This discontinuity is greater for snowfall than for rainfall, as gauge snowfall observations have large errors in windy and cold conditions. This result will certainly impact regional, particularly cross-border, climate and hydrology investigations.

2.1 Introduction

It is known that discontinuities in precipitation measurements may exist across national boundaries because of the different instruments and observation methods used (Sanderson, 1975; Sevruk et al., 1989; Yang et al., 2001; Nitu et al., 2010). For instance, the National Weather Service (NWS) 8-inch gauge is used for precipitation measurements in the United States (U.S.), and the Nipher snow gauge has been used in Canada for decades. Different instruments have also been used in various observational networks within the same country. In the synoptic network, the Type-B rain gauge and Nipher gauge are the standard manual instruments for rain and snow observations in Canada (Mekis et al., 2011; Metcalfe et al., 1993), and recently Geonor automatic gauges have been installed

Instruments also change over time at most operational networks, resulting in significant breaks in data records. It has been realized that combination of regional precipitation records from different sources may result in inhomogeneous precipitation time series and can lead to incorrect spatial interpretations (Yang et al., 2005). Efforts have been reported to examine the precipitation discontinuity within a country (Groisman and Easterling, 1994; Sanderson, 1975). Leeper et al. (2015) found that the stations at the U.S. cooperative Observer program (COOP) reported slightly more precipitation overall (1.5%) with network differences varying seasonally. The COOP gauges were sensitive to wind biases, particularly over winter when COOP observed (10%) less precipitation than the U.S. Climate Reference Network (USCRN). Conversely, wetting and evaporation losses, which dominate in summer, were sources of bias for USCRN. Mekis and Brown (2010) developed an adjustment method to link the Nipher gauge and ruler snowfall measurements over Canada. Yang and Simonenko (2013) compared the measurements among 6 Russian Tretyakov gauges at the Valdai experimental station and reported the differences of less than 5-6% for the study period. These results are useful to determine the homogeneity of precipitation data collected by a standard gauge within the national and regional networks.

Many studies show that the national standard gauges, including the Canadian Nipher, and U.S. 8-inch gauges, under measure precipitation especially for snowfall (Goodison, 1981; Goodison et al., 1998; Yang et al., 1995; Yang et al., 1998; Yang et al., 1999). Compatibility analysis of precipitation measurements by various national gauges suggests little difference (less than 5%) for rainfall observations, but a significant discrepancy (up to 110%) for snowfall measurements (Yang et al., 2001). For instance, the experimental data from Valdai show that the U.S. 8-inch gauge at Valdai systematically measured 30-50% less snow and mixed precipitation than the Canadian Nipher gauge (Yang et al., 2001). This difference in national gauge catch has introduced a significant discontinuity in precipitation records between the U.S. and Canada borders, particularly in windy and cold regions. Differences in the snow measurements across the U.S. and Canada border have also been noticed in other studies as a problem to produce gridded products and to develop precipitation input for basin hydrological investigations (Šeparović et al., 2013; Zhao et al., 2010).

Although Yang et al. (2001) compared the relative catch of many national standard gauges, little has been done to address the inconsistency of precipitation records across the national borders. This is an important issue, since most regional precipitation data and products have been compiled and derived from the combination of various data sources, assuming these data and observations were compatible across the borders and among the national observational networks. Simpson et al. (2005) studied temperature and precipitation distributions over the State of Alaska and west Yukon, and documented precipitation increase from north to south. They also report differences in mean monthly precipitation across the Alaska-Yukon border, i.e. about 5-15 mm in central-east Alaska and 15-40 mm in central-west Yukon. Jones et al. (1994) found a weak gradient in annual precipitation across the AK-YK border, including the headwaters of the Yukon River. Other studies also discuss precipitation distribution and changes over the arctic regions (Legates and Willmott, 1990; Serreze and Hurst, 2000; Yang et al., 2005).

The objective of this work is to examine the inconsistency in precipitation measurements across the border between Alaska and Yukon. We analyze both gauge-measured and bias-corrected monthly precipitation data at several climate stations across the border and quantify the changes in precipitation amounts and patterns due to the bias corrections. We also calculate the precipitation gradients across the border and discuss precipitation distribution for the warm and cold seasons. The methods and results of this study are useful for cold region climate and hydrology investigations and applications.

2.2 Study area, data and methods

The study areas include the northern and central regions of Alaska (AK) and Yukon (YK). We choose 5 climate stations across the Yukon and Alaska border, which use the national standard gauges (NWS 8-inch gauge and the Canadian Nipher gauge) for precipitation observations (Figure 2 - 1). These stations can be classified into 2 groups. The first group, 3 stations about 150 km apart, is in the northern region along the coast of the Beaufort Sea; the Barter Island station is in Alaska and the Komakuk and Shingle Point stations in Yukon. The second group is in the central part of the region; the Eagle station in Alaska and Dawson station in Yukon, about 130 km apart.

The three northern stations selected for this study are located north of the Brooks Range. The approximate distances to the mountain edge are 100 km for the Barter Island station, 90 km for Shingle Point station, and 150 km for the Komakuk station. Both stations in Yukon are along the shore line and the station in Alaska is an island site, very close to the coast line. The altitudes of the stations range from 7 to 49 m asl. According to Manson and Solomon (2007), the summer storm tracks are usually from the northwest coming from the open water in the Beaufort Sea and are the greatest contributor to annual precipitation. The storms are obstructed by the Brooks Range once moving inland. The weather patterns in the surroundings of the stations might be affected by the mountains, but the stations are not separated by the Brooks Range. Given this setting, it is expected to see little impact of mountain range on the precipitation process and distribution along the relatively flat coast line.

These stations have been operated by the NWS and Environment Canada (EC) since the early 1970's. The observations have been done according to the national standards of U.S. and Canada. The detailed information for these stations is given in Table 2 - 1, such as the location, period of measurement used for this work, instrument types for precipitation observations, and a climate summary for yearly temperature, precipitation, and wind speed.

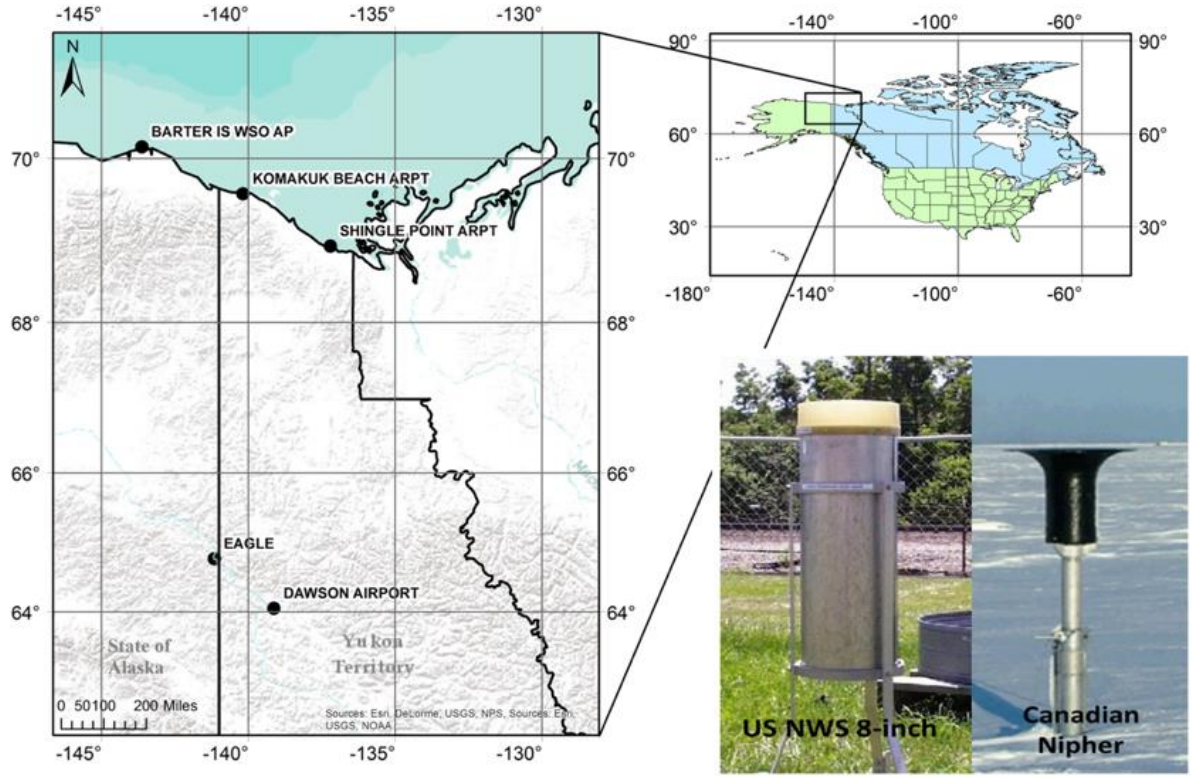

Figure 2 - 1 Study areas and locations of selected climate stations, and photos of the national standard gauges, NWS 8 in gauge (left) and the Nipher snow gauge (right), respectively, for USA and Canada.

Yang et al. (2005) have developed a bias corrected daily precipitation dataset for the northern regions above 45°N. The source data are acquired from the National Centers for Environmental Information (NCEI), i.e. a global daily surface data archive for over 8,000 stations around the world (https://www.ncdc.noaa.gov/data-access/quick-links#ghcn). To focus on the high latitude regions, a subset of the global daily data, about 4,000 stations located north of 45°N with data records longer-than 20 years during 1973-2003 has been created. Yang et al. (2005) applied a consistent procedure derived from the WMO Solid Precipitation Intercomparison (Goodison et al., 1998), using wind speed, temperature and precipitation as inputs (Yang et al., 1998; Yang et al., 2005). They quantify the precipitation gauge measurement biases for the wind-induced undercatch, wetting losses, and trace amount of precipitation. For the U.S. stations, wind data from the standard height was reduced to the gauge level of the NWS 8-in gauge (their standard height is 1 m). Wind

speeds and directions were measured at the Canadian climatic network; the same approach was applied to estimate the wind speed at the gauge height (their standard height is 2 m) on precipitation days. The corrections were done only for those stations with wind observations. Unfortunately, there are many stations in the U.S. without wind information and this is a challenge to perform gauge bias corrections.

This study uses the updated (until 2013) monthly precipitation, temperature and wind speed data from Yang et al. (2005) for the selected AK and YK stations (Table 2 - 1). The selected data periods range from 7 to 10 years for the stations that are considered long enough to examine precipitation patterns in these regions. Missing records affect regional climate data analyses. In this study, a threshold of 0°C of monthly temperature has been used to determine the cold and warm months for snow and rain. Mixed precipitation has not been classified separately. The frequency of missing values was calculated when the bias correction was made in Yang et al. (2005). Any month with less than 20 days (~30% of missing data) of measurements is excluded from data analysis. Statistical methods to compare the measured and corrected monthly and yearly precipitation data across the selected border station pairs are used to analyze these data. They also carry out regression analysis on monthly precipitation records, and calculates the cumulative precipitation amounts to derive the Double Mass Curves (DMC) over the study period. The double mass curve (DMC) is a useful tool to evaluate the consistency of observation records over space and time (Searcy and Hardison, 1960). Some typical issues of observations that DMC can identify include changes in the station location, and in instruments or sensors. A reference station is normally needed for DMC analyses. In this study, the DMC has been applied without a reference station to mainly detect any shifts between the observed and corrected precipitation. Through the data analyses and comparisons with other studies, we document the spatial and temporal variations of bias corrections across the border stations. We also determine the precipitation gradients across the border, and examine the changes, due to the bias-corrections of the U.S. and Canadian gauge data, in precipitation distributions on both seasonal and yearly time scales.

Table 2 - 1 Station information and climate summary

ID			Location			Data Period		Measurement Device	Annual Means				
WMO	Country	Station Name	Latitude (°)	Longitude (°)	Altitude (m)	Start	End	Precipitation gauge	Precipitation (mm)	Missing Precipitation data (%)	Minimum Temperature (ºC)	Maximum Temperature (ºC)	Wind Speed ($m\ s^{-1}$)
700860	US	BARTER IS WSO AP	70.13	-143.63	11	1978	1988	US-8 inch Unshielded	155	0.3	-27.1	4.6	4.0
719690	CA	KOMAKUK BEACH ARPT	69.58	-140.18	7	1978	1988	Nipher Type B gauge	191.8	2.9	-27.5	7.4	3.9
719680	CA	SHINGLE POINT ARPT	68.95	-137.21	49	1978	1988	Nipher Type B gauge	302	6	-26.6	10.6	3.4
701975	US	EAGLE	64.78	-141.16	268	2006	2013	US-8 inch Unshielded	247	0.2	-22.7	15.5	0.9
719660	CA	DAWSON AIRPORT	64.05	-139.13	369	2006	2013	Nipher Type B gauge	258	0.6	-25.8	15.9	1

2.3 Results

Based on the analyses of the measured precipitation (Pm) and corrected precipitation (Pc) data, this section presents the results of the bias corrections of monthly and yearly precipitation for each station, regression and correlation of monthly precipitation data between the stations, and cumulative precipitation via the double mass curves for the warm (monthly temperature > 0ºC) and cold seasons (monthly temperature < 0ºC).

2.3.1 Monthly data and corrections

The monthly mean precipitation and bias corrections are illustrated in Figure 2 - 2 for the northern group during the corresponding observation period (Table 1). In Figure 2 - 2, the missing data percentages are also presented for each month. Barter Island had the lowest percentages of missing data, about 2% as a maximum monthly mean in December. The mean missing percentages for the Komakuk station was about 5% (in May), with the maximum month in July 1984 (16%). For Shingle Point, the mean missing values were 11% for both April and May, with the maximum (26%) in April 1979. Given the generally small percentages of missing records, their impact is considered insignificant on monthly mean and yearly precipitation calculations. Figure 2 - 2 shows that annual precipitation cycle was centered on August, with an approximate maximum Pm around 40 to 80 mm between August and September. This maximum was coincident with the monthly mean daily maximum temperature in the area (around 10ºC).

For the Barter Island station in AK, the corrections were variable through the months. The monthly corrections increased the Pm amount by 3-31 mm for snow to 4-9 mm for rain. The relative increases were 59-136% for snow and 20-41% for rain, with a monthly mean of 9 mm (or 76%). The relative changes were usually large for months with low Pm and small for months with high precipitation. In other words, the monthly correction amounts do not always match with the percentage changes, i.e. a small correction in a dry month can have a large percentage change.

It is important to note that gauge measurements at Barter showed the maximum precipitation in August, but the peak shifted to October due to the corrections; i.e. the mean monthly P_c in October was 98% (about 32mm) more than the P_m (Figure 2 - 2). Closer examination of the monthly precipitation time series for Barter Island (Figure 2 - 3) indicated that, for most of the years, October was the most significant contributor to the total annual (23% for P_m and 22% for P_c). However, there were some years in the study period with the maximum P_m in other months; for example, the highest P_m in 1982 was in September, as documented by Yang et al. (1998b). Climate data and analyses showed the highest wind speed (4.5 m s^{-1}) and cold temperature (about -9ºC) for October, indicating higher under-catch by the U.S. standard gauge for snowfall. On the other hand, the wind speed showed the minimum values in July and August (3.3 m s^{-1}), coincident with the highest temperatures (4.6 and 4 ºC) (Figure 2 - 2). Due to the combination of warm temperatures and low wind speeds, the corrections for summer months were the lowest at this station (20-27%).

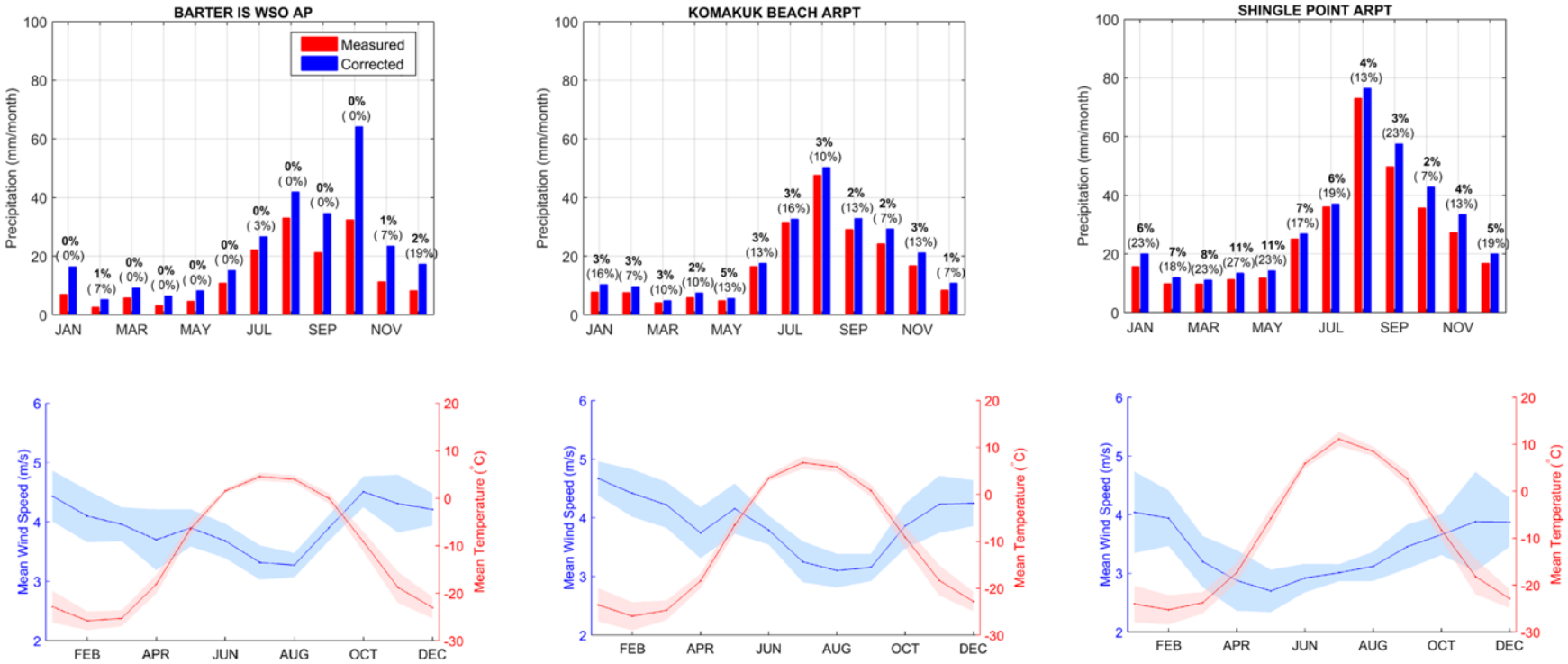

Figure 2 - 2 Monthly mean precipitation at 3 stations during 1977 - 1988 (upper panels) and corresponding monthly mean wind speed and air temperature (bottom panels). Shadows represent the 95% confidence interval for the temperature and wind speed. The percentages above the bars represent the missing data for the corresponding time step. The bold percentage is the monthly mean and the one in the parenthesis is the maximum missing value in the study period.

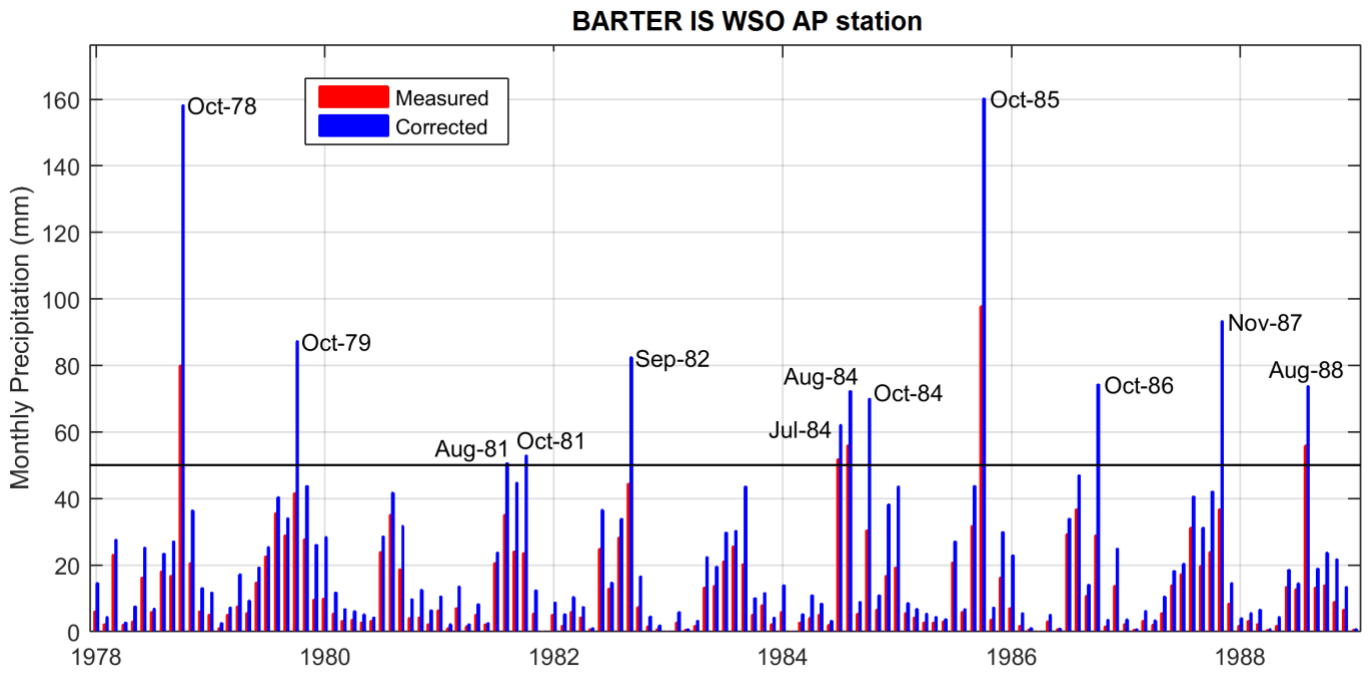

Figure 2 - 3 Monthly precipitation records at the Barter station during 1978-1988. The months with more than 50 mm (black line) are labeled.

For the Komakuk Beach station in Yukon, the corrections increased the precipitation by 0.7-5.5 mm (or 14%-34%) for snow and 1-2.6 mm (4%-10%) for rain, with a total monthly mean change of 2.6 mm (14%) (Figure 2 - 2). The monthly maximum precipitation was in August, i.e. 48mm and 50mm, respectively, for the P_m and P_c. The monthly minimum precipitation was in March, i.e. P_m = 4.2 mm and P_c = 5 mm. For this station, the extremes remained in the same month after the bias corrections. The wind speed had the minimum value in Aug. (3.1 m s^{-1}) and Sept. (3.2 m s^{-1}), and max in Dec. (4.3 m s^{-1}) and Jan (4.7 m s^{-1}). The temperatures were highest in July (6.9ºC) and Aug. (5.8ºC), and lowest in Feb and Mar (-25 ºC). Given this climate condition, the corrections were lower in the summer months (mean of 6%) and higher in winter (mean of 23%).

The monthly corrections for the Shingle Point station in Yukon ranged from 1-7.6 mm (3%-15%) for rain to 1-8.2 mm (14%-28%) for snow, with the monthly mean correction of 4.2 mm (14%). The maximum precipitation was in Aug., about 73-76 mm (or 20% of the annual total) (Figure 2 - 2). The minimum precipitation was in March with 9.8 mm for P_m; and 11 mm for P_c. The monthly wind speeds were generally higher in winter and lower in summer, with the maximum in Feb. (4 m s^{-1}) and minimum in May (2.7 m s^{-1}). The temperatures had a common annual cycle with the maximum in July (11ºC) and the minimum in Feb. (-24.3ºC). Because of the higher wind speeds and cold temperatures in the cold months, the corrections were greater for the winter season.

It was necessary to compare the correction results across the border in order to quantify the effect of biases in gauge observations on precipitation analyses, such as precipitation distribution and seasonal patterns. The mean snowfall corrections were about 96% for Barter Island in Alaska and around 22% for both Shingle Point and Komakuk stations in Yukon; while the rainfall corrections were approximately 32% for Barter and 7% for the two Yukon stations. Bias corrections also demonstrated a clear shift in the maximum precipitation timing for the Barter Island, but no change for the Yukon stations. This remarkable contrast across the border was caused mainly by the difference in gauge types and their catch efficiency. Many experimental studies have shown that the Canadian Nipher snow gauge catches more snowfall relative to the U.S. gauge (Goodison et al., 1998; Yang et al., 1998). For instance, the mean catch ratios for snowfall were about 40% and 85% for 4 m s^{-1} wind speed, respectively, for the NWS 8-in unshielded and Nipher gauges (Figure 2 - 4) (Yang et al., 1998b).

For the central group, the maximum and minimum P_m were in July and March for the Eagle station (Figure 2 - 5). The corrections did not modify the timings of maximum and minimum amounts; they remained in July for the maximum (P_m=67 mm and P_c =70 mm), and in March for the minimum (P_m=3 mm and P_c =4 mm) precipitation. The correction increased the precipitation by 0.6-1.8 mm (8%-22%) for snow and 1-3 mm (5%-10%) for rain, with a monthly mean correction of 1.7 mm (12%). The annual temperature cycle for Eagle showed warmer temperatures relative to the northern station, with the maximum of 16.2°C and above 0°C during April to mid-October. Eagle had lower wind speeds around 1 m s^{-1}(Figure 2 - 5).

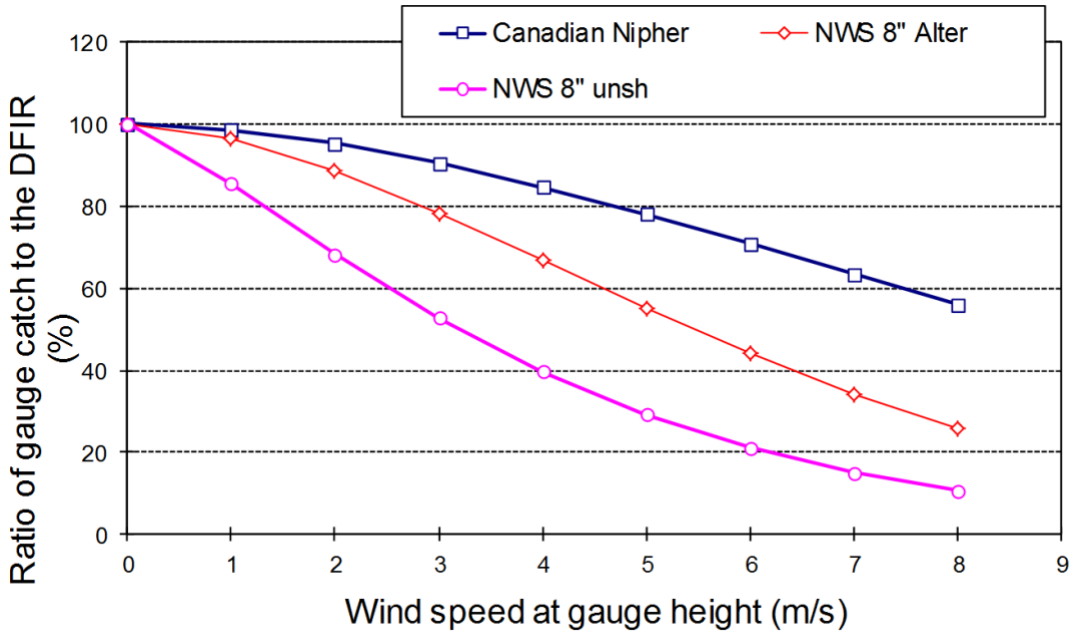

Figure 2 - 4 Comparison of the catch ratio of snowfall as a function of wind speed at gauge height for the Alter-shielded or unshielded NWS 8-inc standard gauge and the Canadian Nipher snow gauge. DFIR is the Double Fence Intercomparison Reference (Yang et al., 1998).

For the Dawson station, precipitation was more homogeneous throughout months; varying from 10 mm to 50 mm in October and June, respectively. Another relative maximum occurs in January with P_m =38 mm (Figure 2 - 5). The precipitation correction was small and fluctuated from 0.3 to 1 mm (or 2%-4%) for snow and 0.4-1.3 mm (3%-4%) for rain. This small correction was due to the lower undercatch correction for the Nipher gauge, besides the warmer temperatures and lighter winds. The temperature annual amplitude was between 16°C in July and -25°C in January, with temperatures above 0°C from April to September. Wind speeds showed a clear annual cycle with the maximum in May (1.6 m s^{-1}) and lighter winds in winter months, with the minimum in January (0.4 m s^{-1}).

The temperature and wind conditions were similar between the Eagle and Dawson stations, with mean temperature around 1°C and wind speed of 1 m s^{-1}. The missing data percentages were also similar for Eagle and Dawson stations; less than 3% for most months, with the maximum of 10% in May 2006 for Eagle and 20% in September 2009 for Dawson. The bias corrections were quite different, with the mean corrections of 16% for snow and 7% for rain at Eagle, and about 2 % and 3% for both rain and snow at Dawson. Overall, the correction was four times greater at Eagle than that at Dawson. This discrepancy reflects again the catch difference between the U.S. and Canadian standard gauges.

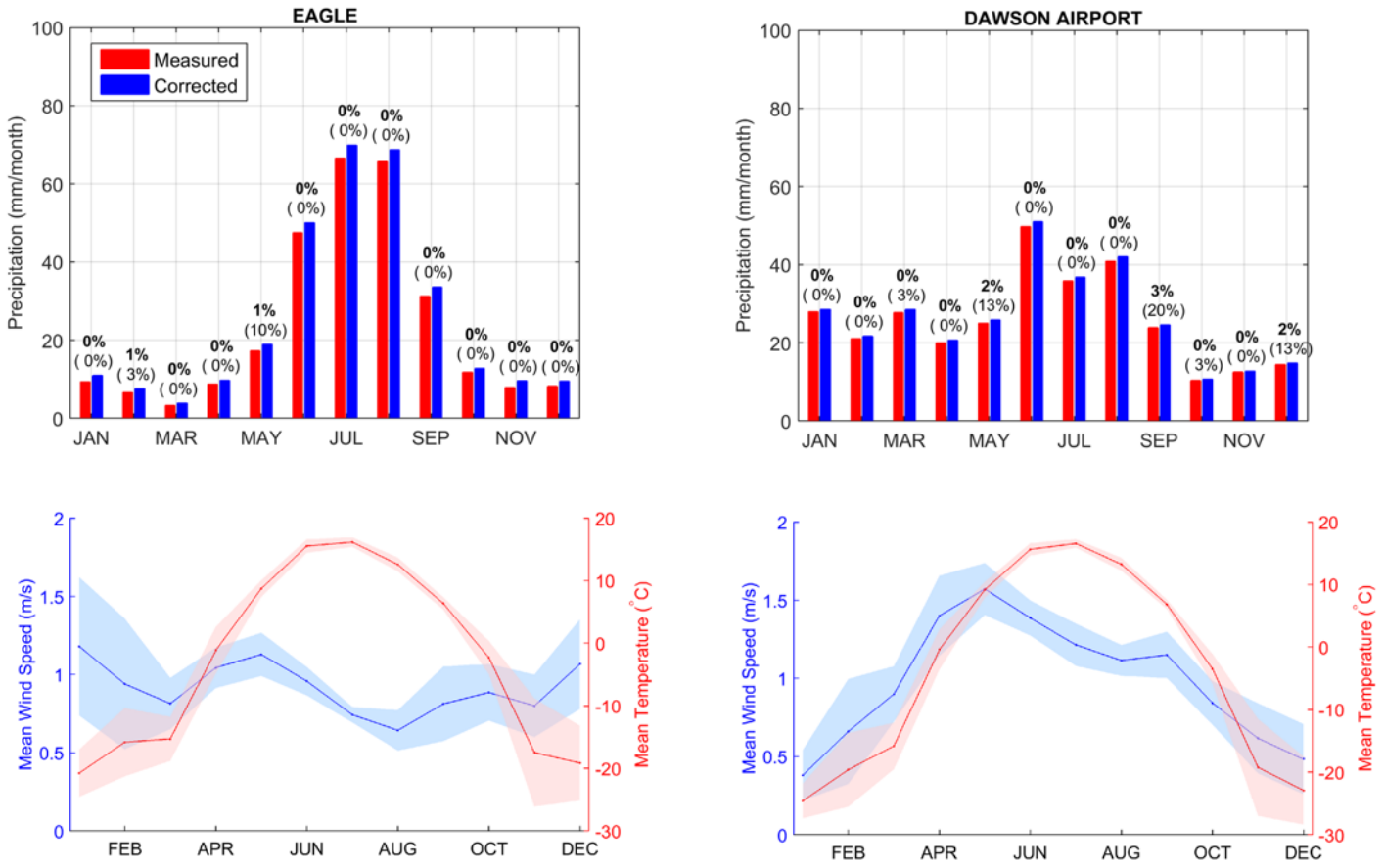

Figure 2 - 5 Monthly mean precipitation at 2 stations during 2006 - 2013 (upper panels) and corresponding monthly mean wind speed and air temperature (bottom panels). Shadows represent the 95% confidence interval for the temperature and wind speed. The percentages above the bars represent the missing data for the corresponding time step. The bold percentage is the monthly mean and the one in the parenthesis is the maximum missing value in the study period.

In order to understand the effect of precipitation bias corrections on regional climate around the AK-YK border, it was useful to examine and compare the temperature and precipitation features between the northern and central regions. The monthly mean temperature threshold of 0°C did not occur exactly at the same time among the 2 groups; the warm months (above 0°C) were between June and September in the northern group and between April and September in the central group. Although both regions had similar mean minimum temperatures, around -24°C and -27°C, the maximum temperature was considerably lower in the northern part, with the average of 8°C in the northern group vs. 16°C for the central region. Additionally, the monthly mean wind speed was higher for the northern region, 4 m s^{-1} vs. 1 m s^{-1}. Therefore, because of the colder temperatures and higher winds in the northern region, the bias corrections were higher in the north relative to the central region.

2.3.2 Yearly data and corrections

The annual Pm and Pc time series for 11 years during 1978-1988 in the northern group are presented in Figure 2 - 6. There were almost no missing data for the whole period, except 3% for 1978. At the Barter Island station in Alaska, the yearly Pm ranged from 114 mm to 211 mm, with the long-term mean of 155 mm. The mean annual corrections ranged from 67 to 138 mm, with a long-term mean of 101 mm (or 65%). The Pc records varied from 181mm to 343 mm. The maximum precipitation was in 1985 for both Pm and Pc (211 mm and 343 mm, respectively). The minimum precipitation was in 1983 for the Pm and Pc (114 mm and 181 mm, respectively).

For Komakuk Beach station in Yukon, the Pm ranged from 103 mm to 306 mm, with the missing data between 0 and to 7% among the years. The bias corrections increased the precipitation by 13 mm to 45 mm (or 8-19%). The long-term mean was about 194 mm for Pm and 220 mm with the corrections. The maximum precipitation occurred in 1981, 306 mm and 347 mm for Pm and Pc, respectively. The minimum precipitation was in 1988 for both the Pm and Pc, 103 mm and 123 mm, respectively.

For Shingle Point station in Yukon, yearly Pm varied from 126 mm to 551 mm and the Pc ranges from 138 to 638 mm. The mean annual total precipitation was about 302 mm for Pm and 341 mm after the corrections (change of 13%). The high and low extreme years were 1981 (Pm =551 mm, Pc = 638 mm), and 1988 (Pm =126 mm, Pc =138 mm). The Shingle station had missing data from 2% in 1983 to 10% in 1979.

Figure 2 - 7 displays the mean annual precipitation in cold and warm seasons for the northern group. The gauge measurements showed annual values from 155 mm at Barter Island, 194 mm at Komakuk to 302 mm at Shingle Point, i.e. a strong precipitation increased from the west to the east, particularly between Komakuk Beach and Shingle Point. However, the corrected data (Pc) showed a different pattern (Figure 2 - 7), i.e. higher precipitation at Barter than Komakuk, so the gradient across the border changed the sign and magnitude. This change was caused mainly by the high correction at the Barter station, particularly for snowfall data during the cold months (Figure 2 - 2).

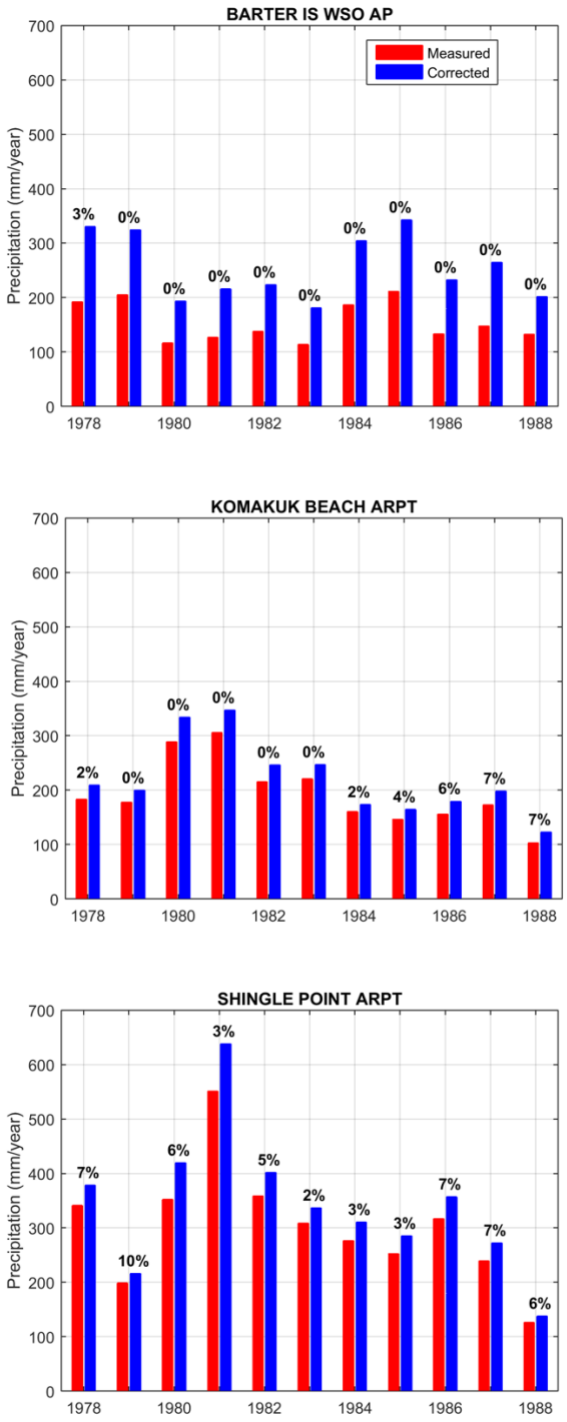

Figure 2 - 6 Annual precipitations during 1978-1988 for the 3 stations in the northern group across the border. The percentages above the bars represent the missing data for the corresponding year.

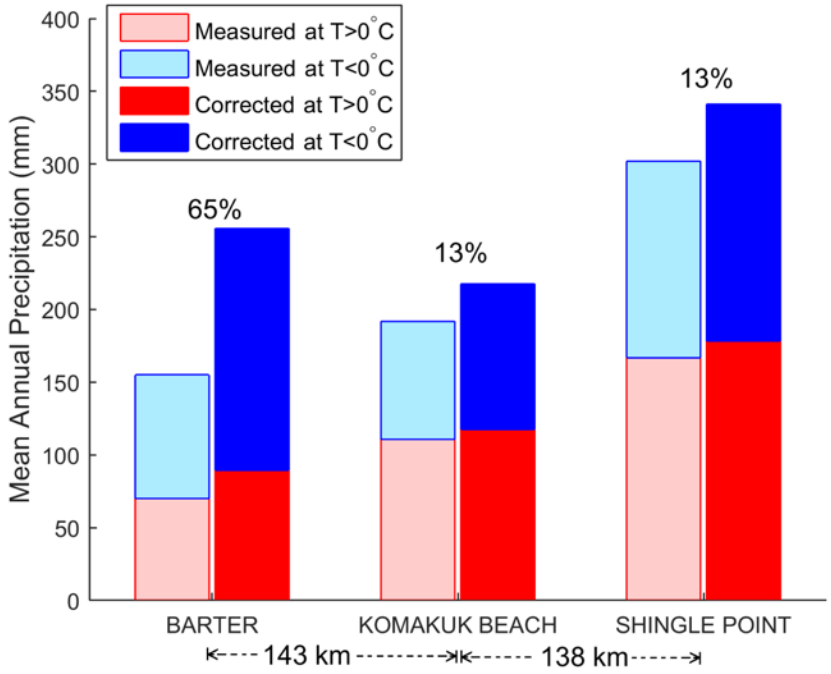

Figure 2 - 7 Mean Annual (1978-1988) measured and corrected precipitation for cold (T<0°C) and warm (T>0°C) months. The percentages are the changes from measured to corrected precipitation. The approximate horizontal distance between the stations is displayed at the bottom.

For the central group, the annual results are shown for 8 years (2006-2013) in Figure 2 - 8. The Pm ranged from 66 to 391 mm at the Eagle, and the bias corrections were 5-27 mm, correspondingly, which on average increase the total precipitation by 7%. While at Dawson, the Pm ranged from 158 to 333 mm, and the adjustments were from 4 mm to 10 mm, with an average increase in yearly precipitation by 3%. The gauge data showed a slight increase (12 mm) of mean precipitation from west to the east, i.e. slightly higher P in Yukon relative to Alaska. This result is consistent with other studies (Simpson et al., 2002; Simpson et al., 2005). The corrected data, on the other hand, suggest a smaller gradient (1 mm) across the border (Figure 2 - 9). This change was mainly due to the higher corrections for the U.S. 8-inch gauge at Eagle.

Similar to the monthly results, the northern stations exhibited higher yearly corrections for snowfall and rainfall measurements relative to the central group. This was because of higher winds in the northern stations, i.e. yearly mean wind speeds of 3.8 m s^{-1} in the north group and 1 m s^{-1} in the central group. This windy and snowy environment in the north produced higher wind-loss for the snowfall measurements by the gauges, which was the largest errors in precipitation records in the high latitudes (Benning et al., 2005; Yang et al., 1998; Yang and Ohata, 2001). It is important to note that gauge measured, and bias corrected data showed different pattern in seasonal and

yearly precipitation in the northern region. In other words, bias corrections of gauge measurements alter the precipitation gradient in the northern areas; this change was mainly due to the difference in the catch efficiency between the U.S. and Canadian standard gauges. The corrections for the U.S. gauge snow measurements were much higher than the Canadian gauge, particularly in the cold and windy coastal regions.

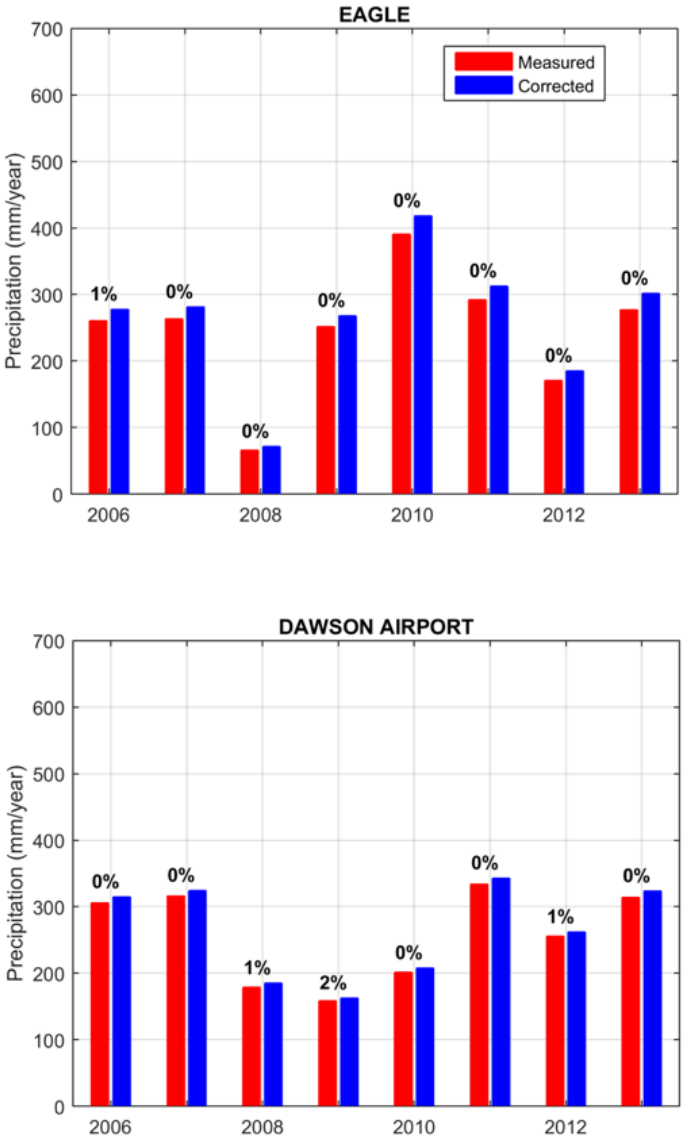

Figure 2 - 8 Annual precipitations during 2006-2013 for two stations in the central part of the AK/YK border. The percentages above the bars represent the missing data for the corresponding year.

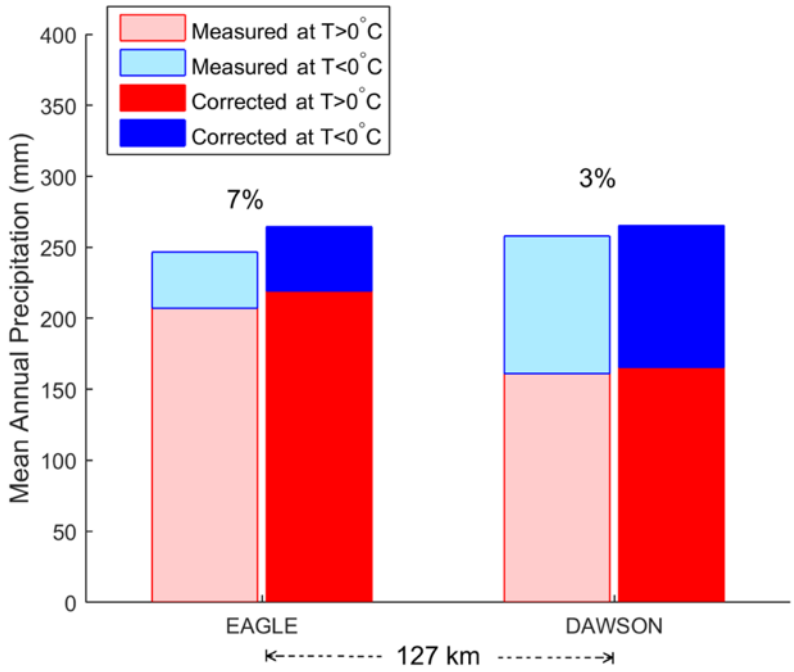

Figure 2 - 9 Mean Annual (2006-2013) measured and corrected precipitation for cold (T<0°C) and warm (T>0°C) months. The percentages are the change from measured to corrected precipitation. The approximate horizontal distance between the stations is displayed at the bottom.

2.3.3 Regression analysis of monthly data

The scatter plots of corresponding monthly precipitation for the two stations across the border and between the two Yukon stations in Canada are illustrated in Figure 2 - 10. For the cold season (Figure 2 - 10.A), the gauge data showed more snowfall at Barter for most years. Regression analysis suggested a weak relationship, with R^2=0.34. The corrected data showed a similar relationship, but a shift in the regression line, indicating a greater precipitation difference over the cold season across the border. For the warm season (Figure 2 - 10.B), the gauge data showed higher precipitation at the Komakuk station, and the regression suggested a much stronger relationship. The corrected data revealed a closer relationship between these two stations, proposing a smaller gradient for the warm months.

The scatter plot between the two stations in the Yukon Territory showed higher precipitation at Shingle point for both cold and warm seasons. It also gave another point of view about the effect of the correction in this area. Relative to the cold months (Figure 2 - 10.C), the corrections were smaller for the warm months (Figure 2 - 10.D), and correlation improved (R^2=0.72-0.76). However, the relationship did not change much in both cases between the measured and corrected

data. This was because of the very small corrections for the lower wind conditions and higher catch efficiency of the Canadian Nipher gauge.

For the central group, the scatter plot between Eagle and Dawson stations illustrated a clear difference in precipitation amount for the cold and warm months (Figure 2 - 10.E-F). The cold months showed more precipitation at Dawson, particularly for the wettest events, while Eagle did not show any comparable amount. The correlation was weak, and insignificant (R^2 =0.13). The shift in the fit line between measured and corrected data was also very small. The warm months showed low precipitation at Dawson; a different pattern from the cold months. The regression was better, R^2 =0.59 with a smaller shift due to the corrections.

Overall, we obtained consistent results among the Alaska and Yukon stations. The correlations were higher in warm months (R^2 = 0.58 to 0.76) and lower for the cold season (R^2 between 0.13 and 0.52). This result may suggest that the rainfall was more homogeneous over the regions in summer, and greater difficulty and errors in snowfall measurements during the cold months.

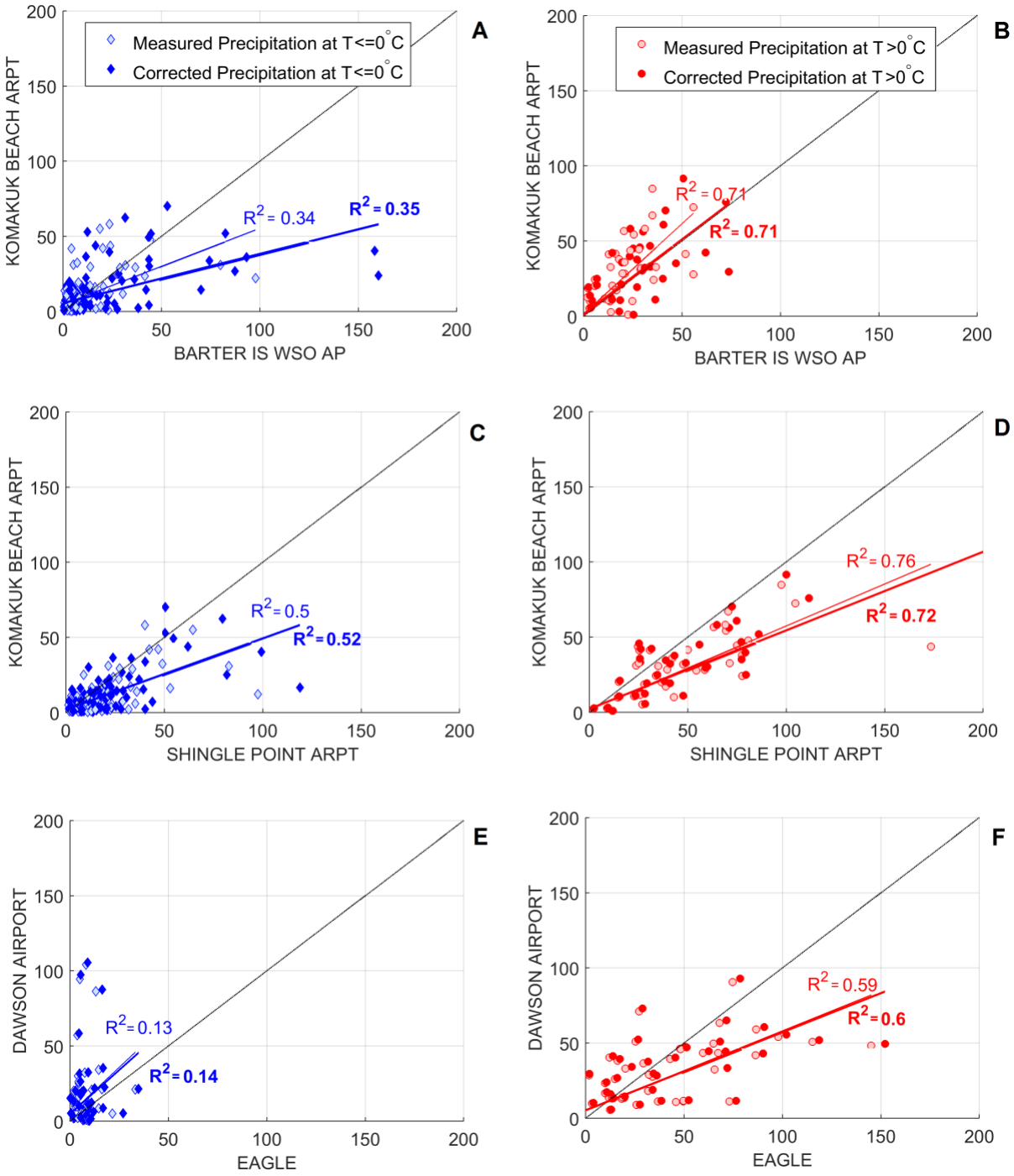

Figure 2 - 10 Scatter plots between station pairs for the measured and corrected precipitation (mm). The red color shows warm months and the blue represents the cold months. A and B - Barter and Komakuk comparison across the border, the highest corrected values for Barter (AK) are labeled with the date to compare with Figure 2 - 4. C and D - Komakuk and Shingle Point comparison within Canada. E and F- Eagle vs. Dawson across the border for the central group.

2.3.4 Cumulative precipitation via double mass curves (DMC)

The DMC plot for Barter Island and Komakuk Beach showed more Pm at Komakuk than Barter (Figure 2 - 11.A). The bias corrections led to a shift of the relationship with a significant increase in the total precipitation amount at Barter. Relatively, the total cumulative precipitation for Barter Island increased by 65% after the correction and by 14% at Komakuk. The difference between the two stations at the last cumulative point (December 1988) is 426 mm for Pm, and 393 mm for Pc. This shift represented a modification in the precipitation difference between these stations, i.e. a change in the gradient's direction (Figure 2 - 7).

The comparison of cumulative precipitation values between Shingle Point and Komakuk, both in Yukon, is illustrated in Figure 2 - 11.B. Shingle Point showed more cumulative precipitation at the end of the period (Pm=3322 mm vs. Pm=2115 mm for Komakuk). Although the relationship was more homogeneous between these stations, there was a break in the records around 1300 mm for Komakuk, maybe associated with changes in instruments or sensors. Examination of the station history and information revealed an anemometer issue around the critical time that was fixed by August 1980. This may affect wind data and thus the corrected precipitation values. Both stations showed increases in total cumulative precipitation by 13%.

The central stations showed a greater amount of Pm in Dawson (2065 mm) than in Eagle (1973 mm) over the study period. Bias corrections changed the total precipitation by 3% and 7% for Dawson and Eagle, respectively, resulting in a shift in the DMC (Figure 2 - 11.C), particularly for the last period of time, to 2123 mm in Dawson and to 2116 mm in Eagle. This shift also represented a slightly smaller precipitation difference between the two stations. During the 8 years, the cumulative difference decreased from 92 mm to 7.3 mm.

In summary, the DMC for measured and corrected precipitation showed that the main change was due to the difference in their corrections (Figure 2 - 11); the north stations showed a greater change compared with the central group. The Pc showed in all the cases a smaller precipitation difference between the two countries. This smaller difference led to a decrease in the precipitation gradient across the border. This result implies that existing precipitation climate maps and information derived from gauge measurement without bias corrections may over-estimate the precipitation gradient in these regions. This overestimation will affect regional climate and hydrology analyses.

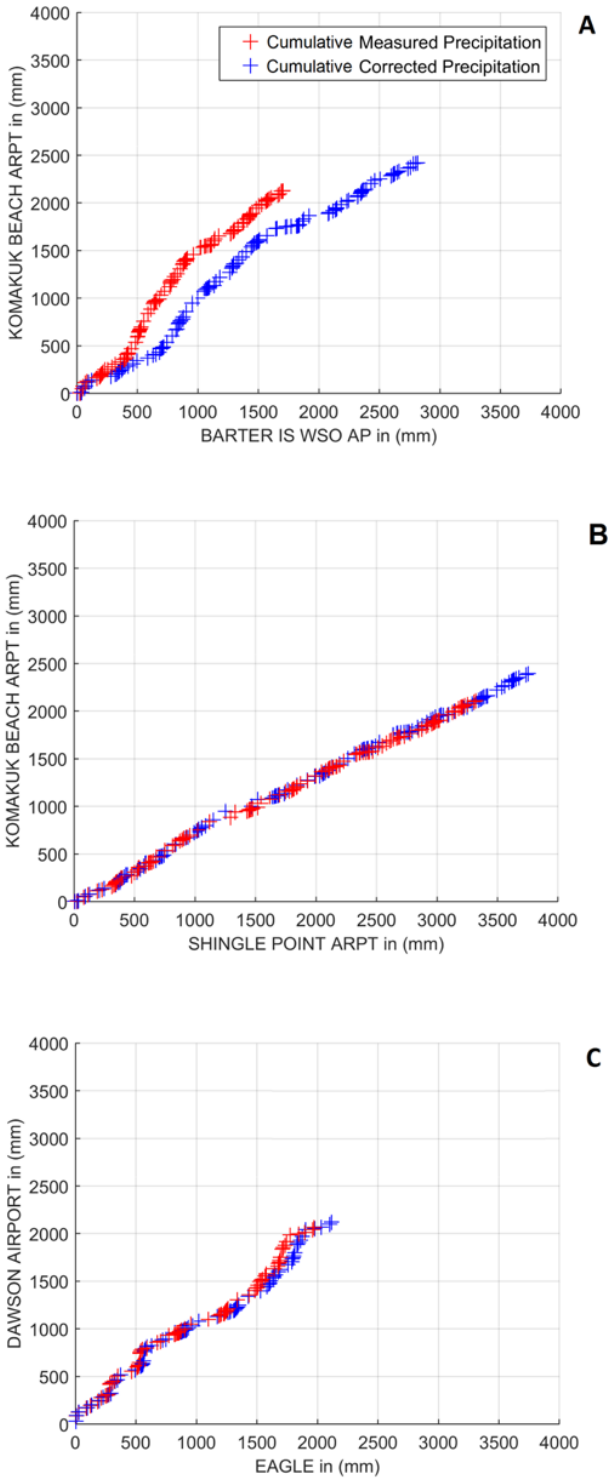

Figure 2 - 11 Double mass curves between station pairs. The red color shows the warm months and blue represents the cold months. The top and the central plots compare the stations for the northern group and the bottom one is the central station comparison across the border.

2.4 Summary and discussion

This study documents and quantifies the inconsistency in precipitation measurements in the northern and central regions of Alaska/Yukon, with a focus on station pairs across the US-Canada border. The monthly bias corrections show large errors in the gauge records due to the windy and cold environment in the northern areas of Alaska and Yukon. The corrections for gauge undercatch increase the snowfall by 136% in January for Barter Island station in Alaska. For the Yukon stations, the increase is about 31% in January and 4% in July. These represent an annual mean loss of 81 mm (101%) in snowfall and 20 mm (29%) of rain at Barter, while at Shingle Point and Komakuk Beach in Yukon the corrections are, on average, about 25 mm (21%) for snow and 8 mm (6%) for rain. For Eagle (AK) and Dawson (YK) stations in the central region, the bias corrections are small. The monthly corrections range from 2% to 22% in winter and from 3% to 10% on summer months.

On the annual scale, Barter Island station in AK shows a yearly mean correction around 65%, five times greater than the correction at Shingle Point and Komakuk Beach (13% and 14%) in Canada. In the central region, Eagle station shows an increase by 7%, meanwhile for Dawson the increase is only 3%. Thus, the bias correction for Alaska is twice that of the Yukon stations. Relative to the northern region, these corrections are small mainly due to warmer temperatures and lower winds in the central region. These results clearly demonstrate that bias corrections may affect the apparent spatial distribution of precipitation across the border.

Regression analyses of the monthly data show small changes in the relationship due to the bias corrections. The most evident change in the regression is between Barter Island and Komakuk Beach for both warm and cold seasons. The rest of the scatter plots, for the Komakuk Beach-Shingle Point and Eagle-Dawson, do not show any appreciable change as the result of the bias corrections. There is a stronger precipitation correlation for the warm months (mainly rainfall) than for the cold month (mainly snowfall) for all the station pairs. The cold months seem to have greater precipitation variability across the regions.

The double mass curve analyses demonstrate a significant change in the precipitation accumulation and difference between the two stations across the AK-YK border for the northern region, little changes for the two stations in Yukon, and a smaller change in the central group. These changes, caused by gauge catch efficiency, alters the precipitation difference, resulting in a smaller and inverted precipitation gradient across the border in the northern region. The double mass curve (DMC) is a useful tool to evaluate the consistency of observation records over space and time (Searcy and Hardison, 1960). Although in this work the DMC has not been constructed against a reference station, the results clearly show some breaks on the slope and gaps in the curves, indicating changes in precipitation relationship across the border that could be caused by any of the two stations. This information provides the timing when significant changes occurred in the precipitation regime. Detail metadata and information for the stations/networks are necessary to understand the changes in precipitation observations and to improve the homogenization of the precipitation records over the high latitudes.

This study shows similar monthly Pm across the north border region and higher P_m in Yukon than Alaska over the central region. This result is similar to other studies (Serreze et al., 2000; Simpson et al., 2005). After the bias corrections, precipitation patterns across the border changed, i.e. higher precipitation in Barter than Komakuk, in other words, an inverted gradient across the borderline. Over the central region, the measured mean annual precipitation is slightly higher in Yukon than Alaska, which is also consistent with Simpson et al. (2002) and (2005). Our results suggest that the gradient between the central pair of stations becomes smaller after the bias correction. This discrepancy should be taken into account when using the precipitation data across the national borders for regional climate and hydrology investigations.

Missing data may affect regional precipitation analyses. In this study, we calculated the missing data percentages for all stations during the corresponding study periods and set up a threshold of 30% to exclude those months with higher missing values from monthly precipitation calculations. We compared the precipitation amounts with and without the application of the threshold. The results do not show any significant changes in the differences of gauge measured annual mean precipitation across the border, although this filter affected annual precipitation in certain years. For instance, the northern station pair (Barter and Komakuk stations) has missing value of 32% on July 1987. Calculations of yearly precipitation for 1987 with and without this month show 16% and 10% difference at Komakuk and Barter Island stations, respectively. Over the study period of 11 years, the annual mean bias correction percentages remain the same (65% in Barter and 13% in Komakuk) with or without the missing months. The mean annual decrease in bias correction amounts after the consideration of missing data is about 1-3% in the northern region. This analysis suggests that the effect of missing data for our study is not significant, particularly with the application of 30% missing threshold. More efforts are needed to further examine the issues of missing records in climate analyses.

Classification of precipitation types is the first step for the bias corrections of gauge records. It is also important for climate change analyses over the cold regions. Leeper et al. (2015), in comparison of USCRN with the COOP station network precipitation measurements, averaged the USCRN hourly temperatures data during precipitation periods into an event mean and used it to group precipitation events into warm (mean temperature > 5°C), near-freezing (mean temperature between 0°C and 5°C), and freezing (mean temperature < 0°C) conditions. Yang et al. (2005) used the daily mean air temperature to estimate precipitation types (snow, mixed, and rain) when this information is not available for the northern regions. In this study, monthly mean temperatures have been used to determine the warm months (mainly for rain) and cold months (mainly for snow). Mixed precipitation has not been classified separately. This approach is reasonable for our analysis to focus on the inconsistency in the monthly and yearly P_m records across the border. Data collection and analyses on shorter timescales, such as daily or hourly steps, are expected to produce better results, since temperatures vary throughout the days in a month, particularly in the spring and fall seasons. Automatic sensors will also be important to decide precipitation types at the operational and research networks.

The bias-corrected precipitation dataset developed by Yang et al. (2005) has been used for this analysis. The corrections have been done systematically on a daily time scale that affects the daily P_m time series. This analysis focuses on the results of monthly and yearly precipitation data and quantifies the changes in precipitation pattern across the AK-YK border. Careful analyses of available daily measured P_m and corrected P_c data are necessary, since in the northern regions with low precipitation in winter, the bias corrections can easily increase the daily P_m by a factor of up to 4-5 (Yang et al., 1998; Benning et al., 2005; Yang et al., 2005; Kane et al., 2015). This means that extreme precipitation events have been very likely and seriously underestimated by using the gauge records without any bias corrections. The consequence is certainly significant for climate change investigations. To fill this knowledge gap, our efforts are underway to examine the daily corrections, particularly on the windy and heavy precipitation days, and to document the possible underestimation of precipitation extremes over the large northern regions.

Automation of the meteorological observation networks and instruments has been a trend over the past few decades around the world, including both the developed and developing nations. There is a large variety of automatic gauges currently used for precipitation measurements at the national networks (Nitu and Wong, 2010). These gauges differ in the measuring system, orifice area, capacity, sensitivity, and configuration. The variation in automatic gauges is much greater relative to the manual standard gauges (Goodison et al., 1998; Sevruk and Klemm, 1989). As demonstrated by (Yang et al., 2001) and this study, the use of different instruments and configurations significantly affect the accuracy and consistency of regional precipitation data. Fortunately, the Geonor gauge has recently been chosen and used at both the U.S. Climate Reference Network (USCRN) and the Surface Weather and Climate Network (SWCN) in Canada. This may reduce the inconsistency in precipitation measurements across U.S. and Canada borders, although the double and single Alter wind shields have been installed with the Geonor gauges in U.S. and Canada, respectively.

Finally, it is important to emphasize that automatic gauges also significantly under catch snowfall (Wolff et al., 2015) and bias corrections are necessary in order to obtain reliable precipitation data for the cold regions and seasons. The WMO SPICE project aims to examine the performance of automatic gauges and instruments for snowfall observations in various climate conditions. It has tested many different automatic gauges, including the Geonor gauge, at more than 20 field sites around the globe (Nitu et al., 2012; Rasmussen et al., 2012; Wolff et al., 2015). The results of this project will be very useful to improve precipitation data quality and regional climate analyses, including the border regions between U.S. and Canada.

Key points for the next chapter

- The systematic wind-undercatch bias on solid precipitation can exceed 100% of the actual measurement in cold environments and significantly varies across different instrument types.
- The inconsistency of systematic wind-undercatch bias on solid precipitation across national borders is especially important in cold and windy environments.
- For warmer regions and seasons this systematic bias still exists, however the inconsistency across national borders is minor for liquid precipitation.
- For summer precipitation, other types of systematic inconsistencies arise. As summer precipitation intensity can be very significant in convective events, many stations, however not all of them, in the U.S. used a high minimum bucket resolution. A standardization of the minimum bucket resolution for all datasets is discussed in the next chapter.

Systematic inconsistencies and errors have to be taken into account in every regional study crossing national borders. For example, when observed solid precipitation is used for empirical validation of atmospheric modelling.

Acknowledgments

The authors gratefully acknowledge the support from the Global Institute of Water Security at the University of Saskatchewan and Environment and Climate Change Canada.

CHAPTER 3

SIMULATING THE CONVECTIVE PRECIPITATION DIURNAL CYCLE IN NORTH AMERICA'S CURRENT AND FUTURE CLIMATE

This manuscript has been modified for inclusion in this thesis. It was originally published as:

Scaff, Lucia, Andreas F. Prein, Yanping Li, Changhai Liu, Roy Rasmussen, and Kyoko Ikeda. 2019. "Simulating the Convective Precipitation Diurnal Cycle in North America's Current and Future Climate." *Climate Dynamics.* https://doi.org/10.1007/s00382-019-04754-9.

Author contributions: L. Scaff, A. Prein and Y. Li designed the study. C. Liu and K. Ikeda performed the WRF simulations. K. Ikeda post-processed the WRF output. All authors contributed to the interpretation of the results and to writing the manuscript.

Keywords

Convection-Permitting Modeling, Diurnal Precipitation Cycle, North America, Weather Research and Forecasting Model, Pseudo Global Warming, Climate Change

Abstract

Convection-permitting models (CPMs) with at least 4-km horizontal grid spacing enable the cumulus parameterization to be switched off and thus simulate convective processes more realistically than coarse resolution models. This study investigates if a North American scale CPM can reproduce the observed warm season precipitation diurnal cycle on a climatic scale. Potential changes in the precipitation diurnal cycle characteristics at the end of the 21st century are also investigated using the pseudo global warming approach under a high-end anthropogenic emission scenario (RCP8.5). Simulations are performed with the Weather Research and Forecasting (WRF) model with 4-km horizontal grid spacing. Results from the WRF historical run (2001-2013) are evaluated against hourly precipitation from 2903 weather stations and a gridded hourly precipitation product in the U.S. The magnitude and timing of the diurnal cycle peak are realistically simulated in most of the U.S. and southern Canada. The model also captures the transition from afternoon precipitation peaks eastward of the Rocky Mountains to night peaks in the central U.S., which is related to propagating mesoscale convective systems. However, the historical climate simulation does not capture the observed early morning peaks in the central U.S. and overestimates the magnitude of the diurnal precipitation peak in the southeast region.

In the simulation of the future climate, both the precipitation amount of the diurnal cycle and precipitation intensity increase throughout the domain, along with an increase in precipitation frequency in the northern region of the domain in May. These increases indicate a clear intensification of the hydrologic cycle during the warm season with potential impacts on future water resources, agriculture, and flooding.

3.1 Introduction

Convective precipitation is essential for North America hydrology during summer (Laing and Fritsch, 1997; Zipser et al., 2006), but deep convection often results in extreme events such as flooding, tornadoes, and hail. Although convective extremes have high societal relevance, their simulation remains a great challenge (Wilson and Roberts, 2006; Browning et al., 2007; Geerts et al., 2017), particularly when the grid spacing of state-of-the-art models is too coarse to realistically simulate deep convective processes (Prein et al., 2015).

In this study we investigate the simulation of the warm season precipitation diurnal cycle in southern Canada, the U.S. and northern Mexico with a focus on the convective precipitation forming on the leeside of the North American Rocky Mountains. Convective storms in this region are characterized by a marked diurnal cycle. These storms typically initiate in late afternoon and early evening near the foothills and then propagate eastward towards the Midwest from night to early morning (e.g., Carbone et al., 2002; Carbone and Tuttle, 2008).

The simulation of these propagating storms is challenging in climate models due to their coarse horizontal grid spacing, which is typically larger than 12-km for regional climate models (Jacob et al., 2014) and 100-km for global climate models (Taylor et al., 2012). At these resolutions cumulus parameterizations are required, but they are the main contributor to errors and uncertainties (Déqué et al., 2007). In addition, the coarse representation of orography (Warrach-Sagi et al., 2013) and the simulation of mesoscale processes, such as boundary layer processes or the land-atmosphere interaction, cause model biases.

Several studies have focused on the added value of higher spatial resolution to simulate precipitation (Hohenegger et al., 2008 from 25-km to 2.2-km; Kendon et al., 2012 from 12-km to 1.5-km; Dirmeyer et al., 2012 from 125 to 10-km; Ban et al., 2014 at 12-km and 2.2-km; Rasmussen et al., 2014 at 4-km; Sun et al., 2016 at 25-km and 4-km) and have shown that even models with 10-km grid spacing cannot reliably simulate convective precipitation. However, convection-permitting models (CPMs) with at least 4-km horizontal grid spacing have shown substantial improvement in the representation of convective precipitation (Prein et al., 2015). One of the most robust benefits of CPMs is their ability to more reliably simulate sub-daily convective precipitation than models with parameterized convection (e.g., Richard et al., 2007; Baldauf et al., 2011; Langhans et al., 2013; Fosser et al., 2014; Rasmussen et al., 2014; Prein et al., 2015; Brisson et al., 2016). Furthermore, CPMs also improve the representation of the topography and land surface interactions (Prein et al., 2013; Fosser et al., 2014; Rasmussen et al., 2014). The horizonal grid spacing of 4-km resolution is chosen because is the upper limit of horizontal grid size to resolve the characteristics of convective systems, such as the transport of energy and momentum and the meso-convective circulation (Weisman et al., 1997).

Various aspects of CPMs over North America have already been evaluated. Coniglio et al. (2013) showed that different planetary boundary layer parameterizations result in changes on the mixed layer of the convective available potential energy and thus to the capping inversion strength. Using

CPM simulations (Liu et al., 2017), Prein et al. (2016) showed that hourly extreme precipitation is well captured in the simulated current climate and described the reasons for increases in hourly extremes at the end of the 21st century. This finding is consistent with those from other studies, showing that, with a warmer climate, hourly precipitation rates are increasing while precipitation frequencies are decreasing (Kendon et al., 2014; Ban et al., 2015; Rasmussen et al., 2017). Additionally, convective hazardous weather is projected to increase in intensity and severity (Trapp et al., 2007; Trapp et al., 2011; Mahoney et al., 2013; Gensini et al., 2015; Hoogewind et al., 2017).

One of the most robust added values of CPMs is their ability to better represent the warm season precipitation diurnal cycle compared to simulations that use convection parameterizations (see Prein et al., 2015 for a review). The improved diurnal cycle also results in (1) a more realistic relationship between static stability and convection (e.g., through convective available potential energy), (2) an improved simulation of cloud cover height and feedback to the surface energy balance (Fosser et al., 2014), and (3) an improved simulation of convergence zones across mountainous terrain (Barthlott et al., 2006; Fosser et al., 2014; Rasmussen et al., 2014). However, challenges remain in convection-permitting modeling, such as the representation of shallow convection boundary layer processes (Brisson et al., 2016) and the treatment of partly under-resolved turbulence (Prein et al., 2015). Furthermore, the high computational cost of CPMs makes it challenging to investigate the robustness of their performance and to assess uncertainties in future climate projections (Prein et al., 2015).

The purpose of this study is to investigate if a continental-scale CPM can reproduce the observed properties of the diurnal cycle of convective precipitation in North America, and if so, how a warmer climate would change these properties. This research focuses on the verification of the magnitude and timing of the diurnal precipitation peak, as well as the hourly precipitation amount, intensity, and frequency in May, June, July and August. Changes in these metrics due to climate change are also presented.

3.2 Data

3.2.1 Numerical simulation

The Weather Research and Forecasting model version 3.4.1 (ARW-WRF, Skamarock et al., 2008) was used over a North American domain (Figure 3 - 1) with 4-km horizontal grid spacing (1360x1016 horizontal grid points and 51 stretched vertical levels). The 4-km grid spacing is chosen as is the coarser resolution at which the up- and down-draft are simulated in the order of magnitude that has been observed in interior valleys across the mountains (Rasmussen et al., 2011). Liu et al. (2017) presents the detailed description of the model configuration for the simulations used in this study. The main model physics are: Thompson and Eidhammer (2014) microphysics scheme, the Noah Multi-Physics Land-surface model (Niu et al., 2011), the planetary boundary layer scheme from Yonsei University (YSU, Hong et al., 2006) and the Rapid Radiative Transfer Model (RRTMG, Iacono et al., 2008) for long and short-wave radiation.

The initial and lateral boundary conditions for the historical simulation are from the ERA-Interim reanalysis (Dee et al., 2011) from October 2000 to September 2013 (WRF-CTR, hereafter). Spectral nudging was applied above the planetary boundary layer on air temperature, geopotential, and horizontal wind (moisture was not nudged), to scales larger than 2,000 km every 6 hours. The spectral nudging helped to improve the model performance (Liu et al., 2017) and only constrains the synoptic scales, leaving the mesoscale (and smaller scales) free to evolve with the model.

The future climate simulation was performed by using the pseudo global warming approach (PGW; WRF-PGW, hereafter). The PGW consists of applying the monthly mean climate perturbations to the 6-hourly ERA-Interim boundary conditions of three-dimensional temperature, moisture, wind, geopotential height, and sea surface temperature. The perturbation corresponds to the average end-of-century (1976-2005 minus 2071-2100) climate change signal of 19 Global Climate Models (GCM) from the Climate Model Intercomparison Project (CMIP5; Taylor et al., 2012), under a high-end emission scenario, which is characterized by the representative concentration pathway RCP8.5 (Riahi et al., 2011). A list of the selected GCMs is presented in Liu et al. (2017).

The PGW approach was originally proposed by Schär et al. (1996) and has been successfully applied in case study experiments (Lackmann, 2015; Trapp and Hoogewind, 2016) and climate change analyses (Hara et al., 2008; Rasmussen et al., 2011; Liu et al., 2017). The PGW approach minimizes the effects of climate internal variability on the results since it assumes that the weather of the current climate reoccurs at the end of the century under warmer conditions. This is an advantage of using the PGW approach instead of a traditional RCM downscaling using a GCM as input. However, the PGW approach is not able to account for sub-monthly or smaller weather changes and approximates the climate change perturbation to monthly means on the lateral boundaries. An analysis with 3 members from GCMs used in CONUS I, shows that the average amplitude of the climate change perturbations on the diurnal cycle are 0.45 ºC for temperature and 0.2 g kg^{-1} for specific humidity. These differences are 10% of the absolute temperature climate change signal and 7.3% for humidity. (c.f., Appendix A). The simulated precipitation diurnal cycle can be influenced by not considering this sub-daily variation on the climate change perturbation. This impact should be quantified in future studies.

3.2.2 Observations

Observed hourly precipitation data (Figure 3 - 1) were selected to evaluate the performance of WRF-CTR from gauges (OBS) and the Stage IV gridded precipitation product (hereafter sIV, Lin and Mitchell, 2005). The OBS dataset is a combination of two weather station networks; one from the U.S. and the other one from Canada. The 2,509 stations are from the TD3240 product (Hammer and Steurer, 2000) from 2001 to 2011 and the DSI-3240 product covering 2012 to 2013 (they are equivalent datasets until 2011) in the contiguous U.S. (CONUS). The Canadian network is operated by Environment and Climate Change Canada (ECCC, previously known as Environment Canada) with 394 stations. We only consider weather stations with five or more years of continuous records within the period from 2001 to 2013.

The sIV integrates surface radar and gauge measurements to produce a 4-km spatially-gridded multi-sensor analysis of hourly precipitation covering the CONUS region. We use sIV data from 2002 to 2013, since data in 2001 has major quality issues (Lin and Mitchell, 2005).

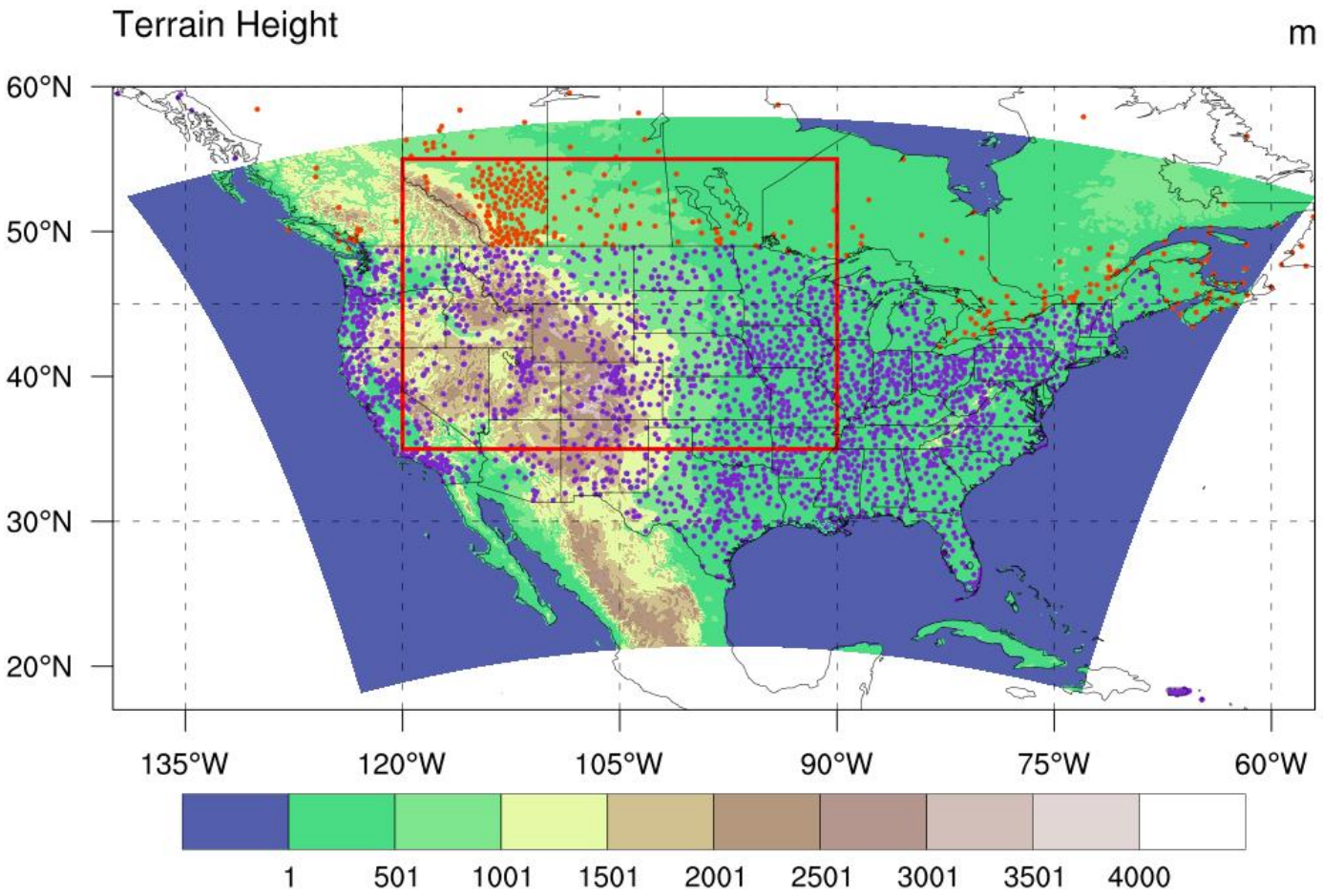

Figure 3 - 1 WRF computational domain. The colors represent topography (m asl) and the station locations are shown in purple dots for the U.S. dataset (from TD3240 and DSI-3240), and orange dots for the Canadian dataset (ECCC network). The red box is the region used in Figure 3 - 6 (Latitude: 35-55°N, Longitude: 90-120°W).

3.3 Method

3.3.1 Datasets standardization

All the datasets (OBS, sIV, WRF-CTR and WRF-PGW) were converted to Local Solar Time (LST) and to the measurement accuracy of the majority (78%) of the TD3240 gauges, which is a bucket size of 2.54 mm. An algorithm was applied to accumulate hourly precipitation over time to stations with smaller bucket sizes (0.245 mm) and to the sIV, WRF-CTR and WRF-PGW dataset. The precipitation is accumulated over time until it exceeds 2.54 mm or a multiple thereof, which is then recorded as a new precipitation record. Any precipitation exceeding 2.54 mm, or its multiples is then added to the next hour of the precipitation time-series. If any missing value is found in the original data, the accumulated value that has not reached 2.54 mm is set to zero and the previous time-steps are also set to zero. The 2.54 mm bucket size is suitable to measure high-intensity precipitation; Mooney et al. (2017) showed that the coarser resolution of the minimum bucket size does not affect the characteristics of the diurnal precipitation cycle. However, the intensity and frequency of weak precipitation (less than 2.54 mm h^{-1}) can be affected by this standardization (Mooney et al., 2017). For instance, 10 hours-long precipitation events with 0.254 mm h^{-1} intensity will be recorded as single events of 2.54 mm. Similar adjustments to observational records have been used in previous studies (e.g. Groisman et al., 2012; Barbero et al., 2017; Mooney et al., 2017).

The observational network is composed of different gauge types (e.g. tipping-bucket and weighting-bucket) and each gauge has different recording errors (e.g. Duchon and Essenberg, 2001; Parker, 2016). For instance, uncertainties arise from the electric signal accuracy, the conversion to a physical-meaningful value, bias associated with wind-induced under-catch, trace amounts, and wetting and evaporation losses (e.g. Yang et al., 1998; Rasmussen et al., 2012; Scaff et al., 2015; Pan et al., 2016). In addition, errors associated with the gauge maintenance and operation over long periods of time are frequently present.

The TD3240 dataset (87% of the OBS) was analyzed in detail to ensure the consistency and quality of the data (Hammer and Steurer, 2000, p. 16). The sIV dataset were processed using an algorithm that includes quality-control processes to produce precipitation (WSR-88, Fulton et al., 1998). The bias of WRF-CTR was within the observational uncertainty comparing different gridded observational datasets at the seasonal timescale, but WRF-CTR has a systematic warm and dry bias during late summer in the central U.S. (Liu et al., 2017).

3.3.2 Diurnal cycle characteristics

Harmonic functions are used to estimate the timing and the magnitude of the diurnal precipitation peak. Diurnal and semi-diurnal components are calculated for the analysis (i.e. the 24-h and 12-h harmonic functions of the diurnal cycle). This method allows us to summarize the diurnal cycle in two distinctive characteristics and eliminates noise from the data (Li et al., 2009; Li and Smith, 2010a). The harmonic analysis approximates the diurnal cycle of precipitation using a combination

of sine and cosine functions, considering the first two harmonics. In eq. (1) the precipitation (P_t) at time t is defined by the linear sum of the mean precipitation P in 24 hours (first term at the right-hand side), and the sine and cosine function for a 24- and 12-h cycle. The cycles are adjusted by the coefficients A_1 and B_1 for the first harmonic (second and third term at the right-hand side) and by the coefficients A_2 and B_2 for the second harmonic (the last two term at the right-hand side) (Wilks, 2011, p. 432).

$$P_t = P + A_1 \cdot \cos\left(\frac{2\pi t}{24}\right) + B_1 \cdot \sin\left(\frac{2\pi t}{24}\right) + A_2 \cdot \cos\left(\frac{4\pi t}{24}\right) + B_2 \cdot \sin\left(\frac{4\pi t}{24}\right) \quad \text{(eq. 1)}$$

Equation 1 is fitted considering a least-squared regression to all datasets on monthly mean hourly precipitation rates in each month between May and August. As the harmonic fit considered to characterize the diurnal cycle uses the first two harmonics (diurnal and semi-diurnal), the amplitude is found as the maximum value of the fitted curve, and the phase is the timing of this maximum.

This calculation was performed for each station in OBS and for each grid point in sIV, WRF-CTR and WRF-PGW. Some examples are shown in Figure 3 - 2 and Figure 3 - 3.

The precipitation amount, intensity and frequency are analyzed in this study. The precipitation amount is the average precipitation for the entire time series for each month and each hour (in units of mm h^{-1}). The intensity is calculated as the nonzero-average of hourly precipitation for each month (in units of mm h^{-1}). The precipitation frequency is the number of hours with nonzero precipitation (in units of number of occurrences).

The eastern propagation of precipitation is analyzed in the central U.S. considering four sub-regions with similar time of maximum precipitation of the diurnal cycle in June. June was chosen because of the high frequency of propagating storms. The data in each sub-region are clustered into 6-h bins; from 15 to 20 h (afternoon), from 21 to 02 h (night), from 03 to 08 h (early morning), and from 09 to 14 h (late morning) in LST.

To quantify the performance of the WRF-CTR, the bias is calculated as the difference between the WRF-CTR and OBS, and WRF-CTR and sIV. The bias is derived by comparing each model grid cell with the closest grid cell in sIV and with rain gauge observations if there are any within the grid cell area. The statistical significance of the climate change signal between the WRF-CTR and WRF-PGW is assessed using the non-parametric Mann-Whitney rank sum test at a significance level of 5% (Wilks, 2011, p. 159).

3.4 Results

3.4.1 Timing of the diurnal precipitation peak

The spatial patterns of the diurnal cycle precipitation peak timing in OBS and sIV are well simulated by WRF-CTR (Figure 3 - 2a-c and Figure B - 1 to B - 3). The transition was well captured from afternoon peaks over the lee-side of the central Rocky Mountains to night peaks in the Great Plains. The night to early morning transition (east of 100°W) is less pronounced in WRF-

CTR than in the OBS and sIV. In July a northward expansion of the eastward propagating signature is present from the Great Plains towards the Canadian Prairies. This signature reaches its northernmost extend in August (Figure B - 3).

WRF-CTR also simulates the observed (from sIV) sharp land-sea contrast of the diurnal precipitation peak along the Atlantic and Pacific coastlines and near the Great Lakes (Figure 3 - 2b) (Figure 3 - 2c). The thermal contrast along the coastal boundary leads to the development of convergence lines (and thus a solenoidal circulation) that helps trigger convective precipitation near the coast. This coastal effect on the precipitation timing, has been studied in the tropics and on islands (Carbone et al., 2000; Keenan and Carbone, 2008; Li and Carbone, 2015).

The largest model biases are found in the central U.S. east of 100°W (Figure 3 - 2d-e), with improperly simulated early morning peaks. Compared to OBS, the largest bias in domain averaged peak timing occurs in June (-0.7 h), whereas compared to the sIV it occurs in May (-4 h, domain average).

3.4.2 Magnitude of the diurnal precipitation peak

The dominant spatial patterns of the diurnal precipitation magnitude are captured in WRF-CTR (Figure 3 - 3). The simulated and observed magnitude increases to the south east and shows a relative maximum in the central U.S. The model overestimates the magnitude around the Florida peninsula (approximately 0.7 mm higher in WRF-CTR than sIV in June, not shown) and northward, along the east coast (Figure 3 - 3d-e). Compared to the OBS, the largest monthly mean bias occurs in June (44%; 14% compared to sIV). The Midwest shows a low bias in WRF-CTR (approx. 0.15 mm in Figure 3 - 3), which is consistent with the low precipitation bias reported in Liu et al. (2017) and Prein et al. (2017). The dry-bias in the Midwest and part of central CONUS (Liu et al., 2017) is likely associated with the model's limited capability in simulating organized convective storms under weakly forced synoptic conditions (Prein et al., 2017). A difficulty in simulation in current climate models is the storms that develop under weak large-scale forcing that heavily depend on local scale processes (e.g., cold pools, moisture gradients). The soil moisture and its role on the water cycle can be another possible feedback to argue about the systematic bias. Soil moisture affects the latent and sensible heat exchange between the land surface and the atmosphere, in turn affects the surface air temperature the atmospheric moisture and precipitation characteristics. The impact of soil moisture on precipitation and its diurnal cycle needs further investigation.

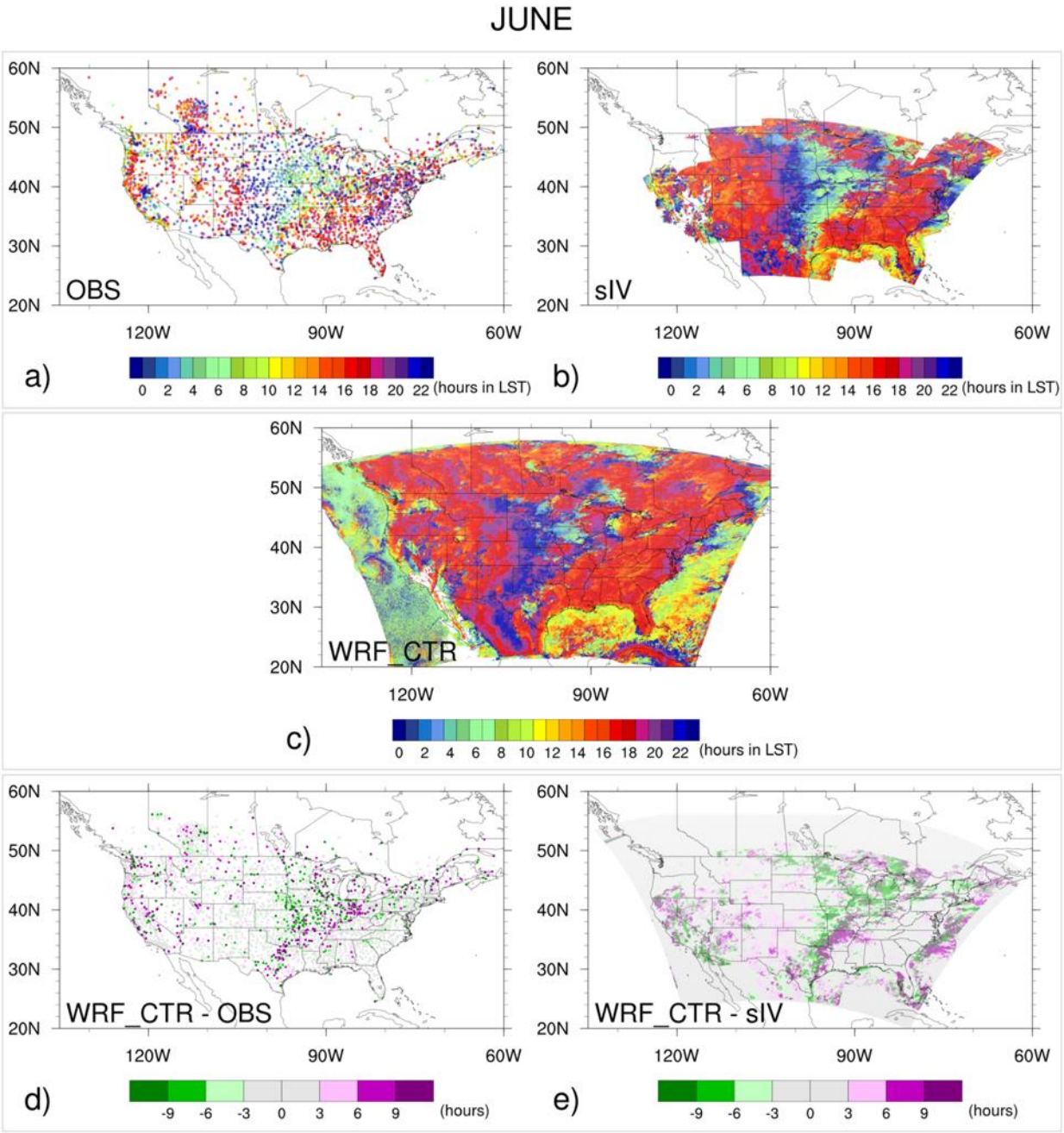

Figure 3 - 2 Timing of the diurnal precipitation peak in hours at Local Solar Time in June derived from the harmonic analysis. a) and b) are: observations (OBS) and stage IV (sIV). c) is the WRF historical runs (WRF-CTR). d) and e) show the differences between OBS and WRF-CTR, and between sIV and WRF-CTR respectively.

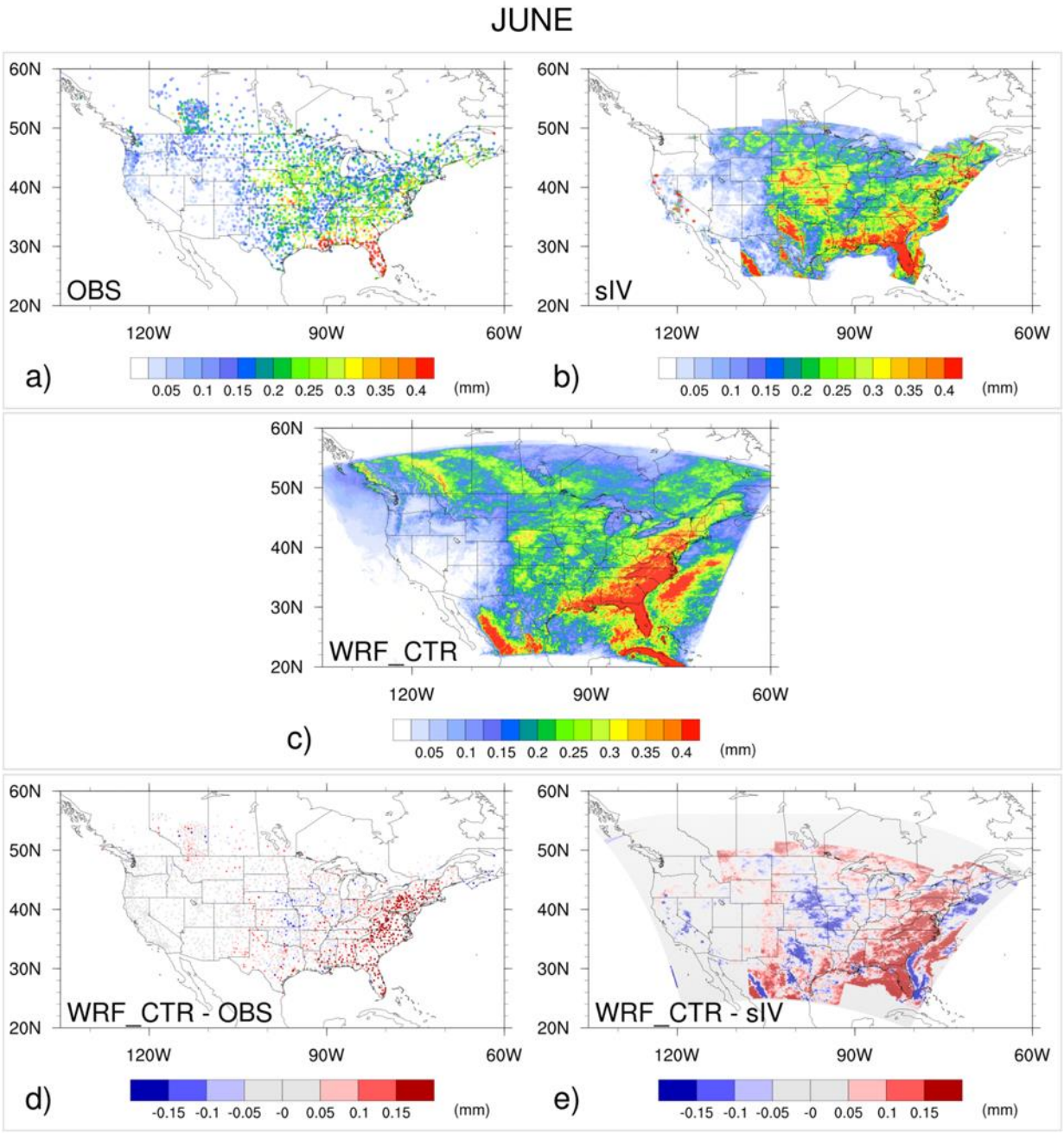

Figure 3 - 3 Magnitude (in mm) of the diurnal precipitation peak in June. a) and b) show observations (OBS) and stage IV (sIV). c) is for the WRF historical runs (WRF-CTR). d) and e) show the differences between OBS and WRF-CTR, and between sIV and WRF-CTR, respectively.

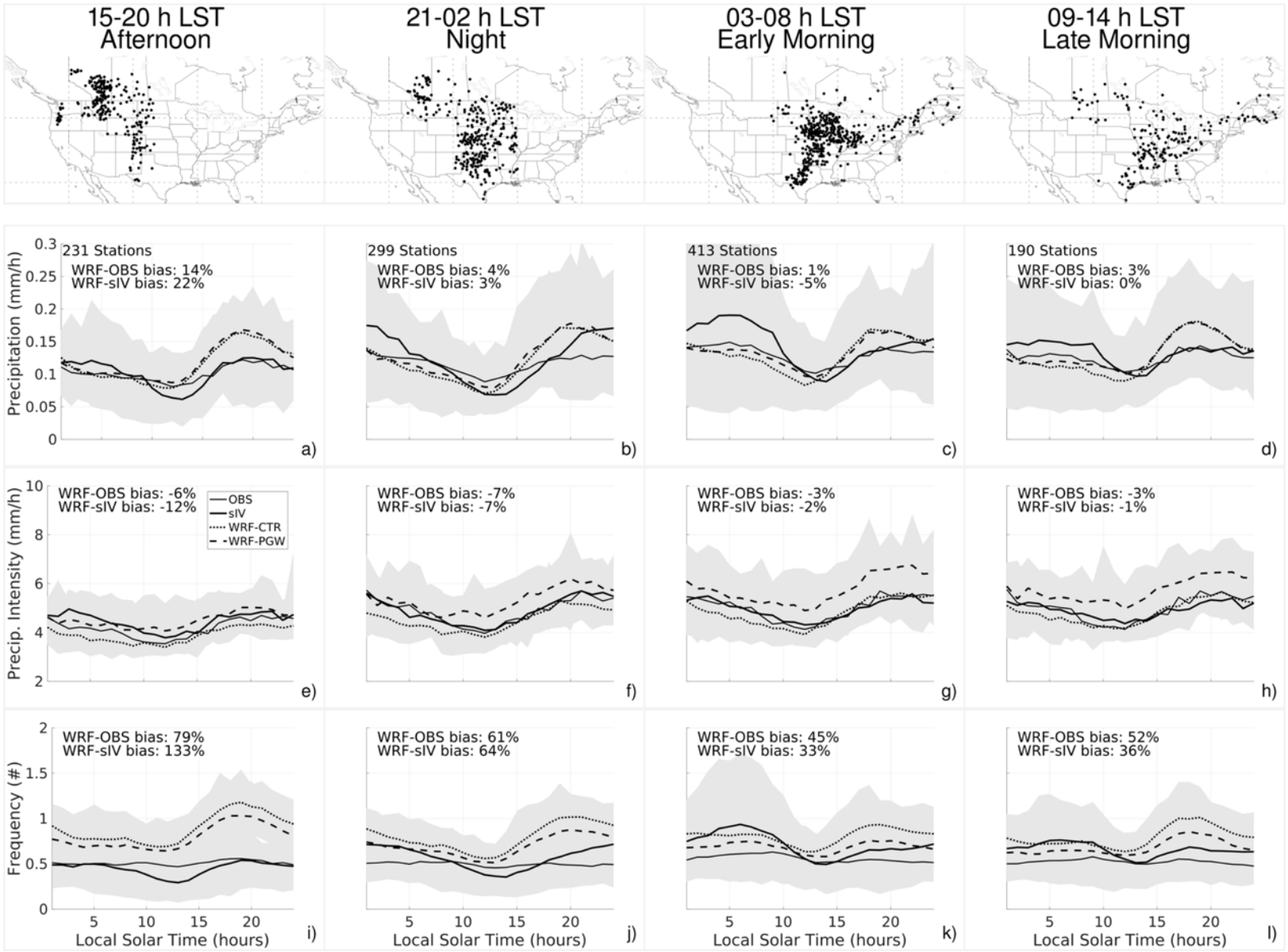
15-20 h LST
Afternoon
21-02 h LST
Night
03-08 h LST
Early Morning
09-14 h LST
Late Morning
Precipitation (mm/h)
231 Stations
WRF-OBS bias: 14%
WRF-sIV bias: 22%
299 Stations
WRF-OBS bias: 4%
WRF-sIV bias: 3%
413 Stations
WRF-OBS bias: 1%
WRF-sIV bias: -5%
190 Stations
WRF-OBS bias: 3%
WRF-sIV bias: 0%
a)
b)
c)
d)
Precip. Intensity (mm/h)
WRF-OBS bias: -6%
WRF-sIV bias: -12%
WRF-OBS bias: -7%
WRF-sIV bias: -7%
WRF-OBS bias: -3%
WRF-sIV bias: -2%
WRF-OBS bias: -3%
WRF-sIV bias: -1%
OBS
sIV
WRF-CTR
WRF-PGW
e)
f)
g)
h)
Frequency (#)
WRF-OBS bias: 79%
WRF-sIV bias: 133%
WRF-OBS bias: 61%
WRF-sIV bias: 64%
WRF-OBS bias: 45%
WRF-sIV bias: 33%
WRF-OBS bias: 52%
WRF-sIV bias: 36%
Local Solar Time (hours)
i)
j)
k)
l)

Figure 3 - 4 Precipitation diurnal cycle from observations (OBS, thin solid line), stage IV data (sIV, bold solid line), WRF-CTR (dotted line) and WRF-PGW (dashed line) in June. The sub-regions are stations clustering with similar precipitation peak timing in June. Only the stations (dots in maps at the top) with a peak precipitation magnitude greater than 0.1 mm h-1 are considered. The shaded area in the time-series shows the inter-annual variability (of 13 years for OBS, WRF-CTR and WRF-PGW, and 12 years for sIV).

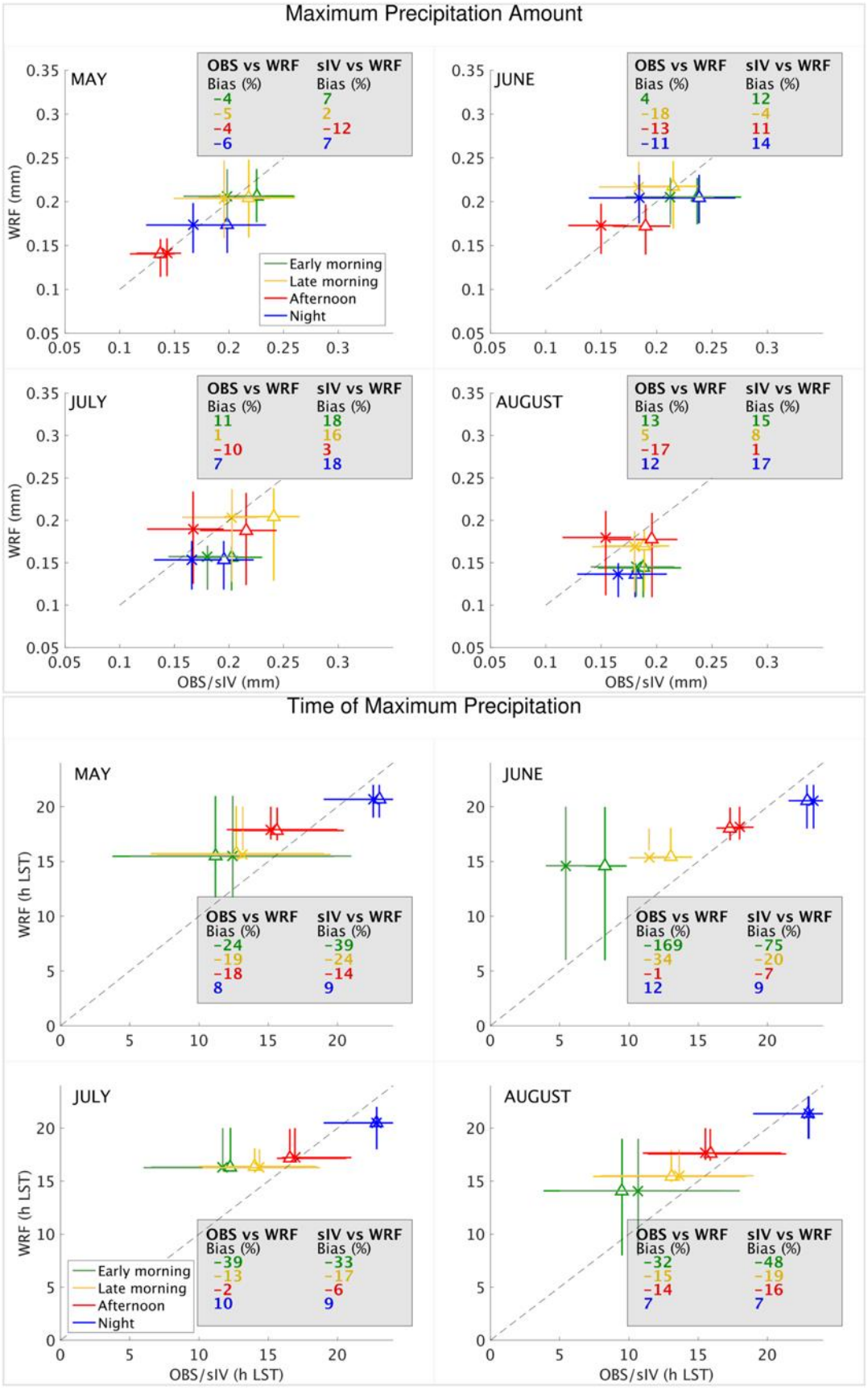
Maximum Precipitation Amount
MAY
JUNE
JULY
AUGUST
OBS vs WRF Bias (%)
sIV vs WRF Bias (%)
MAY: -4 -5 -4 -6 | 7 2 -12 7
JUNE: 4 -18 -13 -11 | 12 -4 11 14
JULY: 11 1 -10 7 | 18 16 3 18
AUGUST: 13 5 -17 12 | 15 8 1 17
Early morning
Late morning
Afternoon
Night
WRF (mm)
OBS/sIV (mm)
Time of Maximum Precipitation
MAY: -24 -19 -18 8 | -39 -24 -14 9
JUNE: -169 -34 -1 12 | -75 -20 -7 9
JULY: -39 -13 -2 10 | -33 -17 -6 9
AUGUST: -32 -15 -14 7 | -48 -19 -16 7
WRF (h LST)
OBS/sIV (h LST)

Figure 3 - 5 The comparison of the magnitude of the precipitation peak (in mm) and the timing (in hours at LST) from a two-harmonic fit of the diurnal cycle. The OBS (crosses) and sIV (triangles) correspond to the horizontal axis and WRF-CTR to the vertical axis**.** Panel shows results for individual months. The horizontal and vertical error-bars at each point represent the 25^{th} and the 75^{th} percentile of spatial variability. The four colors represent four sub-regions defined in Figure 3 - 4. The WRF-CTR biases (as percentages) are shown in gray boxes.

3.4.3 Propagation of organized convection

The simulation of eastward propagating convection is analyzed by investigating the transition on four sub-regions (top panels in Figure 3 - 4). The afternoon and night peak sub-regions are well captured in WRF-CTR (Figure 3 - 4a, b), with a maximum bias of 22%. For the early morning peak sub-region, the simulated hourly precipitation rate is underestimated at night and in the early morning (Figure 3 - 4c). When the model is compared to the sIV product, an overestimation in the afternoon is present (around ±0.05 mm h^{-1}). This is consistent with the underestimation of the frequency of eastward propagating storms that leads to an underestimation of early morning precipitation in WRF-CTR (Prein et al., 2017). In the early morning peak sub-region, the magnitude of the simulated diurnal precipitation is underestimated compared to sIV (Figure 3 - 5, triangles), consistent with the Figure 3 - 3d-e. The simulated magnitude for the late morning and afternoon peak sub-groups varies from a slight overestimation compared to OBS, to an underestimation when compared to sIV (Figure 3 - 5, B – 7 to B - 9). The averaged timing of the diurnal precipitation peak is well simulated in most of the regions (Figure 3 - 5, lower panels), with the lowest skill in the early morning peak sub-region (green in Figure 3 - 5, and Figure B - 1 to B - 3). The early morning peak sub-region shows a delayed peak time in WRF-CTR compared to OBS and sIV. The peak in the sub-regions with late morning and afternoon peaks occurs slightly earlier compared to the OBS and sIV with biases ranging from -1 to -34% (up to 4 hours), while the precipitation peak timing in the night peak sub-region shows a small delay with biases ranging from 7 to 12% (up to 3 hours). The average precipitation intensity shows a maximum bias of -12% (Figure 3 - 4e-h). The average precipitation frequency is typically overestimated in the afternoon and night peak sub-regions in May with bias up to 90% (Figure B - 7i, j) and in June with bias up to 133% (Figure 3 - 4i,j). In July and August, precipitation frequency is better simulated (Figure 3 - 4i-l, bias up to 49%).

The eastward propagation of precipitation (Figure 3 - 6) shows a consistent preferential region between 105° and 95°W amongst datasets. The propagation of precipitation varies through months and latitudes. The sIV shows larger precipitation amounts (dots size in Figure 3 - 6) than OBS, especially between 45-50°N (Figure 3 - 6a-h). The propagation speed in OBS and sIV is approximately 12 m s^{-1}, consistent with Li and Smith (2010b). In all months, the simulated propagation is slightly faster (approximately 14 m s^{-1}) than the OBS and sIV. The magnitude of the precipitation peak shows a strong decay in the model during late night and early morning (0-6 h LST) between 40-45°N in July and August, from 100°W eastward. This result is also highlighted

by Prein et al. (2017), who related the dissipation of the storms to model deficiencies in simulating the propagation of organized convective systems under weak synoptic scale forcing, which typically occur in July and August. The weak synoptic forcing is associated with regions or stable and moderate ridges, or in the transition of baroclinic perturbations, or strong troughs.

3.4.4 Climate change impact on the precipitation diurnal cycle

The diurnal cycle shows no substantial change in the precipitation amount in WRF-PGW (Figure 3 - 4) compared to WRF-CTR. However, the WRF-PGW simulation shows a clear increase in hourly precipitation intensities compared to WRF-CTR in all sub-regions (Figure 3 - 4e-h), while the precipitation frequency decreases in WRF-PGW (Figure 3 - 4i-l), so this decrease and the increase in intensity compensate each other, resulting in similar precipitation magnitude.

Changes in the timing of the diurnal precipitation peak are not systematic and are non-significant in May (Figure 3 - 7a), consistent with the remaining summer months. The magnitude of the diurnal precipitation peak shows an increase throughout the domain in WRF-PGW (Figure 3 - 7b), with statistically significant increase (black circles) in May over the northern region. In July and August, the magnitude of the diurnal precipitation peak significantly decreased in South Dakota, Nebraska, Kansas, Missouri and Michigan (Figure B - 10).

The increase in precipitation intensity (Figure 3 - 7c and Figure B - 11) is present over the entire domain and all months. A statistically significant change occurs in the northern and eastern part of the domain, however the largest increase, but not significant, occurs in the southern part of the domain. The frequency (Figure 3 - 7d) shows an increase in May in the south of Canada and a decrease in the southeast U.S. The region with decreasing frequencies is extended to the central U.S. and southern Canada during mid-summer. A statistically significant frequency decrease is present in July and August over the western U.S. including Nevada, Idaho and Wyoming (Figure B - 11).

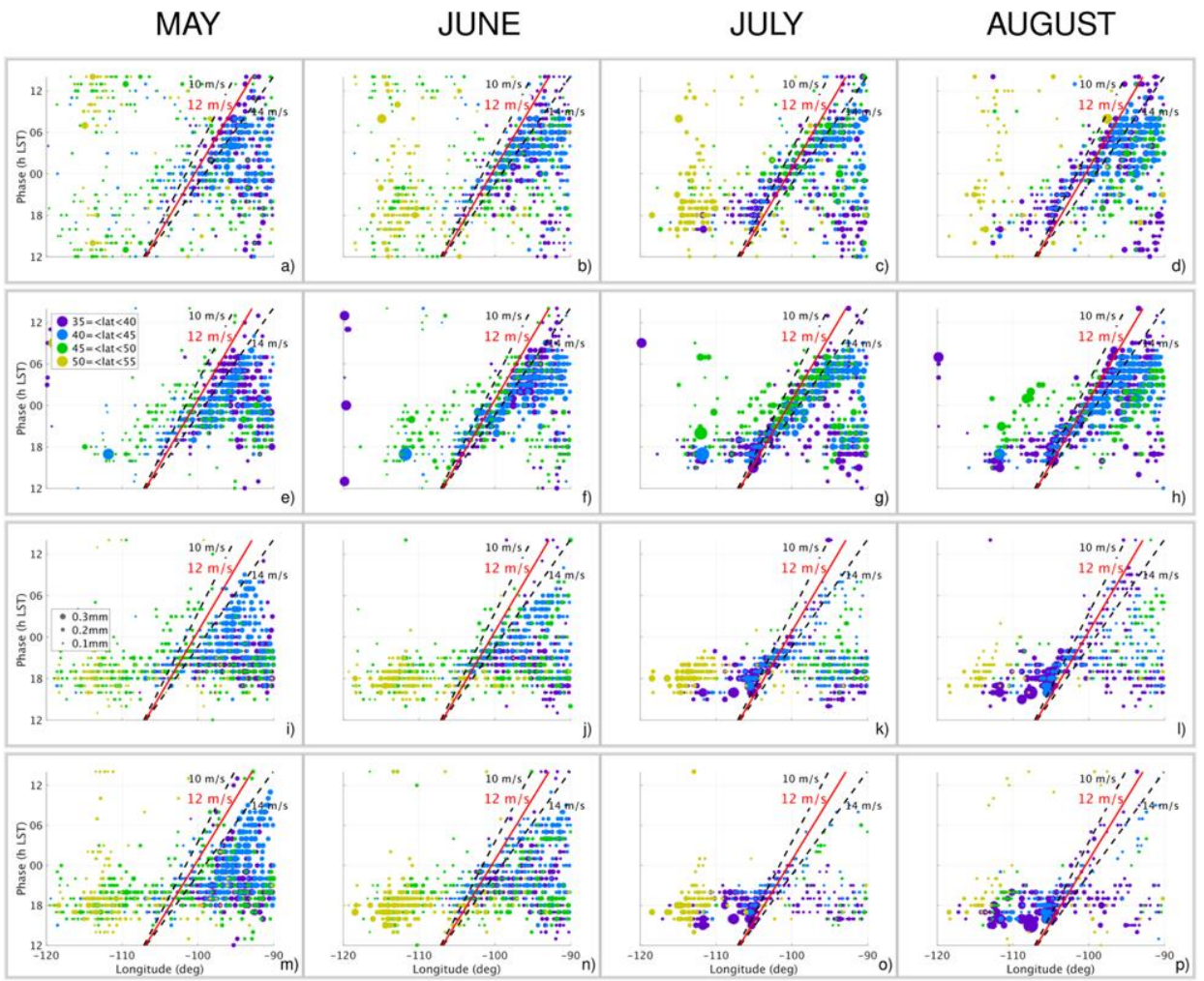

Figure 3 - 6 The timing of the diurnal precipitation peak in hours at Local Solar Time vs. longitude. Different latitudinal bands are shown in different colors. The dot size represents the relative magnitude of the diurnal precipitation peak with values greater than 0.1 mm h^{-1}. The analyzed region is highlighted by a red box in Figure 3 - 1. The red solid lines show a propagation speed of 12 m s^{-1} from Li and Smith (2010). The black dashed lines show a propagation speeds of 10 m s^{-1} and 14 m s^{-1}.

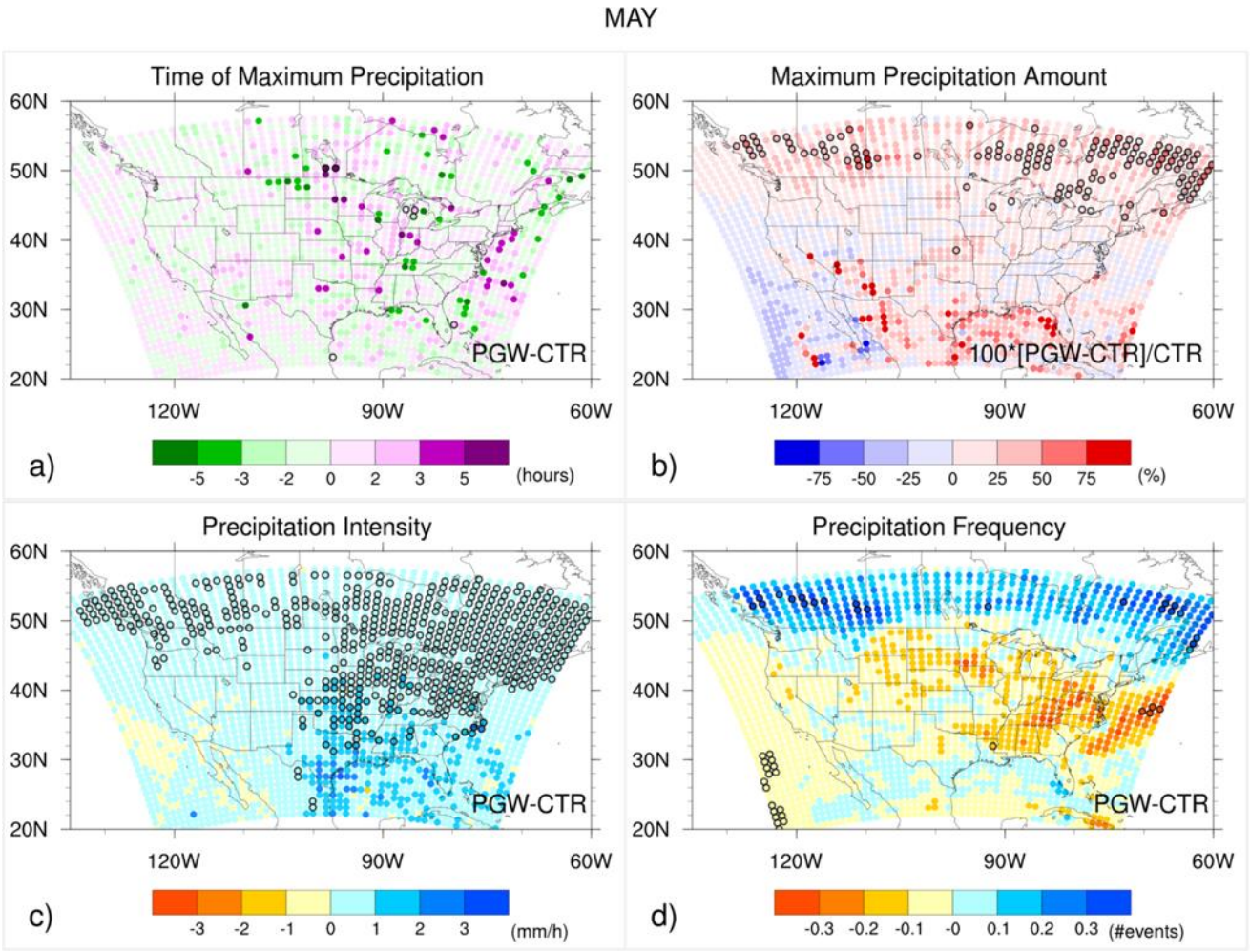

Figure 3 - 7 Difference between WRF-PGW and WRF-CTR in May, for a) timing of the diurnal precipitation peak in hours at Local Solar Time, b) the magnitude of the diurnal precipitation peak (relative change in %), c) average precipitation intensity (mm h^{-1}) and d) average precipitation frequency (# of events). The spatial grid is reduced to one filled circle every 25 model grid cells to enhance the visibility of the results (circle distance ~100-km). Circles with black outlines indicate that at least 20% of the 25x25 grid cells show statistically significant changes (5% level using the Mann-Whitney rank sum test).

3.5 Summary and conclusions

This study investigates if a North American scale convection-permitting model at 4-km horizontal grid spacing can reproduce the observed diurnal cycle of precipitation during the warm season. The evaluation of the climate change impact on the precipitation diurnal cycle is presented.

We use hourly precipitation datasets – a station-based and a gridded dataset which merges station and radar data – to assess the impact of observational uncertainties for the model evaluation. Results show that the simulated timing of the diurnal precipitation peak agrees with observational datasets in areas with afternoon to night peaks. The accurate simulation of the transition from evening to night-time peaks, over the leeside of the Rocky Mountains, is especially encouraging. The observed movement speed of these storms (approx. 12-14 m s^{-1} as Li and Smith, 2010a) is also captured by the model. These results represent an improvement of the diurnal cycle simulation compared with previous simulations at coarser horizontal grid spacing, which use cumulus parameterizations (e.g., Mooney et al., 2017). The hourly precipitation intensity and frequency is also improved compared to coarser resolution models (Fosser et al., 2014; Mooney et al., 2017). However, several biases are documented from this simulation, which include:

- An overestimation in the magnitude of the diurnal precipitation peak over Florida (around 0.7 mm), which is consistent with the overestimation of precipitation reported by Liu et al. (2017). Since there is a significant warm bias along the coast (see Fig. 12 in Liu et al., 2017), we hypothesize that WRF overestimate the sea breeze effect, which should be further investigated.
- In July and August, the diurnal cycle of precipitation intensity is underestimated over the central U.S., which is consistent with a dry bias described by Liu et al. (2017). The modeled precipitation frequency is overestimated in early summer and improves later in the warm season. We are currently working on reducing the dry biases by improving the representation of the land surface, radiation, and turbulence schemes.
- The largest biases simulating the timing of the diurnal precipitation peak are found in the central CONUS, with the early morning peaks. This is related to an underestimation of the frequency of propagating convective systems, which agrees with previous studies (Prein et al., 2017 and Haberlie et al., 2019). The moisture flux within the low-level jet zone is properly represented in the model when compared to the ERA-Interim reanalysis (Rasmussen et al., 2017). More detailed analyses of the low-level jet, cold pools, potential vorticity anomalies as well as other atmospheric processes are needed to better understand the origin of these biases.

The most consistent climate change signal is an increase in precipitation intensity throughout the summer, also consistent with previous studies (e.g. Stone et al., 2000; Prein et al., 2016). This increase with a significant decrease in the precipitation frequency, indicates more precipitation events with high rain rates followed by longer dry periods, which agrees with Rasmussen et al. (2017). This will have impacts on the agricultural sector and will alter future flooding risks.

Regional climate models on a CPM configuration are robust tools to study climate change impacts on precipitation as has also been demonstrated in previous studies (Kendon et al., 2014; Kendon et al., 2017). Future studies should further explore the causes and implications of the central U.S. warmer bias and how they affect the simulation of future climates. Finally, a more thorough assessment of the model's quality outside of the U.S., i.e., in Canada and Mexico, will be beneficial.

Key points for the next chapter

- The regional climate model in a convection-permitting model is able to correctly simulate the characteristics of warm season precipitation, specially from the afternoon to the night peaks of the diurnal cycle.
- Systematic biases were found on the early morning peaks (over the Midwest in the U.S.) of the diurnal cycle and an overestimation of the precipitation amount over the southeast region.
- The CPM simulation at 4-km resolution on hourly timesteps, provides the opportunity to describe in more detailed atmospheric processes on the mesoscale, particularly on places that are less accessible, such as mountain environments, and high latitudes.

Acknowledgments

We gratefully acknowledge the Natural Sciences and Engineering Research Council of Canada (NSERC) for funding the Changing Cold Regions Network (CCRN) through their Climate Change and Atmospheric Research (CCAR) Initiative. L. Scaff and Y. Li gratefully acknowledge the support from the Global Institute of Water Security at the University of Saskatchewan. L. Scaff acknowledges the support from CONICYT-Becas Chile scholarship program. L. Scaff appreciates S. Krogh for providing valuable comments to improve this study. A. Prein, C. Liu, R. Rasmussen and K. Ikeda appreciate the support from the Water System Program at the National Center for Atmospheric Research (NCAR). The National Science Foundation sponsors NCAR. This project was performed at the NCAR facilities Funded under NSF-Water System Program. We would like to acknowledge high-performance computing support from Yellowstone (ark:/85065/d7wd3xhc) provided by NCAR's Computational and Information System Laboratory, sponsored by the National Science Foundation.

CHAPTER 4

CONVECTIVE INITIATION ASSOCIATED WITH THE DRYLINE ON THE LEESIDE OF THE ROCKY MOUNTAINS IN ALBERTA, FROM THE HISTORICAL AND A FUTURE CLIMATE

This chapter is in preparation for a paper to be submitted to a peer-reviewed scientific journal, in collaboration with the following authors: Andreas Prein, Yanping Li, Neil Taylor, Changhai Liu, Roy Rasmussen and Kyoko Ikeda.

Author contributions: L. Scaff and A. Prein designed the study. C. Liu and K. Ikeda performed the WRF simulations. K. Ikeda post-processed the WRF output. N. Taylor provided the field experiment data and helpful conceptual advice. All authors contributed to the interpretation of the results and to writing the manuscript.

Keywords

Convective Initiation, Convection-Permitting Models, Dryline, Pseudo Global Warming

Abstract

Deep moist convection is a significant source of summer precipitation over North America. The dryline is a key mechanism associated with the initiation of convection on the leeside of the Canadian Rockies in the province of Alberta. The dryline is characterized by a strong boundary layer moisture gradient parallel to the mountain barrier. To improve our understanding of convective systems and how they potentially change in a warmer climate in Alberta, more knowledge is needed of the mesoscale features that modulate the dryline and associated convective initiation in this region. A regional climate model in a convection- permitting configuration (CPM) is used to characterize the dryline in a historical climate using ERA-Interim reanalysis as input and to explain its changes in the future climate using a pseudo global warming approach.

Results show that the dryline is present in the initial stage of 37% of the largest storms. Convective initiation associated with the dryline is well coupled to the necessary convective environment, with a maximum of the convective available potential energy in the afternoon, along with a minimum convective inhibition index right after the capping lid dissipation. In the future climate simulation, the dryline is associated with 34% of the largest storms, showing a northern shift of the convective initiation. This displacement is consistent with the changes in the convective environment. There is a clear difference in extreme precipitation over the regime transition from an energy-limited to a moisture-limited environment over the southern part of the domain at dewpoint temperatures above 10°C. At these temperatures, the moisture-limited environment inhibits the intense precipitation formation in this sub-region. The characterization of the dryline provides a reference point to evaluate the current forecast of convective storms initiated by a dryline. It also enables us to assess changes in the convective precipitation characteristics of a warmer climate.

4.1 Introduction

A poleward reduction of solar radiation can suggest a decrease in the diurnal amplitude of summer precipitation. However, an increase in precipitation, along with the strengthening of the diurnal cycle, is present at around 55°N on the leeside of the southern extent of the Canadian Rockies (e.g., Taylor et al., 2008; Scaff et al., 2019). The presence of significant precipitation at higher latitudes can be attributed to mesoscale convection in the form of thunderstorms. During the warm season this region is frequently characterized by sufficient Convective Available Potential Energy (CAPE) to support thunderstorms. A sloping terrain and the development of mesoscale circulations and/or convergence boundaries, such as low-level moisture variation, strong horizontal wind shear, orographic waves, and thermodynamic processes (Sherwood et al., 2010), often trigger convective initiation (CI).

The mechanisms that promote convection on the leeside of the Canadian Rockies in a weak synoptically forced environment (Done et al., 2006; Liu et al., 2006) are frequently associated with mountain-plain circulation, which can be present in the diurnal cycle across the foothills (Smith et al., 1993b). The low-level jet and moisture transport from the south to the east side of the Rockies, along with the subsidence of westerly flow from above the mountains, produce convective instability because of the strong shear around the jet and the strong humidity zonal gradient, known as the dryline. The dryline is a near-surface horizontal moisture boundary between dry-hot and moist-warm air close to the surface (e.g., Schaefer, 1974), however, because this thermal contrast is not always significant (Taylor et al., 2016), the moisture gradient is the defining feature of the dryline. A previous study described the dryline as occurring when the specific humidity gradient is at least 0.03 g kg^{-1} km^{-1} (Hoch and Markowski, 2005). This strong humidity gradient produces an imbalance for which a solenoidal circulation compensates (an increase of the solenoidal term in the vorticity equation). The solenoidal circulation is produced in a baroclinic fluid, in which the pressure and density levels are not parallel The convergence zone is at low levels and at the moist side, where the vertical flow is produced (Ziegler et al., 1997), providing a favorable condition for cloud formation and convective initiation (CI) in its vicinity (Rhea, 1966; Ziegler and Rasmussen, 1998). The dryline's effect on CI, has been identified on the leeside of different mountainous regions, such as southeast Wyoming (Bergmaier and Geerts, 2015), the Great Plains (Rhea, 1966), and west Texas (Parsons et al., 1990). It has also been observed in other less documented mountainous regions, such as central Argentina (Bechis et al., 2016) and northwest Australia (Arnup and Reeder, 2007).

The dryline's effect on CI has been studied in the Canadian Rockies through experimental field campaigns (Strong, 1989; Hill, 2006; Taylor et al., 2011) and using high-resolution atmospheric models for case studies (Erfani et al., 2003; Taylor et al., 2011). The dryline magnitude (specific humidity zonal gradient) related to the initiation of rainfall events has been measured between 0.9 and 4.3 g $kg^{-1}km^{-1}$ during seven events in two summer seasons (Hill, 2006), and up to 18 g kg^{-1} km^{-1} in the latest field experiment performed in the region (Taylor et al., 2011). In a 30-years observation period, the dryline was observed on 32% of days between April and June over the

Great Plains (Hoch and Markowski, 2005). It was also observed on around 11% of days in southwest Wyoming using three years of Reanalysis data, with an average gradient magnitude of 5.3 g kg^{-1} 100 km^{-1} (Bergmaier and Geerts, 2015). Dryline-associated CI in the U.S. has also been studied using high-resolution atmospheric models for individual events. Trier et al. (2015) analyzed the influence of the parameterizations and the physical processes involved in CI triggered by a dryline. Using an ensemble of regional climate atmospheric models in a convection-permitting configuration, they (Trier et al., 2015) found that two types of forcing are equally important for CI; 1) from a direct thermally-generated vertical circulation at the surface below CI and 2) from the temperature and moisture tendencies in the planetary boundary layer scheme from a broader regions, due to changes in the terrain and moisture. These authors also found that horizontal temperature advection strongly influences the location of sustained CI. Campbell et al. (2013) showed an accurate representation of the time and location of CI produced by a dryline in a regional climate model at 1-km resolution and the impact of the dryline "bulge" on CI; however, their simulation showed an eastward bias of the dryline position, which has been also found in other studies (Clark et al., 2015; Coffer et al., 2013).

In a future climate, both the dryline characteristics and their influence over CI can be modified by changes in the key atmospheric forcing involved. On a large scale, the magnitude, frequency and/or location of the dryline could be influenced by a combination of effects. Some of these effects are: the amplification of the Hadley cell (Lu et al., 2007; Seidel et al., 2008); the poleward shift of extratropical cyclones (Mbengue and Schneider, 2013; Shaw et al., 2016); the possible strengthening of the wind circulation (e.g., westerly winds) over the ocean (Kent et al., 2013); and variable changes of the wind over land, e.g., weakening over southern Canada (Wan et al., 2010) and the U.S. (Pryor et al., 2007).

Mechanisms that modulate changes in a warmer climate are dynamical and thermodynamic forcing (Emori and Brown, 2005; Kröner et al., 2016). Some dynamical components of wind circulation, such as confluence, convergence, and vertical wind shear, can produce changes in the magnitude and location of the dryline and associated CI (Schultz et al., 2007). Thermodynamical processes can be partially separated from the rest of the forcing and influence precipitation changes in the future. These thermodynamical forcing are characterized by distinct temperature lapse-rates (Kröner et al., 2016; O'Gorman and Schneider, 2009), the convective environment (Trenberth, 1999; Trapp et al., 2007; Rasmussen et al., 2017), and the scaling rates between extreme precipitation and temperature. The scaling rate is based on the Clausius-Clapeyron relationship between temperature and saturated vapor pressure, which is a thermodynamical relationship. When the assumption about the atmospheric equilibrium (Trenberth et al., 2003) is considered, it is possible to transfer this relation to precipitation and dewpoint temperature (O'Gorman and Schneider, 2009). To date, this is the only approach to relate changes in temperature to extreme precipitation. Several studies observed a similar function to the equivalent Clausius-Clapeyron relationship between extreme precipitation and temperature (Ban et al., 2015), while others have shown super-adiabatic approximations (Ban et al., 2015; Haerter and Berg, 2009; Kendon et al., 2014; Lenderink and van Meijgaard, 2008; Pall et al., 2007; Prein et al., 2016). A further linking

of scaling rates to the extreme precipitation changes in a warmer climate is still controversial, due to the local nature of the temperature chosen and its complicated link to global warming (Boucher et al., 2013).

The purpose of this study is to use a regional climate model in a convection-permitting configuration over a long-term simulation to investigate the impact of a warmer climate on dryline characteristics and CI. This model configuration also allows us to examine the contribution of mesoscale features in the location and timing of CI in extratropical regions. These features need to be better understood, so robust answers to potential changes in a transient climate can be found.

4.2 Datasets

4.2.1 Numerical model simulations

The Weather Research and Forecasting model (WRF, Skamarock et al., 2008) version 3.4.1. was used to simulate the historical climate (WRF-CTR) from 2001 to 2013 and initialized using the ERA-Interim reanalysis (Dee et al., 2011) as boundary and initial conditions. A spectral nudging was used to maintain the large-scale patterns form the ERA-Interim reanalysis (see section 3.2.1. for more details). To simulate the future climate, the Pseudo Global Warming approach (WRF-PGW), introduced by Schär et al. (1996), was used to represent a warmer scenario between 2071 and 2100. Both simulations were performed over a continental domain (Figure 4 - 1a ; Liu et al., 2017; Scaff et al., 2019). The model configuration is detailed in Table 4 - 1. The WRF-PGW simulation was initialized by a perturbed input from ERA-Interim reanalysis as boundary and initial condition. The perturbation was calculated using a monthly average of an ensemble of 19 global climate models from the Climate Model Intercomparison project (CMIP5; Taylor et al., 2012) under a high-emission scenario (RCP8.5, Riahi et al., 2011) for all the input variables (Table 4 – 1). More details about the PGW method applied in the simulations used here are presented in Liu et al. (2017).

Table 4 - 1 Model description of the WRF-CTR and the WRF-PGW. CTR_{BC} is the boundary conditions for the control simulation.

WRF version	3.4.1.
Entire domain	Appox.19-57°N, 139-56°W From approx. 140 m below the surface in the land-surface scheme and up to 50 hPa (~20,000 m asl)
Resolution	Δx: 4-km, Δt: 1 hour
Boundary conditions	CTR_{BC}: ERA-Interim reanalysis every 6 hours PGW: CTR_{BC} + ΔCIMP5 (ensemble of 19 GCM with RCP8.5)
Input variables	Soil and air temperature, geopotential height, wind speed, soil moisture, atmospheric pressure, specific humidity.
Spin up period	3 months
Main physical schemes	
>Microphysics	New Thompson and Eidhammer (2014) scheme
>Land-surface	Noah Multi Physics options, (Noah-MP Niu et al., 2011)
>Planetary boundary layer	Yonsei University (YSU, Hong et al., 2006)
>Cumulus	No cumulus parameterization used.
>Long- and short-wave	Radiative Transfer model (RRTMG, Iacono et al., 2008)

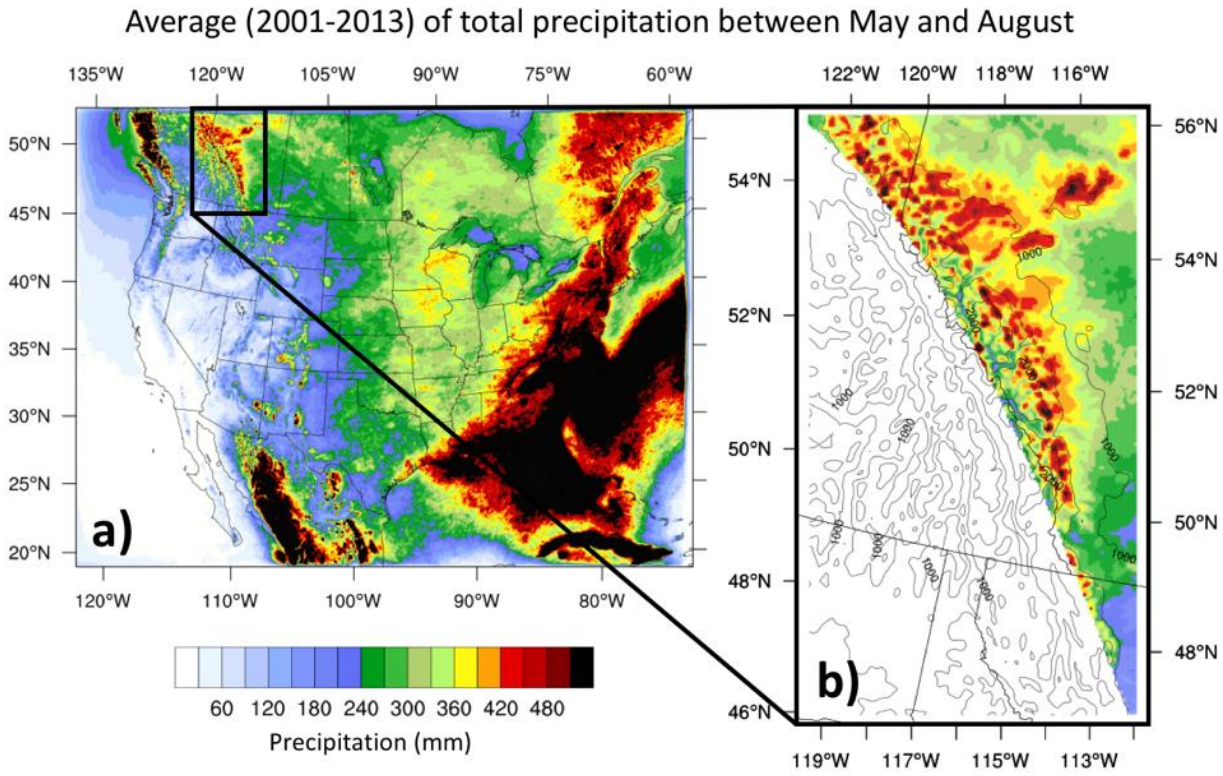

Figure 4 - 1 Annual average of total precipitation between May and August for the current climate. a) shows the entire domain of the WRF simulations and b) shows the study area with the topography altitude in contour intervals (m asl).

4.2.2 Data for model validation

The latest field experiment looking at convective initiation in the leeside of the Canadian Rockies was implemented in July 2008 for a two-week campaign. The experiment was called the Understanding Severe Thunderstorms and Alberta Boundary Layers Experiment (UNSTABLE; Taylor et al., 2011). The selected observed data details used for this validation are in Table 4 - 2, and the entire description of the experimental instrumentation is presented in Taylor et al. (2011). This study uses the observed low-level specific humidity from the UNSTABLE. The field observations were spatially extrapolated to create a regular gridded dataset using an inverse-weighted squared distance technique. The surface records from weather stations that contain wind, pressure, temperature and relative humidity along with radiosondes measurements were also part of this campaign and were available to further examine the model performance.

The ERA5 reanalysis (ECMWF, 2017) is selected to verify the diurnal cycle monthly means of specific humidity at 2 m above the surface. The ERA5 was chosen because of the higher spatial resolution (~0.28°) and temporal resolution (hourly), compared with others reanalysis (e.g., Dee et al., 2011; Saha et al., 2010). ERA5 also contains more variables available compared with others

gridded products, which are normally only for temperature and precipitation (e.g., Mahfouf et al., 2007; Haylock et al., 2008; Hutchinson et al., 2009; Newman et al., 2015).

Table 4 - 2 Summary of selected observations from UNSTABLE used for validation.

Type of Analysis	Variables	N. of stations	Resolution	Mobility	Selected period
Spatially distributed contours	Specific humidity contours	304 in average	1-hour	Mostly fixed	19 hours, 2008 July 13 at 12 pm to July 14 at 06 am
Timeseries	Temperature, pressure, dewpoint temperature, relative humidity, wind speed and direction	1 station: EA3	10-minutes	Fixed	2008 from July 12 at 12 am to July 14 at 12 pm
Vertical profiles skew-T	Temperature, dewpoint temperature, pressure, wind speed and direction	4 stations: MB1, MB2, WVX and EA3	Variable	Mobile and fixed	2008 July 13 at 23 UTC

4.3 Methodology

4.3.1 Study region

Convective Initiation (CI) was analyzed over the leeside of the Canadian Rockies, in the Province of Alberta, Canada (Figure 4 - 1a). For both the observed and simulated average of the warm season precipitation (hereafter defined as the months of May, June, July and August) it is easy to see a relative maximum over the Canadian Rocky mountain foothills, which coincides with the lightning maximum in this region (Burrows et al., 2002). For the analysis, we selected a triangular sub-domain that covers this maximum precipitation (Figure 4 - 1b), with the west boundary of the sub-domain defined using a quadratic regression over the continental water divide (the highest altitudinal points) from the model topographic elevation. The subdomain is close to the simulation northern boundary, so the northern boundary was cropped 250 km southward. The relaxation zone (200 km) and another 50 km from the border were not consider as it might have a strong influence from the boundary condition.

4.3.2 Model validation

An evaluation of the model performance to simulate the dryline and its influence on CI was carried out using the UNSTABLE dataset between July 12 and 14, 2008 (Taylor et al., 2011). These dates were chosen because a dryline developed on July 13 followed by light precipitation at the east side of the dryline. We compare the average of the 19-h available spatially gridded specific humidity dataset from UNSTALBE against the average of the same 19-h from WRF-CTR. Near-surface measurements were also compared from weather stations and the radiosondes in the skew-T diagram to the WRF-CTR. The comparison was performed between the station's location and the closest grid point in the WRF-CTR.

To verify the model in a longer time scale, a comparison is presented between WRF-CTR and the available years from ERA5 reanalysis (ECMWF, 2017) stored in the Research Data Archive. The data available in ERA5 and matching the simulation period in WRF-CTR, was from 2008 until 2013. We compared the diurnal cycle on monthly average for July of specific humidity at 2 m above the surface.

4.3.3 Storm selection

The precipitation events that contribute the most to the warm season precipitation were selected to investigate the influence of the dryline over CI, and to estimate the importance of these precipitation event affected by the dryline, to the total warm season precipitation. These precipitation events were defined as any wet period that contains at least one day with precipitation above the 85% quantile of the 13-year period of the warm season precipitation. For those days above the 85% quantile, a manual inspection was performed on the time series of precipitation and regional maps to identify the initial day of wet periods that defines the precipitation events. This manual inspection is believed to be the best approach to confirm that the evolution of precipitation time series corresponds to a coherent spatial evolution of storms in the region.

The dryline was defined as a surface zonal gradient of specific humidity greater than 0.03 g kg^{-1} km^{-1} (Bergmaier and Geerts, 2015; Coffer et al., 2013; Hoch and Markowski, 2005). The presence of a dryline during the initial day of the selected storms was carried out manually. The hour of the initial day of the storms was selected as a case when a dryline affect CI when a zonal specific humidity gradient: (1) was at least 0.03 g kg^{-1} km^{-1}, (2) was parallel or quasi parallel to the mountain main axis, (3) had a length longer than 100-km and (4) the precipitation was initiated (precipitation above 0.1 mm) on the east side of the dryline. A careful inspection was focused on eliminating any humidity gradient that was produced after the precipitation started, which normally appears around cold pools outflow nearby precipitation. Cases where the initial precipitation occurs on the west side of the dryline were also eliminated, as they are typically related to frontal systems coming from the windward side of the Rockies and that are strong enough to cross the

mountain and generate precipitation at the leeside. Similar precautions have been taken to identify the effect of the dryline on CI (Clark et al., 2015; Coffer et al., 2013; Johnson and Hitchens, 2018).

4.3.4 Convective environmental features

To characterize the stability during CI, we chose the convective available potential energy (CAPE) and the convective inhibition (CIN) indices during the initial day of all the selected precipitation events. The diurnal cycles of these indices (i.e. the maximum CAPE and the minimum CIN) were investigated to understand the evolution of the convective environment under historical and future climate conditions.

4.3.5 Analysis of a warmer climate

The selection of the precipitation events that contributed the most and that are related to CI affected by the dryline in the WRF-PGW was performed using the same criteria aforementioned for the WRF-CTR. To investigate the differences between the CI affected by the dryline from WRF-CTR and WRF-PGW, the following atmospheric forcing features were analyzed: (1) dynamical mechanisms that can cause changes in the circulation terms: convergence, vorticity, deformation and vertical wind shear, and (2) the thermodynamical mechanisms, including changes in the stability parameters (CAPE and CIN), and the adiabatic scaling rate between extreme hourly precipitation and the dewpoint temperature. The scaling rate was calculated for the maximum values of the extreme precipitation (99^{th} percentile) for every dewpoint temperature bin of 1°C overlapping ±1°C, over the initial day of the storms initiated by a dryline, and afterward all the scaling rates are averaged over the domain.

4.4 Results

4.4.1 Model verification of specific humidity

A comparison between an observed and the corresponding simulated low-level specific humidity is presented in Figure 4 - 2. The comparison presents the development of one dryline event between 1200 UTC 13 July 2008 and 0600 UTC 14 July 2008. The strengthening of the zonal gradient of specific humidity over the foothills is captured by WRF-CTR; however, the magnitude is underestimated in the eastern side, and overestimated closer to the mountains. The simulated location of the strongest specific humidity gradient is shifted to the northeast. The dry-bias in the model near the foothills agrees with other results from studies using the boundary layer YSU parameterization (Coffer et al., 2013; Coniglio et al., 2013). These differences were expected as the WRF simulation was designed to capture general climatological features (Liu et al., 2017) instead of individual events. Further validation for this event is provided in Appendix D.

The comparison of ERA5 and WRF-CTR (Figure 4 - 3) shows a similar spatial pattern. Both datasets present comparable magnitudes of the dry and moist side of the longitudinal gradient of specific humidity, from 5 g kg^{-1} over the Mountains to 8-8.5 g kg^{-1} in the Prairies. Because of the

lower resolution in ERA5, the spatial heterogeneity is smoother than in WRF-CTR. In the southern part, the simulated (WRF-CTR) drier air extends northward compared to the ERA5. The complete monthly average of the specific humidity diurnal cycle, every 2 hours, is presented in Appendix E. Afterwards, the model simulations are only used to analyze averaged-values of precipitation, specific humidity and other variables, as it was designed to be used.

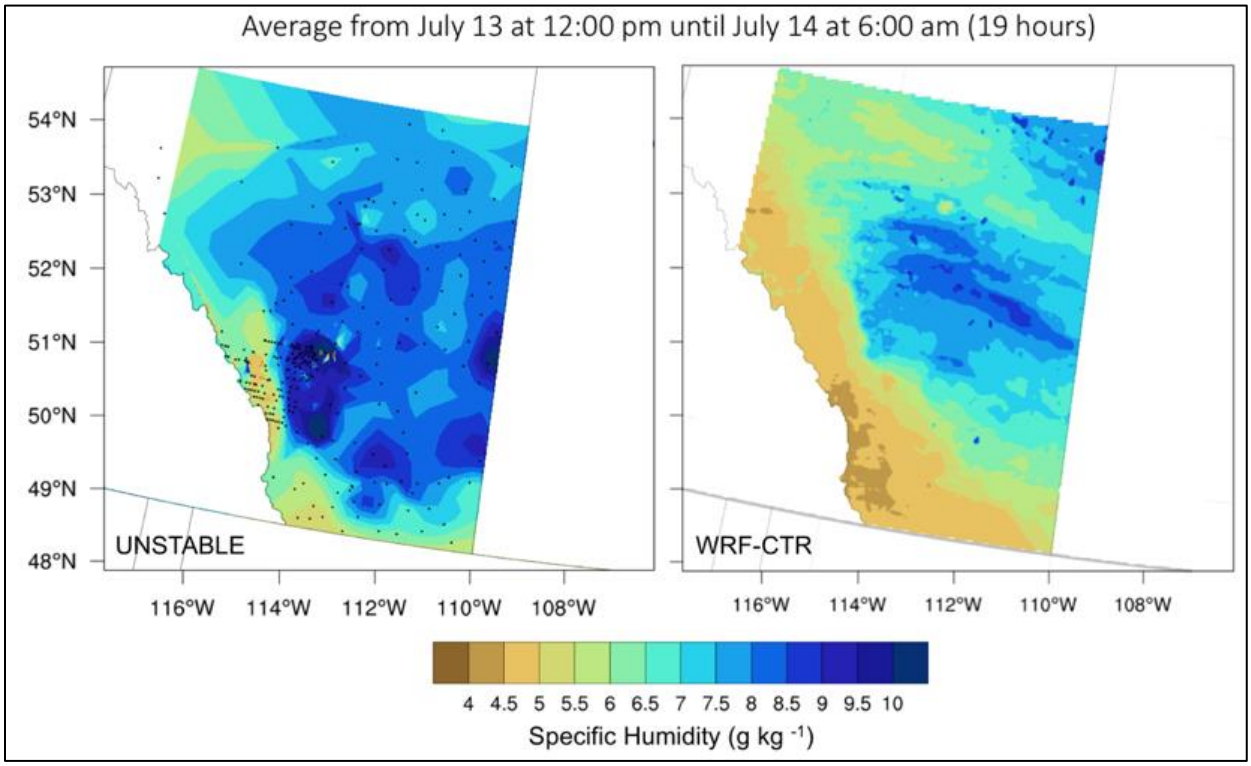

Figure 4 - 2 Comparison of 19-hours average of specific humidity at 2 m height of the UNSTABLE experiment (left) and the WRF-CTR data (right). The black dots on the UNSTABLE panel are the observations used to create the spatially distributed map.

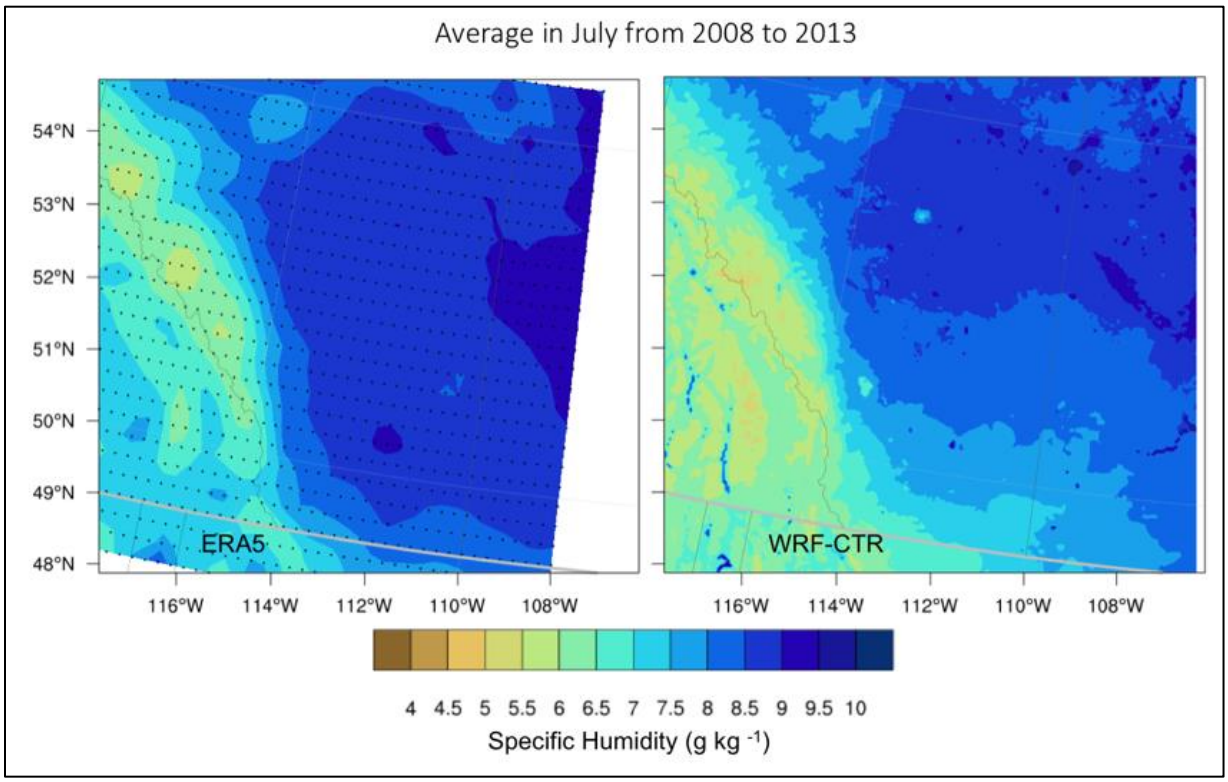

Figure 4 - 3 Comparison of the of 6 years average in July, of specific humidity at 2 m height of the ERA5 reanalysis (left) and the WRF-CTR data (right). The black dots are the grid points location in the ERA5 reanalysis.

4.4.2 Storm characteristics

The daily precipitation over the 85% quantile on the leeside of the Canadian Rockies is 4.8 mm day^{-1} and is associated with 240 days above this threshold. These days contribute around 50.8% of the total warm season precipitation in the region. Considering the criteria to select the storms (section 4.3.3), and the manual detection of the precipitation events' duration, 100 events were found over the 240 days above the 85% quantile. These events are contributing 75% of the total averaged-annual summer precipitation.

Figure 4 - 4a shows an example of a precipitation event. A dryline associated with CI is present on July 4 from 3:00 h to 9:00 h UTC, with individual convective cells developing along the foothills (Figure 4 - 4b-d). Over the following hours the precipitation, moves to the northeast (Figure 4 - 4d-f). The maximum specific humidity zonal gradient is above 0.2 g kg^{-1} km^{-1} with the initiation of individual cells at 20:00 h Local Standard Time (LST) on July 3 (Figure 4 - 4b, blue contours in map). From 23:00 of July 3 to July 4 at 5:00 h LST the dryline seems to dissipate, while more individual convective cells are initiating (Figure 4 - 4c-e, blue contours in map). The dryline shows a re-intensification on the next hours along with a spatial reorganization of the eastward-moving convective cells. The last time-steps presented (Figure 4 - 4g, h) show that the dryline was then accompanied by an active baroclinic perturbation from the north west, which is

increasing the westerly winds above the moisture layer, which in turn, increases the solenoidal circulation and thus the vertical motion along the foothills (cross section in Figure 4 - 4h). The Solenoidal term of the vorticity equation (in red contours over the cross sections) shows low values at the west side of the dryline for the first half of the event, and an intensification for the second part of it (Figure 4 - 4g, h). The vertically-integrated column of liquid water and ice approximates the model output to the presence of clouds (gray shades in the maps, Figure 4 - 4). Around 8 and 11 am LST on July 4 (Figure 4 - 4f, g) gravity waves, produced by the mountains, are present where the precipitation is occurring, this is also a mechanism that is promoting the triggering of CI in this event.

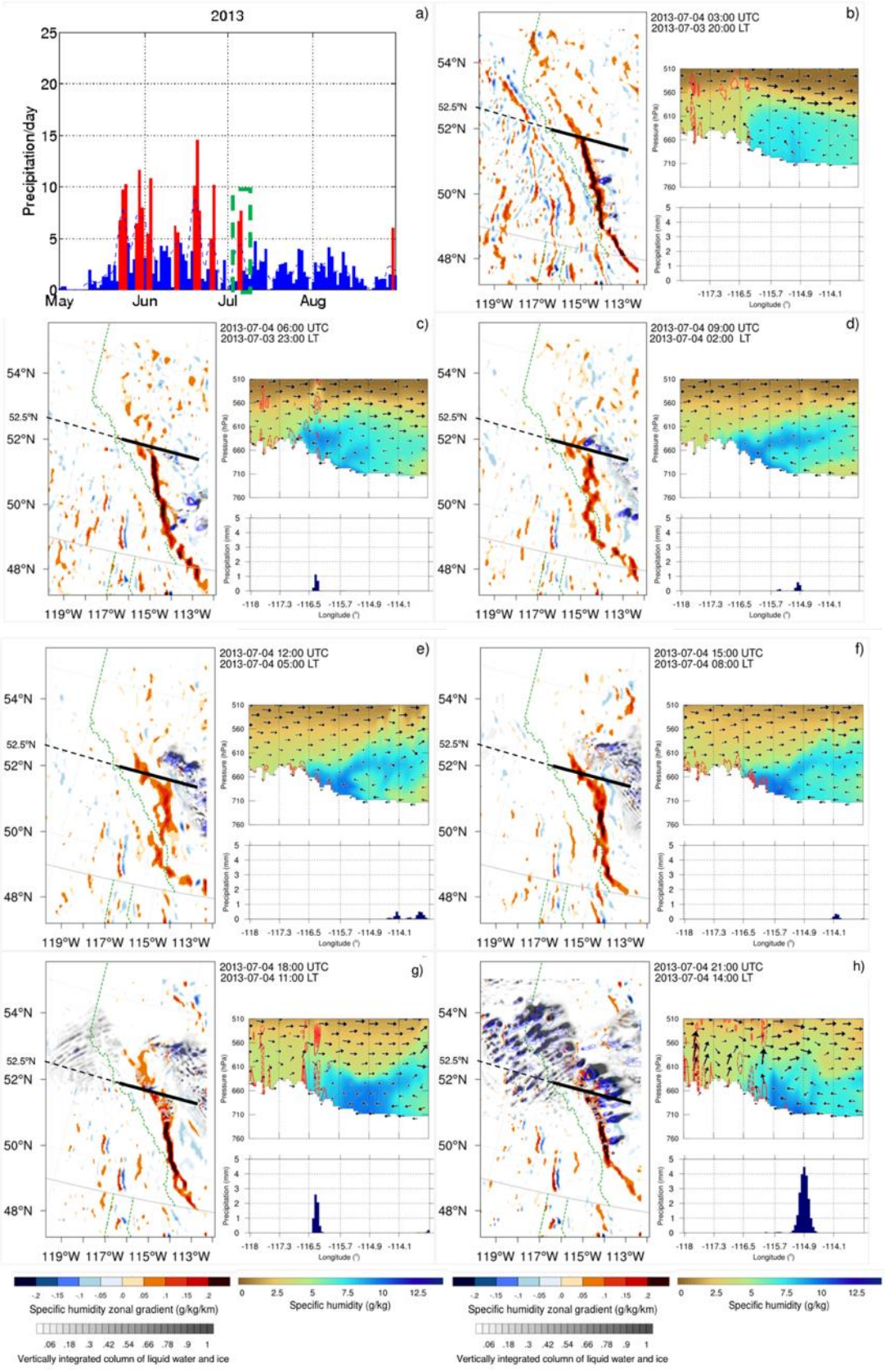
2013
a)
Precipitation/day
May
Jun
Jul
Aug
b)
2013-07-04 03:00 UTC
2013-07-03 20:00 LT
c)
2013-07-04 06:00 UTC
2013-07-03 23:00 LT
d)
2013-07-04 09:00 UTC
2013-07-04 02:00 LT
e)
2013-07-04 12:00 UTC
2013-07-04 05:00 LT
f)
2013-07-04 15:00 UTC
2013-07-04 08:00 LT
g)
2013-07-04 18:00 UTC
2013-07-04 11:00 LT
h)
2013-07-04 21:00 UTC
2013-07-04 14:00 LT
54°N
52.5°N
52°N
50°N
48°N
119°W 117°W 115°W 113°W
Pressure (hPa)
Precipitation (mm)
Longitude (°)
Specific humidity zonal gradient (g/kg/km)
Specific humidity (g/kg)
Vertically integrated column of liquid water and ice

Figure 4 - 4 An example of one dryline convection initiation development in July 2013. a) is the time-series between May and August 2013 of daily precipitation and shows all the mean daily precipitation in blue and the selected days above the 85% quantile in red. The storm detailed in the rest of the panels is enclosed by a green dashed line. The remaining panels (b-h) are every three hours apart. In each panel, the left-hand side shows a latitude-longitude map of specific humidity zonal gradient in shades (g $kg^{-1}km^{-1}$) precipitation in blue contours by 0.5 between 0.1 and 5 mm, and the vertically integrated column of liquid water and ice is presented in grey shades 1 in every panel. The right-hand side shows a cross section at 52.5°N of specific humidity in shades (g kg^{-1}), vertical and zonal wind in arrows across the foothills, the solenoidal term from the vorticity equation in red contours by 0.2 between -0.6 and 0.6 ms^{-1}. And below the cross section is the corresponding precipitation (mm).

4.4.3 The dryline and convection initiation

Out of the 100 precipitation events considered, 37 were initiated when a dryline was present in the WRF-CTR simulation (c.f. Table C.1 for details). The monthly variability shows that a maximum of 52% of the precipitation events that contribute the most, were initiated by a dryline in June, and a minimum of 19% in May. The annual variability shows a range between 9% to 67% of precipitation events initiated affected by a dryline over the 100 events. The usual time of the initiation is between 21:00 and 0:00 h UTC (14:00 to 17:00 h Local Time). The composite of the hours when the CI is linked to the presence of the dryline over these 37 events (Figure 4 - 5) shows a preferential location along the foothills. The average of the simulated dryline maximum (in each event) zonal gradient magnitude is 0.48 g kg^{-1} km^{-1}, with a maximum of 0.87 and a minimum of 0.2 g kg^{-1} km^{-1}, which agrees well with the average dryline gradient observed during the UNSTABLE. The standardized frequency of precipitation initiation (Figure 4 - 5a, contours) is located at the east side of the dryline, due to the strengthening of the westerly wind over the boundary layer that transports the air parcels and clouds to the east with a characteristic eastward tilt in the vertical profile (Ziegler and Rasmussen, 1998). The composite of the cross section over 52.5°N (Figure 4 - 5b) also shows the favorable location of the strongest specific humidity gradient, with a consistent low-level convergence along with the upward vertical wind right over the dryline zone.

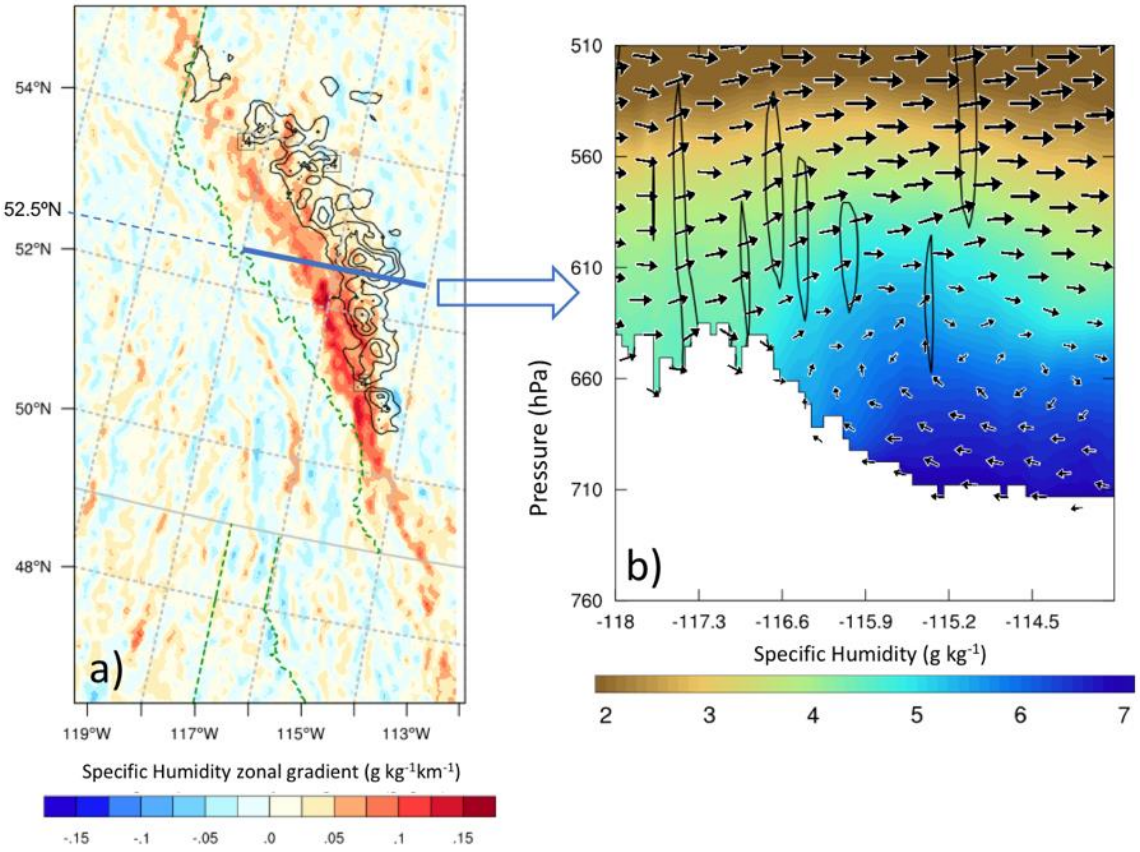

Figure 4 - 5 Composite of the 37-initial hour of the storms that clearly show a convective initiation due to the dryline in the CTR simulation. a) show the specific humidity zonal gradient (g $kg^{-1}km^{-1}$) in colors and the contours are the standardized frequency of precipitation by 0.05 between 0.4 and 1 (mm). b) The cross section at 52.5°N shows the specific humidity in shades (g kg^{-1}), vertical and zonal wind in arrows and vertical wind speed in contours by 0.1 between -0.3 and 0.3 (m s^{-1}).

The convective environment of the 37 precipitation events' initial day shows the maximum CAPE around 14:00 h LST. The composite of CAPE at this time shows its maximum value of 300 J kg^{-1} (Figure 4 - 6a) on the leeside of the Rockies. Simultaneously, the composite of CIN shows its minimum value between 0 and 40 J kg^{-1} (Figure 4 - 6b), however, the previously available time-steps from the model (11 and 8 am LST) evidenced a higher CIN above 150 J kg^{-1} (Figure 4 - 6c, d). This rapid decrease of CIN previous to the maximum CAPE is a typical pattern of convective initiation through capping inversion dissipation due to the diurnal cycle heating (e.g. Doswell, 1987; Knott and Taylor, 2000). The diurnal cycle of the stability parameters on the initial day from the 100 precipitation events was also analyzed for consistency. The 100 precipitation events show an analogous spatial and temporal evolution compared to the subset of the 37 precipitation events initiated by the dryline. The model was able to robustly represent the diurnal evolution of the stability parameters over the region.

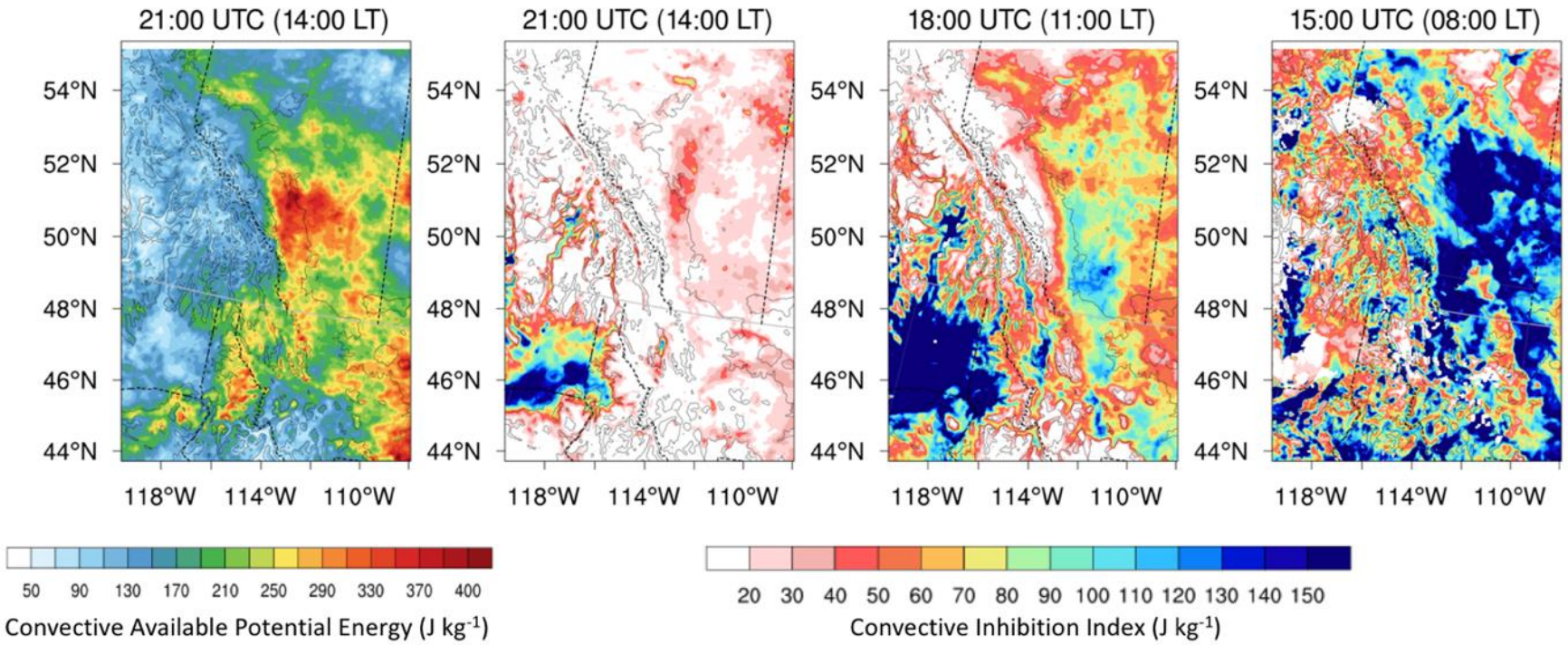

Figure 4 - 6 Composites on selected hours of the averaged-initial day from the 37 storms linked to the dryline in the convective initiation of (a) Convective Available Potential Energy and (b, c, and d) the Convective Inhibition indices.

4.4.4 Changes in a warmer climate

Changes in dryline characteristics

The WRF-PGW simulation has 101 precipitation events that are above the 85% quantile, and the CI of 34 precipitation events are linked to the presence of a dryline (see Table C.2 for details). The most contributing precipitation events that were initiated by a dryline shows a maximum occurrence of 48% in July and a minimum of 20% in August. The annual variability shows a range between 20% to 60% of precipitation events initiated by a dryline over these 101 events. The composite of the zonal gradient specific humidity shows a narrower and more intense dryline than the one from the WRF-CTR, with an average of the maximum specific humidity gradient of 0.55 g kg^{-1} km^{-1}, ranging between 0.31 and 0.86 g kg^{-1} km^{-1}. The standardized frequency of precipitation initiation is more intense and shifted northward (Figure 4 - 7) compared to the WRF-CTR. The composite of the cross section at 52.5°N shows an increase in specific humidity at the moist side of the dryline (east) and a more localized and intense average of the positive vertical velocity over the low-level convergence zone. The total warm season precipitation of the events initiated by a dryline on the WRF-PGW shows an increase of 22% compared to the WRF-CTR, along with a maximum that shifts towards the north (Figure 4 - 8). The next section investigates possible causes to explain the spatial shift of the CI in the future climate.

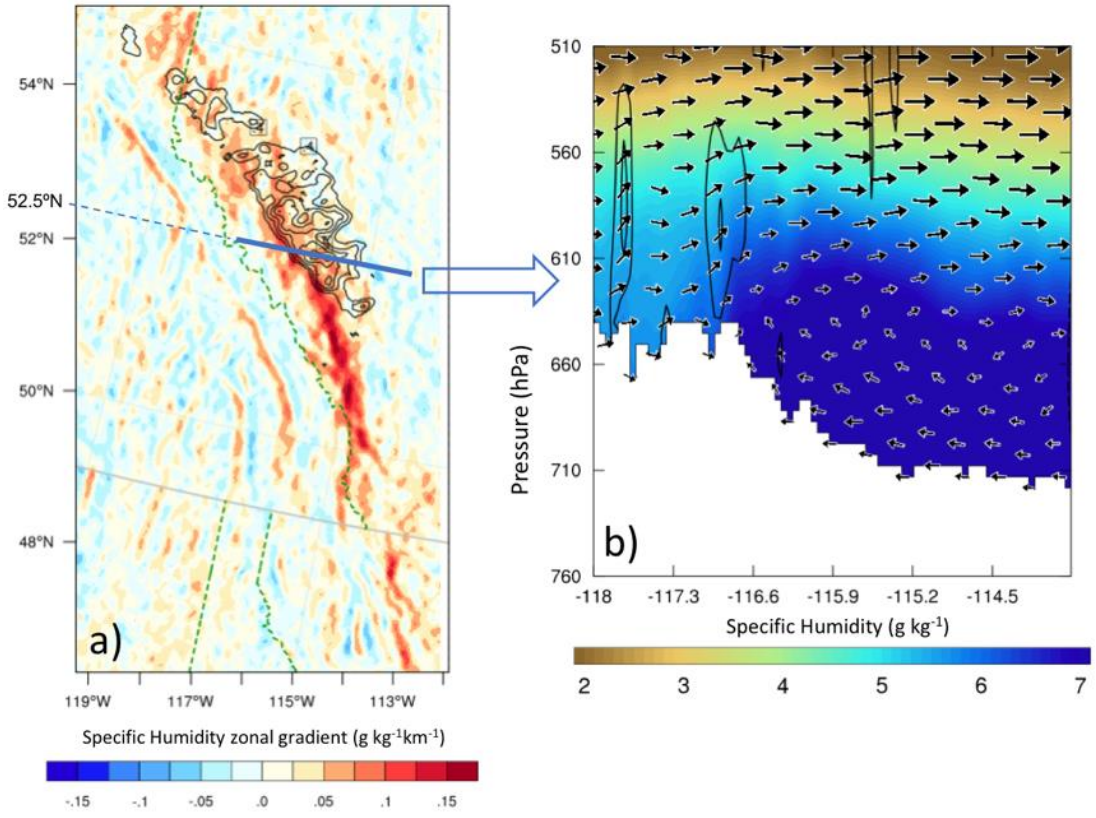

Figure 4 - 7 the same as Figure 4 - 5, but for the PGW. Note that in the PGW there were 34 storms initiated by the dryline.

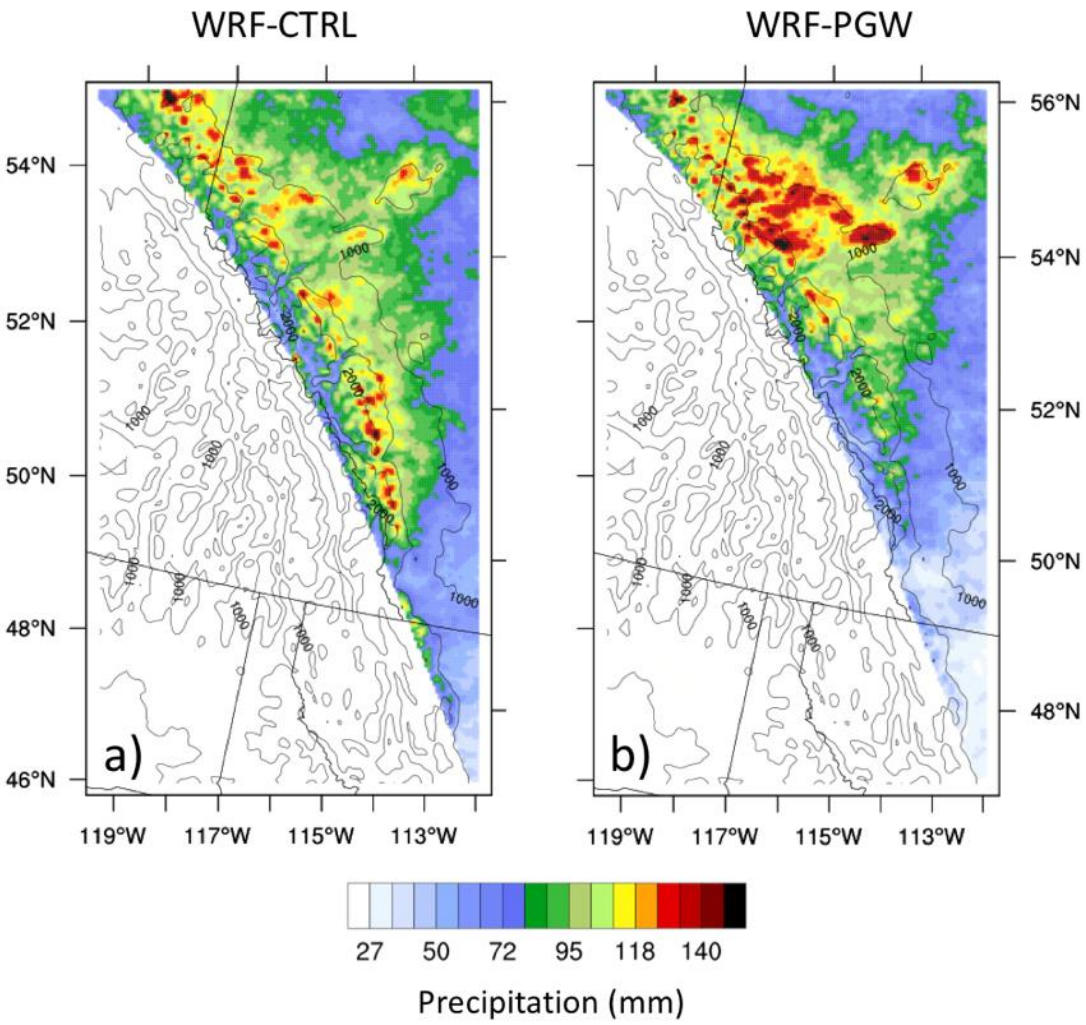

Figure 4 - 8 Composites of total precipitation of the events linked to the dryline. a) shows the WRF-CTR simulation which includes 37 storms. b) shows the WRF-PGW simulation which includes 34 storms.

Changes in the convective environment

The convective environment shows an overall increase of the convective stability parameters on the WRF-PGW simulation (Figure 4 - 9) with several grid points showing a statistically significant increase in the hourly-averaged maximum diurnal CAPE (not shown). Over the north (north of 52°N), the maximum averaged-CAPE in WRF-PGW increases up to 340 J kg^{-1} at 11:00 am LST (Figure 4 - 9a), which represents an increase of 88% over the maximum averaged-CAPE compared with the WRF-CTR. Spatial differences between CAPE in WRF-CTR and WRF-PGW ranges between 30% on the center and southeast, to 150% in the north. The evolution of the CIN in the northern region (Figure 4 - 9b) shows a small increase in the WRF-PGW during the morning with

its minimum value at 11:00 h LST; however, no statistical significance was found in the spatially distributed maps (not shown).

In the southern part of the region, the CAPE shows a smaller increase of the diurnal cycle between 02 and 11 h LST in the WRF-PGW compared to the WRF-CTR (Figure 4 - 9c vs. Figure 4 - 9a), and a 6-h delay of the maximum CAPE, while the CIN shows a stronger increase during the day in WRF-PGW than in the WRF-CTR (Figure 4 - 9d vs. Figure 4 - 9b). The main differences between the evolution of the CAPE and the CIN over both sub-regions (north and south of 52°N) are presented in Figure 4 - 9e. The CAPE has the biggest increase in the north for the WRF-PGW, while the change in the CIN is more important in the southern region during the morning (around 05:00 am LST).

Changes to the thermodynamical forcing

The scaling rates of extreme precipitation for the initial days of the events linked to a dryline (Figure 4 - 10a) showed a difference response compared to Clausius-Clapeyron relationship and between both simulations. The positive and quasi-superadiabatic scaling rate is on average 4°C warmer in the WRF-PGW than in the WRF-CTR for the selected events (Figure 4 - 10a). Over the region north of 52°N, this difference increases to 7°C (Figure 4 - 10b). This is related to the changes in the environmental regimes; extending the energy-limited environment to 18°C (Figure 4 - 10b) on the WRF-PGW, whereas in the region south of 52°N, the transition from the energy-limited to a moisture-limited environment changes only by 3°C from the WRF-CTR (15°C) to the WRF-PGW (18°C) simulation (Figure 4 - 10c). The extreme precipitation intensity (y-axis) presents lower values in the southern region than in the northern sub-region for the WRF-PGW, which is also related to the environmental-regime transition. We also investigated dynamical changes such as circulation, convergence, deformation, vorticity and vertical wind shear, but they do not show any clear change between the WRF-CTR and WRF-PGW (not shown).

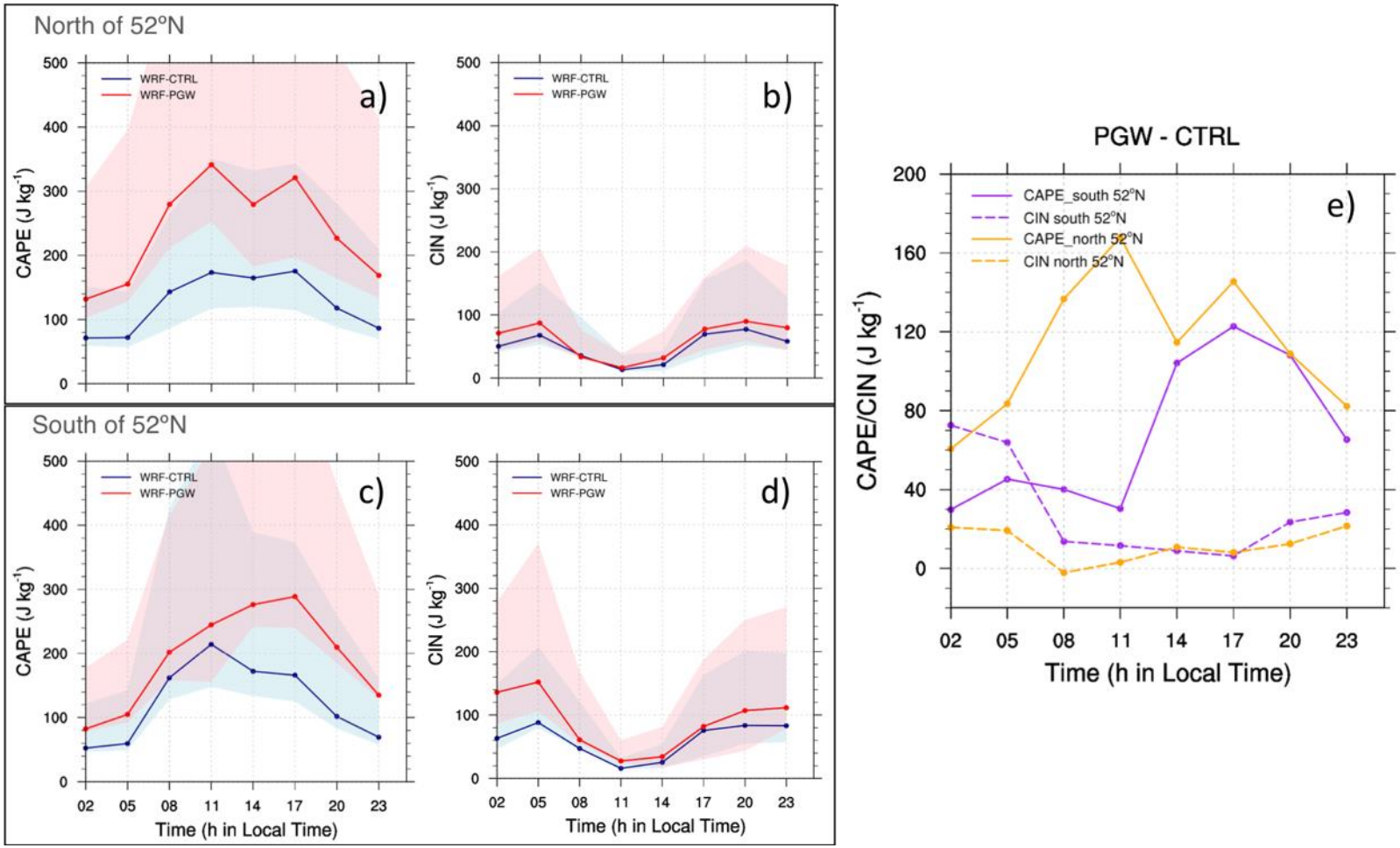

Figure 4 - 9 Panels a), b), c) and d) shows the diurnal evolution of the convective indices north and south of 52°N on the initial day of the storms related to the dryline convective initiation. The solid line is the average and the shaded areas are the upper and lower quartile (25th and 75th). Panel e) summarizes the difference of the average values between WRF-PGW and WRF-CTR of the convective indices shown on the left.

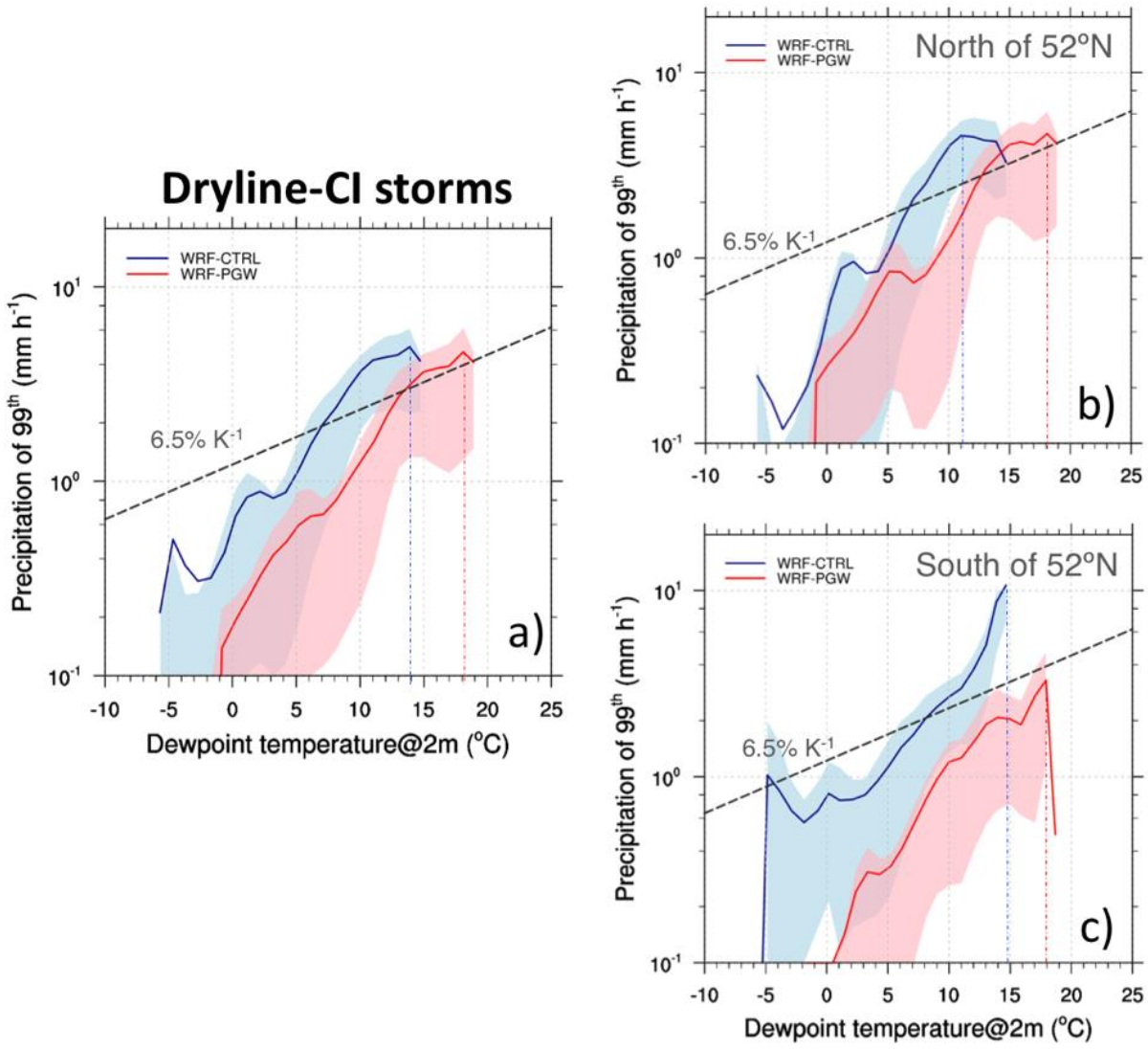

Figure 4 - 10 Scaling rates between extreme precipitation intensity in the y-axis (99th percentile, in log-scale) and the dewpoint temperature in the x-axis for the, a) the initial day of the storms linked to dryline-convective initiation (37 storms in the WRF-CTR and 34 storms in the WRF-PGW). b) and c) show a decomposition of the panel a) into the precipitation north and south of 52°N, correspondingly. The shaded areas represent the percentile 25th and 75th of the scaling rates averaged over the grid points.

4.5 Summary and discussion

The dryline modulates part of the convective initiation of the warm season precipitation at the leeside of the Canadian Rockies. Several precipitation events that show a dryline linked to convective initiation were identified and used to characterize the main features in a decadal scale.

The precipitation events above the 85% quantile were chosen to analyze the events that most contributes to the total warm season (from May to August) precipitation in the region, which is of significance to water-related issues. From the 100 precipitation events associated with the 85% quantile, 37% were linked to a dryline in the initiation on the historical simulation, these events contribute 27% (min: 4%, max: 46%) of the annually-averaged warm season precipitation. This percentage is higher than other studies, such as the 11% found in Wyoming (Bergmaier and Geerts, 2015) for all drylines with and without CI, and 32% in the U.S. Great Plains (Hoch and Markowski, 2005). However, other studies found higher dryline frequency of around 45% (Peterson, 1983; Rhea, 1966). In the present study, several small events that are characterized by a short-time duration of individual convective cells might also be linked to the presence of the dryline in their initiation but as they are not contributing substantially to the total precipitation, they were not considered in this analysis. The simulated magnitude of the dryline found here (0.48 g kg^{-1} km^{-1}) is smaller than previous observed magnitudes found in the Canadian Rockies such as 0.9 to 4.3 g kg^{-1} km^{-1} in Hill (2006), and up to 18 g kg^{-1} km^{-1} in Taylor et al. (2011). However, smaller magnitudes have been also found in other regions, such as Wyoming, with values between 0.05 to 0.1 g kg^{-1} km^{-1} (Bergmaier and Geerts, 2015). These different magnitudes are not only associated with the region, but also to the type of data used to estimate the gradient. In the present study, gridded data from a regional climate model at 4-km resolution were used, as opposed to the previous work mentioned in the Canadian Rockies, which used observed datasets, or the study in Wyoming, which used gridded reanalysis data at 32-km resolution.

The 37 precipitation event composite of the convective environment shows a similar magnitude of CAPE and CIN as the one found for single convective cells in past studies nearby in the Canadian Rockies (Brimelow et al., 2002; Hill, 2006), while significantly higher magnitudes have been found in the U.S. (Ziegler and Rasmussen, 1998; Bergmaier and Geerts, 2015; Trier et al., 2015). This increase towards lower latitudes was expected due to the radiation reduction at higher latitudes (Riemann-Campe et al., 2009).

Other mechanisms besides the dryline, as presented in Figure 4 - 4, show how a combination of processes can play a role in the development of the precipitation events. The dryline as well as the associated secondary circulation, is properly simulated by the regional climate model in a convection-permitting configuration. The model showed a similar regional pattern of the specific humidity gradient as was illustrated for the case of 13 July 2008. The simulation shows a dry and northeast bias, which agrees with other studies (Coffer et al., 2013; Coniglio et al., 2013). Coniglio et al. (2013) suggested that YSU is producing too much vertical mixing at the top of the boundary layer.

In the future climate, the dryline is projected to trigger 34% out of 101 precipitation events above the 85% quantile, which also contributes 27% of the annually-averaged warm season precipitation. The total warm season precipitation is 22% higher in the WRF-PGW than the WRF-CTR, so the precipitation events initiated by a dryline are contributing a larger amount of precipitation in the WRF-PGW. The convective environment is modulating the necessary conditions to produce precipitation events in the afternoon-evening in both simulations. The spatial pattern of CAPE was maintained, and the magnitude was intensified in a warmer climate due to higher temperatures and the increased water vapor held in the atmosphere. The intensification of the maximum CAPE and the sharper dissipation of CIN in the southern region for the WRF-PGW can lead to stronger precipitation event outbreaks due to strengthening of the capping lid dissipation mechanism, which is consistent with less moderate and more intense precipitation (Prein et al., 2016). However, the increasing CAPE along with an increasing CIN in the morning for the WRF-PGW has another effect; the formation of more individual convective cells with lower precipitation intensity. This is the case in the southern part of the domain, where the CI (affected by the dryline) is shifted to the north (Figure 4 - 8 a) over the WRF-PGW.

The main causes of the changes in the precipitation events initiated by a dryline in the future climate can be found in the thermodynamical forcing. The scaling rates show a shift in the extreme precipitation transition from energy- to a moisture-limited environment between south and north of 52°N. At temperatures above 10°C, this difference favors more intense precipitation over the northern part of the region rather than in the south. The scaling rates indicate a quasi-superadiabatic value for these precipitation events, thus the extreme precipitation increases faster than the expected Clausius Clapeyron relationship. However, this result has to be analyzed carefully, given the limitation of the approach. The first limitation is that only days with precipitation above zero are being considered and it is possible that this particular group of days are creating a different selection of the extreme-indices (Schär et al., 2016), compared to previous studies (Ban et al., 2015; Kendon et al., 2014; Prein et al., 2016), in which all the precipitation series are being considered. And second, the dewpoint temperature, calculated in each grid point where the extreme precipitation is occurring, is not a proxy to the large scale (and global) temperature increase due to climate change (Boucher et al., 2013). Therefore, it can only be implied here that the superadiabatic scaling rate is certainly possible in this region and it can increase the precipitation intensity for local warmer temperatures.

To investigate in more detail the shift from an energy- to a moisture-limited regime in the future climate, a back-trajectory analysis could be performed on the precipitation events to assess their moisture source and the possible land-atmospheric feedbacks, such as changes in soil moisture, evaporative fraction and snow albedo. Improvements can also be achieved to better represent the changes in the future climate, for instance considering the potential changes in land-cover types, as it will affect the surface water mass and energy fluxes as well as the feedbacks to precipitation characteristics. If the changes of large-scale features, such as the amplification of the Hadley cell, the poleward shift of the extratropical cyclone, or the intensification of the anticyclone over the northwestern U.S. and southwestern Canada (Stewart et al., 2019) were represented on the

simulation, they could have an impact over the changes found, that should be certainly further investigated. These might change the dryline intensity, increase the risk of heavy rainfall or drying patterns and thus, possible changes in the hydrological regime.

4.6 Conclusion

This study provides a detailed description of the simulated dryline characteristics linked to convective initiation for the most contributing precipitation events, and the impact of a warmer climate over these characteristics in an extratropical region on a decadal scale. The main findings are the following:

- The regional climate model in a convection-permitting configuration demonstrated an ability to characterize the dryline in the mesoscale.
- A higher frequency of the dryline linked to convective initiation was found on the leeside of the Canadian Rockies (37% in the historical climate) compared to other regions.
- The estimate of the magnitude of the dryline is 0.48 g kg^{-1} km^{-1} on average and appears to be dependent on the type of dataset used.
- The impact of a warmer climate on the precipitation events affected by a dryline shows a more frequent, and a northward shift of, convective initiation. The thermodynamical analysis showed that the southern part of the region has a regime that is transitioning from energy- to a moisture-limited environment at lower temperature compared to the northern region. This spatial difference in the transition, can be intensified if one considers the potential large-scale changes in a future warmer climate.

These finding are expected to contribute to a better understanding of the influence of the dryline on convective initiation in the historical climate, and how would change in the future climate. Furthermore, this study provides a reference point to evaluate forecasts of convective precipitation affected by the dryline, that could also benefit our current prediction skills (timing and location of CI). The future climate analysis offers an assessment of possible changes of convective precipitation on a decadal scale, which can be used to inform civil infrastructure design, environmental impact assessment and adaptation measures.

Acknowledgments

We would like to acknowledge high-performance computing support from Cheyenne (doi:10.5065/D6RX99HX) provided by NCAR's Computational and Information Systems Laboratory, sponsored by the National Science Foundation.

CHAPTER 5

CONCLUSIONS

5.1 Concluding remarks

Key to this research was the use of observational data and the regional climate model in a convection-permitting configuration (CPM). First, the thesis quantified inconsistencies of precipitation measurements across a national border showing the magnitude of systematic errors to which observational datasets are subject to hold under extreme weather conditions. Second, it validated the simulated diurnal cycle of precipitation of a regional climate model in a CPM against a large dataset of observations and a gridded precipitation product in summer on a decadal and continental scale. Third, it characterized a mesoscale feature that directly affects the initiation of convection over complex topography at extratropical latitudes. All the objectives in this thesis have been addressed, as shown in the summary presented below.

Objective 1: To quantify the inconsistency in precipitation measurements across the northern national border between the U.S. and Canada.

The wind-undercatch systematic bias from precipitation measures using different instruments shows inconsistent values across national borders, a particular problem in cold and windy environments. Chapter 2 analyzes and quantifies the wind-undercatch bias between two sets of weather stations: one in the Yukon Territory, Canada and the other in Alaska, U.S. In January, for the Yukon stations, the correction for the systematic bias for solid precipitation is as high as 31%, whereas the Alaskan stations are corrected by as much as 136%. In July, this difference declines to 4% in the Yukon and to 20% in Alaska. In the Yukon, the annual average of the systematic bias correction is 13%, while in Alaska it is 65%. However, near the center of the border, the correction decreases to 3% in the Yukon and 7% in Alaska. These results show a discontinuity in precipitation records in the region, thus clearly demonstrating the need for careful procedures both in producing the records and in collecting the metadata required to identify the status and changes at stations over the years.

Many factors affect the measurements of solid precipitation, including wind speed, type of instrumentation and type of ice crystals. These variables can help scientist to better estimate the corrections from observed data taken over long periods in different environments. To correct precipitation measurements, a function is built from the average curve of all the measurements from various atmospheric conditions. The records taken for the reference point contains dispersion and uncertainty. The reference point is normally the double fence intercomparison reference (DFIR) gauge, considered the “true” measurement by the Weather Meteorological Organization (WMO). Although achieving a true measurement for any combination of wind and precipitation is

a great challenge, the scientific community is motivated to find a measurement with the most certainty. Obtaining this measurement has implications for hydrometeorological studies and any study related to climate change.

The results of this study found that the wind-undercatch systematic bias is smaller for liquid precipitation, as is the average inconsistency across national borders in warmer environments or seasons. On the southern border between Canada and the U.S., Li (2016) found that the bias correction for liquid precipitation is about 3% in Canadian stations and 16% in the U.S. stations for different time periods and environments.

There are two main limitations of the study reported in Chapter 2. (1) Mixed precipitation was not classified, and the approach considered only liquid and solid precipitation. Although this approach is likely appropriate for studying monthly and yearly records, analyzing an intermediate mixed phase of precipitation in a daily or hourly analysis, would probably provide more accurate results. (2) The relationship between wind speed and gauge undercatch was based on field experiments in limited environments, which, for instance, do not normally exceed wind speeds of 7 m s^{-1} on a daily scale. The empirical origin restricts the results to the observable spectrum and to the instruments used in the measurements.

Objective 2: To investigate if a CPM in North America can reproduce the diurnal cycle of convective precipitation and how a warmer climate would change this cycle.

Chapter 3 presents a verification of the main characteristics of the summer precipitation diurnal cycle. Results showed that the regional climate model (RCM) in a CPM can represent the continental patterns of the amplitude and timing of the maximum summer precipitation in the diurnal cycle. The regional climate model in this configuration realistically simulates the propagating signal from the afternoon precipitation peaks to the night peaks. However, the model's performance deteriorates in the representation of the timing and amplitude of the early morning peaks in the Midwestern U.S. and the amplitude in the south east part of the domain. The simulation of the warmer climate shows a consistent increase in amplitude of the diurnal cycle of precipitation. This increase is driven by more intense precipitation over most of the domain, except in the north, where the precipitation is also more frequent.

This study considers a representative scenario based on 19 global climate models to simulate a future projection, which limits the analysis to only one representation. Due to the high uncertainty and broad spread of future projection, the results of future changes should be interpreted with caution. With more realizations and the advance of physical and computational tools, the probabilistic uncertainty should diminish in the near future. The main systematic biases found in the simulations still need to be explained, not only to better simulate the current climate but also to improve modelling capabilities and decrease future simulation uncertainties.

Objective 3: To characterize the contribution of a mesoscale feature to initiate convective precipitation on the leeside of the Canadian Rockies and investigate its changes under a future warmer climate

Results in Chapter 4 shows that on the leeside of the Canadian Rockies, the dryline is present in the initiation of 37% of precipitation events that contribute the most precipitation. The simulated dryline magnitude is 0.48 g kg^{-1} km^{-1} in the current climate and shows a corresponding secondary circulation produced by the solenoidal imbalance across the dryline, which has been proposed in past studies (Ziegler and Rasmussen, 1998). Convection is typically initiated at around 17:00 h local time and is synchronizes with the diurnal cycle of the convective environmental conditions represented by the maximum Convective Available Potential Energy (CAPE) and minimum Convective Inhibition index (CIN). In the simulation of a future warmer climate, the environment shows a larger convective environment than the historical simulation, with higher CAPE and a sharper decrease of CIN. This condition is accompanied by an intensification and a northern shift of the convective initiation associated with the dryline. In the simulated warmer scenario, the dryline is present in 34% of the precipitation events that contribute the most precipitation. Thermodynamical changes were found to be related to the northern shift. The scaling rate between extreme precipitation and the dewpoint temperature indicates a different regime transition in the future climate. This transition occurs because the environment in the south is energy-limited environment, while the environment in the northern part of the domain is moisture-limited. Under future climate scenarios, the northern part shows intense extreme precipitation when dewpoint temperatures are above 10°C, whereas the southern part shows lower amounts of extreme precipitation. In the north, a larger super-adiabatic scaling rate is present up to 18°C, which indicates that the regime is transitioning from an energy-limited to a moisture-limited environment.

This study analyzes the simulated convective initiation and dryline frequency in a 13-years period, which help to quantify, on a decadal scale, the presence of the dryline in the most contributing storms. However, it limits the analysis to averaged values, leaving out more detailed descriptions of the small-scale processes involved. To better characterize the physical processes linking the dryline and the CI, we need to integrate field experiments data and numerical simulations, tailored for the specific area and events. The results found in this study, help to provide a reference point to the CI prediction and to understand the importance of the dryline in the total precipitation over the region. The simulated future climate shows a change in the heavy precipitation characteristics associated with the dryline in the warm season. This information can contribute to better water resources management and inform hydrological studies of future changes in the water cycle over the headwaters of Saskatchewan River Basin.

5.2 Concluding discussion

5.2.1 Measuring solid precipitation

The national standard instrumentation for both the U.S. and Canada now includes automatic instruments to measure precipitation. This instrumentation should help to develop cheaper and more frequent records from daily timesteps to hourly or even to measurements by minute (NOAA, 2002; Mekis et al., 2018). As the recording frequency increases, the accuracy of the precipitation and wind measurements also increases. This increased accuracy may lead to two main issues. First, further complexity has to be considered in the interaction between wind and precipitation. Contributing to this complexity are the turbulent fluxes, the fall velocity of precipitation particles, a more specific classification of precipitation types, and the need for more details on the closeness of the wind and precipitation measurement (Smith, 2008; Fischer, 2011; Thériault et al., 2012). Second, because the WMO standard defines the "true" measurements from the manual DFIR station's reporting measurements once a day, the wind-undercatch corrections are not directly transferable to records at higher frequencies (Smith, 2008).

Another challenge to overcome is the lack of metadata. In 2011, for example, this problem led to an overestimation of the observed temperature trends on several stations over the U.S. (Fall et al., 2011). More information from the stations could improve the correction of precipitation records (Mekis et al., 1999, 2018; Groisman et al., 1994; González-Rouco et al., 2001; Fall et al., 2011; Menne et al., 2009; Dai et al., 1997; Brunetti et al., 2004) and also lessen the doubts about the reliability of the entire dataset that arises from these errors (Menne et al., 2009). The metadata should provide information related to changes in the station's configuration, location, and maintenance, missing data information, calibration formulas, resolution, and rounding approaches on records.

Understanding one cause of systematic error in observing precipitation is critical to understand the sensitivity of measurements of any type and how these biases or uncertainties can be easily transferred to inaccurate conclusion in not only historical analyses of precipitation and temperature but also in modeling studies for future climate assessments. To build the reliability of these models, empirical confirmation and accurate measurements are crucial. In this work, simultaneous research into how the environment affects observations and, how the CPM model simulations are performing, provides a broader perspective on the many sources of data and reliability depending on each particular environment that wants to be studied.

5.2.2 Challenges in RCM-CPM

Simulations using an RCM in a CPM configuration have shown great progress in realistically representing the mesoscale features in the atmosphere: an increase in spatial resolution has improved the representation of topographical features, and the simulation of cumulus convection without parameterization. Having a higher resolution and explicitly resolving convective processes, elevates the importance of smaller scales and the related parameterizations in

representing moist convection. Despite this progress, these models have limitations and challenges. This study, we highlighted the main systematic errors found in the summer precipitation diurnal cycle over the continental domain. Key errors include the systematic overrepresentation of precipitation amounts in the southeast (Florida Peninsula), underestimation of precipitation in the midwest, problems with the timing of the maximum precipitation diurnal cycle in the early morning, and dry bias on specific humidity on the leeside of the Canadian Rockies. These errors or systematic biases result from shortcomings in our current modeling capabilities. Reasons for these biases could relate to the coarse spatial resolution used to resolve more detailed topography or to the necessary parameterization of the sub-grid processes. A more complex reason for the biases could be erroneous physical properties, possibly leading to complicated feedback. An example of this kind of feedback is the physical radiative properties of clouds, which might produce an overestimated reflection and create a compensating error in the energy balance due to an underestimation in cloud cover fraction (Brissonet al., 2016). Although CPM simulates cloud properties more effectively than coarser resolution models (Prein et al., 2017; Langhans et al., 2013), these properties remain one of the most sensitive components of the energy balance in our current model capabilities (Boucher et al., 2013; Fan et al., 2016; Thompson et al., 2016). To move forward from diagnosing the model weaknesses to improvements, further work is needed. First, it is necessary to isolate the causes of the systematic errors, to then perform sensitivity experiments to diagnose which parameter or processes are associated with these causes. For example, the land surface model scheme has evolved in the latest years, to improve, among many processes, the representation of cold environment characteristics; to better simulate the snow depth, the surface fluxes and runoff (Niu et al., 2011). To do so, they found out that including a simple groundwater model, a multi-layer snow model and a more permeable frozen soil scheme, would help to improve the representation of these cold environment processes. Another strategy to decrease model errors is applying assimilation techniques such as nudging, which help to overcome large scale biases in regional climate models (Lucas-Picher et al., 2016).

The CPM simulations are designed to give responses on the mesoscale at an average time scale. So, the CPM answers how the average precipitation characteristics will change in the future over areas of at least 100 km^2 (minimum characteristic horizontal scale of mesoscale processes, Holton et al., 2012). The accuracy then has to be calculated with the ability of the model to simulate the specific features that we are looking for. For example, assessing changes the areas in which summer precipitation shows a night peak, the performance of the future simulation will be more reliable than the areas which are dominated by a morning peak.

This study has demonstrated that the main characteristics of a mesoscale feature can be described in detail using a CPM simulation to analyze the representation of the dryline affecting convection initiation. The data and method presented here provide answers to critical questions about these characteristics, such as the average magnitude, frequency, and changes of the dryline in a warmer climate. However, this study has raised further questions: Why does the average initiation of precipitation have a heterogeneous spatial pattern not directly correlated to the dryline magnitude? What controls the distance of the convective initiation to the dryline? How much are other

mesoscale processes involved in triggering convection, such as gravity waves or mechanisms related to elevated convection? To improve forecast simulations on the current and future climate, these questions have to be approached with a combination of detailed field observations and modelling tools. Simulations at large spatial and temporal scale are essential to diagnose our ability to robustly reproduce mesoscale atmospheric characteristics. Many simulations have been already performed in grid spacing smaller or equal to 4-km in a continental domain (Ban et al., 2014; Berthou et al., 2018; Kendon et al., 2012; Leutwyler et al., 2017; Liu et al., 2017), or even on a near-global scale (Fuhrer et al., 2018; Judt, 2018; Schwitalla and Coauthors, 2018). Analyses on these simulations are in progress to improve our understanding of the future climate.

5.3 Outlook

Observational capabilities are improving, but a careful inspection of stations metadata relates to maintenance and operations should be as important as the actual records. One path forward to better understand this subject is to continue the research from laboratory and field experiments (Colli et al., 2015; Thériault et al., 2012) to quantify the dependence of small scale features (e.g., snowflakes geometry and turbulent fluxes) on precipitation wind-undercatch and apply these findings in the field. Another direction to increase the accuracy of the current precipitation wind-undercatch corrections is to use longer records from experimental sites designed to update the estimation of instruments performance (e.g., the Solid Precipitation Intercomparison Experiment; [SPICE]). A more reliable observational dataset will lead to better model evaluations, and, indeed, to a more reliable climate change analysis integrating observations and our modelling capabilities.

Today, special attention is paid to reducing uncertainties in climate projections to obtain a better range of potential changes in the next 100 years. Efforts focus on improving both, the computational and physical aspects of climate modeling. A convergence between GCM and RCM will happen (National Research Council, 2012). The mission is to build efficient global simulations with resolutions on the km-scale with the best possible physics in parameterizations and the dynamical core itself. These global or near-global models at a km-scale fit neither in the GCM nor the RCM. The structure is different and another set of modeling platforms needs to be used, such as ICON (Reinert et al., 2015), MPAS (Skamarock et al., 2012) or NICAM (Tomita and Satoh, 2004).

As for computational efficiency, cost is still constraining the goal of having sufficient CPM climate simulations at resolutions higher than 10 km and domains on a continental scale, to produce ensembles and thus an estimation of the uncertainty. Initiatives such as CORDEX (Giorgi et al., 2009) help to increase the number of realizations of RCM simulations; however, these simulations at resolutions on a km-scale are too expensive. One method to reduce these costs is to improve the efficiency in performing these simulations by modifying the use of GPU instead of using CPU (Fuhrer et al., 2018; Leutwyler et al., 2016). Another challenge is the high cost of transferring output data. Some ideas to modify the experimental design have been proposed, such as more

efficiently distributing the simulation outputs by transferring restarting files (Schär at al., 2016) or implementing online analyses on cloud platforms (Prein et al., 2017).

Both the parameterizations and the dynamical core that connects the circulation, moisture, energy and momentum conservation, need to adjust to higher resolutions. The coupling of large-scale circulation and moisture seems to be one of the reasons for the large spread of GCM simulations. This coupling depends on unrepresented small scale processes, such as convection and cloud formation (Stevens and Bony, 2013). Following the idea of a convergence between RCM and GCM, one can ask if the RCM at a km-scale better able to represent the interaction between large-scale circulation and water in the atmosphere. Scientists working on the latest Coupled Model Intercomparison Project (CMIP6) aim to advance the of clouds and the role they play in large scale circulation, including the system's sensitivity (Eyring et al., 2017). Some attempts currently focus on finding particular relationships to explain the broad spread of the GCMs. Thackeray et al. (2018) found that the variability in tropical and subtropical precipitation changes across GCM models are related to a trade-off between extreme and non-extreme precipitation, meaning that the models balance an increase in non-extreme precipitation with a decrease in extreme precipitation, and vice versa. This finding could be used to constrain the simulations and thus verify the improvement of the model spread (Prein and Pendergrass, 2019). It is hoped that a clear answer will emerge soon. Another physical aspect that can improve in climate modelling is the representation of sub-grid processes using physical parameterizations. The adjustment of parameterization to a higher resolution scale is ongoing, and the land-surface schemes have shown a great advancement in representing of the land and the atmosphere interaction (Niu et al., 2011), as well as the microphysical schemes (Thompson and Eidhammer, 2014). However, many of the present issues rely on incomplete understanding of the physical processes. For example, there remains insufficient knowledge about how a cloud droplet develops into a precipitating hydrometeor, how to represent heterogeneous distributions of cloud condensation nuclei, and how to accurately represent a turbulent flow impacts on a stable boundary layer. These scientific gaps are directly linked to limitations in modelling capabilities.

The rapid development of high-performance computers and the progress of near-global km-scale simulations show promise in improving the integration of the large-scale circulation represented by the GCM and the prominent role of moist convection and cloud formation represented by the RCM in a CPM configuration. Along with an increased interest in more precise answers to the impact of a warmer climate, these strategies will lead to more robust understanding of the atmosphere.

REFERENCES

Akaeda, K., Reisner, J., Parsons, D., 1995. The Role of Mesoscale and Topographically Induced Circulations in Initiating a Flash Flood Observed during the TAMEX Project. Mon. Weather Rev. doi:10.1175/1520-0493(1995)123<1720:TROMAT>2.0.CO;2

Akinremi, O.O., Mcginn, S.M., Cutforth, H.W., 1999. Precipitation trends on the Canadian prairies. J. Clim. 12, 2996–3003. doi:10.1175/1520-0442(1999)012<2996:PTOTCP>2.0.CO;2

Alexander, L.S., Sills, D.M.L., Taylor, P.A., 2018. Initiation of Convective Storms at Low-Level Mesoscale Boundaries in Southwestern Ontario. Weather Forecast. 33, 583–598. doi:10.1175/WAF-D-17-0086.1

Arnup, S.J., Reeder, M.J., 2007. The Diurnal and Seasonal Variation of the Northern Australian Dryline. Mon. Weather Rev. 135, 2995–3008. doi:10.1175/MWR3455.1

Baldauf, M., Seifert, A., Förstner, J., Majewski, D., Raschendorfer, M., Reinhardt, T., 2011. Operational Convective-Scale Numerical Weather Prediction with the COSMO Model: Description and Sensitivities. Mon. Weather Rev. 139, 3887–3905. doi:10.1175/MWR-D-10-05013.1

Ban, N., Schmidli, J., Schär, C., 2014. Evaluation of the new convective-resolving regional climate modeling approach in decade-long simulations. J. Geophys. Res. Atmos. 119, 7889–7907. doi:10.1002/2014JD021478.Received

Ban, N., Schmidli, J., Schär, C., 2015. Heavy precipitation in a changing climate: Does short-term summer precipitation increase faster? Geophys. Res. Lett. 42, 1165–1172. doi:10.1002/2014GL062588

Barbero, R., Fowler, H.J., Lenderink, G., Blenkinsop, S., 2017. Is the intensification of precipitation extremes with global warming better detected at hourly than daily resolutions? Geophys. Res. Lett. 44, 974–983. doi:10.1002/2016GL071917

Barrett, B.S., Garreaud, R., Falvey, M., 2009. Effect of the Andes Cordillera on Precipitation from a Midlatitude Cold Front. Mon. Weather Rev. 137, 3092–3109. doi:10.1175/2009MWR2881.1

Barthlott, C., Corsmeier, U., Meißner, C., Braun, F., Kottmeier, C., 2006. The influence of mesoscale circulation systems on triggering convective cells over complex terrain. Atmos. Res. 81, 150–175. doi:10.1016/j.atmosres.2005.11.010

Bawden, A.J., Linton, H.C., Burn, D.H., Prowse, T.D., 2014. A spatiotemporal analysis of hydrological trends and variability in the Athabasca River region, Canada. J. Hydrol. 509, 333–342. doi:http://dx.doi.org/10.1016/j.jhydrol.2013.11.051

Bechis, H., Salio, P.V., Ruiz, J., 2016. Some Mechanisms Leading to the Formation of an Argentinian Dryline, in: AGU Annual Meeting 2016, Session A23F Global Convection, Hydrology, and Climate II Posters. San Francisco, U.S.A.

Benning, J., Yang, D., 2005. Adjustment of Daily Precipitation Data at Barrow and Nome Alaska for 1995–2001. Arctic, Antarct. Alp. Res. 37, 276–283. doi:10.1657/1523-0430(2005)037[0276:AODPDA]2.0.CO;2

Bergmaier, P.T., Geerts, B., 2015. Characteristics and Synoptic Environment of Drylines Occurring over the Higher Terrain of Southeastern Wyoming. Weather Forecast. 30, 1733–1748. doi:10.1175/WAF-D-15-0061.1

Berthou, S., Kendon, E.J., Chan, S.C., Ban, N., Leutwyler, D., Schär, C., Fosser, G., 2018. Pan-European climate at convection-permitting scale: a model intercomparison study. Clim. Dyn. 0, 1–25. doi:10.1007/s00382-018-4114-6

Betts, A., Ball, J., Beljaars, A., Miller, M.J., Viterbo, P.A., 1996. The land surface-atmosphere interaction: A review based on observational and global modeling perspective. J. Geophys. Res. 101, 7209–7225.

Betts, A.K., 2002. Evaluation of the diurnal cycle of precipitation, surface thermodynamics, and surface fluxes in the ECMWF model using LBA data. J. Geophys. Res. 107, 8045. doi:10.1029/2001JD000427

Boucher, O., Randall, D., Artaxo, P., Bretherton, C., Feingold, G., Forster, P., Kerminen, V.-M., Kondo, Y., Liao, H., Lohmann, U., Rasch, P., Satheesh, S.K., Sherwood, S., Stevens, B., Zhang, X.Y., 2013. Clouds and Aerosols. Clim. Chang. 2013 Phys. Sci. Basis Work. Gr. I Contrib. to Fifth Assess. Rep. Intergov. Panel Clim. Chang. 9781107057, 571–658. doi:10.1017/CBO9781107415324.016

Brimelow, J.C., Reuter, G.W., Poolman, E.R., 2002. Modeling Maximum Hail Size in Alberta Thunderstorms. Weather Forecast. 17, 1048–1062. doi:10.1175/1520-0434(2002)017<1048:MMHSIA>2.0.CO;2

Brisson, E., van Weverberg, K., Demuzere, M., Devis, A., Saeed, S., Stengel, M., van Lipzig, N.P.M., 2016a. How well can a convection-permitting climate model reproduce decadal statistics of precipitation, temperature and cloud characteristics? Clim. Dyn. 1–19. doi:10.1007/s00382-016-3012-z

Brisson, E., Van Weverberg, K., Demuzere, M., Devis, A., Saeed, S., Stengel, M., van Lipzig, N.P.M., 2016b. How well can a convection-permitting climate model reproduce decadal statistics of precipitation, temperature and cloud characteristics? Clim. Dyn. 47, 3043–3061. doi:10.1007/s00382-016-3012-z

Browning, K. a., Blyth, A.M., Clark, P. a., Corsmeier, U., Morcrette, C.J., Agnew, J.L., Ballard, S.P., Bamber, D., Barthlott, C., Bennett, L.J., Beswick, K.M., Bitter, M., Bozier, K.E., Brooks, B.J., Collier, C.G., Davies, F., Deny, B., Dixon, M. a., Feuerle, T., Forbes, R.M., Gaffard, C., Gray, M.D., Hankers, R., Hewison, T.J., Kalthoff, N., Khodayar, S., Kohler, M., Kottmeier, C., Kraut, S., Kunz, M., Ladd, D.N., Lean, H.W., Lenfant, J., Li, Z., Marsham, J., McGregor, J., Mobbs, S.D., Nicol, J., Norton, E., Parker, D.J., Perry, F., Ramatschi, M., Ricketts, H.M. a, Roberts, N.M., Russell, A., Schulz, H., Slack, E.C., Vaughan, G., Waight, J., Wareing, D.P., Watson, R.J., Webb, A.R., Wieser, A., 2007. The convective storm initiation project. Bull. Am. Meteorol. Soc. 88, 1939–1955. doi:10.1175/BAMS-88-12-1939

Brunetti, M., Buffoni, L., Mangianti, F., Maugeri, M., Nanni, T., 2004. Temperature, precipitation and extreme events during the last century in Italy. Glob. Planet. Change 40, 141–149. doi:10.1016/S0921-8181(03)00104-8

Burlingame, B.M., Evans, C., Roebber, P.J., 2017. The Influence of PBL Parameterization on the Practical Predictability of Convection Initiation during the Mesoscale Predictability Experiment (MPEX). Weather Forecast. 32, 1161–1183. doi:10.1175/WAF-D-16-0174.1

Burrows, W.R., King, P., Lewis, P.J., Kochtubajda, B., Snyder, B., Turcotte, V., 2002. Lightning occurrence patterns over Canada and adjacent United States from lightning detection network observations. Atmos. - Ocean 40, 59–80. doi:10.3137/ao.400104

Campbell, P.C., Geerts, B., Bergmaier, P.T., 2013. A Dryline in Southeast Wyoming. Part I: Multi-scale Analysis Using Observations and Modeling on 22 June 2010. Mon. Weather Rev. 130917124004000. doi:10.1175/MWR-D-13-00049.1

Carbone, R.E., Tuttle, J.D., 2008. Rainfall Occurrence in the U.S. Warm Season: The Diurnal Cycle*. J. Clim. 21, 4132–4146. doi:10.1175/2008JCLI2275.1

Carbone, R.E., Tuttle, J.D., Ahijevych, D.A., Trier, S.B., 2002. Inferences of predictability associated with warm season precipitation episodes. J. Atmos. Sci. 59, 2033–2056. doi:10.1175/1520-0469(2002)059<2033:IOPAWW>2.0.CO;2

Carbone, R.E., Wilson, J.W., Keenan, T.D., Hacker, J.M., 2000. Tropical Island Convection in the Absence of Significant Topography. Part I: Life Cycle of Diurnally Forced Convection. Mon. Weather Rev. 128, 3459–3480. doi:10.1175/1520-0493(2000)128<3459:TICITA>2.0.CO;2

Chubb, T., Manton, M.J., Siems, S.T., Peace, A.D., Bilish, S.P., 2015. Estimation of Wind-Induced Losses from a Precipitation Gauge Network in the Australian Snowy Mountains. J. Hydrometeorol. 16, 2619–2639. doi:10.1175/JHM-D-14-0216.1

Clark, A.J., Coniglio, M.C., Coffer, B.E., Thompson, G., Xue, M., Kong, F., 2015. Sensitivity of 24-h Forecast Dryline Position and Structure to Boundary Layer Parameterizations in Convection-Allowing WRF Model Simulations. Weather Forecast. 30, 613–638. doi:10.1175/WAF-D-14-00078.1

Coffer, B.E., Maudlin, L.C., Veals, P.G., Clark, A.J., 2013. Dryline Position Errors in Experimental Convection-Allowing NSSL-WRF Model Forecasts and the Operational NAM. Weather Forecast. 28, 746–761. doi:10.1175/WAF-D-12-00092.1

Collados-Lara, A.J., Pardo-Igúzquiza, E., Pulido-Velazquez, D., Jiménez-Sánchez, J., 2018. Precipitation fields in an alpine Mediterranean catchment: Inversion of precipitation gradient with elevation or undercatch of snowfall? Int. J. Climatol. 38, 3565–3578. doi:10.1002/joc.5517

Colle, B., Smith, R., Wesley, D., 2013. Theory, Observations, and Predictions of Orographic Precipitation, in: Chow, F.K., De Wekker, S.F.J., Snyder, B.J. (Eds.), Mountain Weather Research and Forecasting SE - 6, Springer Atmospheric Sciences. Springer Netherlands, pp. 291–344. doi:10.1007/978-94-007-4098-3_6

Colli, M., Rasmussen, R., Thï¿½riault, J.M., Lanza, L.G., Bruce Baker, C., Kochendorfer, J., 2015. An improved trajectory model to evaluate the collection performance of snow gauges. J. Appl. Meteorol. Climatol. 54, 1826–1836. doi:10.1175/JAMC-D-15-0035.1

Coniglio, M.C., Correia, J., Marsh, P.T., Kong, F., 2013. Verification of Convection-Allowing WRF Model Forecasts of the Planetary Boundary Layer Using Sounding Observations. Weather Forecast. 28, 842–862. doi:10.1175/WAF-D-12-00103.1

Dai, A., Fung, I.Y., Del Genio, A.D., Dai, A., Fung, I.Y., Genio, A.D. Del, 1997. Surface Observed Global Land Precipitation Variations during 1900–88. J. Clim. 10, 2943–2962. doi:10.1175/1520-0442(1997)010<2943:SOGLPV>2.0.CO;2

DeBeer, C.M., Wheater, H.S., Carey, S.K., Chun, K.P., 2016. Recent climatic, cryospheric, and hydrological changes over the interior of western Canada: A review and synthesis. Hydrol. Earth Syst. Sci. 20, 1573–1598. doi:10.5194/hess-20-1573-2016

Dee, D.P., Uppala, S.M., Simmons, a. J., Berrisford, P., Poli, P., Kobayashi, S., Andrae, U., Balmaseda, M. a., Balsamo, G., Bauer, P., Bechtold, P., Beljaars, a. C.M., van de Berg, L., Bidlot, J., Bormann, N., Delsol, C., Dragani, R., Fuentes, M., Geer, a. J., Haimberger, L., Healy, S.B., Hersbach, H., Hólm, E. V., Isaksen, L., Kållberg, P., Köhler, M., Matricardi, M., Mcnally, a. P., Monge-Sanz, B.M., Morcrette, J.J., Park, B.K., Peubey, C., de Rosnay, P., Tavolato, C., Thépaut, J.N., Vitart, F., 2011. The ERA-Interim reanalysis: Configuration and performance of the data assimilation system. Q. J. R. Meteorol. Soc. 137, 553–597. doi:10.1002/qj.828

Déqué, M., Rowell, D.P., Lüthi, D., Giorgi, F., Christensen, J.H., Rockel, B., Jacob, D., Kjellström, E., De Castro, M., Van Den Hurk, B., 2007. An intercomparison of regional climate simulations for Europe: Assessing uncertainties in model projections. Clim. Change 81, 53–70. doi:10.1007/s10584-006-9228-x

Deser, C., Knutti, R., Solomon, S., Phillips, A.S., 2012. Communication of the role of natural variability in future North America climate. Nat. Clim. Chang. 2, 775–780. doi:10.1038/NCLIMATE1562

Dirmeyer, P.A., Cash, B.A., Kinter, J.L., Jung, T., Marx, L., Satoh, M., Stan, C., Tomita, H., Towers, P., Wedi, N., Achuthavarier, D., Adams, J.M., Altshuler, E.L., Huang, B., Jin, E.K., Manganello, J., 2012. Simulating the diurnal cycle of rainfall in global climate models: Resolution versus parameterization. Clim. Dyn. 39, 399–418. doi:10.1007/s00382-011-1127-9

Done, J.M., Craig, G.C., Gray, S.L., Clark, P.A., Gray, M.E.B., 2006. Mesoscale simulations of organized convection: Importance of convective equilibrium. Q. J. R. Meteorol. Soc. 132, 737–756. doi:10.1256/qj.04.84

Dore, M.H.I., Simcisko, P., 2013. Projecting Future Climate Scenarios for Canada Using General Circulation Models : An Integrated Review. pp. 3–27. doi:10.1007/698

Doswell, C.A., 1987. The Distinction between Large-Scale and Mesoscale Contribution to Severe Convection: A Case Study Example. Weather Forecast. doi:10.1175/1520-0434(1987)002<0003:TDBLSA>2.0.CO;2

Duchon, C.E., Essenberg, G.R., 2001. Comparative rainfall observations from pit and aboveground rain gauges with and without wind shields. Water Resour. Res. 37, 3253–3263. doi:10.1029/2001WR000541

ECMWF, 2017. ERA5 Reanalysis Monthly Means. doi:10.5065/D63B5XW1

Eltahir, Rafael, B., Parsons, R.M., 1996. precipitation Recycling. Rev. Geophys. 34, 367–378.

Emori, S., Brown, S.J., 2005. Dynamic and thermodynamic changes in mean and extreme precipitation under changed climate. Geophys. Res. Lett. 32, 1–5. doi:10.1029/2005GL023272

Erfani, A., Méthot, A., Goodson, R., Bélair, S., Yeh, K.-S., Côté, J., Moffet, R., 2003. Synoptic and mesoscale study of a severe convective outbreak with the nonhydrostatic Global Environmental Multiscale (GEM) model. Meteorol. Atmos. Phys. 82, 31–53. doi:10.1007/s00703-001-0585-8

Eyring, V., Bony, S., Meehl, G.A., Senior, C.A., Stouffer, R.J., Taylor, K.E., 2017. Overview of the Coupled Model Intercomparison Project Phase 6 (CMIP6) Experimental Design and Organization. Livermore, California.

Fall, S., Watts, A., Nielsen-Gammon, J., Jones, E., Niyogi, D., Christy, J.R., Pielke, R.A., 2011. Analysis of the impacts of station exposure on the U.S. Historical Climatology Network temperatures and temperature trends. J. Geophys. Res. Atmos. 116, 1–15. doi:10.1029/2010JD015146

Fan, J., Wang, Y., Rosenfeld, D., Liu, X., 2016. Review of Aerosol–Cloud Interactions: Mechanisms, Significance, and Challenges. J. Atmos. Sci. 73, 4221–4252. doi:10.1175/JAS-D-16-0037.1

Fischer, A.P., 2011. The measurement factors in estimating snowfall derived from snow cover surfaces using acoustic snow depth sensors. J. Appl. Meteorol. Climatol. 50, 681–699. doi:10.1175/2010JAMC2408.1

Fosser, G., Khodayar, S., Berg, P., 2014. Benefit of convection permitting climate model

simulations in the representation of convective precipitation. Clim. Dyn. 44, 45–60. doi:10.1007/s00382-014-2242-1

Fuhrer, O., Chadha, T., Hoefler, T., Kwasniewski, G., Lapillonne, X., Leutwyler, D., Lüthi, D., Osuna, C., Schär, C., Schulthess, T.C., Vogt, H., 2018. Near-global climate simulation at 1km resolution: Establishing a performance baseline on 4888 GPUs with COSMO 5.0. Geosci. Model Dev. 11, 1665–1681. doi:10.5194/gmd-11-1665-2018

Fulton, R. a., Breidenbach, J.P., Seo, D.-J., Miller, D. a., O'Bannon, T., 1998. The WSR-88D Rainfall Algorithm. Weather Forecast. 13, 377–395. doi:10.1175/1520-0434(1998)013<0377:TWRA>2.0.CO;2

Garreaud, R., Fuenzalida, H. a., 2007. The Influence of the Andes on Cutoff Lows: A Modeling Study*. Mon. Weather Rev. 135, 1596–1613. doi:10.1175/MWR3350.1

Geerts, B., Parsons, D., Ziegler, C.L., Weckwerth, T.M., Biggerstaff, M.I., Clark, R.D., Coniglio, M.C., Demoz, B.B., Ferrare, R.A., Gallus, W.A., Haghi, K., Hanesiak, J.M., Klein, P.M., Knupp, K.R., Kosiba, K., McFarquhar, G.M., Moore, J.A., Nehrir, A.R., Parker, M.D., Pinto, J.O., Rauber, R.M., Schumacher, R.S., Turner, D.D., Wang, Q., Wang, X., Wang, Z., Wurman, J., 2017. The 2015 Plains Elevated Convection at Night Field Project. Bull. Am. Meteorol. Soc. 98, 767–786. doi:10.1175/BAMS-D-15-00257.1

Gensini, V.A., Mote, T.L., 2015. Downscaled estimates of late 21st century severe weather from CCSM3. Clim. Change 129, 307–321. doi:10.1007/s10584-014-1320-z

Giorgi, F., Jones, C., Asrar, G.R., 2009. Addressing climate information needs at the regional level : the CORDEX framework 58, 175–183.

González-Rouco, J.F., Jiménez, J.L., Quesada, V., Valero, F., 2001. Quality control and homogeneity of precipitation data in the southwest of Europe. J. Clim. 14, 964–978. doi:10.1175/1520-0442(2001)014<0964:QCAHOP>2.0.CO;2

Goodison, B.E., 1981. Compatibility of Canadian snowfall and snow cover data. Water Resour. Res. 17, 893–900. doi:10.1029/WR017i004p00893

Goodison, B.E., Louie, P.Y.T., Yang, D., 1998. Report No . 67 WMO SOLID PRECIPITATION MEASUREMENT INTERCOMPARISON.

Goovaerts, P., 2000. Geostatistical approaches for incorporating elevation into the spatial interpolation of rainfall 228, 113–129.

Groisman, P.Y., Easterling, D.R., 1994. Variability and Trends of Total Precipitation and Snowfall over the United States and Canada. J. Clim. 7, 184–205. doi:10.1175/1520-0442(1994)007<0184:VATOTP>2.0.CO;2

Groisman, P.Y., Knight, R.W., Easterling, D.R., Karl, T.R., Hegerl, G.C., Razuvaev, V.N., 2005. Trends in intense precipitation in the climate record. J. Clim. 18, 1326–1350. doi:10.1175/JCLI3339.1

Groisman, P.Y., Knight, R.W., Karl, T.R., 2012. Changes in Intense Precipitation over the Central United States. J. Hydrometeorol. 13, 47–66. doi:10.1175/JHM-D-11-039.1

Guinard, K., Mailhot, A., Caya, D., 2015. Projected changes in characteristics of precipitation spatial structures over North America. Int. J. Climatol. 35, 596–612. doi:10.1002/joc.4006

Haberlie, A.M., Ashley, W.S., 2019. Climatological representation of mesoscale convective systems in a dynamically downscaled climate simulation. Int. J. Climatol. 39, 1144–1153. doi:10.1002/joc.5880

Haerter, J.O., Berg, P., 2009. Unexpected rise in extreme precipitation caused by a shift in rain type? Nat. Geosci. 2, 372–373. doi:10.1038/ngeo523

Hammer, G., Steurer, P., 2000. Data documentation for hourly precipitation data TD-3240.

Asheville, NC, USA.
Hapuarachchi, H.A.P., Wang, Q.J., Pagano, T.C., 2011. A review of advances in flash flood forecasting. Hydrol. Process. 25, 2771–2784. doi:10.1002/hyp.8040
Hara, M., Yoshikane, T., Kawase, H., Kimura, F., 2008. Estimation of the Impact of Global Warming on Snow Depth in Japan by the Pseudo-Global-Warming Method. Hydrol. Res. Lett. 2, 61–64. doi:10.3178/hrl.2.61
Hartmann, D.L., Klein Tank, A.M.G., Rusticucci, M., Alexander, L. V., Brönnimann, S., Charabi, Y.A.R., Dentener, F.J., Dlugokencky, E.J., Easterling, D.R., Kaplan, A., Soden, B.J., Thorne, P.W., Wild, M., Zhai, P., 2013. Observations: Atmosphere and surface. Clim. Chang. 2013 Phys. Sci. Basis Work. Gr. I Contrib. to Fifth Assess. Rep. Intergov. Panel Clim. Chang. 9781107057, 159–254. doi:10.1017/CBO9781107415324.008
Haylock, M.R., Hofstra, N., Klein Tank, A.M.G., Klok, E.J., Jones, P.D., New, M., 2008. A European daily high-resolution gridded data set of surface temperature and precipitation for 1950-2006. J. Geophys. Res. Atmos. 113. doi:10.1029/2008JD010201
Hill, L.M., 2006. Drylines observed in Alberta during A-GAME. University of Alberta.
Hobbs, P. V., Locatelli, J.D., Martin, J.E., 1996. A New Conceptual Model for Cyclones Generated in the Lee of the Rocky Mountains. Bull. Am. Meteorol. Soc. 77, 1169–1179.
Hoch, J., Markowski, P., 2005. A climatology of springtime dryline position in the U.S. Great Plains region. J. Clim. 18, 2132–2137. doi:10.1175/JCLI3392.1
Hohenegger, C., Brockhaus, P., Schär, C., 2008. Towards climate simulations at cloud-resolving scales. Meteorol. Zeitschrift 17, 383–394.
Hong, S.-Y., Noh, Y., Dudhia, J., 2006. A new vertical diffusion package with an explicit treatment of entrainment processes. Mon. Weather Rev. 134, 2318–2341. doi:10.1175/MWR3199.1
Hoogewind, K.A., Baldwin, M.E., Trapp, R.J., 2017. The impact of climate change on hazardous convective weather in the United States: Insight from high-resolution dynamical downscaling. J. Clim. 30, 10081–10100. doi:10.1175/JCLI-D-16-0885.1
Houze Jr., R.A., 1997. Stratiform precipitation in the tropics: A meteorological paradox? Bull. Amer. Meterol. Soc. 78, 2179–2196.
Houze Jr, R.A., 2014. Cloud Dynamics. Academic press.
Houze Jr, R.A., 2012. Orographic effects on precipitating clouds. Rev. Geophys. 50, 1–47. doi:10.1029/2011RG000365
Houze Jr, R.A., Wilton, D.C., Smull, B.F., 2007. Monsoon Convection in the Himalayam Region as seen by the TRMM Precipitation Radar. Q. J. R. … 133, 1389–1411. doi:10.1002/qj
Hutchinson, M.F., McKenney, D.W., Lawrence, K., Pedlar, J.H., Hopkinson, R.F., Milewska, E., Papadopol, P., 2009. Development and Testing of Canada-Wide Interpolated Spatial Models of Daily Minimum–Maximum Temperature and Precipitation for 1961–2003. J. Appl. Meteorol. Climatol. 48, 725–741. doi:10.1175/2008JAMC1979.1
Iacono, M.J., Delamere, J.S., Mlawer, E.J., Shephard, M.W., Clough, S.A., Collins, W.D., 2008. Radiative forcing by long-lived greenhouse gases: Calculations with the AER radiative transfer models. J. Geophys. Res. Atmos. 113, 2–9. doi:10.1029/2008JD009944
Isotta, F.A., Frei, C., Weilguni, V., Perčec Tadić, M., Lassègues, P., Rudolf, B., Pavan, V., Cacciamani, C., Antolini, G., Ratto, S.M., Munari, M., Micheletti, S., Bonati, V., Lussana, C., Ronchi, C., Panettieri, E., Marigo, G., Vertačnik, G., 2014. The climate of daily precipitation in the Alps: Development and analysis of a high-resolution grid dataset from pan-Alpine rain-gauge data. Int. J. Climatol. 34, 1657–1675. doi:10.1002/joc.3794
Jackson, P., Mayr, G., Vosper, S., 2013. Chapter 3: Dynamically-Driven Winds, in: Chow, F.K.,

De Wekker, S.F.J., Snyder, B.J. (Eds.), Mountain Weather Research and Forecasting SE - 3, Springer Atmospheric Sciences. Springer Netherlands, pp. 121–218. doi:10.1007/978-94-007-4098-3_3

Jacob, D., Petersen, J., Eggert, B., Alias, A., Christensen, O.B., Bouwer, L.M., Braun, A., Colette, A., Déqué, M., Georgievski, G., Georgopoulou, E., Gobiet, A., Menut, L., Nikulin, G., Haensler, A., Hempelmann, N., Jones, C., Keuler, K., Kovats, S., Kröner, N., Kotlarski, S., Kriegsmann, A., Martin, E., van Meijgaard, E., Moseley, C., Pfeifer, S., Preuschmann, S., Radermacher, C., Radtke, K., Rechid, D., Rounsevell, M., Samuelsson, P., Somot, S., Soussana, J.F., Teichmann, C., Valentini, R., Vautard, R., Weber, B., Yiou, P., 2014. EURO-CORDEX: New high-resolution climate change projections for European impact research. Reg. Environ. Chang. 14, 563–578. doi:10.1007/s10113-013-0499-2

Jian Lu, Vecchi, G.A., Thomas, R., 2007. Expansion of the Hadley cell under global warming. Geophys. Res. Lett. 34, 1–5. doi:10.1029/2006GL028443

Jiang, X., Lau, N.C., Klein, S. a., 2006. Role of eastward propagating convection systems in the diurnal cycle and seasonal mean of summertime rainfall over the U.S. Great Plains. Geophys. Res. Lett. 33, 1–6. doi:10.1029/2006GL027022

Johnson, Z.F., Hitchens, N.M., 2018. Effects of Soil Moisture on the Longitudinal Dryline Position in the Southern Great Plains. J. Hydrometeorol. 19, 273–287. doi:10.1175/JHM-D-17-0091.1

Jones, S.H., Fahl, C.B., 1994. Magnitude and Frequency of Floods in Alaska and Conterminous Basins of Canada. Anchorage, Alaska.

Judt, F., 2018. Insights into Atmospheric Predictability Through Global Convection-Permitting Model Simulations. J. Atmos. Sci. JAS-D-17-0343.1. doi:10.1175/JAS-D-17-0343.1

Kane, D.L., Stuefer, S.L., 2015. Reflecting on the status of precipitation data collection in Alaska: a case study. Hydrol. Res. 46, 478–493. doi:10.2166/nh.2014.023

Keenan, T.D., Carbone, R.E., 2008. Propagation and Diurnal Evolution of Warm Season Cloudiness in the Australian and Maritime Continent Region. Mon. Weather Rev. 136, 973–994. doi:10.1175/2007MWR2152.1

Kendon, E.J., Ban, N., Roberts, N.M., Fowler, H.J., Roberts, M.J., Chan, S.C., Evans, J.P., Fosser, G., Wilkinson, J.M., 2017. Do convection-permitting regional climate models improve projections of future precipitation change? BAM 98, 79–94. doi:10.1175/BAMS-D-15-0004.1

Kendon, E.J., Roberts, N.M., Fowler, H.J., Roberts, M.J., Chan, S.C., Senior, C.A., 2014. Heavier summer downpours with climate change revealed by weather forecast resolution model. Nat. Clim. Chang. 4, 570–576. doi:10.1038/nclimate2258

Kendon, E.J., Roberts, N.M., Senior, C.A., Roberts, M.J., 2012. Realism of rainfall in a very high-resolution regional climate model. J. Clim. 25, 5791–5806. doi:10.1175/JCLI-D-11-00562.1

Kent, E.C., Fangohr, S., Berry, D.I., 2013. A comparative assessment of monthly mean wind speed products over the global ocean. Int. J. Climatol. 33, 2520–2541. doi:10.1002/joc.3606

Knott, S.R.J., Taylor, N.M., 2000. Operational Aspects of the Alberta Severe Weather Outbreak of 29 July 1993.

Kochendorfer, J., Nitu, R., Wolff, M., Mekis, E., Rasmussen, R., Baker, B., Earle, M., Reverdin, A., Wong, K., Smith, C.D., Yang, D., Roulet, Y.A., Meyers, T., Buisan, S., Isaksen, K., Brækkan, R., Landolt, S., Jachcik, A., 2018. Testing and development of transfer functions for weighing precipitation gauges in WMO-SPICE. Hydrol. Earth Syst. Sci. 22, 1437–1452. doi:10.5194/hess-22-1437-2018

Krasting, J.P., Broccoli, A.J., Dixon, K.W., Lanzante, J.R., 2013. Future Changes in Northern

Hemisphere Snowfall. J. Clim. 26, 7813–7828. doi:10.1175/JCLI-D-12-00832.1
Kröner, N., Kotlarski, S., Fischer, E., Lüthi, D., Zubler, E., Schär, C., 2016. Separating climate change signals into thermodynamic, lapse-rate and circulation effects: theory and application to the European summer climate. Clim. Dyn. 48, 1–16. doi:10.1007/s00382-016-3276-3
Lackmann, G.M., 2015. Hurricane Sandy before 1900 and after 2100. Bull. Am. Meteorol. Soc. 96, 547–560. doi:10.1175/BAMS-D-14-00123.1
Laing, A.G., Fritsch, J.M., 1997. The global population of mesoscale convective complexes. Q. J. R. Meteorol. Soc. 123, 389–405. doi:10.1002/qj.49712353807
Lang, S., Tao, W.-K., Simpson, J., Ferrier, B., 2003. Modeling of Convective – Stratiform Precipitation Processes: Sensitivity to Partitioning Methods. J. Adv. Model. Earth Syst. 42, 505–527. doi:10.1175/1520-0450(2003)042<0505:MOCSPP>2.0.CO;2
Langhans, W., Schmidli, J., Fuhrer, O., Bieri, S., Schär, C., 2013. Long-term simulations of thermally driven flows and orographic convection at convection-parameterizing and cloud-resolving resolutions. J. Appl. Meteorol. Climatol. 52, 1490–1510. doi:10.1175/JAMC-D-12-0167.1
Leeper, R.D., Rennie, J., Palecki, M.A., 2015. Observational Perspectives from U.S. Climate Reference Network (USCRN) and Cooperative Observer Program (COOP) Network: Temperature and Precipitation Comparison. J. Atmos. Ocean. Technol. 32, 703–721.
Legates, D.R., Willmott, C.J., 1990. Mean seasonal and spatial variability in gauge-corrected, global precipitation. Int. J. Climatol. 10, 111–127. doi:10.1002/joc.3370100202
Lenderink, G., van Meijgaard, E., 2008. Increase in hourly precipitation extremes beyond expectations from temperature changes. Nat. Geosci. 1, 511–514. doi:10.1038/ngeo262
Leutwyler, D., Fuhrer, O., Lapillonne, X., Lüthi, D., Schär, C., 2016. Towards European-scale convection-resolving climate simulations with GPUs: A study with COSMO 4.19. Geosci. Model Dev. 9, 3393–3412. doi:10.5194/gmd-9-3393-2016
Leutwyler, D., Lüthi, D., Ban, N., Fuhrer, O., Schär, C., 2017. Evaluation of the convection-resolving climate modeling approach on continental scales. J. Geophys. Res. Atmos. 122, 5237–5258. doi:10.1002/2016JD026013
Li, Y., 2016. Investigation of discontinuity in precipitation measurements across Canada and U.S. border. U. of Saskatchewan.
Li, Y., Carbone, R.E., 2015. Offshore propagation of coastal precipitation. J. Atmos. Sci. 72, 4553–4568. doi:10.1175/JAS-D-15-0104.1
Li, Y., Smith, R.B., 2010a. The Detection and Significance of Diurnal Pressure and Potential Vorticity Anomalies East of the Rockies. J. Atmos. Sci. 67, 2734–2751. doi:10.1175/2010JAS3423.1
Li, Y., Smith, R.B., 2010b. Observation and Theory of the Diurnal Continental Thermal Tide. J. Atmos. Sci. 67, 2752–2765. doi:10.1175/2010JAS3384.1
Li, Y., Smith, R.B., Grubišić, V., 2009. Using Surface Pressure Variations to Categorize Diurnal Valley Circulations: Experiments in Owens Valley. Mon. Weather Rev. 137, 1753–1769. doi:10.1175/2008MWR2495.1
Lin, Y.-L., 2007. Mesoscale dynamics. Cambridge University Press.
Lin, Y., Mitchell, K.E., 2005. The NCEP Stage II/IV hourly precipitation analyses: development and applications. Prepr. 19th Conf. Hydrol. Am. Meteorol. Soc. San Diego, CA, 9-13 January 2005, Pap. 1.2 2–5.
Liu, C., Ikeda, K., Rasmussen, R., Barlage, M., Newman, A.J., Prein, A.F., Chen, F., Chen, L., Clark, M., Dai, A., Dudhia, J., Eidhammer, T., Gochis, D., Gutmann, E., Kurkute, S., Li, Y.,

Thompson, G., Yates, D., 2017. Continental-scale convection-permitting modeling of the current and future climate of North America. Clim. Dyn. 1–25. doi:10.1007/s00382-016-3327-9

Liu, C., Moncrieff, M.W., Tuttle, J.D., Carbone, R.E., 2006. Explicit and parameterized episodes of warm-season precipitation over the continental United States. Adv. Atmos. Sci. 23, 91–105. doi:10.1007/s00376-006-0010-9

Lothon, M., Campistron, B., Chong, M., Couvreux, F., Guichard, F., Rio, C., Williams, E., 2011. Life Cycle of a Mesoscale Circular Gust Front Observed by a C-Band Doppler Radar in West Africa. Mon. Weather Rev. 139, 1370–1388. doi:10.1175/2010MWR3480.1

Lucas-Picher, P., Cattiaux, J., Bougie, A., Laprise, R., 2016. How does large-scale nudging in a regional climate model contribute to improving the simulation of weather regimes and seasonal extremes over North America? Clim. Dyn. 46, 929–948. doi:10.1007/s00382-015-2623-0

Lundquist, J.D., Minder, J.R., Neiman, P.J., Sukovich, E., 2010. Relationships between Barrier Jet Heights, Orographic Precipitation Gradients, and Streamflow in the Northern Sierra Nevada. J. Hydrometeorol. 11, 1141–1156. doi:10.1175/2010JHM1264.1

Mahfouf, J.-F., Brasnett, B., Gagnon, S., 2007. A Canadian Precipitation Analysis (CaPA) Project: Description and Preliminary Results. Atmosphere-Ocean 45, 1–17. doi:10.3137/ao.v450101

Mahoney, K., Alexander, M., Scott, J.D., Barsugli, J., 2013. High-resolution downscaled simulations of warm-season extreme precipitation events in the colorado front range under past and future climates. J. Clim. 26, 8671–8689. doi:10.1175/JCLI-D-12-00744.1

Mailhot, A., Beauregard, I., Talbot, G., Caya, D., Biner, S., 2012. Future changes in intense precipitation over Canada assessed from multi-model NARCCAP ensemble simulations. Int. J. Climatol. 32, 1151–1163. doi:10.1002/joc.2343

Mailhot, A., Kingumbi, A., Talbot, G., Poulin, A., 2010. Future changes in intensity and seasonal pattern of occurrence of daily and multi-day annual maximum precipitation over Canada. J. Hydrol. 388, 173–185. doi:10.1016/j.jhydrol.2010.04.038

Manson, G.K., Solomon, S.M., 2007. Past and future forcing of Beaufort Sea coastal change. Atmosphere-Ocean 45, 107–122. doi:10.3137/ao.450204

Martin, J.E., 1999. Quasigeostrophic Forcing of Ascent in the Occluded Sector of Cyclones and the Trowal Airstream. Mon. Weather Rev. 127, 70–88. doi:10.1175/1520-0493(1999)127<0070:QFOAIT>2.0.CO;2

Mbengue, C., Schneider, T., 2013. Storm track shifts under climate change: What can be learned from large-scale dry dynamics. J. Clim. 26, 9923–9930. doi:10.1175/JCLI-D-13-00404.1

Mearns, L.O., Sain, S., Leung, L.R., Bukovsky, M.S., Mcginnis, S., Biner, S., Caya, D., Arritt, R.W., Gutowski, W., Takle, E., Snyder, M., Jones, R.G., Nunes, A.M.B., Tucker, S., Herzmann, D., Mcdaniel, L., Sloan, L., 2013. Climate change projections of the North American Regional Climate Change Assessment Program 965–975. doi:10.1007/s10584-013-0831-3

Medina, S., Houze, R. a., Kumar, A., Niyogi, D., 2010. Summer monsoon convection in the Himalayan region: Terrain and land cover effects. Q. J. R. Meteorol. Soc. 136, 593–616. doi:10.1002/qj.601

Mekis, É., Brown, R., 2010. Derivation of an adjustment factor map for the estimation of the water equivalent of snowfall from ruler measurements in Canada. Atmosphere-Ocean 48, 284–293. doi:10.3137/AO1104.2010

Mekis, E., Donaldson, N., Reid, J., Zucconi, A., Hoover, J., Li, Q., Nitu, R., Melo, S., 2018. An

Overview of Surface-Based Precipitation Observations at Environment and Climate Change Canada. Atmos. - Ocean 56, 71–95. doi:10.1080/07055900.2018.1433627
Mekis, E., Hogg, W.D., 1999. Rehabilitation and analysis of Canadian daily precipitation time series. Atmosphere-Ocean 37, 53–85. doi:10.1080/07055900.1999.9649621
Mekis, É., Vincent, L. a., 2011. An Overview of the Second Generation Adjusted Daily Precipitation Dataset for Trend Analysis in Canada. Atmosphere-Ocean 49, 163–177. doi:10.1080/07055900.2011.583910
Menne, M.J., Williams, C.N., Vose, R.S., 2009. The U.S. historical climatology network monthly temperature data, version 2. Bull. Am. Meteorol. Soc. 90, 993–1007. doi:10.1175/2008BAMS2613.1
Metcalfe, J.R., Goodison, B.E., 1993. Correction of Canadian winter precipitation data, in: Proc. Eighth Symp. on Meteorological Observations and Instrumentation. Amer. Meteor. Soc., Anaheim, CA, pp. 338–343.
Mooney, P.A., Broderick, C., Bruyère, C.L., Mulligan, F.J., Prein, A.F., 2017. Clustering of observed diurnal cycles of precipitation over the United States for evaluation of a WRF multiphysics regional climate ensemble. J. Clim. 30, 9267–9286. doi:10.1175/JCLI-D-16-0851.1
Mooney, P.A., Mulligan, F.J., Broderick, C., 2016. Diurnal cycle of precipitation over the British Isles in a 0.44° WRF multiphysics regional climate ensemble over the period 1990–1995. Clim. Dyn. 47, 1–20. doi:10.1007/s00382-016-3026-6
National Research Council, U., 2012. A National Strategy for Advancing Climate Modeling. Washington DC. doi:10.17226/13430
Neiman, P.J., Ralph, F.M., Wick, G. a., Lundquist, J.D., Dettinger, M.D., 2008. Meteorological Characteristics and Overland Precipitation Impacts of Atmospheric Rivers Affecting the West Coast of North America Based on Eight Years of SSM/I Satellite Observations. J. Hydrometeorol. 9, 22–47. doi:10.1175/2007JHM855.1
Newman, A.J., Clark, M.P., Craig, J., Nijssen, B., Wood, A., Gutmann, E., Mizukami, N., Brekke, L., Arnold, J.R., 2015. Gridded Ensemble Precipitation and Temperature Estimates for the Contiguous United States. J. Hydrometeorol. 16, 2481–2500. doi:10.1175/JHM-D-15-0026.1
Nitu, R., Rasmunssen, R., Baker, B., Lanzinger, E., Joe, P., Yang, D., Smith, C., Roulet, Y.A., Goodison, B., Liang, H., Sabatini, F., Kochendorfer, J., Wolff, M., Hendrikx, J., Vuerich, E., Lanza, L., Aulamo, O., Vuglinsky, V., 2012. WMO INTERCOMPARISON OF INSTRUMENTS AND METHODS FOR THE MEASUREMENT OF SOLID PRECIPITATION AND SNOW ON THE GROUND : Organization of the Experiment.
Nitu, R., Wong, K., 2010. CIMO Survey on National Summaries of Methods and Instruments for Solid Precipitation Measurement at Automatic Weather Stations, Moc.Cma.Gov.Cn.
Niu, G.Y., Yang, Z.L., Mitchell, K.E., Chen, F., Ek, M.B., Barlage, M., Kumar, A., Manning, K., Niyogi, D., Rosero, E., Tewari, M., Xia, Y., 2011. The community Noah land surface model with multiparameterization options (Noah-MP): 1. Model description and evaluation with local-scale measurements. J. Geophys. Res. Atmos. 116, 1–19. doi:10.1029/2010JD015139
NOAA, N. center for environmental information, 2002. U.S. Cimate Reference Network [WWW Document]. URL https://www.ncdc.noaa.gov/crn/overview.html (accessed 9.24.18).
NOAA, NESDIS, 2002. Climate Reference Network (CRN) Site Information Handbook.
O'Gorman, P.A., Schneider, T., 2009. The physical basis for increases in precipitation extremes in simulations of 21st-century climate change. Proc. Natl. Acad. Sci. 106, 14773–14777. doi:10.1073/pnas.0907610106

Pall, P., Allen, M.R., Stone, D.A., 2007. Testing the Clausius-Clapeyron constraint on changes in extreme precipitation under CO2 warming. Clim. Dyn. 28, 351–363. doi:10.1007/s00382-006-0180-2

Pan, X., Yang, D., Li, Y., Barr, A., Helgason, W., Hayashi, M., Marsh, P., Pomeroy, J., Janowicz, R.J., 2016. Bias corrections of precipitation measurements across experimental sites in different ecoclimatic regions of western Canada. Cryosphere 10, 2347–2360. doi:10.5194/tc-10-2347-2016

Parker, W.S., 2016. Reanalyses and Observations: What's the Difference? Bull. Am. Meteorol. Soc. 97, 1565–1572. doi:10.1175/BAMS-D-14-00226.1

Parsons, D.B., Schapiro, M.A., Hardesty, R.M., Zamora, R.J., Intrieri, J.M., 1990. The Finescale Structure of a West Texas Dryline. Mon. Weather Rev. doi:10.1175/1520-0493(1991)119<1242:TFSOAW>2.0.CO;2

Peterson, R.E., 1983. The west Texas dryline: Occurrence and behavior, in: Preprints, 13th Conf. on Severe Local Storms, Tulsa, OK, Amer. Meteor. Soc., J9–J11.

Prein, A.F., Holland, G.J., Rasmussen, R.M., Done, J., Ikeda, K., Clark, M.P., Liu, C.H., 2013. Importance of regional climate model grid spacing for the simulation of heavy precipitation in the colorado headwaters. J. Clim. 26, 4848–4857. doi:10.1175/JCLI-D-12-00727.1

Prein, A.F., Langhans, W., Fosser, G., Ferrone, A., Ban, N., Goergen, K., Keller, M., Tolle, M., Gutjahr, O., Feser, F., Brisson, E., Kollet, S., Schmidli, J., Van Lipzig, N.P.M., Leung, R., 2015. A review on regional convection-permitting climate modeling: Demonstrations, prospects, and challenges. Rev. Geophys. 53, 323–361. doi:10.1002/2014RG000475

Prein, A.F., Liu, C., Ikeda, K., Bullock, R., Rasmussen, R., Holland, G., Clark, M.P., 2017a. Simulating North American mesoscale convective systems with a convection-permitting climate model. Clim. Dyn. doi:DOI 10.1007/s00382-017-3993-2

Prein, A.F., Liu, C., Ikeda, K., Trier, S.B., Rasmussen, R.M., Holland, G.J., Clark, M.P., 2017b. Increased rainfall volume from future convective storms in the US. Nat. Clim. Chang. 7, 880–884. doi:10.1038/s41558-017-0007-7

Prein, A.F., Pendergrass, A.G., 2019. Can We Constrain Uncertainty in Hydrologic Cycle Projections? Geophys. Res. Lett. doi:10.1029/2018GL081529

Prein, A.F., Rasmussen, R., Stephens, G., Prein, A.F., Rasmussen, R., Stephens, G., 2017c. Challenges and Advances in Convection-Permitting Climate Modeling. Bull. Am. Meteorol. Soc. BAMS-D-16-0263.1. doi:10.1175/BAMS-D-16-0263.1

Prein, A.F., Rasmussen, R.M., Ikeda, K., Liu, C., Clark, M.P., Holland, G.J., 2016. The future intensification of hourly precipitation extremes. Nat. Clim. Chang. 7, 1–6. doi:10.1038/nclimate3168

Pryor, S.C., Barthelmie, R.J., Riley, E.S., 2007. Historical evolution of wind climates in the USA. J. Phys. Conf. Ser. 75. doi:10.1088/1742-6596/75/1/012065

Rasmussen, K.L., Houze, R. a., 2011. Orogenic Convection in Subtropical South America as Seen by the TRMM Satellite. Mon. Weather Rev. 139, 2399–2420. doi:10.1175/MWR-D-10-05006.1

Rasmussen, K.L., Prein, A.F., Rasmussen, R.M., Ikeda, K., Liu, C., 2017. Changes in the convective population and thermodynamic environments in convection-permitting regional climate simulations over the United States. Clim. Dyn. 0, 1–26. doi:10.1007/s00382-017-4000-7

Rasmussen, R., Baker, B., Kochendorfer, J., Meyers, T., Landolt, S., Fischer, A.P., Black, J., Thériault, J.M., Kucera, P., Gochis, D., Smith, C., Nitu, R., Hall, M., Ikeda, K., Gutmann, E.,

2012. How Well Are We Measuring Snow? The NOAA/FAA/NCAR Winter Precipitation Test Bed. Bull. Am. Meteorol. Soc. 93, 811–829. doi:10.1175/BAMS-D-11-00052.1

Rasmussen, R., Ikeda, K., Liu, C., Gochis, D., Clark, M., Dai, A., Gutmann, E., Dudhia, J., Chen, F., Barlage, M., Yates, D., Zhang, G., 2014. Climate Change Impacts on the Water Balance of the Colorado Headwaters: High-Resolution Regional Climate Model Simulations. J. Hydrometeorol. 15, 1091–1116. doi:10.1175/JHM-D-13-0118.1

Rasmussen, R., Liu, C., Ikeda, K., Gochis, D., Yates, D., Chen, F., Tewari, M., Barlage, M., Dudhia, J., Yu, W., Miller, K., Arsenault, K., Grubišić, V., Thompson, G., Gutmann, E., 2011. High-resolution coupled climate runoff simulations of seasonal snowfall over Colorado: A process study of current and warmer climate. J. Clim. 24, 3015–3048. doi:10.1175/2010JCLI3985.1

Rasmussen, R., Landolt, S., Baker, B., Kochendorfer, J., Collins, B., Colli, M., Lanza, L., Thériault, J.M., 2014. Examination of the performance of single alter shielded and unshielded snowgauges using observations from the marshall field site during the spice WMO field program and numerical model simulations, in: WMO Technical Conference on Meteorological and Environmental Instruments and Methods of Observation. Saint Petersburg, Russia, pp. 1–8.

Reinert, D., Pilar, R., Baldauf, M., 2015. The ICON (ICOsahedral Non-hydrostatic) modelling framework of DWD and MPI-M : Description of the non-hydrostatic dynamical core 563–579. doi:10.1002/qj.2378

Rhea, J.O., 1966. A Study of Thunderstorm Formation Along Dry Lines. J. Appl. Meteorol. doi:10.1175/1520-0450(1966)005<0058:ASOTFA>2.0.CO;2

Riahi, K., Rao, S., Krey, V., Cho, C., Chirkov, V., Fischer, G., Kindermann, G., Nakicenovic, N., Rafaj, P., 2011. RCP 8.5-A scenario of comparatively high greenhouse gas emissions. Clim. Change 109, 33–57. doi:10.1007/s10584-011-0149-y

Richard, E., Buzzi, A., Zängl, G., 2007. Quantitative precipitation forecasting in the Alps: The advances achieved by the Mesoscale Alpine Programme. Q. J. R. Meteorol. Soc. 133, 831–846.

Riemann-Campe, K., Fraedrich, K., Lunkeit, F., 2009. Global climatology of Convective Available Potential Energy (CAPE) and Convective Inhibition (CIN) in ERA-40 reanalysis. Atmos. Res. 93, 534–545. doi:10.1016/j.atmosres.2008.09.037

Roe, G.H., 2005. Orographic Precipitation. Annu. Rev. Earth Planet. Sci. 33, 645–671. doi:10.1146/annurev.earth.33.092203.122541

Rood, S.B., Pan, J., Gill, K.M., Franks, C.G., Samuelson, G.M., Shepherd, A., 2008. Declining summer flows of Rocky Mountain rivers: Changing seasonal hydrology and probable impacts on floodplain forests. J. Hydrol. 349, 397–410. doi:10.1016/j.jhydrol.2007.11.012

Rotunno, R., Klemp, J.B., Weisman, M.L., 1988. A Theory for Strong, Long-Lived Squall Lines. J. Atmos. Sci. doi:10.1175/1520-0469(1988)045<0463:ATFSLL>2.0.CO;2

Saha, S., Moorthi, S., Pan, H., Wu, X., 2010. The NCEP climate forecast system reanalysis. BAMS 1015–1057. doi:10.1175/2010Bams3001.1

Sanderson, M., 1975. NOTES AND CORRESPONDENCE: A comparison of Canadian and United States Standard Methods of Measuring Precipitation. J. Appl. Meteorol. 14, 1197–1199.

Scaff, L., Prein, A.F., Li, Y., Liu, C., Rasmussen, R., Ikeda, K., 2019. Simulating the convective precipitation diurnal cycle in North America's current and future climate. Clim. Dyn. doi:10.1007/s00382-019-04754-9

Scaff, L., Rutllant, J.A., Rahn, D., Gascoin, S., Rondanelli, R., 2017. Meteorological Interpretation of Orographic Precipitation Gradients along an Andes West Slope Basin at 30°S (Elqui Valley, Chile). J. Hydrometeorol. 18, 713–727. doi:10.1175/JHM-D-16-0073.1

Scaff, L., Yang, D., Li, Y., Mekis, E., 2015. Inconsistency in precipitation measurements across Alaska and Yukon border. Cryosph. 9, 3709–3739. doi:10.5194/tcd-9-3709-2015

Schaefer, J.T., 1974. The Life Cycle of the Dryline. J. Appl. Meteorol. doi:10.1175/1520-0450(1974)013<0444:TLCOTD>2.0.CO;2

Schär, C., Ban, N., Fischer, E.M., Rajczak, J., Schmidli, J., Frei, C., Giorgi, F., Karl, T.R., Kendon, E.J., Tank, A.M.G.K., O'Gorman, P.A., Sillmann, J., Zhang, X., Zwiers, F.W., 2016. Percentile indices for assessing changes in heavy precipitation events. Clim. Change 137, 201–216. doi:10.1007/s10584-016-1669-2

Schär, C., Coauthors, 2016. Challenes in convection-resolving climate modeling [WWW Document]. CPM Work. URL https://ral.ucar.edu/sites/default/files/public/events/2016/gewex-convection-permitting-climate-modeling-workshop/docs/schaer-convectionresolving-gewex-ncar-160906.pdf

Schär, C., Frei, C., Lüthi, D., Davies, H.C., 1996a. Surrogate climate-change scenarios for regional climate models. Geophys. Res. Lett. 23, 669. doi:10.1029/96GL00265

Schär, C., Frei, C., Lüthi, D., Davies, H.C., 1996b. Surrogate climate change scenarios for regional climate models. Geophys. Res. Lett. 23 VN, 669–672. doi:10.1029/96GL00265

Schultz, D.M., Weiss, C.C., Hoffman, P.M., 2007. The Synoptic Regulation of Dryline Intensity. Mon. Weather Rev. 135, 1699–1709. doi:10.1175/MWR3376.1

Schwitalla, T., Coauthors, A., 2018. Novel seasonal latitude-belt simulation from 60N to 60S with 3 km resolution [WWW Document]. GEWEX Annu. Meet. URL https://www.gewexevents.org/wp-content/uploads/website_S25_1615_Schwitalla.pdf

Searcy, J., Hardison, C., 1960. Double-Mass Curves. United States Department of the Interior, Washington DC.

Seidel, D.J., Fu, Q., Randel, W.J., Reiohler, T.J., 2008. Widening of the tropical belt in a changing climate. Nat. Methods 1, 21–24. doi:10.1038/ngeo.2007.38

Seluchi, M., Garreaud, R.D., Norte, F.A., Saulo, A.C., 2006. Influence of the Subtropical Andes on Baroclinic Disturbances: A Cold Front Case Study. Mon. Weather Rev. 134, 3317–3335.

Seneviratne, S.I., Corti, T., Davin, E.L., Hirschi, M., Jaeger, E.B., Lehner, I., Orlowsky, B., Teuling, A.J., 2010. Investigating soil moisture-climate interactions in a changing climate: A review. Earth-Science Rev. 99, 125–161. doi:10.1016/j.earscirev.2010.02.004

Šeparović, L., Alexandru, A., Laprise, R., Martynov, A., Sushama, L., Winger, K., Tete, K., Valin, M., 2013. Present climate and climate change over North America as simulated by the fifth-generation Canadian regional climate model. Clim. Dyn. 41, 3167–3201. doi:10.1007/s00382-013-1737-5

Serreze, M.C., Hurst, C.M., 2000. Representation of mean arctic precipitation from NCEP-NCAR and ERA reanalyses. J. Clim. 13, 182–201. doi:10.1175/1520-0442(2000)013<0182:ROMAPF>2.0.CO;2

Sevruk, B., Klemm, S., 1989. Types of standard precipitation gauges, in: Proceedings of International Workshop on Precipitation Measurement, WMO/IAHS/ETH. St. Moritz, Switzerland.

Shaw, T.A., Baldwin, M., Barnes, E.A., Caballero, R., Garfinkel, C.I., Hwang, Y.T., Li, C., O'Gorman, P.A., Rivière, G., Simpson, I.R., Voigt, A., 2016. Storm track processes and the opposing influences of climate change. Nat. Geosci. 9, 656–664. doi:10.1038/ngeo2783

Sherwood, S.C., Roca, R., Weckwerth, T.M., Andronova, N.G., 2010. Tropospheric Water Vapor, Convection, and Climate. Rev. Geophys. 48, 1–29. doi:10.1029/2009RG000301.1.INTRODUCTION

Shook, K., Pomeroy, J., 2012. Changes in the hydrological character of rainfall on the Canadian prairies. Hydrol. Process. 26, 1752–1766. doi:10.1002/hyp.9383

Simpson, J.J., Hufford, G.L., Daly, C., Berg, J.S., Fleming, M.D., 2005. Comparing maps of mean monthly surface temperature and precipitation for Alaska and adjacent areas of Canada produced by two different methods. Arctic 58, 137–161.

Simpson, J.J., Hufford, G.L., Fleming, M.D., Berg, J.S., Ashton, J.B., 2002. Long-term climate patterns in Alaskan surface temperature and precipitation and their biological consequences. IEEE Trans. Geosci. Remote Sens. 40, 1164–1184. doi:10.1109/TGRS.2002.1010902

Skamarock, W.C., Klemp, J.B., Duda, M.G., Fowler, L.D., Park, S.-H., Ringler, T.D., 2012. A Multiscale Nonhydrostatic Atmospheric Model Using Centroidal Voronoi Tesselations and C-Grid Staggering. Mon. Weather Rev. 140, 3090–3105. doi:10.1175/MWR-D-11-00215.1

Skamarock, W.C., Klemp, J.B., Dudhia, J., Gill, D.O., Barker, D.M., Duda, M.G., Huang, X.-Y., Wang, W., Powers, J.G., 2008. A description of the advanced research WRF version 3. NCAR Technical Note NCAR/TN-475 + STR., NCAR technical note NCAR/ …. doi:10.5065/D68S4MVH

Smith, C.D., 2008. Correcting the Wind Bias in Snowfall Measurements Made with a Geonor T-200B Precipitation Gauge and Alter Wind Shield. Toronto, CMOS conference Bulletin.

Smith, R.B., 1979. The Influence of Mountains on the Atmosphere. Adv. Geophys. doi:10.1016/S0065-2687(08)60262-9

Smith, S.B., Yau, M.K., 1993a. The Causes of Severe Convective Outbreaks in Alberta. Part I: A Comparison of a Severe Outbreak with Two Nonsevere Events. Mon. Weather Rev. doi:10.1175/1520-0493(1993)121<1099:TCOSCO>2.0.CO;2

Smith, S.B., Yau, M.K., 1993b. The Causes of Severe Convective Outbreaks in Alberta. Part II: Conceptual Model and Statistical Analysis. Mon. Weather Rev.

Spencer, P.L., Stensrud, D.J., 1998. Simulating Flash Flood Events: Importance of the Subgrid Representation of Convection. Mon. Weather Rev. 126, 2884–2912. doi:10.1175/1520-0493(1998)126<2884:SFFEIO>2.0.CO;2

St. Jacques, J.-M., Lapp, S.L., Zhao, Y., Barrow, E.M., Sauchyn, D.J., 2013. Twenty-first century central Rocky Mountain river discharge scenarios under greenhouse forcing. Quat. Int. 310, 34–46. doi:10.1016/j.quaint.2012.06.023

Steger, C., Kotlarski, S., Jonas, T., Schär, C., 2013. Alpine snow cover in a changing climate: A regional climate model perspective. Clim. Dyn. 41, 735–754. doi:10.1007/s00382-012-1545-3

Steiner, M., 2004. Comments on "Modeling of Convective–Stratiform Precipitation Processes: Sensitivity to Partitioning Methods." J. Appl. Meteorol. 43, 958–961. doi:10.1175/1520-0450(2004)043<0958:COMOCP>2.0.CO;2

Stevens, B., Bony, S., 2013. What Are Climate Models Missing? Science (80-.). 340, 1053–1054.

Stewart, I.T., Cayan, D.R., Dettinger, M.D., 2005. Changes toward Earlier Streamflow Timing across Western North America. J. Clim. 18, 1136–1155.

Stewart, R.E., Szeto, K.K., Bonsal, B.R., Hanesiak, J.M., Kochtubajda, B., Li, Y., Thériault, J.M., DeBeer, C.M., Tam, B.Y., Li, Z., Liu, Z., Bruneau, J.A., Marinier, S., Matte, D., 2019. A Review and Synthesis of Future Earth System Change in the Interior of Western Canada: Part I – Climate and Meteorology. Hydrol. Earth Syst. Sci. Discuss. 1–45.

doi:10.5194/hess-2019-51
Stocker, T.F., Qin, D., Plattner, G.-K., Alexander, L.V., Allen, S.K., Bindoff, N.L., Bréon, F.-M., Church, J.A., Cubasch, U., Emori, S., Forster, P., Friedlingstein, P., Gillett, N., Gregory, J.M., Hartmann, D.L., Jansen, E., Kirtman, B., Knutti, R., Kumar, K.K., Lemke, P., Marotzke, J., Masson-Delmotte, V., Meehl, G.A., Mokhov, I.I., Piao, S., Ramaswamy, V., Randall, D., Rhein, M., Rojas, M., Sabine, C., Shindell, D., Talley, L.D., Vaughan, D.G., Xie, S.-P., 2013. Technical Summary, in: Stocker, T.F., D. Qin, G.-K. Plattner, M. Tignor, S.K. Allen, J. Boschung, A. Nauels, Y. Xia, V.B. and P.M.M. (eds.)]. (Ed.), Climate Change: The Physical Science Basis. Contribution of Working Group I to the Fifth Assessment Report of the Intergovernmental Panel on Climate Change. Cambridge University Press, Cambridge, Cambridge, United Kingdom and New York, NY, USA, pp. 1–84.
Stone, D. a., Weaver, A.J., Zwiers, F.W., 2000. Trends in Canadian precipitation intensity. Atmosphere-Ocean 38, 321–347. doi:10.1080/07055900.2000.9649651
Strong, G.S., 1989. LIMEX-85: 1 . Processing of Data Sets from an Alberta Mesoscale U pper-Air Experiment. Climatol. Bull. 23, 98–118.
Sun, X., Xue, M., Brotzge, J., McPherson, R.A., Hu, X.-M., Yang, X.-Q., 2016. An evaluation of dynamical downscaling of Central Plains summer precipitation using a WRF-based regional climate model at a convection-permitting 4 km resolution. J. Geophys. Res. Atmos. 121, 13,801-13,825. doi:10.1002/2016JD024796
Sushama, L., Laprise, R., Caya, D., Frigon, A., Slivitzky, M., 2006. Canadian RCM projected climate-clange signal and its sensitivity to model errors. Int. J. Climatol. 26, 2141–2159.
Szeto, K., 2002. Moisture recycling over the Mackenzie basin. Atmosphere-Ocean 40, 181–197. doi:10.3137/ao.400207
Szeto, K., Henson, W., Stewart, R., Gascon, G., 2011. The Catastrophic June 2002 Prairie Rainstorm. Atmosphere-Ocean 49, 380–395. doi:10.1080/07055900.2011.623079
Taylor, K.E., Stouffer, R.J., Meehl, G.A., 2012. An overview of CMIP5 and the experiment design. Bull. Am. Meteorol. Soc. 93, 485–498. doi:10.1175/BAMS-D-11-00094.1
Taylor, N.M., Sills, D.M.L., Hanesiak, J.M., Milbrandt, J. a., Smith, C.D., Strong, G.S., Skone, S.H., McCarthy, P.J., Brimelow, J.C., 2008. The understanding severe thunderstorms and Alberta boundary layers experiment (UNSTABLE) Operation plan. doi:10.1175/2011BAMS2994.1
Taylor, N.M., Sills, D.M.L., Hanesiak, J.M., Milbrandt, J.A., Smith, C.D., Strong, G.S., Skone, S.H., McCarthy, P.J., Brimelow, J.C., 2011. The understanding severe thunderstorms and Alberta boundary layers experiment (UNSTABLE) 2008, Bulletin of the American Meteorological Society. doi:10.1175/2011BAMS2994.1
Taylor, N.M., Sills, D.M.L., Hanesiak, J.M., Smith, C.D., Brimelow, J.C., 2016. CHARACTERIZATION OF THE DRYLINE IN ALBERTA: OBSERVATIONS FROM UNSTABLE 2008, in: 28th Conference on Severe Local Storms, Poster Session: Overviews and Results of Field Programs. Portland, OR, pp. 1–14.
Thackeray, C.W., DeAngelis, A.M., Hall, A., Swain, D.L., Qu, X., 2018. On the Connection Between Global Hydrologic Sensitivity and Regional Wet Extremes. Geophys. Res. Lett. 45, 11343–11351. doi:10.1029/2018GL079698
Thériault, J.M., Rasmussen, R., Ikeda, K., Landolt, S., 2012. Dependence of snow gauge collection efficiency on snowflake characteristics. J. Appl. Meteorol. Climatol. 51, 745–762. doi:10.1175/JAMC-D-11-0116.1
Thompson, G., Eidhammer, T., 2014. A Study of Aerosol Impacts on Clouds and Precipitation

Development in a Large Winter Cyclone. J. Atmos. Sci. 71, 3636–3658. doi:10.1175/JAS-D-13-0305.1

Thompson, G., Tewari, M., Ikeda, K., Tessendorf, S., Weeks, C., Otkin, J., Kong, F., 2016. Explicitly-coupled cloud physics and radiation parameterizations and subsequent evaluation in WRF high-resolution convective forecasts. Atmos. Res. 168, 92–104. doi:10.1016/j.atmosres.2015.09.005

Tomita, H., Satoh, M., 2004. A new dynamical framework of nonhydrostatic global model using the icosahedral grid. fluid Dyn. Res. 34, 357–400. doi:10.1016/j.Fuiddyn.2004.03.003

Trapp, Robert J, Diffenbaugh, N.S., Brooks, H.E., Baldwin, M.E., Robinson, E.D., Pal, J.S., 2007. Changes in severe thunderstorm environment frequency during the 21st century caused by anthropogenically enhanced global radiative forcing. Proc. Natl. Acad. Sci. 104, 19719–19723. doi:10.1073/pnas.0705494104

Trapp, Robert J., Halvorson, B.A., Diffenbaugh, N.S., 2007. Telescoping, multimodel approaches to evaluate extreme convective weather under future climates. J. Geophys. Res. Atmos. 112, 1–13. doi:10.1029/2006JD008345

Trapp, R.J., Hoogewind, K.A., 2016. The realization of extreme tornadic storm events under future anthropogenic climate change. J. Clim. 29, 5251–5265. doi:10.1175/JCLI-D-15-0623.1

Trapp, R.J., Robinson, E.D., Baldwin, M.E., Diffenbaugh, N.S., Schwedler, B.R.J., 2011. Regional climate of hazardous convective weather through high-resolution dynamical downscaling. Clim. Dyn. 37, 677–688. doi:10.1007/s00382-010-0826-y

Trenberth, K.E., 1999. Conceptual Framework For Changes of extremes of the hydrological cycle with climate change. Clim. Change 43, 327–339.

Trenberth, K.E., Dai, A., Rasmussen, R.M., Parsons, D.B., 2003. The changing character of precipitation. Bull. Am. Meteorol. Soc. 84, 1205-1217+1161. doi:10.1175/BAMS-84-9-1205

Trier, S.B., Romine, G.S., Ahijevych, D.A., Trapp, R.J., Schumacher, R.S., Coniglio, M.C., Stensrud, D.J., 2015. Mesoscale Thermodynamic Influences on Convection Initiation near a Surface Dryline in a Convection-Permitting Ensemble. Mon. Weather Rev. 143, 3726–3753. doi:10.1175/MWR-D-15-0133.1

Vincent, L. a., Mekis, É., 2006. Changes in Daily and Extreme Temperature and Precipitation Indices for Canada over the Twentieth Century. Atmosphere-Ocean 44, 177–193. doi:10.3137/ao.440205

Vincent, L. a., Wang, X.L., Milewska, E.J., Wan, H., Yang, F., Swail, V., 2012. A second generation of homogenized Canadian monthly surface air temperature for climate trend analysis. J. Geophys. Res. 117, 1–13. doi:10.1029/2012JD017859

Wallace, J.M., Hobbs, P. V., 2006. Atmospheric Science an introductory survey, International Geophysics Series.

Wan, H., Wang, X.L., Swail, V.R., 2010. Homogenization and trend analysis of Canadian near-surface wind speeds. J. Clim. 23, 1209–1225. doi:10.1175/2009JCLI3200.1

Warrach-Sagi, K., Schwitalla, T., Wulfmeyer, V., Bauer, H.S., 2013. Evaluation of a climate simulation in Europe based on the WRF-NOAH model system: Precipitation in Germany. Clim. Dyn. 41, 755–774. doi:10.1007/s00382-013-1727-7

Weckwerth, T.M., Bennett, L.J., Jay Miller, L., Van Baelen, J., Di Girolamo, P., Blyth, A.M., Hertneky, T.J., 2014. An Observational and Modeling Study of the Processes Leading to Deep, Moist Convection in Complex Terrain. Mon. Weather Rev. 142, 2687–2708. doi:10.1175/MWR-D-13-00216.1

Weckwerth, T.M., Parsons, D.B., 2006. A Review of Convection Initiation and Motivation for

IHOP_2002. Mon. Weather Rev. 134, 5–22. doi:10.1175/MWR3067.1
Weisman, M.L., Skamarock, W.C., Klemp, J.B., 1997. The Resolution Dependence of Explicitly Modeled Convective Systems. Mon. Weather Rev. 125, 527–548. doi:10.1175/1520-0493(1997)125<0527:TRDOEM>2.0.CO;2
Wentz, F.J., Ricciardulli, L., Hilburn, K., Mears, C., 2007. How much more rain will global warming bring? Science 317, 233–235. doi:10.1126/science.1140746
Whitfield, P.H., Pomeroy, J.W., 2016. Changes to flood peaks of a mountain river: implications for analysis of the 2013 flood in the Upper Bow River, Canada. Hydrol. Process. 30, 4657–4673. doi:10.1002/hyp.10957
Wilks, D.S., 2011. Statistical methods in the atmospheric sciences, Third Edit. ed. Academic press.
Wilson, J.W., Feng, Y., Chen, M., Roberts, R.D., 2010. Nowcasting Challenges during the Beijing Olympics: Successes, Failures, and Implications for Future Nowcasting Systems. Weather Forecast. 25, 1691–1714. doi:10.1175/2010WAF2222417.1
Wilson, J.W., Roberts, R.D., 2006. Summary of Convective Storm Initiation and Evolution during IHOP: Observational and Modeling Perspective. Mon. Weather Rev. 134, 23–47. doi:10.1175/MWR3069.1
Wolff, M.A., Isaksen, K., Petersen-Øverleir, A., Ødemark, K., Reitan, T., Brækkan, R., 2015. Derivation of a new continuous adjustment function for correcting wind-induced loss of solid precipitation: results of a Norwegian field study. Hydrol. Earth Syst. Sci. 19, 951–967. doi:10.5194/hess-19-951-2015
Yang, D., Goodison, B., Metcalfe, J., Louie, P., Elomaa, E., Hanson, C., Golubev, V., Gunther, T., Milkovic, J., Lapin, M., 2001. Compatibility evaluation of national precipitation gage measurements. J. Geophys. Res. 106, 1481–1491. doi:10.1029/2000JD900612
Yang, D., Goodison, B.E., Ishida, S., Benson, C.S., 1998a. Adjustment of daily precipitation data at 10 climate stations in Alaska: Application of World Meteorological Organization intercomparison results. Water Resour. Res. 34, 241–256. doi:10.1029/97WR02681
Yang, D., Goodison, B.E., Metcalfe, J.R., Golubev, V.S., Bates, R., Pangburn, T., Hanson, C.L., 1998b. Accuracy of NWS 8″ standard nonrecording precipitation gauge: Results and application of WMO intercomparison. J. Atmos. Ocean. Technol. 15, 54–68. doi:10.1175/1520-0426(1998)015<0054:AONSNP>2.0.CO;2
Yang, D., Goodison, B.E., Metcalfe, J.R., Golubev, V.S., Elomaa, E., Gunther, T., Bates, R., Pangburn, T., Hanson, C.L., Emerson, D., Copaciu, V., Milkovic, J., 1995. Accuracy of tretyakov precipitation gauge: Result of wmo intercomparison. Hydrol. Process. 9, 877–895. doi:10.1002/hyp.3360090805
Yang, D., Ishida, S., Goodison, B.E., Gunther, T., 1999. Bias correction of daily precipitation measurements for Greenland. J. Geophys. Res. 104, 6171. doi:10.1029/1998JD200110
Yang, D., Kane, D., Zhang, Z., Legates, D., Goodison, B., 2005. Bias corrections of long-term (1973–2004) daily precipitation data over the northern regions. Geophys. Res. Lett. 32, L19501. doi:10.1029/2005GL024057
Yang, D., Ohata, T., 2001. A Bias-Corrected Siberian Regional Precipitation Climatology. J. Hydrometeorol. 2, 122–139. doi:10.1175/1525-7541(2001)002<0122:ABCSRP>2.0.CO;2
Yang, D., Simonenko, A., 2013. Comparison of Winter Precipitation Measurements by Six Tretyakov Gauges at the Valdai Experimental Site. Atmosphere-Ocean 52, 39–53. doi:10.1080/07055900.2013.865156
Yates, D., Warner, T.T., Brandes, E.A., Leavesley, G.H., Sun, J., Mueller, C.K., 2001. Evaluation of Flash-Flood Discharge Forecasts in Complex Terrain using Precipitation. J. Hydrol. Eng.

265–274.
Yu, R., Zhou, T., Xiong, A., Zhu, Y., Li, J., 2007. Diurnal variations of summer precipitation over contiguous China. Geophys. Res. Lett. 34, 2–5. doi:10.1029/2006GL028129
Zardi, D., Whiteman, C.D., 2013. Chapter 2: Diurnal Mountain wind systems, in: Mountain Weather Research and Forecasting.
Zhang, X., Vincent, L. a., Hogg, W.D., Niitsoo, A., 2000. Temperature and precipitation trends in Canada during the 20th century. Atmosphere-Ocean 38, 395–429. doi:10.1080/07055900.2000.9649654
Zhao, K., Stadnyk, T., Koenig, K., Crawford, J., 2010. Better Precipitation Product over the Red River Basin.
Ziegler, C.L., Lee, T.J., Pielke, R. a., 1997. Convective Initiation at the Dryline: A Modeling Study. Mon. Weather Rev. 125, 1001–1026. doi:10.1175/1520-0493(1997)125<1001:CIATDA>2.0.CO;2
Ziegler, C.L., Rasmussen, E.N., 1998. The Initiation of Moist Convection at the Dryline: Forecasting Issues from aCase Study Perspective. Weather Forecast. 13, 1106–1131. doi:10.1175/1520-0434(1998)013<1106:TIOMCA>2.0.CO;2
Zipser, E.J., Cecil, D.J., Liu, C., Nesbitt, S.W., Yorty, D.P., 2006. Where are the most: Intense thunderstorms on Earth? Bull. Am. Meteorol. Soc. 87, 1057–1071. doi:10.1175/BAMS-87-8-1057

APPENDICES

Appendix A

This appendix is part of chapter 3.

Analysis of the diurnal cycle on GCMs from CMIP5 at the lateral boundaries of WRF-CONUS -I

On the CONUS I project (Liu et al., 2017, Figure A - 1), the future climate is simulated using the Pseudo Global Warming approach (PGW, Schär et al., 1996). The PGW employs a delta from the difference of a monthly mean ensemble of each 30 years from the historical and a future climate. The future climate considers the RCP8.5 scenario (Riahi et al., 2011). The ensemble used on the delta is estimated with 19 Global Climate Models (GCMs) from the CMIP5 (Taylor et al., 2012). The delta used on the CONUS I is a constant value on the diurnal cycle for each month, so a potential limitation on not considering the diurnal cycle variation, can produce an underrepresentation on the climate change of simulated diurnal cycle over the CONUS I between the historical and future simulations. To gain some insights on how different the constant and the 6h-variable delta are, a subset of 3 GCMs used in CONUS I are selected (Table A.1 for details). The comparison is implemented over air temperature and specific humidity at 5 vertical levels in July and over the closest grid points to the WRF boundaries (Figure A - 2).

Figure A - 3 shows some examples of the 30-years average of air temperature diurnal cycle on the historical (blue) and the future (red) climate from different models and vertical levels. The difference at 6h time steps (green dots) compared to a constant monthly value (green solid line) of the delta between the RCP8.5 and the historical simulations is presented. To summarize each model diurnal cycle, each panel on Figure A - 4 shows the average of all the closest grid points from each GCM to the WRF boundaries on the 5 vertical levels. The differences between the future and the historical climate ranges between 6ºC on the lowest level for the CamESM2 at 18 h and 2.6ºC on the GFDL-ESM2M at the highest level at 0 h. The most variable model in the vertical levels is the CanESM2, while the GFDL-ESM2M shows the smallest change. The CSIRO-Mk3-6-0 shows the smallest amplitude in the temperature diurnal cycle. To compare the difference between the constant and the variable delta, Figure A - 5 shows a synthesis of this difference for the three models and all vertical levels. The average absolute difference of the temperature deltas is 0.184ºC.

The specific humidity shows the most vertically variable diurnal cycle and the highest change (approx. 3.9 g kg^{-1}) between the future and the historical climate on the CanESM2 model (Figure A - 6), while the other two models (CSIRO-Mk3-6-0 and GFDL-ESM2M) show a smaller change between the two simulations (approx. 2.2 g kg^{-1}). The average of all the GCMs on all the closest grid points and all the vertical levels is presented in Figure A - 7, showing an average absolute difference of the deltas of 0.0728 g kg^{-1}. The CONUS I project used not only 19 different GCMs, but also many of them considers more than one realization. Referring to Table 1 on Liu et al.,

2017, 38 members were used in each historical and future simulation to calculate the ensemble-mean monthly climate change signal (the delta). Therefore, we expect that the result of this present analysis is representative of the entire ensemble used. This analysis (3 members used here), shows a maximum distance on the diurnal cycle between the maximum and the minimum difference of the deltas of 0.45 ºC on temperature and 0.2 g kg^{-1} on specific humidity. The differences represent a 10% and 7.3% (Table A.2) over the climate change, correspondingly. The average absolute difference between a 6h variable and a constant delta over the climate change signal are 4.1% and 2.7% correspondingly (Table A.2).

The impacts of neglecting this signal on the precipitation diurnal cycle analysis is unknown and should be analyzed in future studies. An analysis of a set of simulations equivalent to CONUS I would be necessary and unfortunately, we don't have the resources to perform such simulations for this revision. However, we think that this limitation should not invalidate this study, as one could expect that: 1) using a large model domain has the advantage of decreasing the dependence of the regional climate integration to the lateral boundary conditions in the interior of the domain, and 2) summer precipitation is strongly influence by local scale processes due to the predominant weak large-scale forcing.

Table A.1 Selection from three GCMs.

GCMs	CanESM2 CSIRO-Mk3-6-0 GFDL-ESM2M
Ensemble	r1i1p1
Future scenario	RCP 8.5
Time step	6 hours
Time period	Historical: 1976-2005 Future: 2076-2100
Month	July
Variables	Air temperature (ta) Specific humidity (hus)
Vertical levels	900, 850, 700, 500 and 300 hPa

Table A.2 Summary of the change between future and historical simulations in July and the difference on the variable and constant delta. The bottom rows show the average of absolute difference between the variable and constant deltas and the percentage over the 3 GCM average, and the maximum distance of the delta difference and the percentage over the 3 GCM average delta.

Future-historical = 6h-variable delta- c.f. Fig. A - 4 and A - 6			
	Statistics	Air temperature (ºC)	Specific humidity (g kg^{-1})
Models average	Minimum	1.575	-0.037
	Maximum	7.897	6.725
	Average	4.532	2.727

Delta difference (variable delta - constant delta)- c.f. Fig. A - 5 and A - 7			
	Time (hours)	Air temperature (ºC)	Specific humidity (g kg^{-1})
Models average	0	-0.231	0.117
	6	0.148	-0.064
	12	0.220	-0.082
	18	-0.137	0.029
	Average absolute difference	0.184	0.073
	% over the average	4.1%	2.7%
	Maximum distance	0.451	0.199
	% over the average	10.0%	7.3%

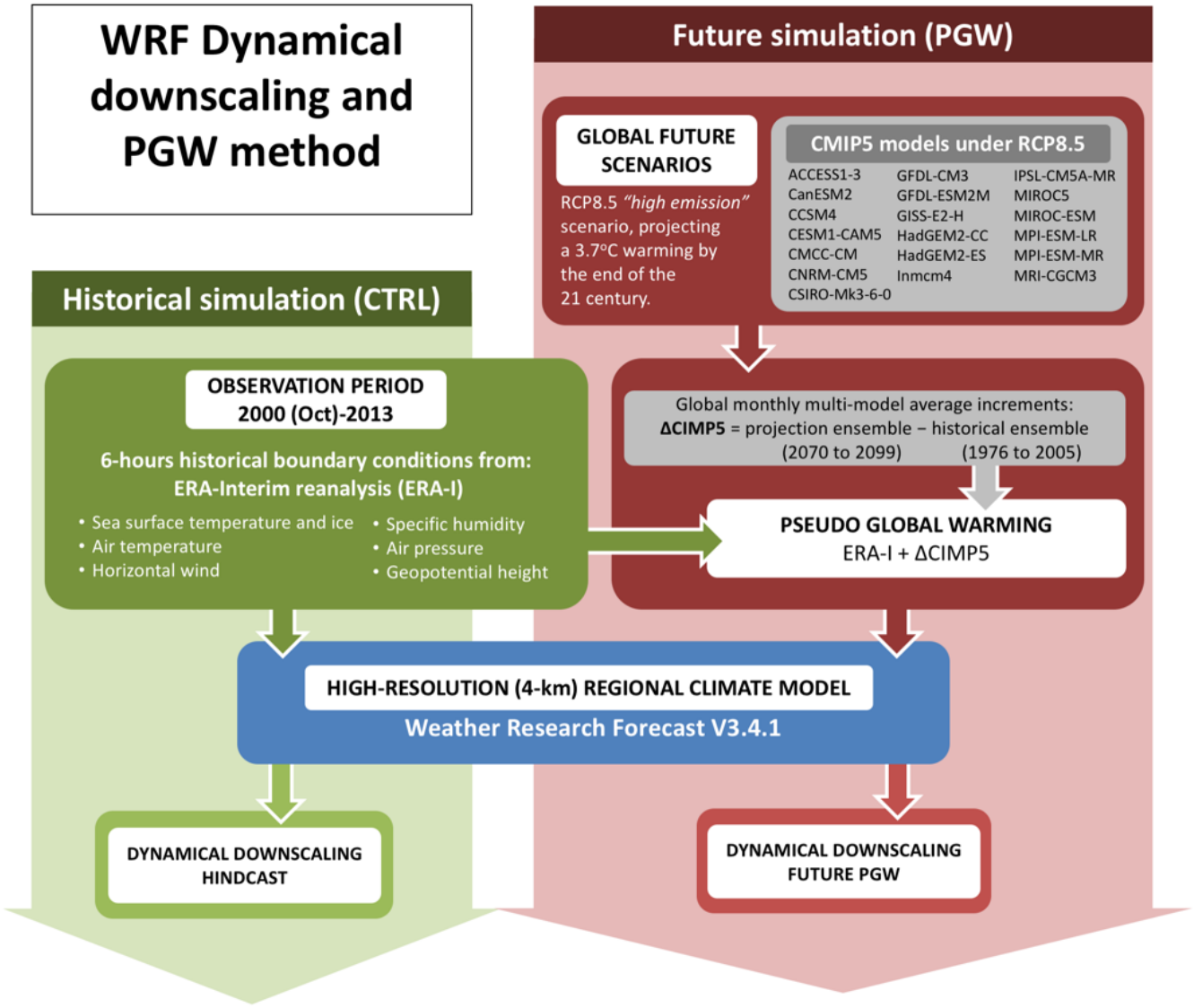

Figure A - 1 Methodology of CONUS I simulations. The historical simulation is on the green column and the future climate simulation is presented in the red column.

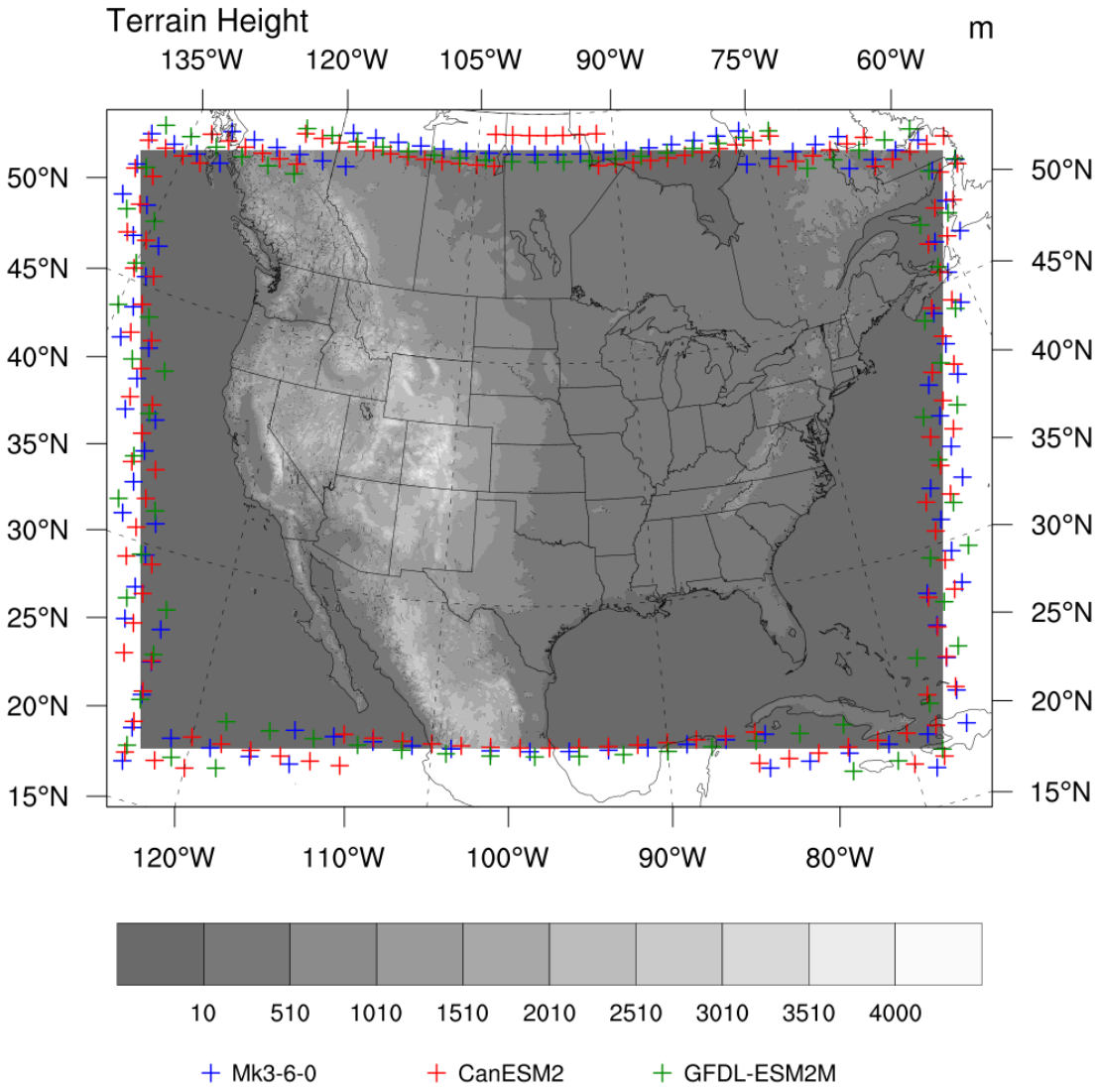

Figure A - 2 CONUS I domain and the location of the closest grid points from GCMs.

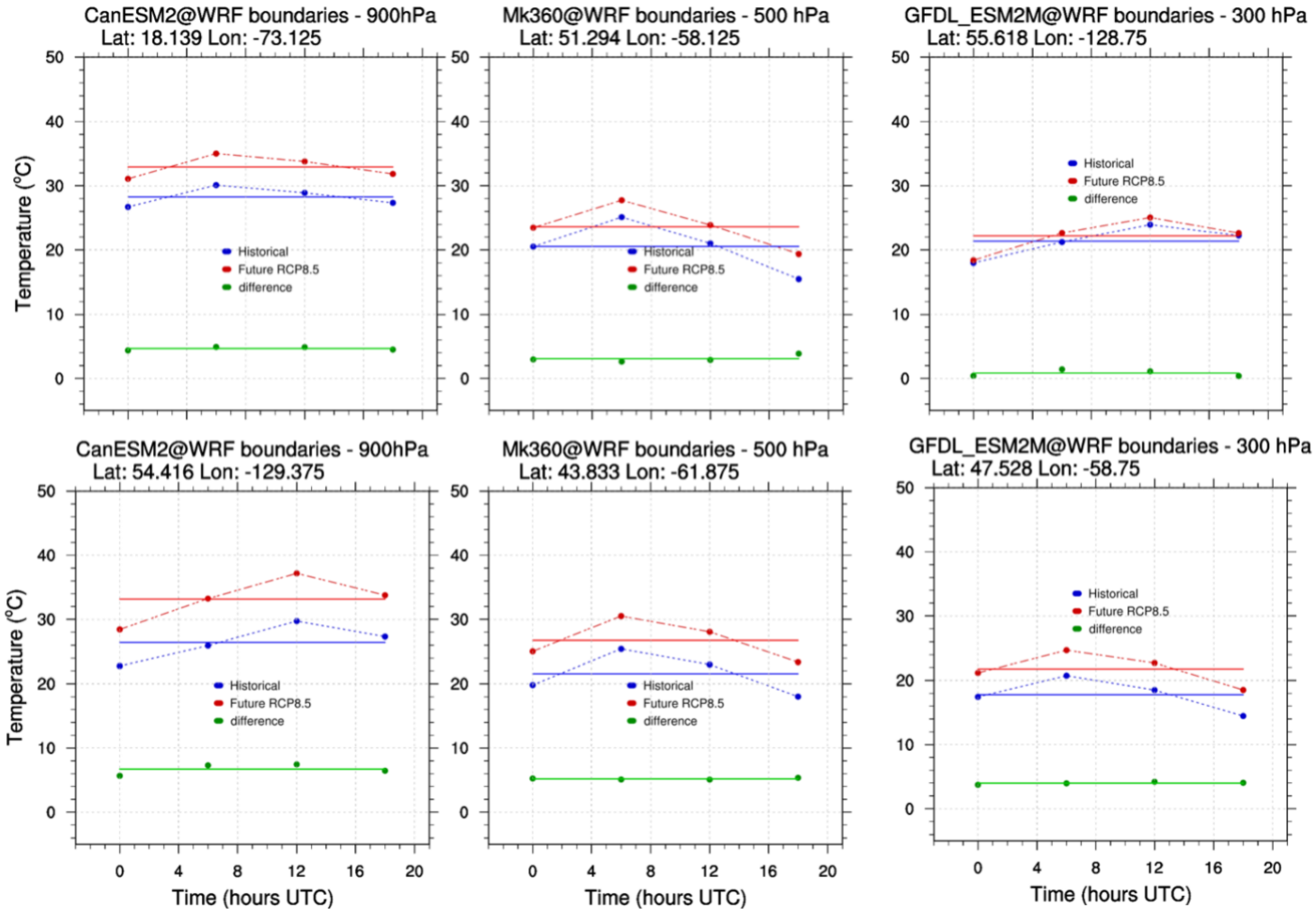

Figure A - 3 Example of the diurnal cycle of air temperature on different GCMs, coordinates and vertical levels. Blue and red dots represent the historical and the future, correspondingly, while green dots represents the difference of the last two simulations at each 6h time steps, the solid lines represent the average of these 4 hours.

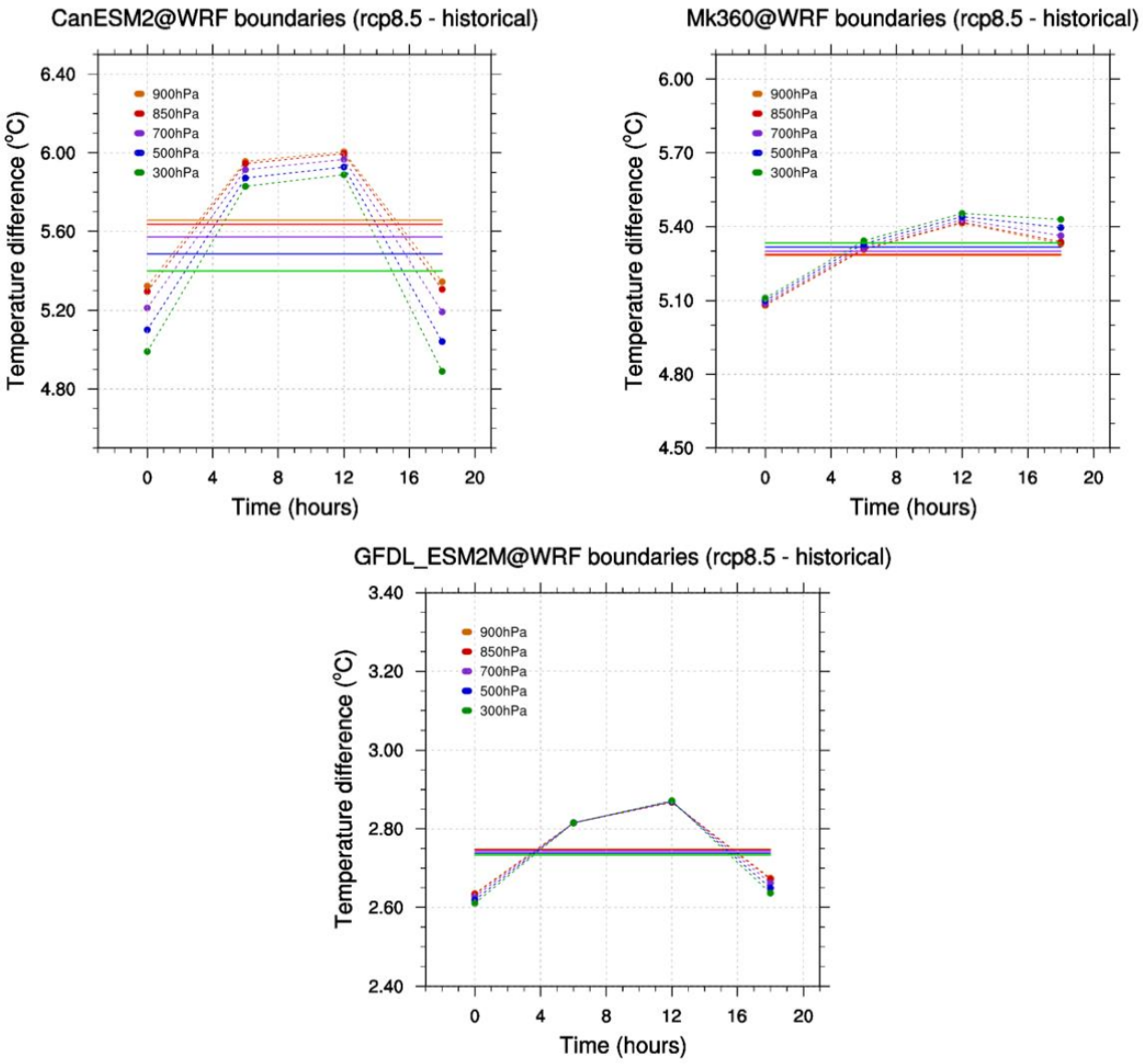

Figure A - 4 Average of air temperature difference between the future and the historical simulations at 5 vertical levels. The average is calculated over all the closest grid points of the corresponding GCM to the WRF boundaries, and over the 30 years period in each simulation. The dots and dashed lines represent the 6h variable diurnal cycle, and the solid line represent the average temperature on the diurnal cycle.

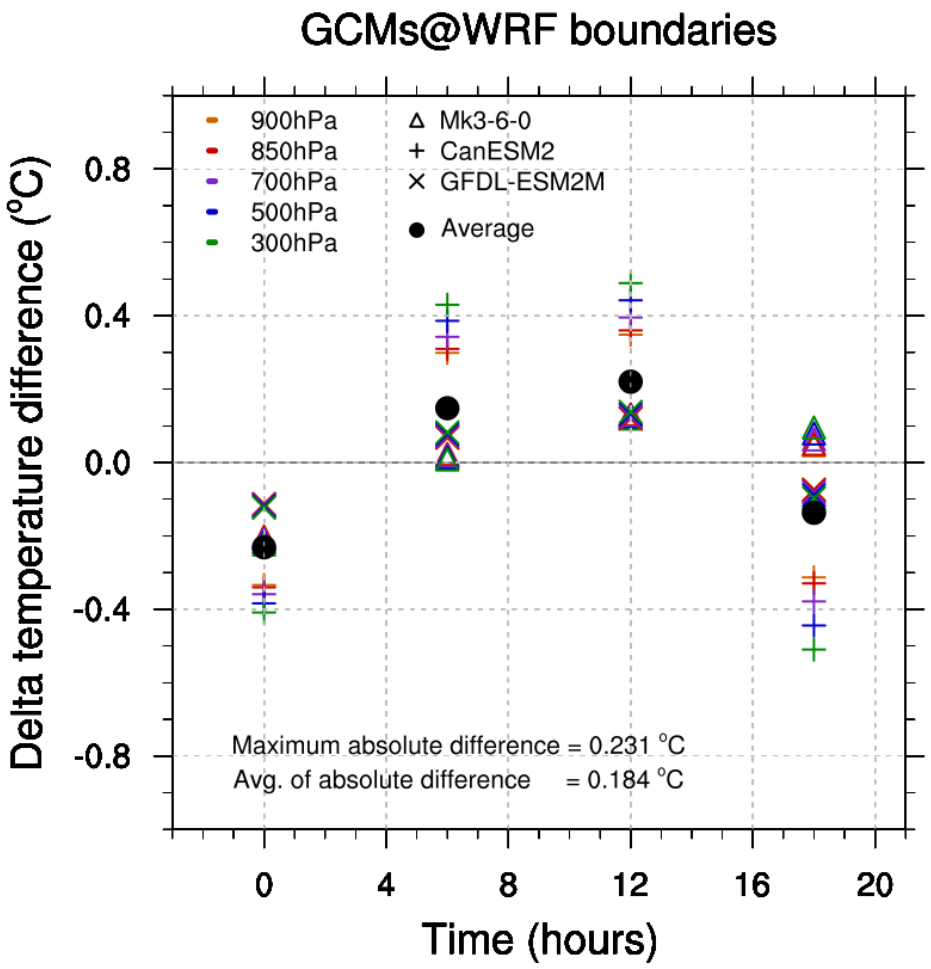

Figure A - 5 Difference between the variable and constant delta temperature (future – historical simulations) for all 3 GCMs and 5 vertical levels. Black dots are the average over the vertical levels and the GCMs.

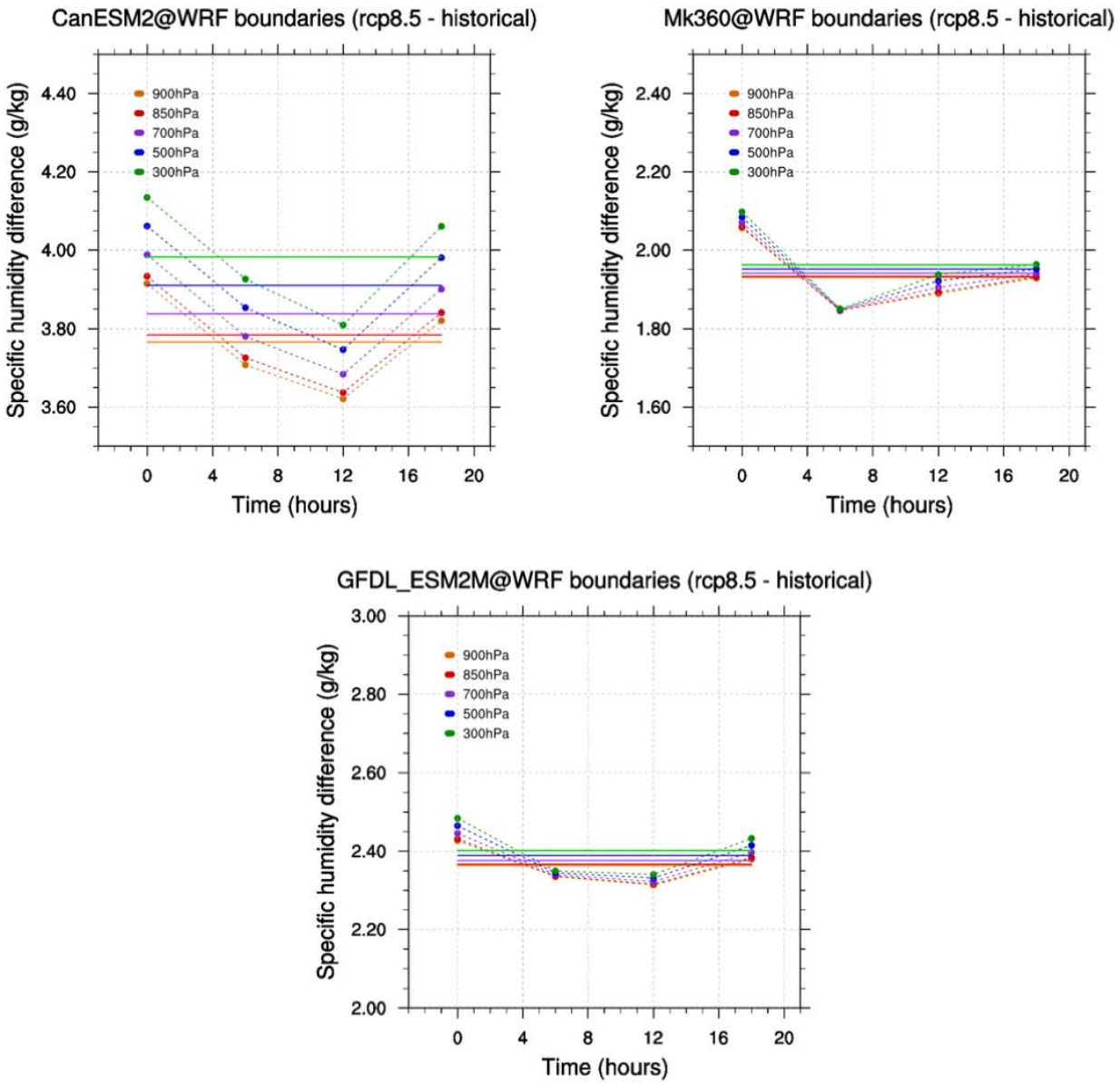

Figure A - 6 Average of specific humidity difference between future and historical simulations at 5 vertical levels. This average is calculated over all closest grid points of the corresponding GCM to WRF boundaries and over the 30 years period in each simulation. Dots and dashed lines represent the 6h variable diurnal cycle, and the solid line represent the monthly average specific humidity on the diurnal cycle.

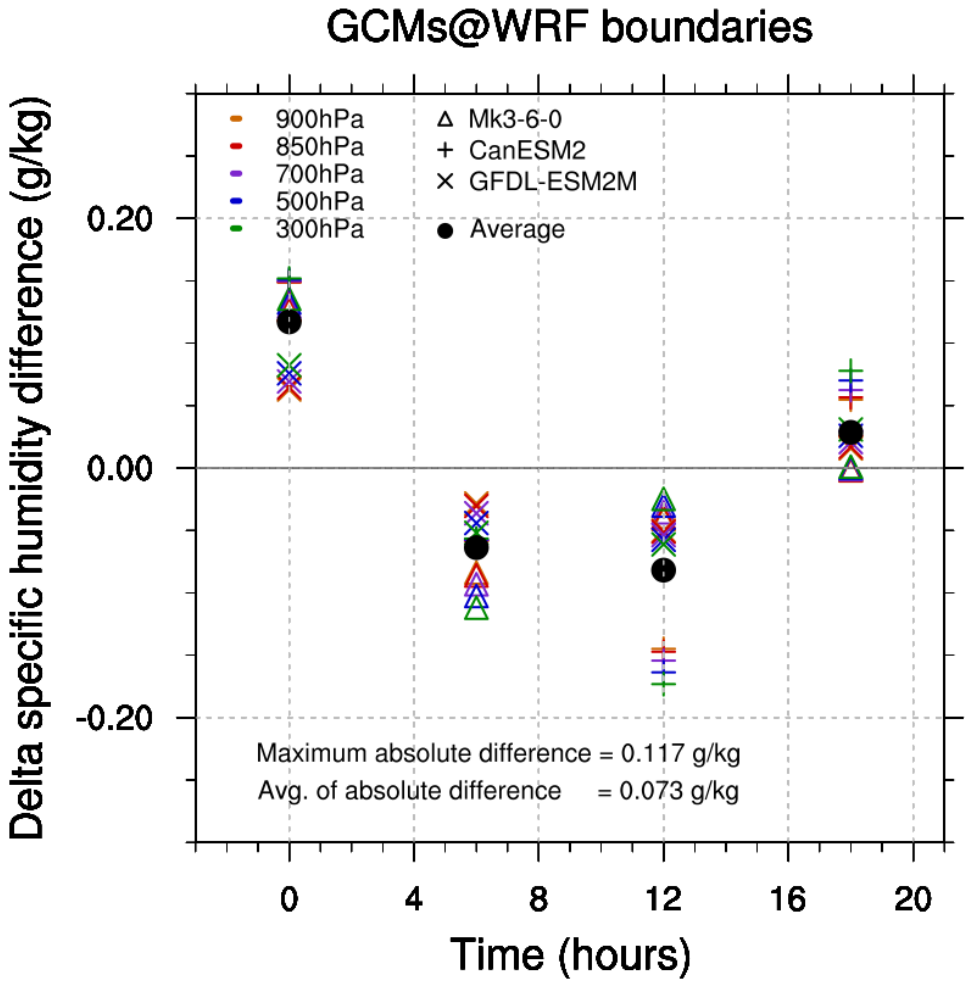

Figure A - 7 Difference between variable and constant delta (future – historical simulations) for 3 GCMs realizations and 5 vertical levels of specific humidity in g kg^{-1}. Black dots are the average over the vertical levels and the GCMs.

Appendix B

This appendix is part of chapter 3.

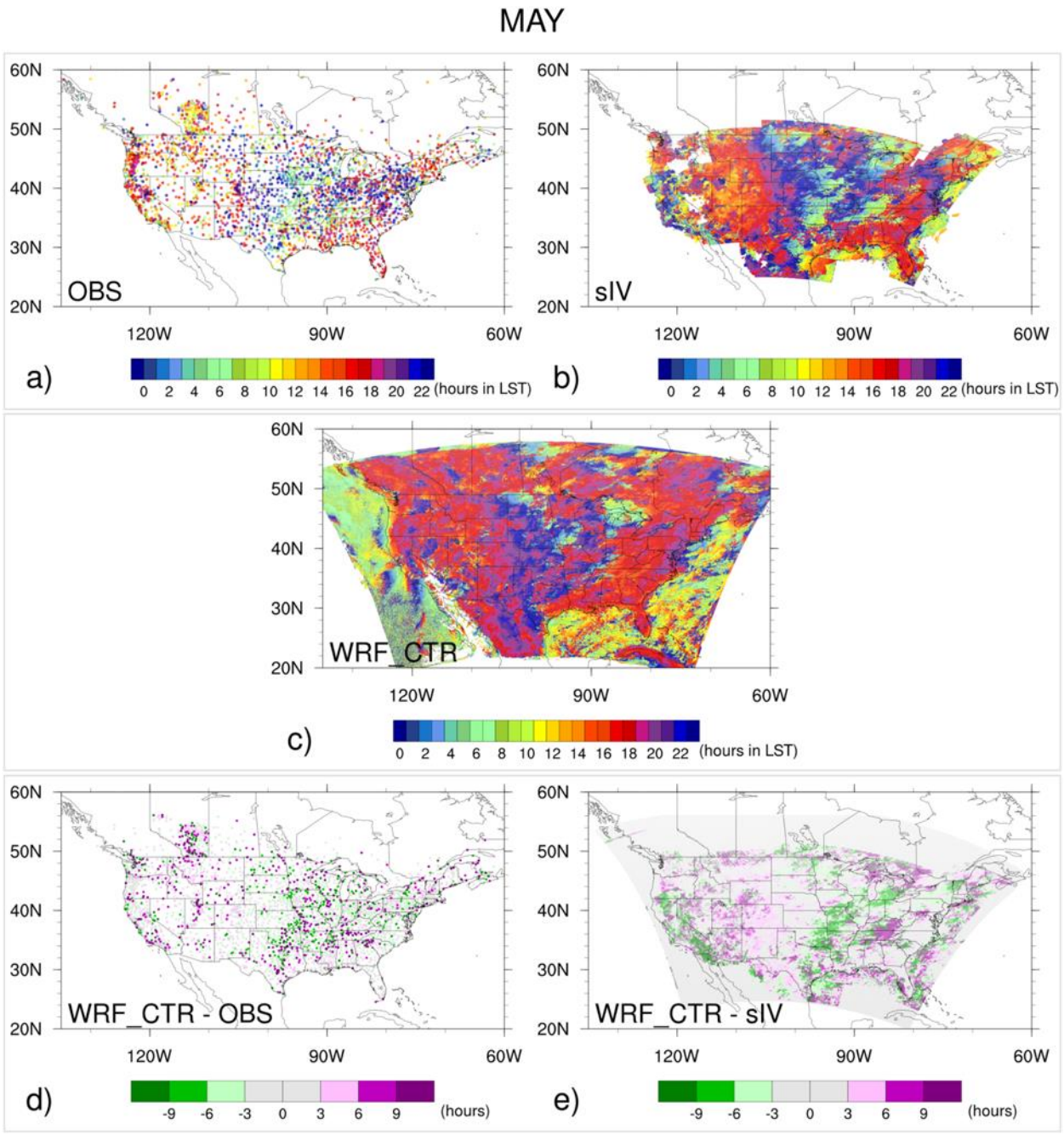

Figure B - 1 The maps show the precipitation maximum timing from two-harmonic fit of the diurnal cycle (in hours at Local Solar Time) in May. The two upper panels are: observations (OBS) and stage IV (sIV). The middle panel is for the WRF historical runs (WRF). The two bottom panels show the differences between OBS and WRF (left), and between sIV and WRF (right).

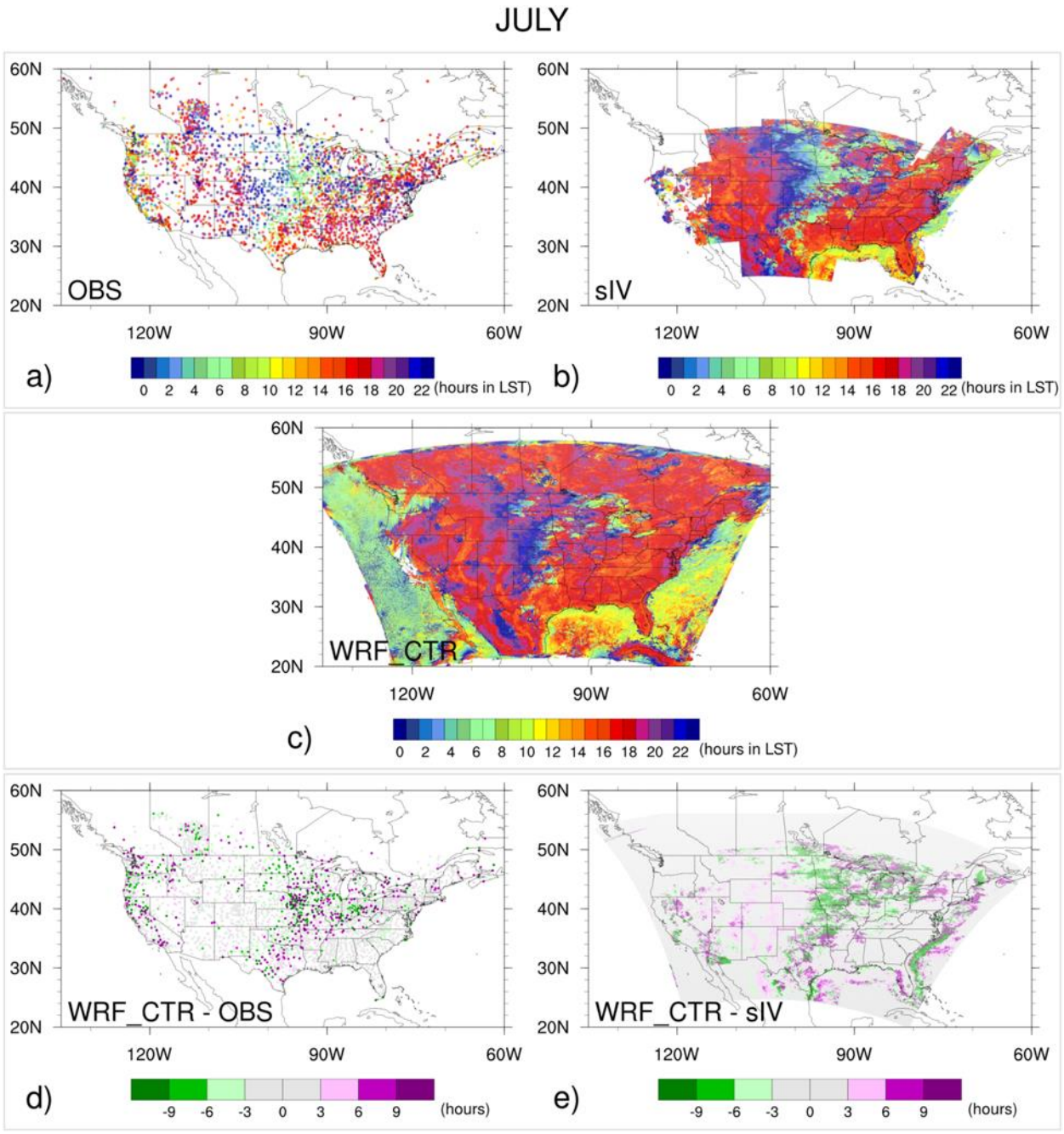

Figure B - 2 The maps show the precipitation maximum timing from two-harmonic fit of the diurnal cycle (in hours at Local Solar Time) in July. The two upper panels are: observations (OBS) and stage IV (sIV). The middle panel is for the WRF historical runs (WRF). The two bottom panels show the differences between OBS and WRF (left), and between sIV and WRF (right).

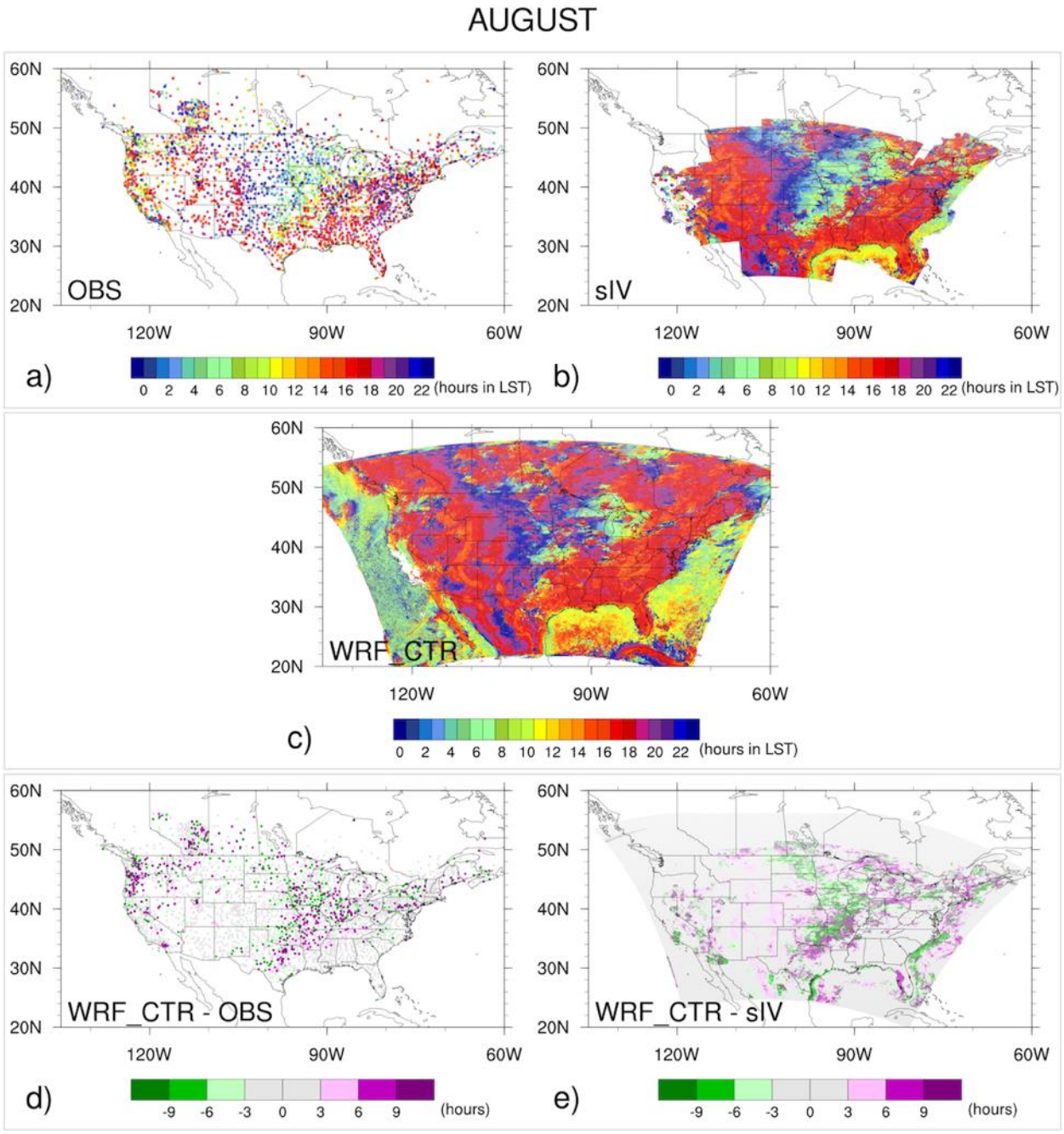

Figure B - 3 The maps show the precipitation maximum timing from two-harmonic fit of the diurnal cycle (in hours at Local Solar Time) in August. The two upper panels are: observations (OBS) and stage IV (sIV). The middle panel is for the WRF historical runs (WRF). The two bottom panels show the differences between OBS and WRF (left), and between sIV and WRF (right).

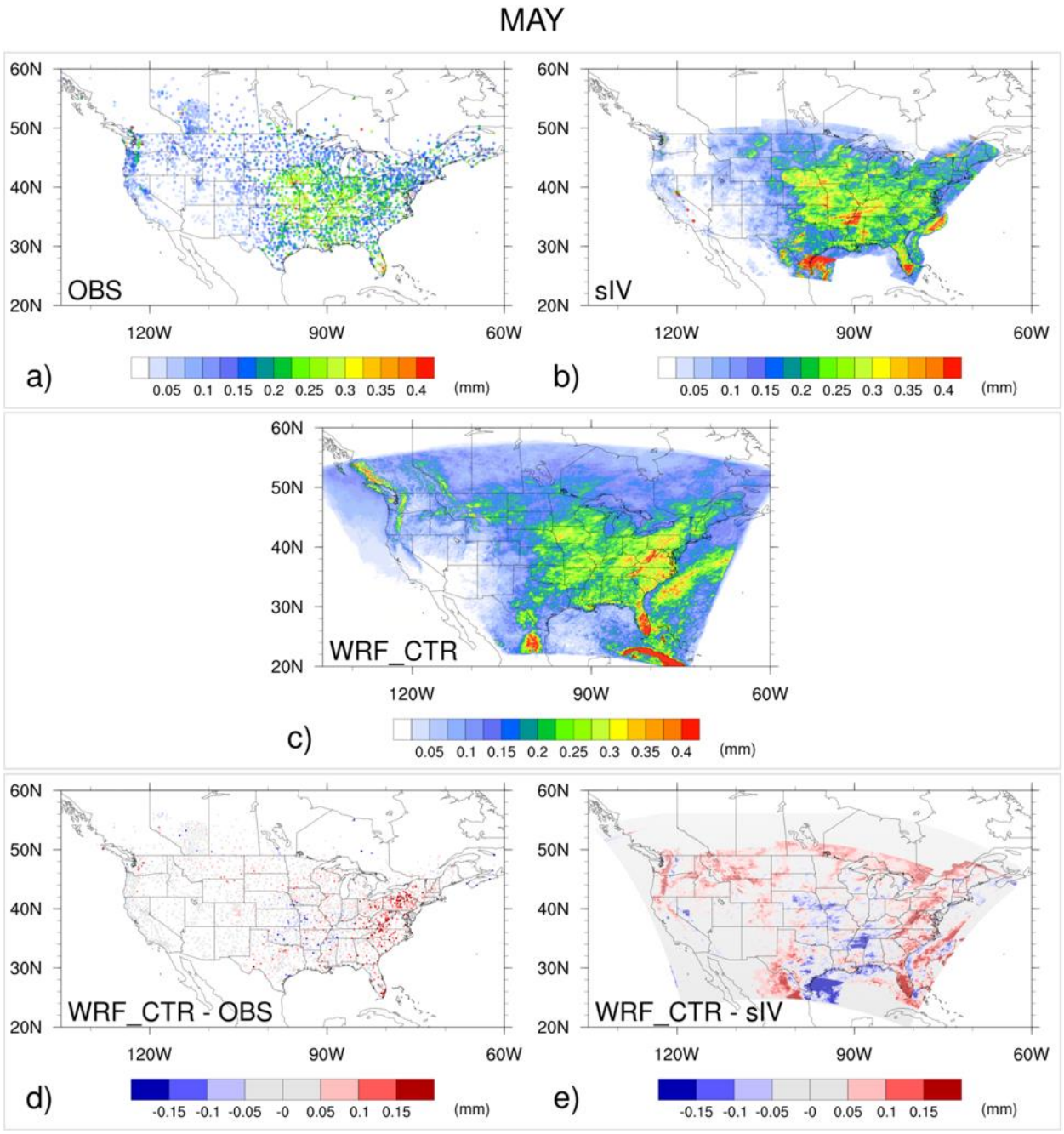

Figure B - 4 The maps show the maximum precipitation amount from two-harmonic fit of the diurnal cycle (in mm) in May. The two upper panels are for: observations (OBS) and stage IV (sIV). The middle panel is for the WRF historical runs (WRF). The two bottom panels show the differences between OBS and WRF (left), and between sIV and WRF (right).

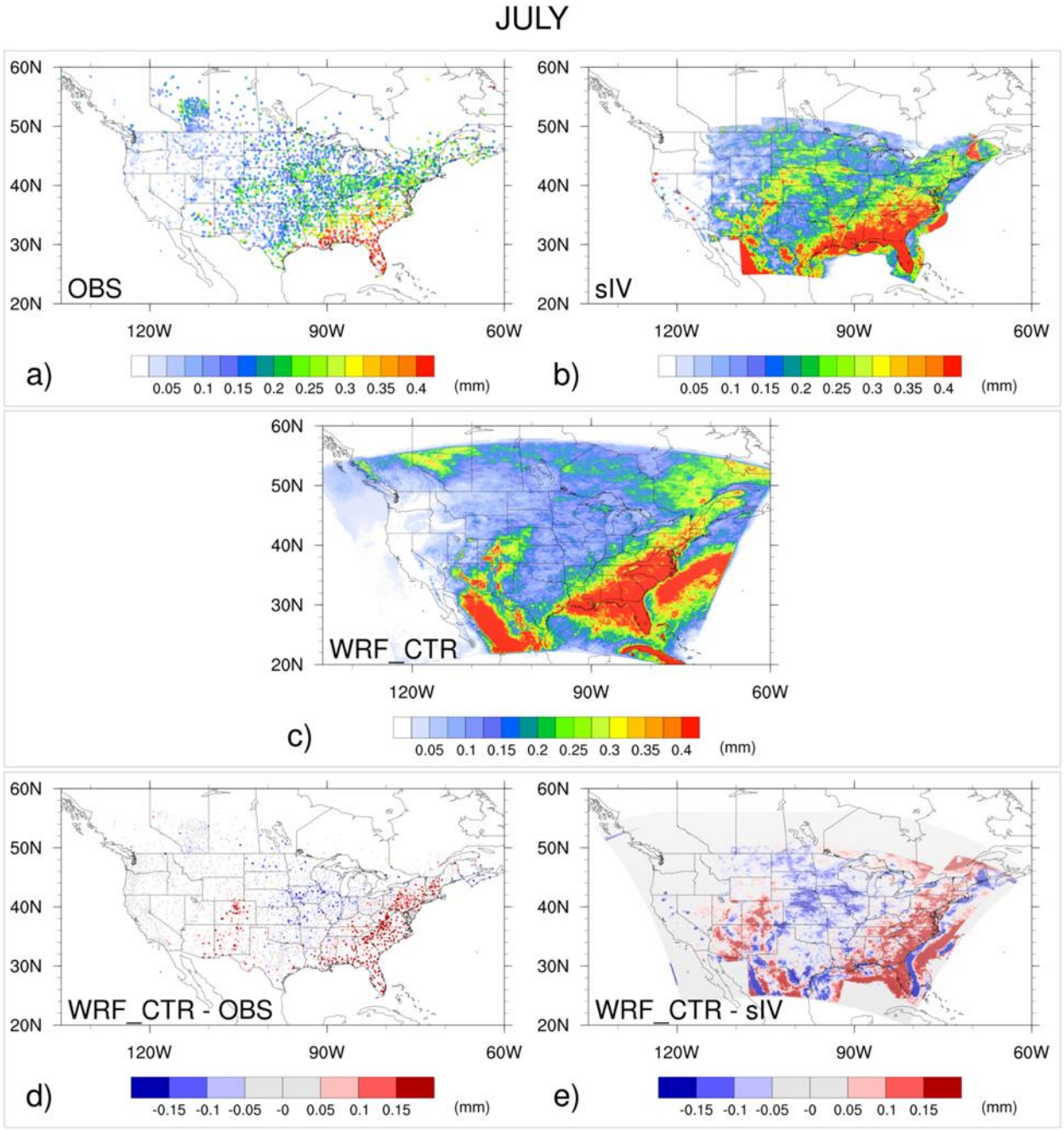

Figure B - 5 The maps show the maximum precipitation amount from two-harmonic fit of the diurnal cycle (in mm) in July. The two upper panels are for: observations (OBS) and stage IV (sIV). The middle panel is for the WRF historical runs (WRF). The two bottom panels show the differences between OBS and WRF (left), and between sIV and WRF (right).

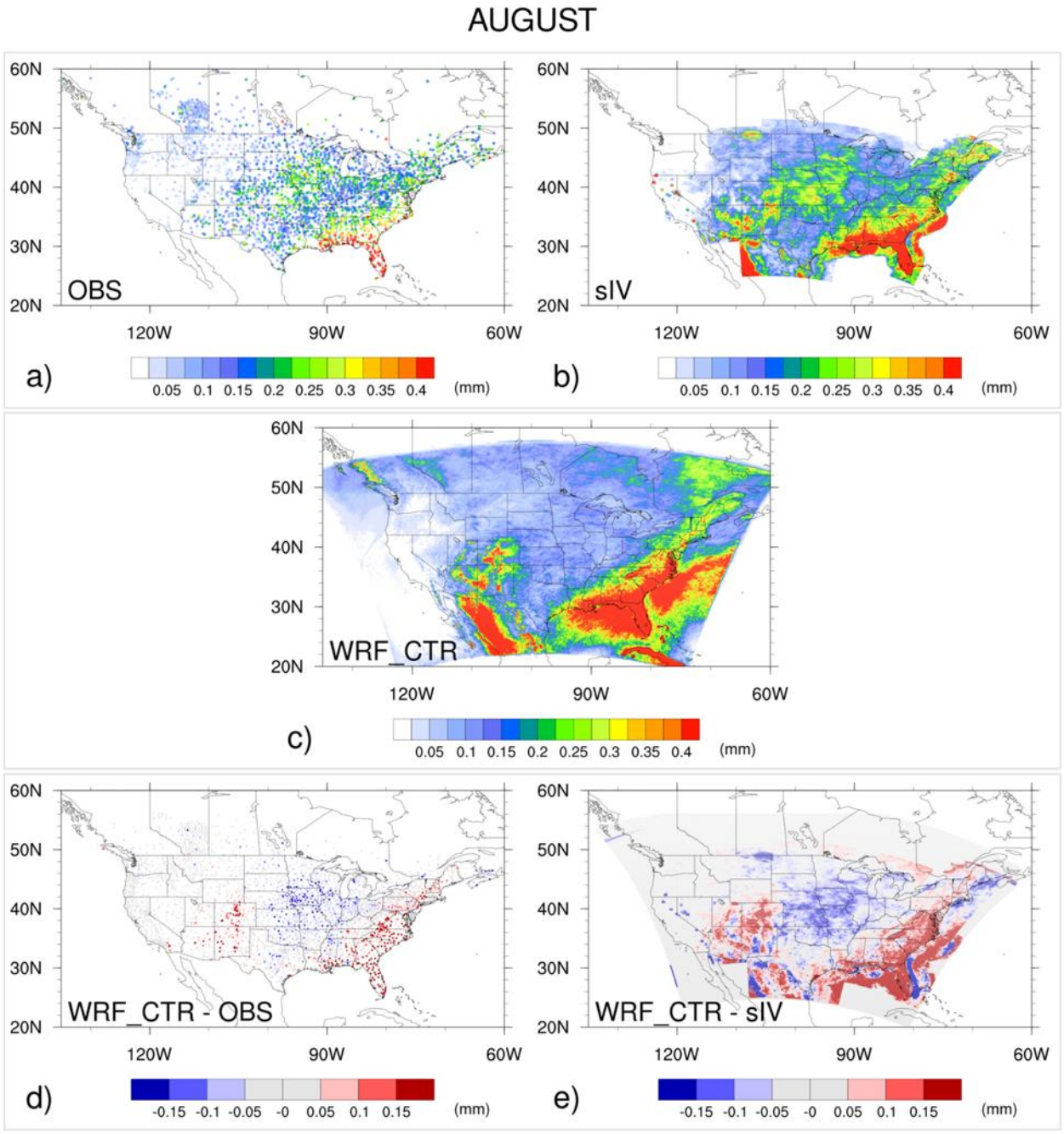

Figure B - 6 The maps show the maximum precipitation amount from the two-harmonic fit of the diurnal cycle (in mm) in August. The two upper panels are for: observations (OBS) and stage IV (sIV). The middle panel is for the WRF historical runs (WRF). The two bottom panels show the differences between OBS and WRF (left), and between sIV and WRF (right).

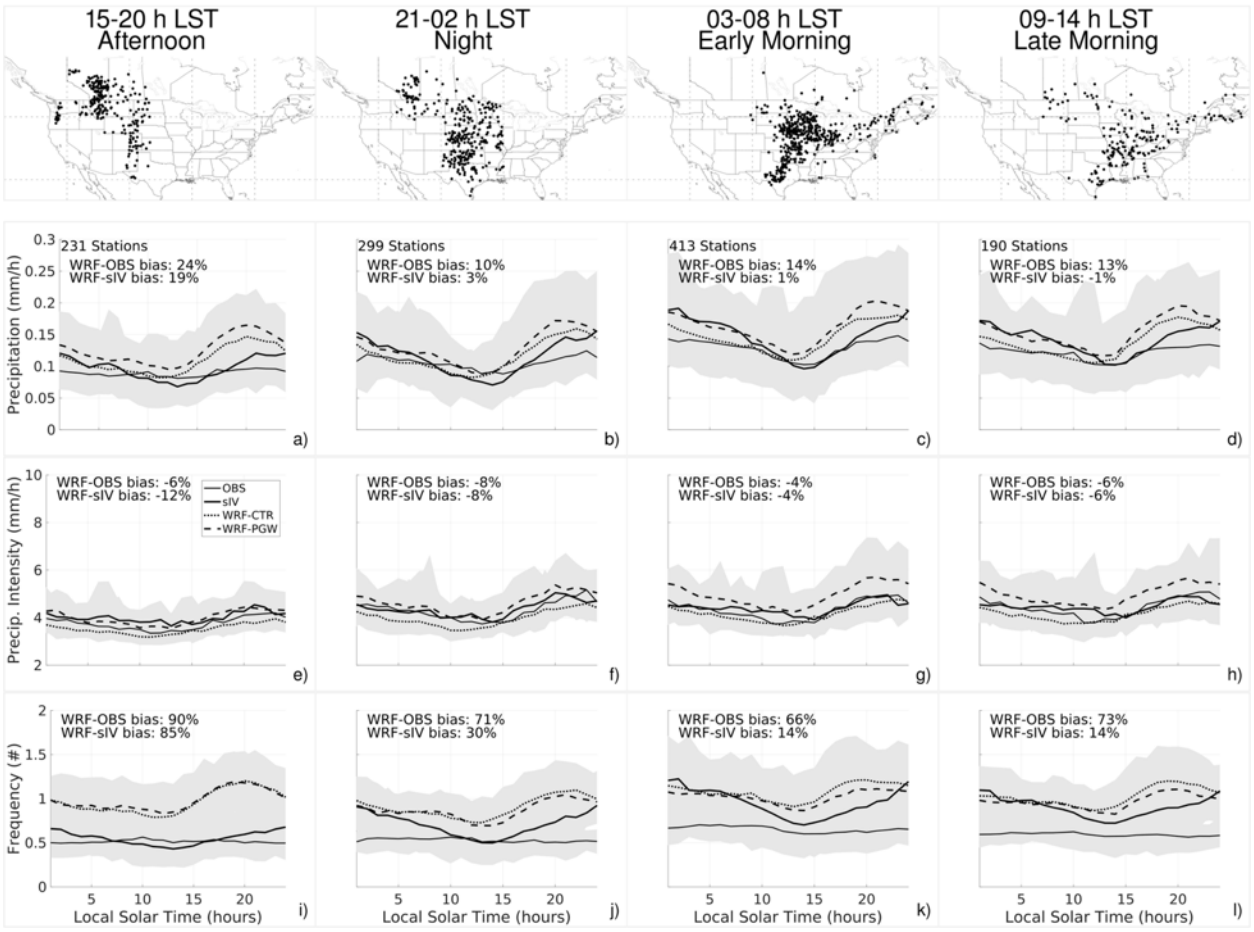

Figure B - 7 Precipitation diurnal cycle from observations (OBS, thin solid line), stage IV (sIV, bold solid line) and WRF outputs for the control (WRF-CTR, dots line) and the future projection (WRF-PGW, dashed line) runs, in May. The sub-regions are defined using the precipitation maximum timing from the two-harmonic fit of the diurnal cycle in June and are limited to the stations (dots in maps at the top) with a maximum precipitation amount from the two-harmonic fit of the diurnal cycle greater than 0.1 mm. The shaded area in the time-series represent the range of the inter-annual variability (of 13 years for OBS, WRF-CTR and WRF-PGW, and 12 years for sIV).

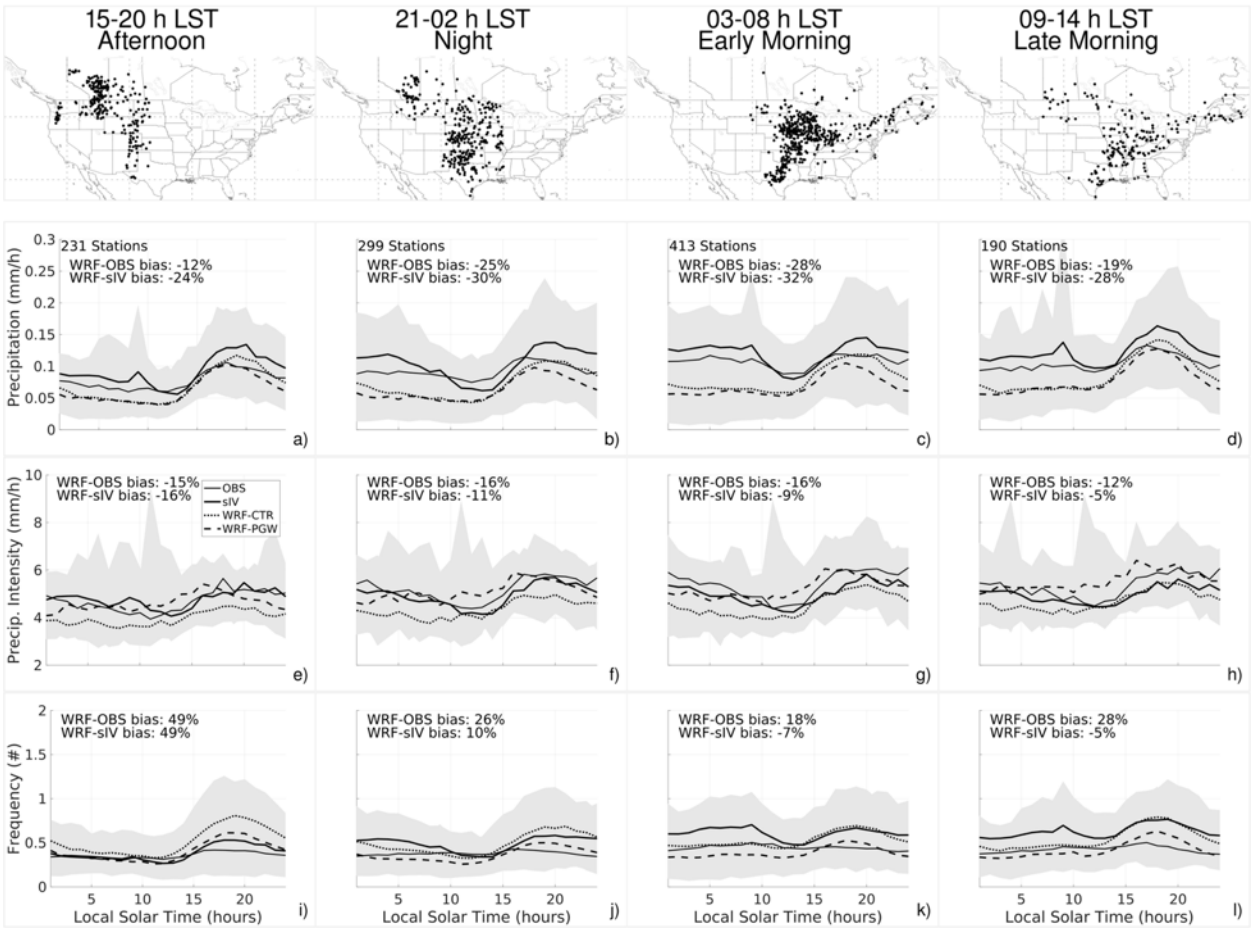

Figure B - 8 Precipitation diurnal cycle from observations (OBS, thin solid line), stage IV (sIV, bold solid line) and WRF outputs for the control (WRF-CTR, dots line) and the future projection (WRF-PGW, dashed line) runs, in July. The sub-regions are defined using the precipitation maximum timing from the two-harmonic fit of the diurnal cycle in June and are limited to the stations (dots in maps at the top) with a maximum precipitation amount from the two-harmonic fit of the diurnal cycle greater than 0.1 mm. The shaded area in the time-series represent the range of the inter-annual variability (of 13 years for OBS, WRF-CTR and WRF-PGW, and 12 years for sIV).

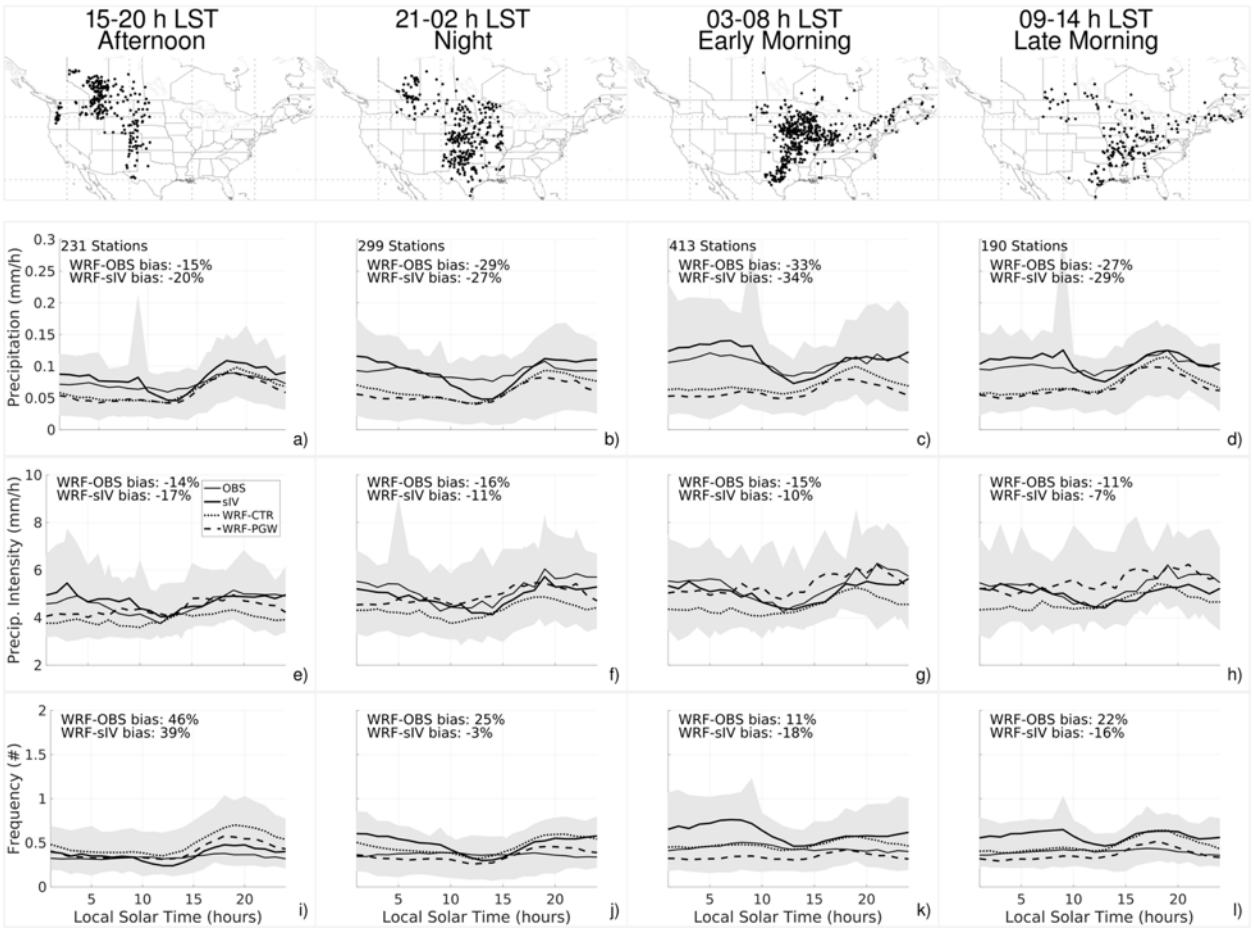

Figure B - 9 Precipitation diurnal cycle from observations (OBS, thin solid line), stage IV (sIV, bold solid line) and WRF outputs for the control (WRF-CTR, dots line) and the future projection (WRF-PGW, dashed line) runs, in August. The sub-regions are defined using the precipitation maximum timing from the two-harmonic fit of the diurnal cycle in June and are limited to the stations (dots in maps at the top) with a maximum precipitation amount from the two-harmonic fit of the diurnal cycle greater than 0.1 mm. The shaded area in the time-series represent the range of the inter-annual variability (of 13 years for OBS, WRF-CTR and WRF-PGW, and 12 years for sIV).

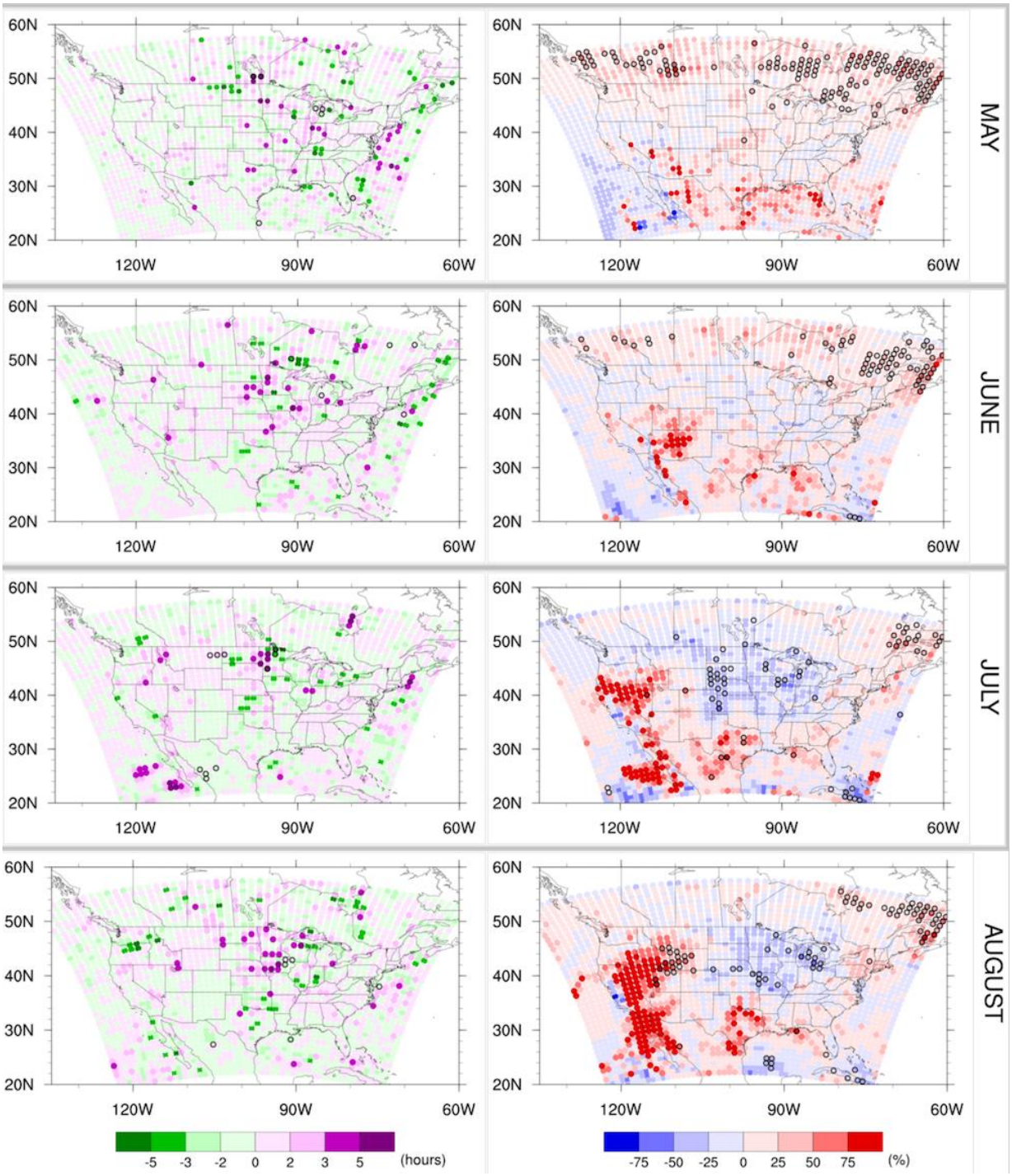

Figure B - 10 The maps show the difference between WRF-PGW and WRF-CTR for May, June, July and August. The left column presents the precipitation maximum timing from the two-harmonic fit of the diurnal cycle (in hours at Local Solar Time). The right column presents the precipitation maximum amount from the two-harmonic fit of the diurnal cycle (%). The spatial grid is reduced to one filled circle every 25 grids cells from the model (circle distance ~100-km). The hollow black circles highlight the locations with at least 20% of the grid points used show statistical significance at 5% level using the Mann-Whitney rank sum test.

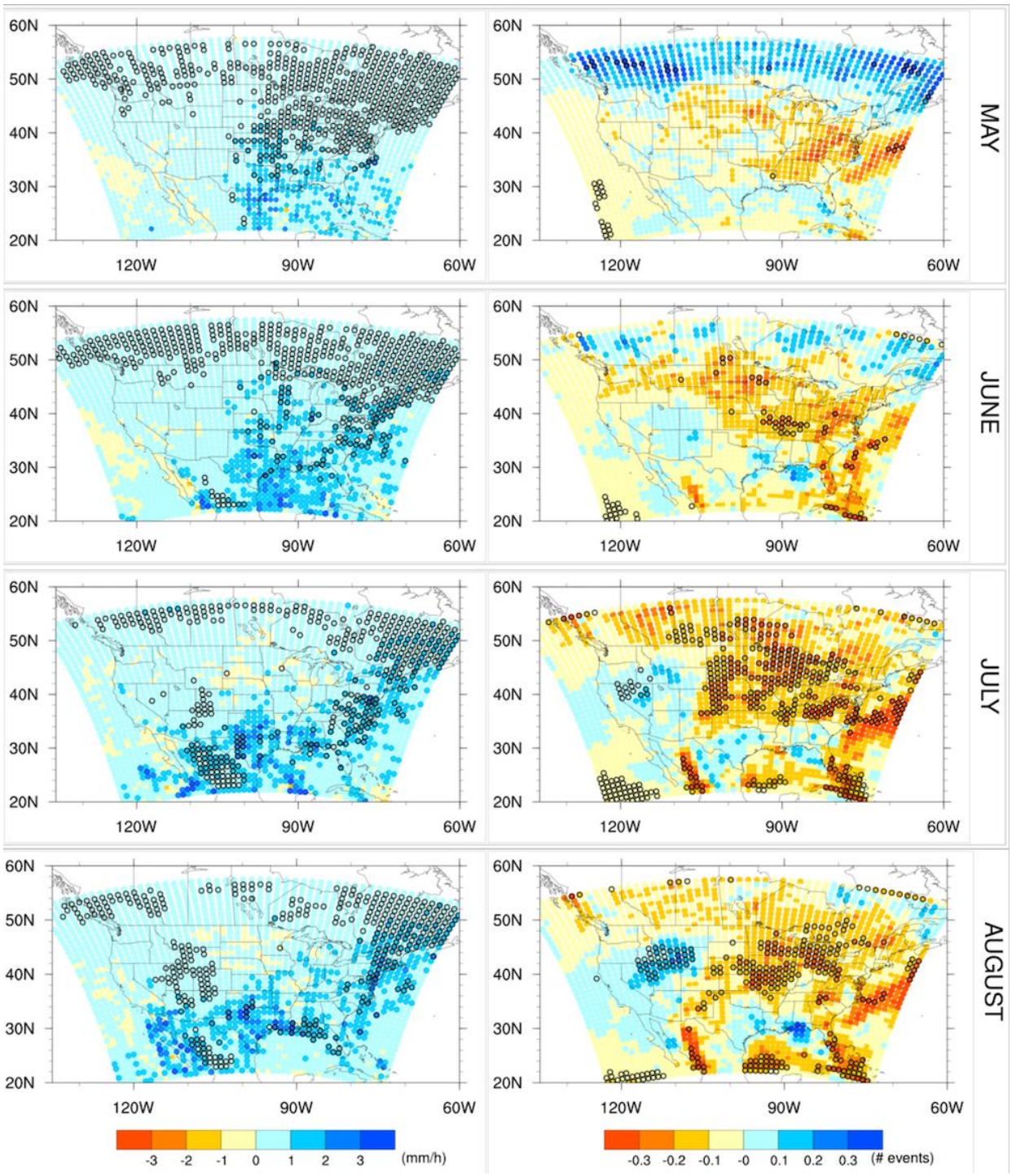

Figure B - 11 The maps show the difference between WRF-PGW and WRF-CTR for May, June, July and August. The left column presents the precipitation intensity (mm h^{-1}) and the right column presents the precipitation frequency (# of events). The spatial grid is reduced to one filled circle every 25 grids cells from the model (circle distance ~100-km). The hollow black circles highlight the locations with at least 20% of the grid points used show statistical significance at 5% level using the Mann-Whitney rank sum test.

Appendix C

This appendix is part of chapter 4.

Table C.1 Dates and main features of the selected precipitation events on the WRF-CTR.

Initial date	Convective initiation	Final date	Storm duration	Maximum dryline magnitude
(yyyymmdd)	(h in UTC)	(yyyymmdd)	(days)	(g kg^{-1} km^{-1})
20010527	0	20010530	4	0.48
20010603	0	20010608	6	0.39
20010614	0	20010618	5	0.42
20010623	0	20010702	10	0.63
20020503	21	20020508	6	0.27
20020613	21	20020620	8	0.41
20020717	3	20020721	5	0.48
20020829	18	20020901	4	0.40
20030525	18	20030527	3	0.51
20030607	18	20030614	8	0.33
20030619	21	20030624	6	0.49
20030804	3	20030813	10	0.58
20040803	0	20040808	6	0.67
20050723	0	20050725	3	0.64
20060519	21	20060530	12	0.58
20060607	0	20060612	6	0.33
20060810	0	20060812	3	0.52
20070603	0	20070607	5	0.60
20070608	3	20070619	12	0.32
20070628	3	20070630	3	0.54
20070714	0	20070720	7	0.50
20070808	3	20070813	6	0.31
20080601	6	20080612	12	0.20
20080621	3	20080623	3	0.48
20080630	21	20080707	8	0.42
20080818	0	20080822	5	0.63
20090511	0	20090515	5	0.31
20090705	0	20090716	12	0.53
20090801	21	20090808	8	0.70
20100717	0	20100723	7	0.54
20110606	0	20110609	4	0.46
20110706	21	20110717	12	0.42
20120713	0	20120719	7	0.50
20120813	3	20120815	3	0.38
20130611	0	20130616	6	0.37
20130617	0	20130623	7	0.46
20130704	3	20130707	4	0.87
			Average	0.48
			Maximum	0.20
			Minimum	0.87

Table C.2 Dates and main features of the selected precipitation events on the WRF-PGW.

Initial date	Convective initiation	Final date	Storm duration	Maximum dryline magnitude
(yyyymmdd)	(h in UTC)	(yyyymmdd)	(days)	(g kg^{-1} km^{-1})
20010527	0	20010530	4	0.34
20010623	0	20010702	10	0.86
20010727	3	20010730	4	0.63
20010818	0	20010820	3	0.79
20020604	0	20020606	3	0.50
20020613	21	20020620	8	0.35
20020730	21	20020803	5	0.31
20030619	21	20030624	6	0.66
20040503	21	20040506	4	0.37
20040526	21	20040602	8	0.40
20040628	21	20040705	8	0.44
20050530	21	20050620	22	0.35
20050621	0	20050703	13	0.76
20060709	21	20060714	6	0.74
20060728	3	20060802	6	0.45
20070604	0	20070607	4	0.69
20070609	6	20070613	5	0.37
20070803	21	20070806	4	0.52
20070808	21	20070811	4	0.41
20080531	21	20080620	21	0.44
20080701	3	20080707	7	0.75
20090518	0	20090522	5	0.39
20090620	21	20090623	4	0.40
20090705	0	20090715	11	0.52
20100526	0	20100529	4	0.42
20100614	21	20100619	6	0.70
20110606	3	20110609	4	0.62
20110706	21	20110716	11	0.57
20120713	0	20120719	7	0.63
20120721	0	20120731	11	0.66
20130611	21	20130616	6	0.45
20130617	0	20130623	7	0.54
20130704	21	20130708	5	0.86
20130709	0	20130715	7	0.68
			Average	0.55
			Maximum	0.31
			Minimum	0.86

Appendix D

This appendix is part of chapter 4.

Results of the WRF-CTR validation against the UNSTABLE during one dryline event

On the dryline event on July 2008, one surface weather station is validated against the WRF-CTR (EA3, located on the yellow triangle on Figure D - 1a). The temporal evolution for three days (form July 12th until July 14th of 2008) was compared with the closest grid point from the model (Figure D - 2). The simulation was able to capture the temperature diurnal cycle (Figure D - 2a) with a systematic warm bias of 2°C. The air pressure is also well represented with a negative bias of 4 hPa. The moisture variables, dewpoint temperature and the relative humidity Figure D - 2b), are underestimated on the model, consistently with the low-level specific humidity maps (Figure D - 1). The simulated relative humidity is around 10% to 40% lower that the observed at EA3. The wind (Figure D - 2c) shows an adequate representation, with slightly higher wind magnitude in the model and a close simulated wind direction to the observed one.

The simulation captures the large-scale evolution of the radiosonde's vertical profiles (Figure D - 3). Even though the nocturnal inversion layer is approximately simulated in some locations (not shown), the low-level changes, such as a capping inversion are still not completely reproduced at this grid spacing (Figure D - 3d). One of the four skew-T diagrams is located on the west side of the observed strongest specific humidity gradient (see Figure D - 3a, station MB1). The observations clearly show a drier surface over the MB1 profile, which is consistent with the radiosonde. The others three radiosondes (at MB2, WVX and EA3, in b, c, d) were located on the east side of the specific humidity gradient (the moist side) which is clear in the observed sounding, however the model is representing a drier/warmer atmosphere.

The air temperature profiles are better simulated than the dew point temperature in Figure D - 3, which is consistent with the surface measurements (Figure D - 2). The model normally shows a drier lower atmosphere form the surface up to 830-700 hPa however, above this height, the simulation appears to hold more moisture than the observations. This may be explained by the vertical resolution of the model and of the ERA-Interim as input. Another factor that affect the model performance on reproducing the air temperature and the moisture is the nudging process, which has been applied over the temperature field, but it is not applied over any moisture variable. The performance of smoother modeled profiles, and dry/wet biases at low levels have also been identified in previous studies in the U.S. during convective events (Coniglio et al., 2013; Trier et al., 2015; Weckwerth et al., 2014). This difference at low levels in the vertical profiles directly affect the amount of CAPE, which in turn is critical to the environmental conditions on convective initiation and its further development (Coniglio et al., 2013).

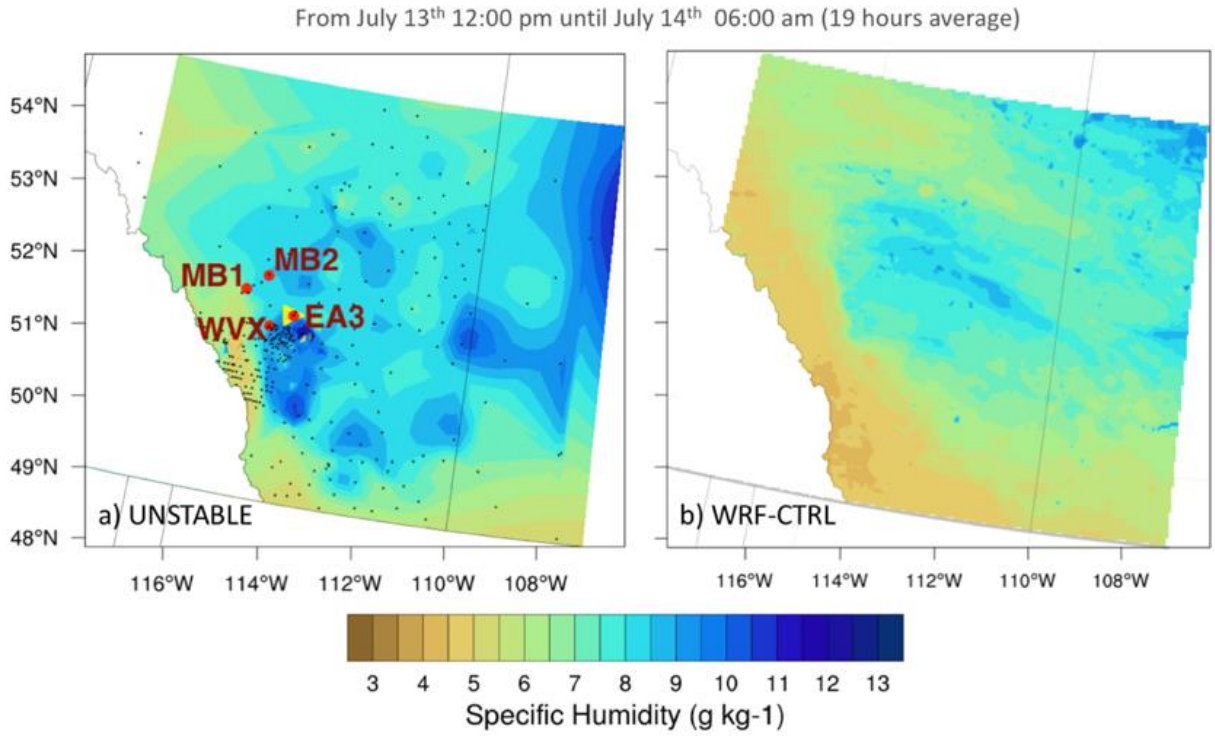

Figure D - 1 Comparison of surface specific humidity in shades for one dryline event in July 2008. a) are presenting an interpolation of observational data from UNSTABLE with black dots showing the data measurements location. b) show the WRF-CTR simulation for the same hour as shown on a). The red dots are the locations where the radiosondes were launched, and the yellow triangle is the surface station we use to validate WRF-CTR.

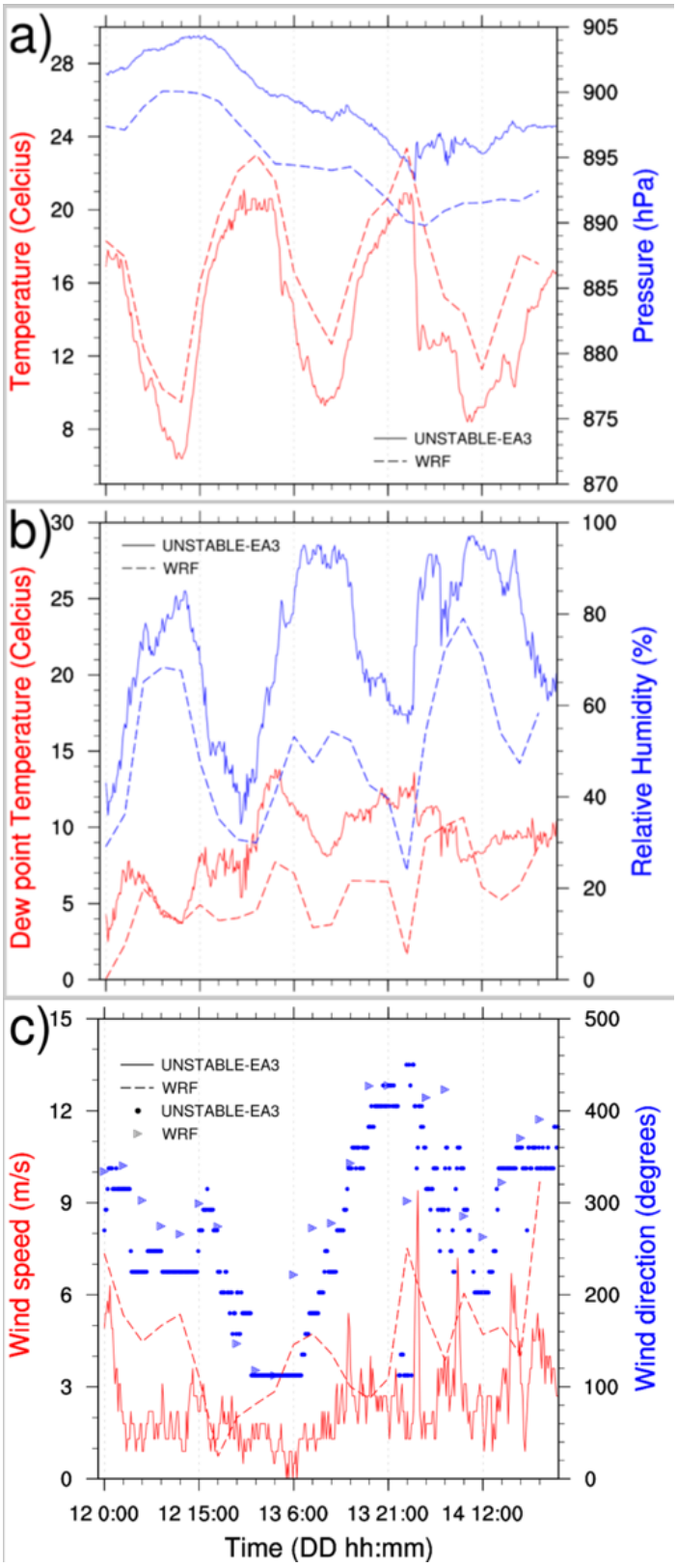

Figure D - 2 Timeseries from the surface weather station EA3. The location of this station in Figure D - 1.

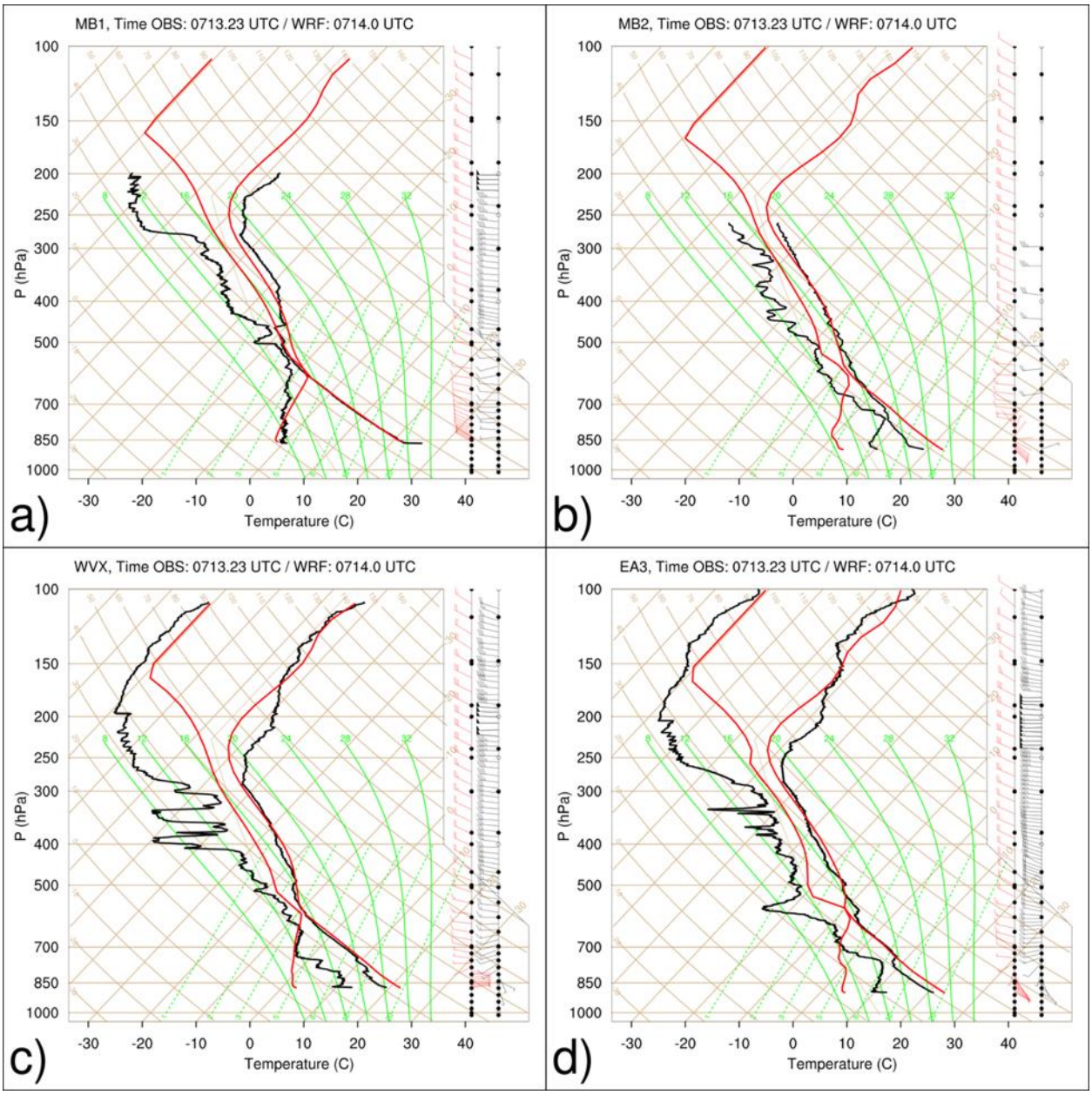

Figure D - 3 Radiosondes comparison between UNSTABLE (black lines and black wind barbs) and WRF-CTR simulation (red lines and red wind barbs) in four locations simultaneously (corresponding to one timestep of the dryline event presented in Figure D - 1). The location of the four stations are presented in red dots Figure D - 1a).

Appendix E

This appendix is part of chapter 4.

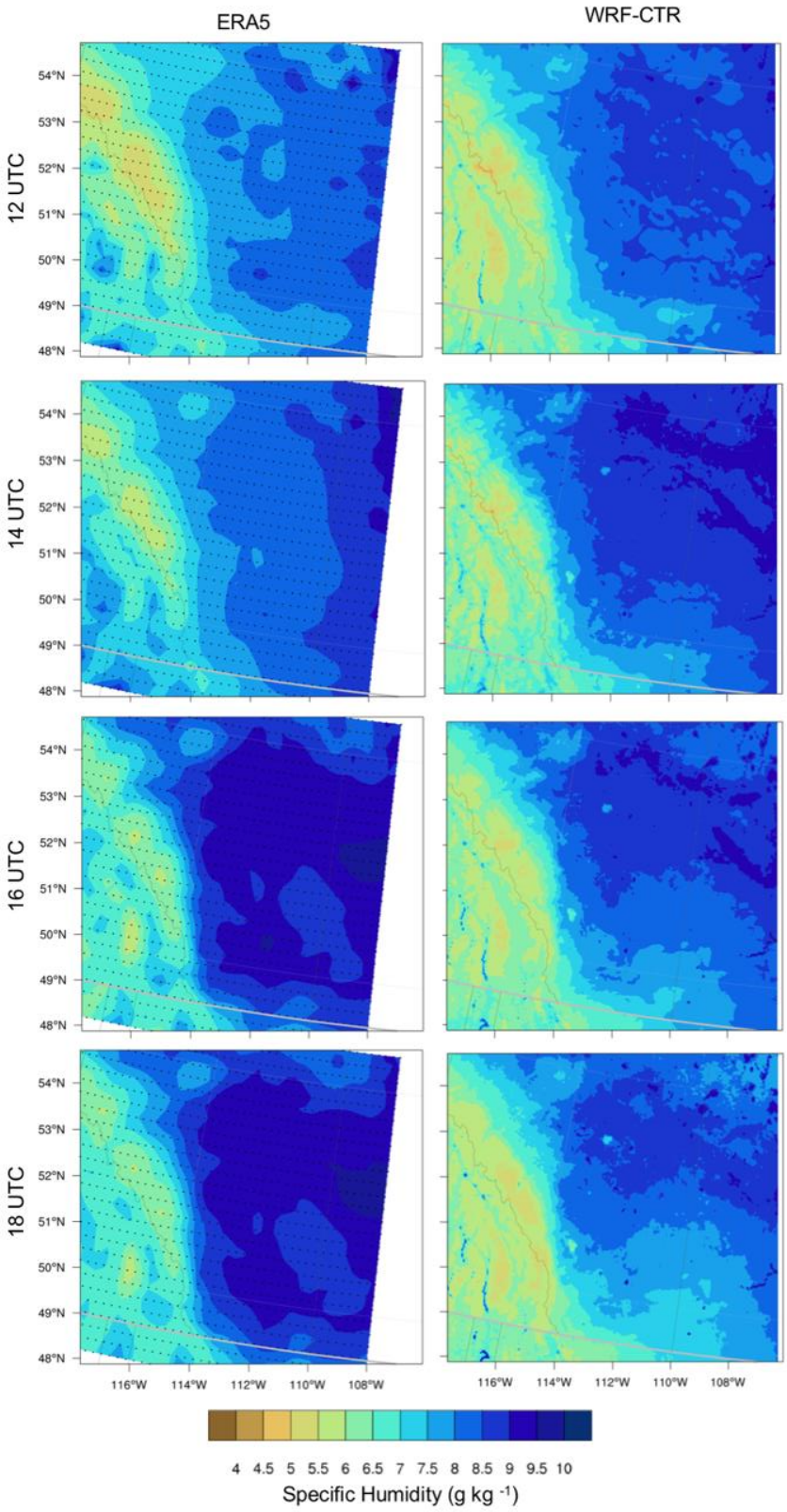

Figure E - 1 Comparison of monthly average of specific humidity in g kg^{-1} between ERA5 and WRF-CTR from 12 UTC until 18 UTC.

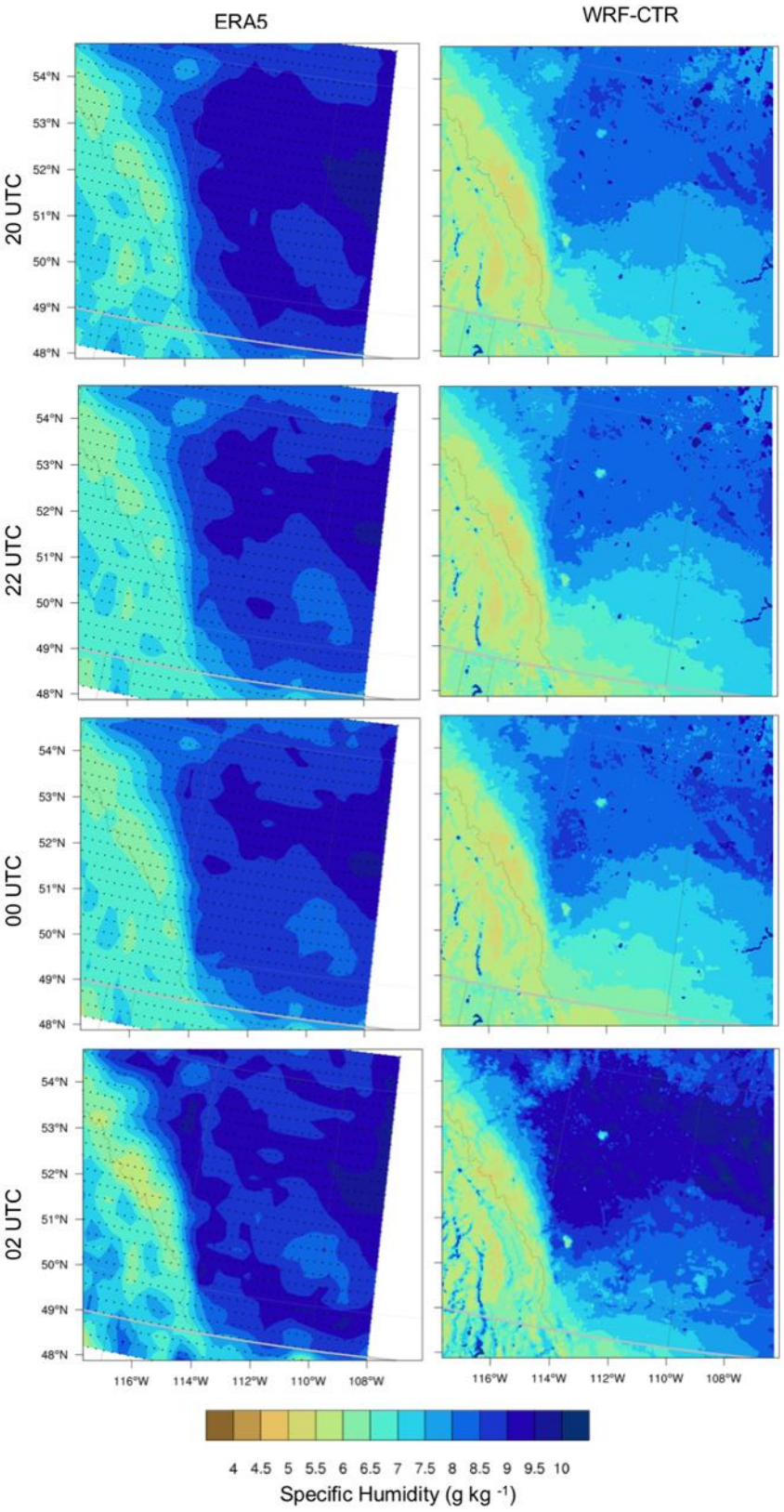

Figure E - 2 Comparison of monthly average of specific humidity in g kg^{-1} between ERA5 and WRF-CTR from 20 UTC until 02 UTC.

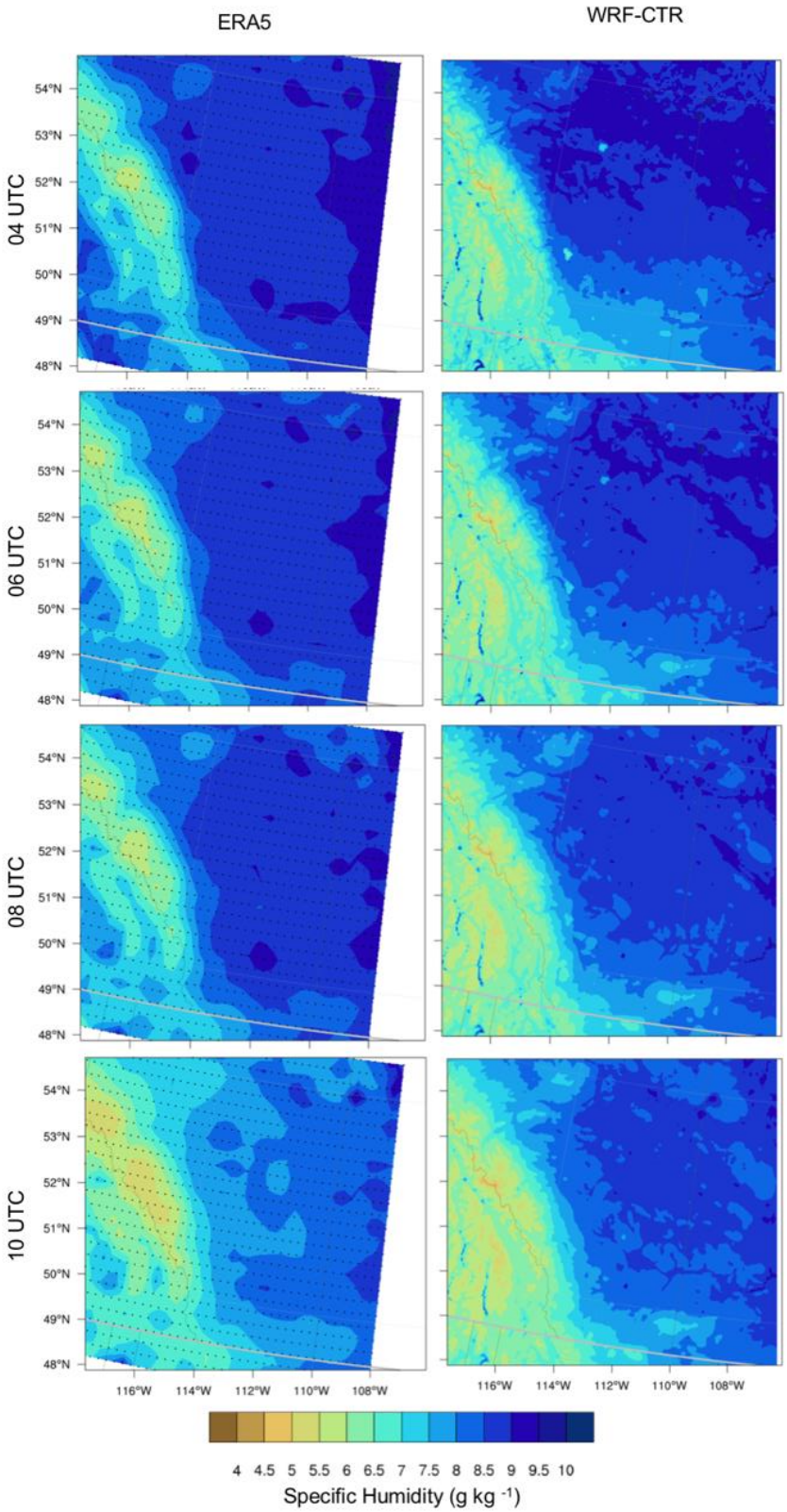

Figure E - 3 Comparison of monthly average of specific humidity in g kg^{-1} between ERA5 and WRF-CTR from 04 UTC until 10 UTC.